System architecture and circuit design for micro and nanoresonators-based mass sensing arrays

Grégory Arndt

N° d'ordre : 2011-24-TH

PhD Thesis

SPECIALITY: PHYSICS

Ecole Doctorale « Sciences et Technologies de l'Information des Télécommunications et des Systèmes »

Université Paris Sud

by :

Gregory ARNDT

Subject:

System architecture and circuit design for micro and nanoresonators-based mass sensing arrays

Defended the 12 December 2011 with the following jury members:

Dr Julien Arcamone	CEA-LETI, Minatec	Supervisor
Dr Nuria Barniol	Universitat Autonoma de Barcelona	Rapporteur
Dr Alain Bosseboeuf	Université Paris 11, IEF	President of the jury
Dr Eric Colinet	CEA-LETI, Minatec	Supervisor
Mme Rose-Marie Capella	Direction Générale de l'Armement	Examiner
Dr Philip Feng	Case Western University, ECSE Faculty	Rapporteur
Dr Jérôme Juillard	Supélec, SSE	Supervisor
Dr Pascal Nouet	CNRS, LIRMM	Examiner

Acknowledgments

I gratefully acknowledge the guidance provided by my director, Prof. Jérôme Juillard, for my entire PhD project. I always appreciated his advice and admired how available he always was even when our backgrounds and our research interests diverged. I am also very grateful for his help and guidance during the difficult task of scientific writing. I extend my thanks to Dr. Eric Colinet, particularly for the support and the supervision during my use of the many different devices employed in the different projects. I also thank him for choosing my PhD subject, and his tolerance to my attitude which can sometimes be quite stubborn. I am particularly grateful for his vision which provided depth and substance to my PhD. Dr. Julien Arcamone and Gérard Billot guided and taught me about the fabrication process and analog design and I will always be grateful for the skills they gave me.

Towards the end of my PhD, I particularly appreciated the help provided by Julien Philippe during his internship. He has characterized many co-integrated devices and provided invaluable expertise. I also appreciated his positive attitude and thoroughly enjoyed working with him. I also acquired first-hand experience of management through our interaction. I wish him all the best in his ongoing PhD studies. I am also grateful for the time and the interesting technical discussions I had with Paul Ivaldi, Dr. Cécilia Dupré, Dr. Laurent Duraffourg, Dr. Patrick Villard, Dr. Thomas Ernst, Dr. Sébastien Hentz, Patrick Audebert, Sylvain Dumas, Dr. Guillaume Jourdan and many others. I have also appreciate the enjoyable and profitable time spent in Leti due largely to the input and friendship of Olivier Martin, Matthieu Dubois, Eric Sage, Dr. Marc Belleville, and Pierre Vincent.

I thank Prof. Nuria Barniol and Dr. Philip Feng for their time and interest towards my PhD manuscript and defense. I appreciated their constructive remarks and advice. I also thank Prof. Pascal Nouet and Prof. Alain Bosseboeuf for coming to my PhD defense and their interesting questions. I was particularly grateful that Prof. Alain Bosseboeuf accepted to be the president of the jury.

Finally, my thoughts go to my family (particularly my parents) and friends who encouraged me during my studies. I am sure I could not have finished my PhD without their support.

Contents

Abstract

This manuscript focuses on micro or nanomechanical resonators and their surrounding readout electronics environment. Mechanical components are employed to sense masses in the attogram range (10^{-18} g) or extremely low gas concentrations. The study focuses particularly on circuit architectures and on resonators that can be implemented in arrays.

In the first chapter, several architectures for tracking the resonance frequency of the mechanical structure (used to measure a mass) are compared. The two major strategies are frequency locked-loops and self-oscillating loops. The former is robust and versatile but is area-demanding and difficult to implement into a compact integrated circuit. Self-oscillating loops are compact but are sensitive to parasitic signals and nonlinearity. This architecture was chosen as the focus of the PhD project because of its compactness, which is necessary for the employment of arrays of sensors.

In the second chapter, the electromechanical response of a sensor composed of a mechanical resonator and an appropriate electronics is assessed. Four resonators were chosen for mass spectrometry on the basis of their power consumption and integrability. Their transduction mechanisms are described and an electrical model of each component is developed. The study then focuses on the integration scheme of the resonators with their readout electronics. The technological process, development cost and electrical model of stand-alone, 2D- and 3D-integration schemes are described. Finally, the phase-noise improvement of integrating mechanical resonators in collectively addressed arrays is assessed.

In the third chapter, two self-oscillating loops using either a piezoelectric or a cross-beam resonator are described. The former demonstrates that is it possible to build a self-oscillating loop even when the resonator has a large V-shaped feed-through. In the second oscillator an excellent mass resolution is measured, comparable to that obtained with frequency-locked loops. The oscillator time response is below 100 µs, a level that cannot be reached with other architectures. The design of a promising integrated circuit in which four resonators self-oscillate simultaneously is described. Thanks to its compactness (7×7 mm^2), it is also possible to implement the circuits in arrays so as to operate 12 or more sensors. Finally, the integration on the same wafer of the resonator and its sustaining electronics is explored. We first focus on two projects whereby the electronics are 2D-integrated with a resonator using either capacitive or piezoresistive detection, and then on a third project using a 3D-integration scheme in which the circuitry is first fabricated and then the resonator is constructed on top on it.

General introduction

The omnipresence of CMOS technology in our everyday life demonstrates the success of microelectronics and the quest to make electronic circuits ever more compact. A key component of all circuits is the transistor which transforms an electrical signal to create logic functions (AND, NO, OR ...), memories, amplifiers, or more complex digital or analog electronic functions. As the dimensions of transistors diminish, they become faster and cheaper. Using the extraordinary capacity of the engineered fabrication process that is inherent to CMOS technology, scientists have also developed mechanical structures that interact physically at the micro- or nano-scale. Such components, called MicroElectroMechanical Systems (MEMS) are used as sensors that transform a physical stimulus into an electrical response, or as actuators where an electrical stimulus is converted into a mechanical or a physical response. Among the most sought after MEMS components are resonators that can be used to determine the stiffness or mass of the structure from its mechanical resonance.

As with transistors, the size of MEMS components is shrinking: progressing from MicroElectronicMechanical Systems to NanoElectroMechanical Systems (NEMS). For the sake of simplicity, the word "MEMS" is used throughout the rest of the thesis to designate indifferently MEMS or NEMS. Reducing the dimensions of the mechanical device has several benefits. Among them, the fabrication process is getting compatible with a CMOS process because the release dimensions are low.

In fact, the term NEMS refers to mechanical components that present at least two submicron dimensions. Scaling down the dimensions of the mechanical device presents several benefits: compact sensors can be fabricated, the sensing capability can be enhanced and the quality factor of the mechanical structure in air is commonly improved [Li 2007]. Indeed, the mechanical displacement of the nanoscale proof mass can be smaller than the mean free path of air reducing the effects of the viscous damping of air. Smaller components interact better with the nanoscale world and can sense unprecedented physical and biological variations. A notable challenge is to measure directly the mass of a single molecule [Knobel 2008, Naik 2009]. In practice, the limit of mass detection (or mass resolution) is commonly used by researchers to assess the performance of the device.

MEMS components have many other applications such as the measurement of force [Mamin 2001, Kobayashi 2011] (as in living cells), thermal fluctuation [Paul 2006], or biochemical reaction [Campbell 2006, Burg 2007]. In particular, NEMS components should eventually be used in mass spectrometry [Chiu 2008, Naik 2009] or gas

analysis [Boisen 2000, Hagleitner 2001, Lang 1998, Tang 2002]. With their fast response and their excellent mass resolution, the nano-devices can potentially achieve similar resolution to conventional mass spectrometers or gas chromatographs but at a lower cost, an enhanced compactness, and with a faster time response because they work at a higher frequency.

Mass spectrometry is used in a large range of applications such as medicine, biology, geochemistry and many others. In a conventional mass spectrometer the sample is first ionized, a mass analyzer is used to determine the mass-to-charge ratio of the ionized particles and finally a detector counts the number of ions [Aebersold 2003, Russell 1997, Domon 2006]. Conventional mass spectrometry can therefore be applied only to ionizable particles. Their inherent limits of resolution and response time have hindered progress of biology or other sciences [Naik 2009]. Critical parameters of mass spectrometers are their mass accuracy, resolving power (the ratio between the mass of the detected molecule and the minimum detectable mass) and dynamic range (ratio between the maximum detectable mass and the minimum detectable mass) [Domon 2006]. To obtain high-quality data commonly requires very long measurement times that can last up to 24 hours for certain samples. The limited performance of even the best equipment makes it impossible to reach what might be called the holy grail of biology: the measurement of the mass of every molecule of a single cell.

The Roukes group at the California institute of technology [Naik 2009] proposed to use MEMS components as an alternative to conventional mass spectrometers. The latest nano-components in the literature have mass resolutions sufficient to measure single molecules in a few seconds or less [Jensen 2008, Yang 2006]. A MEMS-based mass spectrometer would have several advantages: it would be sensitive to non-ionized molecules, would have a mass resolution independent of the mass of the molecule and would be relatively cheap thanks to microfabrication. To construct a MEMS-based mass spectrometer, several challenges must be resolved, notably the design and fabrication of robust MEMS components, the development of an architecture compatible with large arrays of MEMS devices, and the implementation of arrays of sensors with low coupling effects within the arrays.

The three years of research summarized up in this manuscript focus on the architecture analysis of a sensor constructed from a passive MEMS component and its associated readout electronics. The topologies of several relevant MEMS devices for mass spectrometry applications are presented and compared. The interface between the MEMS component and the first electronic amplifier is described in detail and its influence on the performance of the sensor is evaluated. Finally, the design and characterization of several MEMS-based sensors relevant for mass spectrometers are presented.

The manuscript is organized as follows. In the first chapter, a simple generic model of a MEMS resonator is introduced. From the description of the nano-device, different architectures that measure the resonance frequency of the nano-component are

presented. They can be divided into two categories: open and closed loop measurements. It is shown that although the first is simple to implement, it has a limited dynamic range and is expensive to design and fabricate. Open-loop architectures have therefore been rejected for mass spectrometry applications. In closed-loop architectures, the sensor (composed of the mechanical resonator and its sustaining electronics) has a larger dynamic range and in most cases is limited by the nano-component and not by the architecture itself. Two major types of closed loops are presented in the literature: self-oscillating loops and frequency-locked loops. The latter, comprising a phase-comparator, a low-pass filter and a Voltage-Controled Oscillator (VCO), is the most popular in the MEMS domain because it is robust and has low distortion. Most of all, the frequency range of the loop can be adjusted to prevent any undesired parasitic oscillations. Self-oscillating loops, comprising amplifiers and filters, are much cheaper to implement and can be very compact. In this architecture, the electronics compensates the attenuation and the phase-shift introduced by the nano-device at the resonance frequency so that the loop oscillates at this frequency. This approach is adopted in the rest of this work because the compactness of architecture is crucial when designing arrays of nano-resonators (as in mass spectrometers or gas analyzers). In the last section of chapter 1, various frequency measurement techniques necessary for self-oscillating loops are presented and compared.

The second chapter is dedicated to the theoretical assessment of different MEMS resonators. First, the electromechanical behavior of different resonator topologies is described. Four nano-resonators that meet the requirements of mass spectrometry were chosen on the basis of the following criteria: they should be individually addressable and have a low power consumption (to allow an implementation of the components in arrays). They use either electrostatic or piezoelectric actuation, and capacitive, piezoresistive or piezoelectric detection. In the second section, different MEMS and electronics integration schemes are presented. The process flow of each scheme is described and compared. A simple electrical model assesses the connection losses and the feed-through introduced by each integration scheme. Different actuation and layout techniques for enhancing the electrical response of the resonators are then described. Using the electromechanical behavior of the resonators, the integration schemes, and the results presented in the first chapter, it is then possible to determine the theoretical mass resolution of each nano-component and thus to objectively compare each resonator. The comparison is based on the 65nm-CMOS process flow of STMicroelectronics, which is compatible with the fabrication of nano-resonators and high frequency analog circuits. The last section is dedicated to the theoretical assessment of collectively-addressed parallel arrays of MEMS resonators. It is shown that an intrinsic electrical limitation remains when the size of the array increases.

In the third chapter, the different designs and experimental characterizations realized during the PhD project are presented. The initial focus is on stand-alone self-oscillating loops in which the sustaining electronics are built using commercial

amplifiers. The first self-oscillating loop uses a piezoelectric cantilever that introduces large feed-through. The main objective is to prevent the loop from oscillating at undesired frequencies due to the the feed-through. The frequency resolution of the loop is then compared to that of a frequency-locked loop. The second self-oscillating loop is based on a crossbeam resonator that oscillates at 20 MHz. The objective here is to implement a differential actuation that would compensate for the feed-through introduced by the coupling between each cable and within the silicon chip. The time response of the loop is then measured and shows to have state-of-the-art mass resolution. The second section presents the design of an ASIC for stand-alone crossbeams. The design comprises four self-oscillating loops (including four frequency counters) making it possible to operate four different crossbeams in parallel. Each self-oscillating loop is controlled and can be deactivated using an SPI interface with the computer. The coupling in the ASIC and in the MEMS chip can thus be evaluated. The final section presents the design and preliminary characterization of co-integrated MEMS-CMOS devices. In the first two designs, the nano-component is fabricated on the same wafer and next to the electronic circuit (2D monolithic integration). In the third design, the resonator and circuit are co-integrated in a 3D approach: the nano-device is fabricated on top of the transistors.

1 Harmonic detection of resonance

This chapter describes general architectures of electronic readout for MEMS resonators. It first presents a system architecture oriented description of the MEMS component and what limits its performance. It also describes common open- and closed-loop architectures for measuring the resonance frequency of the MEMS device. The limitations and specifications of the electronics are determined and compared. This chapter therefore provides a general description of the architecture of the MEMS component and its electronic readout and provides guidelines to design optimal MEMS resonators matching with their readout electronics.

In the manuscript, the following notation convention is used. The complex amplitude of a signal is written in italic, while its temporal expression is written using the "sans serif" font. For example, the complex amplitude voltage at the input of the electronics is referred to $V_{elec}(f)$, while its expression in the temporal domain is written $\mathsf{V_{elec}}(t)$. The DC component of the signal is referred with the subscript "-DC": $V_{elec-DC}$ in the example. The small signal component of $\mathsf{V_{elec}}(t)$ is referred to $\mathsf{v_{elec}}(t)$. Obviously, the amplitude of $\mathsf{v_{elec}}(t)$ is $v_{elec}(f)$ in the frequency domain. Generally, the power spectral density of the noise expressed at a node is referred to $S_{xx}(f)$ where xx describes the noise source. For example, the electronic noise expressed at v_{elec} is referred to $S_{elec}(f)$ (the node where the noise is expressed is given in the text when needed).

1.1 MEMS resonator model

The aim of this section is to establish a model of the MEMS component that is common to all resonant MEMS topologies presented in the manuscript, and that makes it possible to introduce the objectives and the constraints of harmonic detection of resonance. It provides the expressions of MEMS response to an input signal and of the MEMS generated noise. The physical explanations of the MEMS resonator will be further described in chapter 2.

1.1.1 Mechanical resonance

MEMS resonators are composed of a vibrating body acting as a mechanical resonator, means of actuation and means of detection (fig. 1.1). They can be decomposed into three main blocks: the actuation converts the input voltage into a force,

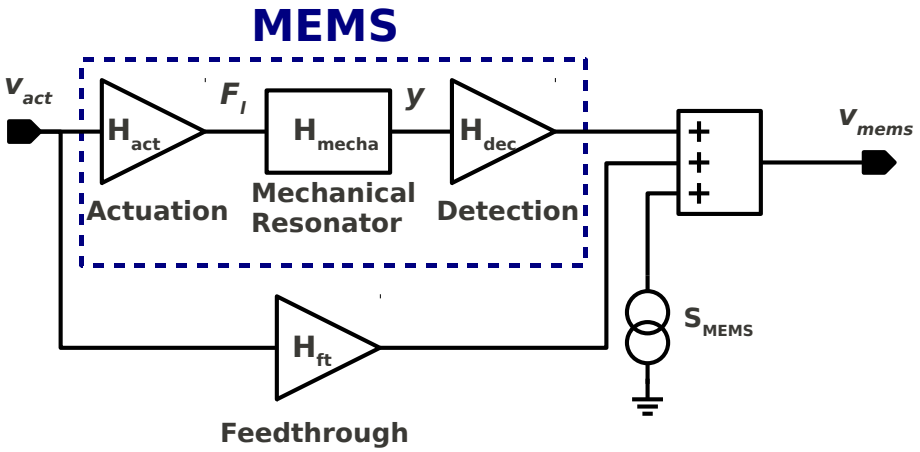

Figure 1.1: General MEMS model

the mechanical resonator creates a mechanical displacement of the vibrating mass from the applied force and finally, the detection converts the motion into an electrical signal. The complex representation of the input voltage, the force per unit of length acting on the vibrating mass, the mechanical displacement and the MEMS output electrical signal are denoted $v_{act}(f)$, $F_l(f)$, $y(f)$ and $v_{MEMS}(f)$ respectively. The mechanical resonator behavior is usually approximated as a mass-spring-damper system with a high quality factor Q and a resonance frequency $f_r = \sqrt{k/m}/(2\pi)$ where k and m are respectively the stiffness and the mass of the proof mass [Boisen 2011]. The force-to-displacement transfer function H_{mecha} can be modeled by a Lorentzian function:

$$H_{mecha} = \frac{y}{F_l} = \frac{\eta_A L}{m\left(2\pi f_r\right)^2} \frac{1}{1 + j\frac{f}{Qf_r} - \left(\frac{f}{f_r}\right)^2} \quad \text{(mechanical response)}, \tag{1.1}$$

where f is the frequency of F_l, and $\eta_A \approx 1$ is a normalization constant required to use the mass-spring-damper system approximation (more details on η_A is given in appendix B). L is the length along which the force is applied. The Resonance frequencies of the MEMS presented in this manuscript are in the range of 30 kHz to 100 MHz [Mile 2010, Colinet 2010, Ivaldi 2011b]. The quality factor of the MEMS can vary from 50 to 10 000 and highly depends on the environment of the device. If the MEMS is operated under atmospheric pressure, the air creates some viscous damping on the MEMS vibrating mass and thus reduces the mechanical displacement [Bao 2000]. The corresponding quality factor is generally around 100 [Li 2007, Bao 2000]. If the MEMS is operated at low pressure, the viscous damping is negligible and the quality factor depends on the mechanical characteristics of the vibrating mass. The quality factor is generally larger than 1000 [Bao 2000]. The transfer functions of the actuation H_{act} and the detection H_{det} can be considered independent of the frequency around f_r and introduce negligible phase-shift. The transfer function of the MEMS $H_{MEMS} = H_{act} \times H_{mecha} \times H_{det}$ therefore has the

following expression:

$$H_{MEMS} = \frac{v_{MEMS}}{v_{act}} = \frac{g_{MEMS}/Q}{1 + j\frac{f}{Qf_r} - \left(\frac{f}{f_r}\right)^2} \quad \text{(MEMS response)}, \tag{1.2}$$

where $g_{MEMS} = \frac{\eta_A Q L}{m(2\pi f_r)^2} |H_{act} H_{det}|$ is the modulus of H_{MEMS} at $f = f_r$. Note that the argument of H_{MEMS} at f_r is $\arg(H_{MEMS}) = -90°$. Figure 1.2 presents a typical resonance response of a MEMS corresponding to equation (1.2). The MEMS has a bandpass filter behavior. It can be determined that at $f = f_r\left(1 \pm \frac{1}{2Q}\right)$, the MEMS gain is reduced by 3 dB (or divided by $\sqrt{2}$). Similarly to amplifiers, it is said that the MEMS has a bandwidth of f_r/Q.

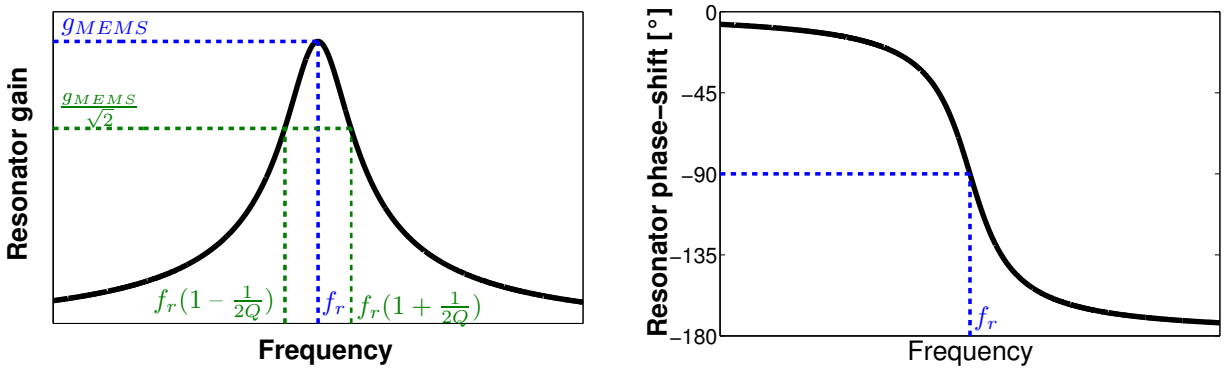

Figure 1.2: Theoretical Bode diagram of a MEMS resonator.

If the vibration amplitude is large, the resonator response becomes nonlinear, due for example due to mechanical stiffening effects, and the performance of the device as a sensing element can be jeopardized. All studies in this manuscript are therefore limited to resonators whose responses are considered linear. The critical actuation voltage, critical actuation force and critical mechanical displacement below which the behavior of the system can be considered as linear are respectively called v_{act-c}, F_{l-c} and y_c. Much work has been accomplished to study the nonlinear regime of micromechanical resonators [Juillard 2009, Kacem 2008, Mestrom 2009] but this topic is not treated in this manuscript.

1.1.2 Feed-through transmission

In addition to the previous electromechanical description of the resonator, it can be necessary to introduce input-to-output parasitic elements in the MEMS component model. They introduce so-called feed-through transmission that adds to the MEMS output signal a signal varying with v_{act}. Feed-through transmission may come from

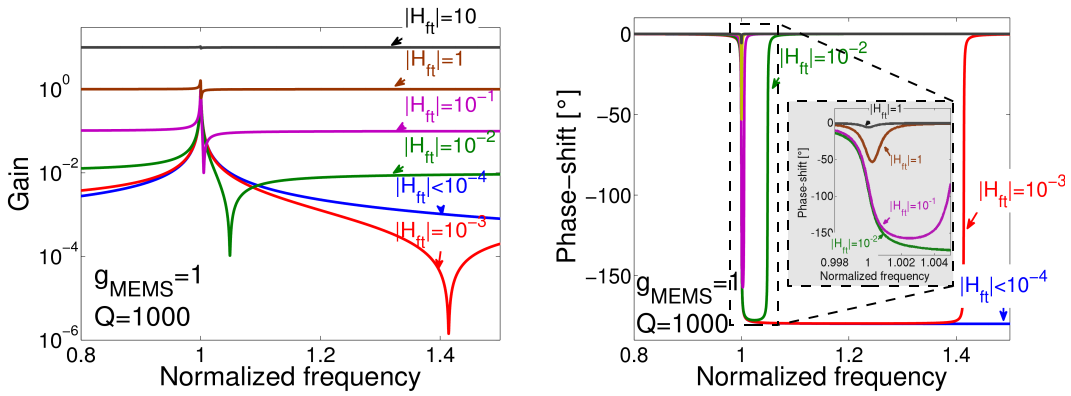

Figure 1.3: Theoretical effect of a constant feed-through on the gain (left) and the argument (right) of the MEMS transfer function

intrinsic capacitance in the MEMS, material losses (e.g. dielectric losses) or parasitic coupling [Lee 2009b, Arcamone 2010]. These effects can be modeled by adding to H_{MEMS} another transfer function $H_{ft}(f)$ that is independent of the mechanical resonator. The MEMS transfer function including feed-through transmission $H_{MEMSft}(f)$ becomes:

$$H_{MEMSft}(f) = \frac{g_{MEMS}/Q}{1 + j\frac{f}{Qf_r} - \left(\frac{f}{f_r}\right)^2} + H_{ft}(f). \tag{1.3}$$

To simplify the notations, H_{MEMSft} will be denoted H_{MEMS} in the rest of the manuscript. H_{ft} is usually modeled as a frequency independent transfer function with a real gain. Similarly to [Lee 2009b] figure 1.3 (left) shows the theoretical effect of a constant feed-through on the MEMS modulus response. Figure 1.3 (right) shows the theoretical effect of the feed-through on the phase-shift response induced by the MEMS. In figure 1.3, the feed-through is modeled by a frequency independent real gain. If the feed-through gain has a value close to the MEMS gain at the resonance, then the detection of the resonance frequency may become challenging.

Sometimes a more complex description of H_{ft} is required (see chapter 3). It can occur when the feed-through is locally compensated with adjustable components such as a variable capacitance and/or a variable resistance. The feed-through is locally minimized around f_r but can be significant out of the band of interest. Indeed, the MEMS intrinsic feedthrough can vary with the frequency and thus the feedthrough compensation is largely increased out of the resonance frequency. A model of V-shape feed-through can be expressed as the following:

$$H_{ft}(f) \propto \frac{f_r^{p_{ft}} - f^{p_{ft}}}{f_r^{p_{ft}}} \quad \text{(V-shape feed-through)}, \tag{1.4}$$

where p_{ft} is a parameters that models the frequency dependence of the V-shape feed-through. Figure 1.4 depicts a V-shape feed-through. A more detailed description of

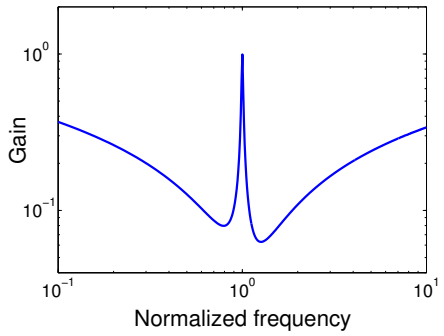

Figure 1.4: Illustration of a V-shape feed-through.

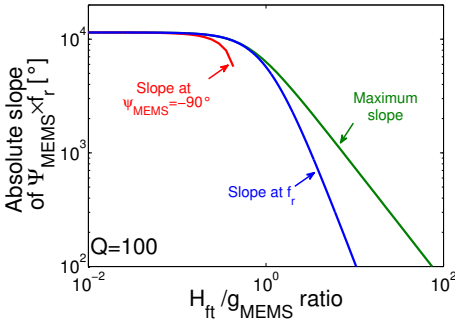

Figure 1.5: Evolution of $\left|\frac{\partial\psi_{MEMS}}{\partial f}\right|$ versus the feed-through transmission.

the V-shape model is given in chapter 3.

It will be shown that a key feature in MEMS resonators is the absolute value of the phase-slope, $\left|\frac{\partial\psi_{MEMS}}{\partial f}\right|$ because the resolution of the sensors improves when $\left|\frac{\partial\psi_{MEMS}}{\partial f}\right|$ increases. When there is no feed-through, the maximum of $\left|\frac{\partial\psi_{MEMS}}{\partial f}\right|$ is obtained for $f = f_r$ and its value is $2Q/f_r$. However, the feed-through can reduce this slope and thus the resolution of the sensor. Three scenarios are described in this subsection: the slope at f_r, the maximum absolute slope and the slope at the frequency where $\psi_{MEMS} = -90°$. It is assumed in this subsection that H_{ft} is real, positive and constant around f_r. From (1.3), we have:

$$\begin{aligned}\psi_{MEMS}(f) &= \arg\left[\frac{\frac{g_{MEMS}}{Q}\left(1-\frac{f^2}{f_r^2}\right) - j\frac{f}{Qf_r}\frac{g_{MEMS}}{Q} + H_{ft}\left[\left(1-\frac{f^2}{f_r^2}\right)^2 + \left(\frac{f}{Qf_r}\right)^2\right]}{\left(1-\frac{f^2}{f_r^2}\right)^2 + \left(\frac{f}{Qf_r}\right)^2}\right] \\ &= -\frac{\pi}{2} - \arctan\left[Q\left(\frac{f_r}{f}-\frac{f}{f_r}\right) + \frac{H_{ft}}{g_{MEMS}}\left[\frac{f_r}{f}Q^2\left(1-\frac{f^2}{f_r^2}\right)^2 + \left(\frac{f}{f_r}\right)\right]\right].\end{aligned} \tag{1.5}$$

The slope at f_r is thus:

$$\frac{\partial\psi_{MEMS}}{\partial f}(f_r) = \frac{1}{f_r}\frac{\frac{H_{ft}}{g_{MEMS}} - 2Q}{1+\left(\frac{H_{ft}}{g_{MEMS}}\right)^2} \approx -\frac{2Q/f_r}{1+\left(\frac{H_{ft}}{g_{MEMS}}\right)^2}. \tag{1.6}$$

It is clear that $\left|\frac{\partial\psi_{MEMS}}{\partial f}\right|(f_r)$ reduces with feed-through.

In the other scenarios, the calculations are more complex and thus are not presented in the manuscript. Figure 1.5 depicts the evolution of the slope versus the feed-through. One can see that the slope is optimum if the feed-through is ten times or more smaller than g_{MEMS}. The slope at $\psi_{MEMS} = -90°$ then decreases quickly. It

is also shown on the figure that it can be interesting to actuate the MEMS resonator at a frequency slightly different from f_r in order to improve the slope.

1.1.3 MEMS noise sources

The readers interested in thebasics of noise analysis should consult [Rubiola 2008]. The definitions and the notations related to noise processes are based on the same book. The random processes in the manuscript are considered as stationary[1] and ergodic[2]. A noise process is commonly described by its power spectral density (PSD) defined as:

$$\begin{aligned} S_x(f) &\equiv \mathcal{F}[\Gamma_\tau(\mathsf{x})] \equiv \int_{\mathbb{R}} \Gamma_\tau(\mathsf{x})\, e^{-2\pi j f \tau} \mathrm{d}\tau \quad \text{(power spectral density)} \\ &\equiv \int_{\mathbb{R}} \mathbb{E}_\tau\{\mathsf{x}(t)\,\mathsf{x}(t+\tau)\}\, e^{-2\pi j f \tau} \mathrm{d}\tau, \end{aligned} \tag{1.7}$$

where $\mathcal{F}[\mathsf{x}(t)] \equiv \int_{\mathbb{R}} \mathsf{x}(t)\, e^{-2\pi j f t} \mathrm{d}t$ is the Fourier transform of $\mathsf{x}(t)$, $\mathbb{E}\{\}$ is the statistical expectation and $\Gamma_\tau(\mathsf{x}) \equiv \mathbb{E}_\tau\{\mathsf{x}(t)\,\mathsf{x}(t+\tau)\}$ is the auto-correlation function of $\mathsf{x}(t)$. The most common noise representation is white noise where the power spectral density is independent of the frequency. In opposition, other noises are referred to colored noises. For example, pink or flicker noise has a PSD inversely proportional to the frequency.

An inherent noise in the resonator is thermomechanical noise that can be modeled as a white noise acting at the input of the mechanical resonator block [Cleland 2002]. Other noise sources can be considered such as Johnson noise or from more complex phenomena as invariant fluctuations [Cleland 2002]. The different noises generated by the MEMS can be modeled as a noise source at the output of the MEMS that is composed of white noise, frequency-dependent noise, and more complex behavior (e.g. long term temperature variations), with a PSD $S_{MEMS}(f)$. Another important characteristic of the MEMS is its phase-noise. Its definition is based on the expression of a "noisy" signal:

$$\mathsf{v}_{MEMS}(t) = v_{MEMS}[1+\alpha(t)]\cos[2\pi f_r t + \varphi(t)], \tag{1.8}$$

where v_{MEMS} is the noiseless amplitude of the signal, f_r is the signal frequency, t is the time, $\alpha(t)$ is the relative amplitude noise and $\varphi(t)$ is the phase-noise. Assuming that the noise is equilibrated , the PSD of $\alpha(t)$ and $\varphi(t)$ are determined from $S_{MEMS}(f)$ as follows:

$$S_\alpha(f) = S_\varphi(f) = 2\frac{|S_{MEMS}(f)|}{v_{mems}^2} \quad \text{(phase noise)}. \tag{1.9}$$

[1] This condition is closely related to the concept of repeatability [Rubiola 2008].
[2] This condition is closely related to the concept of reproducibility [Rubiola 2008].

Based on the MEMS model illustrated in figure 1.1, various possible readout architectures used for the harmonic detection of resonance are described in the following sections of this chapter. We also provide a methodology capable of evaluating the performance of a MEMS resonator with its surrounding electronics.

1.2 Open loop resonant frequency tracking

Since f_r depends upon the mass and the stiffness of the beam, the MEMS can be used to sense a mass variation of the beam. In this context, the readout electronics should therefore dynamically track the MEMS resonance frequency. Major criteria to evaluate the sensor performance are the frequency resolution, the dynamic range and the mass responsitivity. The latter only depends on the design of the MEMS whereas the resolution and the dynamic range depend both on the MEMS characteristics and the frequency tracking readout architecture. The mass responsitivity $\Re$ is defined as follows:

$$\Re = \frac{\Delta f}{\Delta m} \quad \text{(mass responsitivity)}, \tag{1.10}$$

where Δf is the MEMS resonance frequency variation when the MEMS is loaded by a mass variation Δm.

A mass uniformly added to the MEMS vibrating mass affects f_r as follows:

$$\Delta f = \frac{\mathrm{d}f_r}{\mathrm{d}m}\Delta m \approx \frac{f_r}{2m}\Delta m \Rightarrow \Re = \frac{f_r}{2m} \tag{1.11}$$

The resolution σ_m is the minimal detectable mass. It is determined from the frequency resolution σ_{f_r}. Since the relationship between σ_m and σ_{f_r} only depends on the responsitivity of the resonator, it is quite common to characterize and analyze the sensor performance from the MEMS frequency resolution:

$$\sigma_m = \frac{\sigma_{f_r}}{\Re} \quad \text{(mass resolution)}. \tag{1.12}$$

σ_{f_r} is the variance of the resonance frequency variation. The resonance frequency presents long term variation due to environmental changes such as temperature variations. Under such considerations, the classical variance estimator, defined as $\sigma_{f_r} = \sqrt{\lim_{T\to\infty} \frac{1}{T}\int_0^T \left[f - \mathbb{E}\left\{f\right\}\right]^2 \mathrm{d}t}$ improperly estimates the frequency resolution as its value is dominated by the long term environmental variations.

It is often replaced by the Allan variance estimator [Rubiola 2008] that estimates the variance of two consecutive elements and thus reducing the effect of long time drift. The figure 1.6 illustrates the measurement of the frequency resolution of a periodic signal. The transition times of the signal (defined from the rising edges)

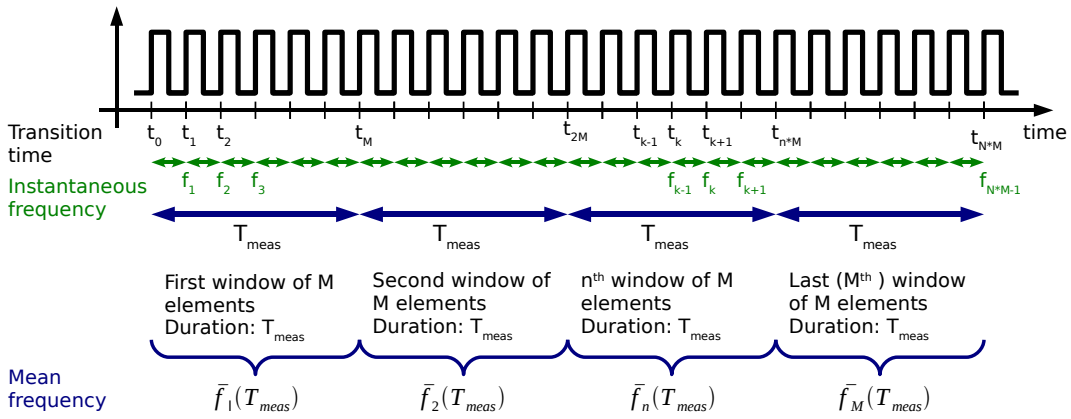

Figure 1.6: Frequency measurement.

are denoted t_k starting at t_0 and finishing at $t_{N\times M}$. From the elements t_k, the instantaneous period and the instantaneous frequency are calculated:

$$\begin{cases} T_k = t_k - t_{k-1} & \text{(instantaneous period)} \\ f_k = \frac{1}{t_k - t_{k-1}} & \text{(instantaneous frequency)} \end{cases}. \tag{1.13}$$

The elements f_k are decomposed into measurement windows in which they are averaged over a time lapse T_{meas}:

$$\overline{f_n}\,(T_{meas}) = \frac{1}{M} \sum_{k=(n-1)\times M}^{n\times M} f_k, \qquad \text{(mean frequency over } T_{meas}) \tag{1.14}$$

where M is the number of elements f_k during T_{meas}. Finally the Allan variance for a integration time T_{meas} is defined as:

$$\sigma^2_{\delta f/\mathrm{f}}\,(T_{meas}) = \mathbb{E}\left\{ \frac{1}{2} \left[\frac{\overline{f_{n-1}}\,(T_{meas}) - \overline{f_n}\,(T_{meas})}{\overline{f_n}\,(T_{meas})} \right]^2 \right\} \quad \text{(AVAR)}. \tag{1.15}$$

The Allan deviation is defined from the standard variance as:

$$\sigma_{\delta f/\mathrm{f}}\,(T_{meas}) = \sqrt{\sigma^2_{\delta f/\mathrm{f}}\,(T_{meas})} = \sqrt{\mathrm{AVAR}} \quad \text{(ADEV)}. \tag{1.16}$$

$\sigma_{\delta f/f}$ can also be determined from the PSD of the resonance frequency measurement:

$$\sigma^2_{\delta f/f}\,(T_{meas}) = \int_0^\infty S_{\delta f/f} \frac{2\sin^4(\pi T_{meas} f)}{(\pi T_{meas} f)^2} \mathrm{d}f, \tag{1.17}$$

where $S_{\delta f/f}\,(f)$ is the PSD of the relative frequency variation. Figure 1.7 presents the relation between the spectrum of $S_{\delta f/f}$ and $\sigma^2_{\delta f/f}$. It can be seen that in the case where the noise is white, $\sigma_{\delta f/f}$ reduces when T_{meas} is increased. However, colored noises and frequency drifts limit the frequency resolution and define a range of values

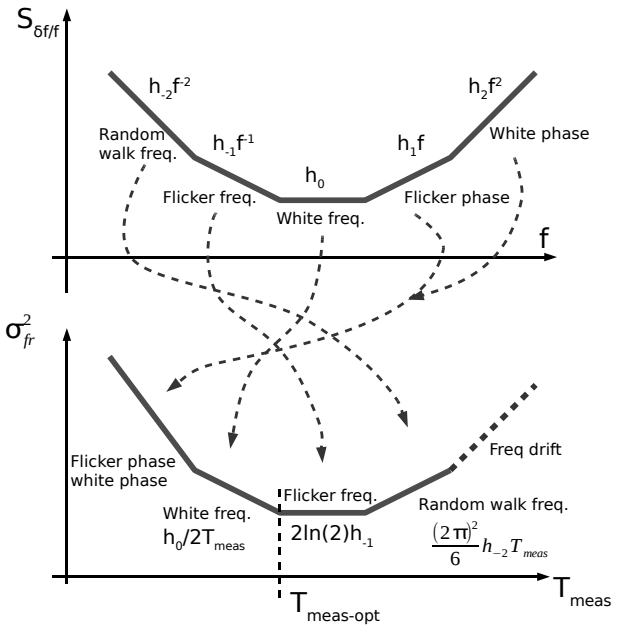

Figure 1.7: Relationship between the PSD spectra and the Allan variance reproduced from [Rubiola 2008]

of T_{meas} for which $\sigma_{\delta f/f}$ is minimal. If the measurement time lapse is larger than $T_{meas-opt}$, not only the measurement will be longer but it can also deteriorate the frequency resolution.

Finally the dynamic range of the sensor should be evaluated. It will be show in the following sections that when a "large" mass is added to the mechanical resonator, the mass resolution of the sensors can be reduced (open-loop architecture) and/or the responsitivity can behave nonlinearily (open- and closed-loop architecture). In some cases, the electronic circuit is simply not operational at a large frequency shift. A first definition of the dynamic range can be based on the added mass (or the frequency shift) for which the resolution is reduced by 3 dB.

Furthermore, with large added mass, the MEMS response $\Delta f = f(\Delta m)$ is generally not linear anymore because the added mass to mechanical structure modifies the geometry of the proof mass and thus changes it stiffness. It can also add further stress in the proof mass that will affect the resonance frequency of the MEMS. It should be mentioned that the nonlinear responsitivity can be calibrated and compensated but only to some extend. The dynamic range is therefore determined from the evolution of the resolution versus the added mass but is also limited to an upper value due to the nonlinear behavior of the responsitivity. A typical value of 10% can be taken for the dynamic range of the MEMS resonator.

1.2.1 Frequency sweep

The open-loop response of a MEMS resonator can be obtained by measuring the gain and phase of the device over a range of frequency. The measurement being done, a curve similar to figure 1.2 can be obtained. The resonance frequency corresponds to the maximum of the gain. This technique is however very time consuming because one has to sweep the whole frequency span. Moreover, in order to achieve a good frequency resolution, the minimal step of frequency sweep must be very narrow what increases largely the measurement duration (because a large number of points are required).

The frequency resolution is limited by the equivalent output voltage noises of the MEMS response and the electronic equipments. From the PSD of the MEMS+electronics noise expressed at v_{MEMS}, one can determine the corresponding PSD of the phase noise of as:

$$S_{\varphi_{MEMS+elec}}(f) = 2\frac{S_{MEMS+elec}(f)}{\left[\left|H_{MEMS}(f)\right| v_{act-c}\right]^2}. \tag{1.18}$$

The PSD of the frequency noise can be determined from $S_{\varphi_{MEMS+elec}}$:

$$S_f = f^2 S_{\varphi_{MEMS+elec}} = 2f^2\frac{S_{MEMS+elec}}{\left(\left|H_{MEMS}\right| v_{act-c}\right)^2}. \tag{1.19}$$

The frequency resolution is defined as the standard deviation of the frequency measurement:

$$\begin{aligned}\sigma_{f_r} &\equiv \sqrt{\int_{f_r-1/T_{meas}}^{f_r+1/T_{meas}} \left|S_f(f)\right| \mathrm{d}f} \\ &\approx f_r\sqrt{2\frac{\left|S_{\varphi_{MEMS+elec}}(f_r)\right|}{T_{meas}}} \quad \text{(Open-loop frequency resolution)} \\ &\approx 2f_r\frac{\sqrt{\left|S_{MEMS+elec}\right|}}{g_{MEMS}v_{act-c}\sqrt{T_{meas}}}.\end{aligned} \tag{1.20}$$

It is assumed that $1/T_{meas} \ll f_r$ and that in the interval $\left[f_r - \frac{1}{T_{meas}}\,;\, f_r + \frac{1}{T_{meas}}\right]$ the variations of $S_{MEMS+elec}$ and $S_{\varphi_{MEMS+elec}}$ are negligible. It will be shown in section 1.3 that the frequency resolution with this measurement technique is worse than the one obtained in closed-loop measurements.

1.2.2 Amplitude or phase-shift variation measurement

This technique has been developed to avoid the frequency sweep technique previously mentioned. It consists in setting the actuation frequency to f_r [Albrecht 1991,

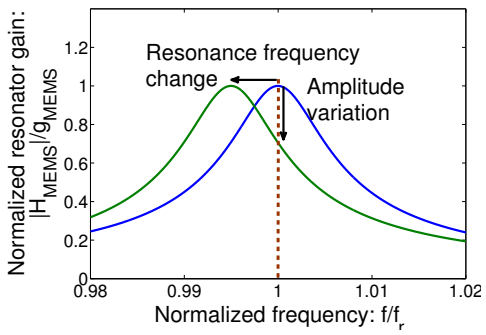

Figure 1.8: Illustration of a measurement of an-amplitude variation.

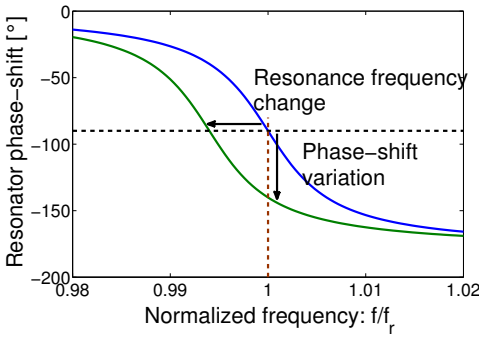

Figure 1.9: Illustration of a measurement of a phase-shift variation.

Taylor 2010]. When the resonance frequency decreases (due to an added mass on the MEMS), the voltage at the output of the resonator is reduced. The figure 1.8 presents the Lorentzian curve of $|H_{MEMS}|$ for two resonance frequencies. It is clear from equation (1.2) that if f_r decreases due to an added mass (the corresponding resonant frequency is denoted $f_r^{\Delta m}$, the resonant frequency when no mass is loaded is denoted f_{r0}) then $|H_{MEMS}|$ decreases with $f_r^{\Delta m}$ so that by measuring $|H_{MEMS}|$, it is possible to determine $f_r^{\Delta m}$.

The corresponding resolution can be determined similarly to subsection 1.2.1:

$$\begin{aligned}\sigma_{f_r} &\approx f_r^{\Delta m}\frac{\sqrt{2\left|S_{MEMS+elec}\left(f_{r0}\right)\right|}}{\left|H_{MEMS}\left(f_{r0}\right)\right|v_{act-c}\sqrt{2T_{meas}}} \\ &\approx f_r^{\Delta m}\sqrt{Q^2\left[1-\left(\frac{f_{r0}}{f_r^{\Delta m}}\right)^2\right]^2+\left[\frac{f_{r0}}{f_r^{\Delta m}}\right]^2}\frac{\sqrt{2\left|S_{MEMS+elec}\left(f_r^{\Delta m}\right)\right|}}{g_{MEMS}v_{act-c}\sqrt{2T_{meas}}}.\end{aligned} \tag{1.21}$$

If the ratio $f_{r0}/f_r^{\Delta m}$ increases (i.e. $f_r^{\Delta m}$ decreases) then the frequency resolution also decreases. The evolution of the frequency resolution for a varying f_r is depicted in fig. 1.10. This measurement scheme both suffers from a limited dynamic range and a limited frequency resolution. From eq. (1.21), if the dynamic range is determined when the resolution is increased by 3 dB, then the amplitude variation measurement has a dynamic range of 0.5 %.

It is possible to improve the frequency resolution by measuring the MEMS phase-shift variation rather than the amplitude variation (fig. 1.9). The phase-shift introduced by the resonator is :

$$\psi_{MEMS} = \arg\left(H_{MEMS}\right) = -\arctan\left[\frac{\frac{f_{r0}}{Qf_r^{\Delta m}}}{1-\left(\frac{f_r^0}{f_r^{\Delta m}}\right)^2}\right]. \tag{1.22}$$

It is therefore possible to determine the variation of the resonance frequency from

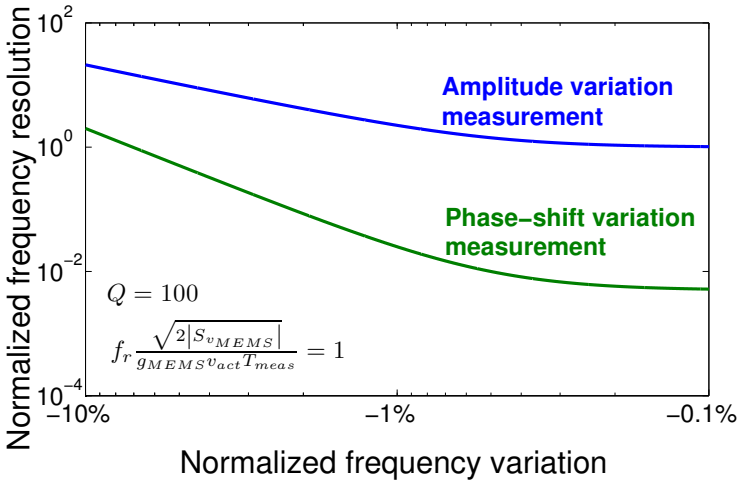

Figure 1.10: Evolution of the frequency resolution versus the resonant frequency variation for amplitude and phase-shift variation measurements.

the phase-shift introduced by the MEMS:

$$\tan\left(\psi_{MEMS}\right) + \frac{f_{r0}}{Q f_r^{\Delta m}} - \left(\frac{f_{r0}}{f_r^{\Delta m}}\right)^2 \tan\left(\psi_{MEMS}\right) = 0. \tag{1.23}$$

From $f_r^{\Delta m} \leq f_{r0}$ and eq. (1.23), it is clear that $\psi_{MEMS} \leq -90°$. The resonance frequency can be determined by selecting the real and positive solution:

$$f_r^{\Delta m} = f_{r0} \frac{2\tan\left(\psi_{MEMS}\right)}{1/Q + \sqrt{\left(1/Q\right)^2 + \left[2\tan\left(\psi_{MEMS}\right)\right]^2}}. \tag{1.24}$$

This frequency measurement technique is based on ψ_{MEMS}. To calculate the resolution of this technique, the phase-noise at the output of the MEMS should be determined from equation (1.9). If the noise is low, the frequency resolution is determined from the slope of the transfer function between ψ_{MEMS} and $f_r^{\Delta m}$:

$$\begin{aligned}\sigma_{f_r} &= \left.\frac{\mathrm{d}f_r^{\Delta m}}{\mathrm{d}\psi_{MEMS}}\right|_{f=f_r^0} \sqrt{\frac{\left|S_{\varphi_{MEMS+elec}}\left(f_{r0}\right)\right|}{2T_{meas}}} \\ &\underset{\psi_{MEMS}\approx -90°}{\approx} \frac{f_{r0}}{2Q} \frac{\sqrt{2\left|S_{MEMS+elec}\left(f_{r0}\right)\right|}}{g_{MEMS} v_{act-c} \sqrt{2T_{meas}}} = \frac{f_{r0}}{2Q} \sqrt{\frac{\left|S_{\varphi_{MEMS+elec}}\left(f_{r0}\right)\right|}{2T_{meas}}}.\end{aligned} \tag{1.25}$$

The expression of $\frac{\mathrm{d}f_r^{\Delta m}}{\mathrm{d}\psi_{MEMS}}$ is complex and therefore is not presented in the manuscript. Note that it depends on the feed-through as described in subsection 1.1.2. The evolution of the frequency resolution versus f_r and therefore $\frac{\mathrm{d}f_r^{\Delta m}}{\mathrm{d}\psi_{MEMS}}$ is depicted in Fig. 1.10 (it was considered in this case that the feed-through was negligible). One can

see from figure 1.10 that the phase-shift variation measurement presents a better frequency resolution than the two other open-loop measurements previously described. The dynamic range of the measurement is however limited as for the amplitude variation measurement. Numeric resolution of eq. 1.25 shows that if the dynamic range is determined when the resolution is increased by 3 dB, then the phase-shift variation measurement has a dynamic range of about 0.32 %. In general, the phase-shift variation measurement is preferred to amplitude variation measurement due to its better frequency resolution to the cost of a little dynamic range reduction.

It has been shown in the three presented open-loop measurements that they either suffer from a poor frequency resolution or a limited dynamic range. Closed-loop measurement techniques allow overcoming these limitations.

1.3 Closed loop resonant frequency tracking

In order to improve the dynamic range of the sensor, oscillator architectures are implemented. Such systems consist in embedding the MEMS in a loop so that it oscillates at its resonance frequency. f_r can then be measured by determining the oscillation frequency. There are two major architectures of oscillators: self-oscillating loops (SOL) and Frequency-Locked Loops (FLL) [Rubiola 2008]. The first one, depicted in figure 1.11a amplifies and filters the MEMS output signal so that the transfer functions of the MEMS and the sustaining electronics respect specific conditions in terms of gain and phase only at f_r. On the other hand, the FLL topology depicted in figure 1.11b consists in controlling the actuation frequency based on the phase-shift introduced by the MEMS. The feedback electronic circuit ensures that the MEMS induced phase-shift always remains at its value corresponding to the resonance frequency: the MEMS thus oscillates at f_r.

In that regard, the FLL feedback electronics can be considered as a nonlinear amplifier and a phase-shifter. However, the main difference with SOL architectures lays on the use in the architecture of a supposedly high quality VCO. Indeed, the VCO is a signal source that provides a sinusoidal signal at a single frequency, with little distortions and phase-noise. The MEMS actuation is as close as possible to ideal. Moreover, the architecture offers the ability to control the phase-shift introduced by the MEMS and the actuation frequency (that is controlled by u at the input of the VCO). It is then possible to set boundaries to the oscillation frequency and avoid any undesired oscillations that would originate from parasitic crosstalk.

The SOL and the FLL architectures are described in more details in the following subsections. They are compared in terms of complexity, cost and frequency resolution.

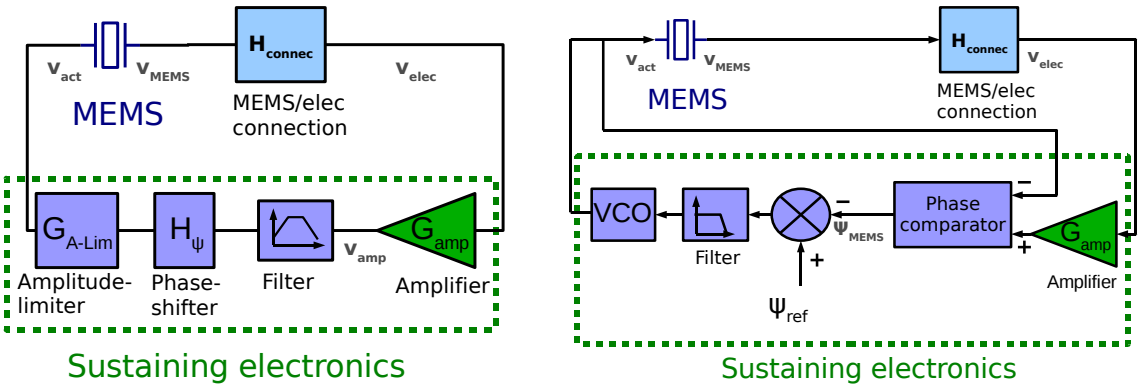

Figure 1.11: General architecture of (a) a self-oscillating loop, (b) a frequency-locked loop

1.3.1 Self-oscillating loop

SOL architectures are very compact, quite simple to implement and it makes them very attractive for MEMS designers. For example, Vittoz [Vittoz 1988] realized in 1988 an oscillator based on a quartz resonator and a sustaining electronics with about 30 transistors. The literature presents several realizations of ASIC for self-oscillating loops [Verd 2005, Arcamone 2007]. Their area consumption varies with the technological implementation of the electronics. The area can be as small as 200 µm^2 (if the output buffer stage in omitted, see chapter 3) but integrated circuit are generally in the order of 0.1 to few mm^2 [Verd 2005, Arcamone 2007, Vittoz 1988, Zuo 2010]. If the electronic is realized using commercial discrete circuits, the area of the oscillator is around few hundreds of mm^2 [Akgul 2009].

The main interests of self-oscillating loop are therefore their compactness and low-cost. They can however be overwhelmed by distortion, nonlinearity, parasitic oscillations... Those limitations are described in this section.

1.3.1.1 Oscillation conditions

To study SOL, one must virtually open the loop for example between the amplitude-limiter block and the MEMS. The corresponding transfer function is analyzed in order to determine the oscillation conditions. In the case illustrated on fig. 1.11a, the system is composed of a MEMS resonator and a linear sustaining electronic circuit. The open-loop transfer function $H_{OL}(f)$ is:

$$H_{OL}(f) = H_{MEMS}(f) \times H_{elec}(f) \quad \text{(open-loop transfer function)}, \tag{1.26}$$

where $H_{elec}(f)$ is the transfer function of the sustaining electronic circuit. The oscillations build up at frequencies closed to f_{osc} if:

$$|H_{OL}(f_{osc})| > 1 \text{ and } \arg[H_{OL}(f_{osc})] = 0 \quad \text{(Barkhausen criteria)}. \tag{1.27}$$

These relationships are known as the Barkhausen criteria. The oscillations stabilize when:

$$H_{OL}\left(f_{osc}\right) = 1. \tag{1.28}$$

The sustaining electronic circuit must ensure that the conditions of equation (1.27) are respected only at f_r. It must also include a mechanism that stabilizes the oscillations to a given amplitude to prevent the MEMS to oscillate at large amplitudes or from behaving nonlinearly.

A SOL contains amplifiers, filtering blocks and a phase-shifter block. The amplification and the phase-shifting block ensure that the conditions of equation (1.27) are respected at f_r. In other words, based on equation (1.2), the sustaining electronic must respect in terms of gain and phase the following conditions (assuming that the feed-through is negligible):

$$|H_{elec}| > 1/g_{MEMS} \text{ and } \arg\left(H_{elec}\right) = +90°. \tag{1.29}$$

The literature presents many techniques to realize the phase-shifter.

- The simplest one uses a first order inverting low-pass filter operating in its cut-off frequency regime [Rubiola 2008, Bienstman 1995, Arndt 2011]. It has a transfer function $H_{LPF} = \frac{-1}{1+jf/f_c}$ and its cut-off frequency f_c satisfies $f_c \ll f_r$. The phase-shift introduced by the low-pass filter is about $\arg\left(H_{LPF}\right) \approx +90°$ but this filter has a gain of $|H_{LPF}| \approx f_r/f_c \ll 1$ and attenuates the signal. It can be shown by studying the gain at the frequency corresponding to $\arg\left[H_{OL}\left(f_{osc}\right)\right] = 0$, that the optimum value of f_c that respects the conditions in phase while introducing a maximum gain is $f_c = f_r$. However, this optimum can be matter of debate because it supposes that the feed-through is negligible. Moreover the slope of $\psi_{MEMS}\left(f_{osc}\right)$ is reduced compared to $\psi_{MEMS}\left(f_r\right)$ and it will be shown in the following subsection that the oscillator resolution depends on the slope of $\psi_{MEMS}\left(f_{osc}\right)$. The oscillator resolution is therefore reduced if f_c/f_r is increased. It is rather common to set $f_c \approx f_r/10$.
- Instead of using a low-pass filter, it is also possible to use a first order high-pass filter with a transfer function of $H_{HPF} = \frac{jf/f_c}{1+jf/f_c}$ so that its cut-off frequency f_c satisfies $f_c \gg f_r$. Attenuation for the high-pass and low-pass filter are similar.
- A delay line is another interesting candidate to realize a phase-shift block. It consists in a low-resistive line with a distributed grounded capacitance. The distributed R-C filters introduces a large delay while introducing negligible attenuation. The delay line at frequency below 10 MHz is however very difficult to implement in an integrated circuit.
- Other phase-shifter topologies use an active component such as a series of inverters [Rubiola 2008, Bahreyni 2007]. Obviously, the value of the delay τ is:

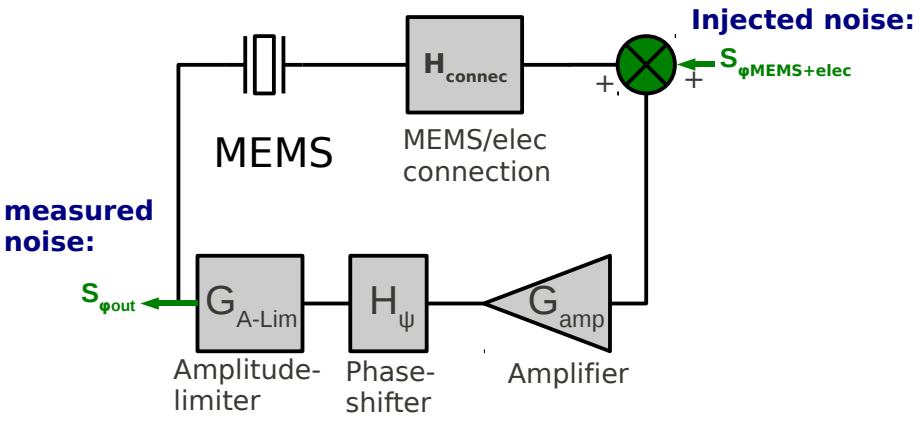

Figure 1.12: Noise injection in a self-oscillating loop

$\tau = 3/(4f_r)$ corresponding to a phase-shift of $+90° = -270°$. A Delay Lock-Loop (DLL) can also be used to realize the phase-shifter [Susplugas 2004]. Interests and drawbacks of each phase-shifter architecture are described in subsection 1.3.1.4.

In addition to the phase-shifter other filtering blocks are implemented to prevent that eq. (1.27) is satisfied for other frequencies than f_r.

Finally, concerning the mechanism that stabilizes the oscillations, one solution can be an Automatic Gain Control (AGC) so that the sustaining electronic circuit always remains linear [Rubiola 2008, He 2010]. It consists of an amplifier whose gain is adapted in real time as the input amplitude increases. Other mechanisms such as saturation mechanisms can be used to stabilize the oscillations but they introduce more nonlinearity. These mechanisms are described later in this subsection.

1.3.1.2 Frequency resolution of the oscillator

From equation (1.12), the mass resolution of the oscillator is determined from its relative frequency variation noise. In fact, in oscillators, a phase-noise measurement is usually preferred and the relative frequency variation noise can then be easily determined from the phase-noise [Rubiola 2008]:

$$S_{\delta f/f} = \left(\frac{f_r - f}{f_r}\right)^2 S_\varphi. \tag{1.30}$$

In the literature, Leeson's formula [Leeson 1966, Rubiola 2008] relates the PSD of the phase-noise introduced in the loop to the PSD of the closed-loop phase-noise

that is usually measured at the electronics output (Fig. 1.12):

$$H_{\varphi}(f) = \frac{\text{Closed-loop phase-PSD}}{\text{Open-loop phase injected-PSD}} = \frac{S_{\varphi_{out}}(f)}{S_{\varphi_{MEMS+elec}}(f)}$$
$$= 1 + \left[\frac{1}{(f-f_r)\,\frac{\partial \psi_{MEMS}}{\partial f}\,(f_{osc})}\right]^2 \quad \text{(Leeson formula).} \tag{1.31}$$

The PSD of the closed-loop relative frequency variation noise can be determined from equation (1.30).

Assuming that $|f - f_r| \ll 1/\left|\frac{\partial \psi_{MEMS}}{\partial f}\right|(f_{osc})$ and $f_{osc} \approx f_r$ it is possible to determine the PSD of the oscillator relative frequency variation:

$$S_{\delta f/f} = \frac{S_{\varphi_{MEMS+elec}}}{\left[f_{osc}\frac{\partial \psi_{MEMS}}{\partial f}\,(f_{osc})\right]^2}. \tag{1.32}$$

Assuming that $S_{\varphi_{MEMS+elec}}$ does not vary with f (i.e. white noise), the frequency resolution of the loop is:

$$\sigma_{f_r} = \frac{1}{\frac{\partial \psi_{MEMS}}{\partial f}\,(f_{osc})}\sqrt{\frac{S_{\varphi_{MEMS+elec}}}{2T_{meas}}} \quad \text{(SOL frequency resolution)}$$
$$= \frac{f_r}{2Q}\sqrt{\frac{S_{\varphi_{MEMS+elec}}}{2T_{meas}}} \quad \text{if } H_{ft} \ll g_{MEMS} \text{and } f_{osc} \approx f_r. \tag{1.33}$$

Comparing the frequency resolution of the SOL-architecture with the open-loop architectures expressed in equations (1.20), (1.21) and (1.25) of pages 16, 17 and 18, it is clear that the SOL-architecture provides a frequency resolution better or equal to the ones of the open-loop architectures.

The noise introduced in the loop comes from the contribution of the MEMS thermomechanical noise S_{thermo} expressed at F_l, other MEMS noise $S_{MEMS_{\bar{th}}}$ expressed at v_{MEMS}, the electronics circuit noise S_{elec} expressed at v_{elec}, the total electronic noise expressed at the input of the electronics is:

$$S_{MEMS+elec} = S_{thermo}\left|H_{mecha}H_{det}H_{connec}\right|^2 + S_{MEMS_{\bar{th}}}\left|H_{connec}\right|^2 + S_{elec}, \tag{1.34}$$

where H_{connec} is the transfer function of the MEMS-to-electronics connection. From equation (1.9), the phase-noise introduced at the amplifier input has therefore the following expression:

$$S_{\varphi_{MEMS+elec}} = 2\left[\frac{S_{thermo}}{F_{l-c}^2} + \frac{S_{MEMS_{\bar{th}}}}{\left|F_{l-c}\times H_{mecha}H_{det}\right|^2} + \frac{S_{elec}}{\left|F_{l-c}\times H_{mecha}H_{det}H_{connec}\right|^2}\right].$$

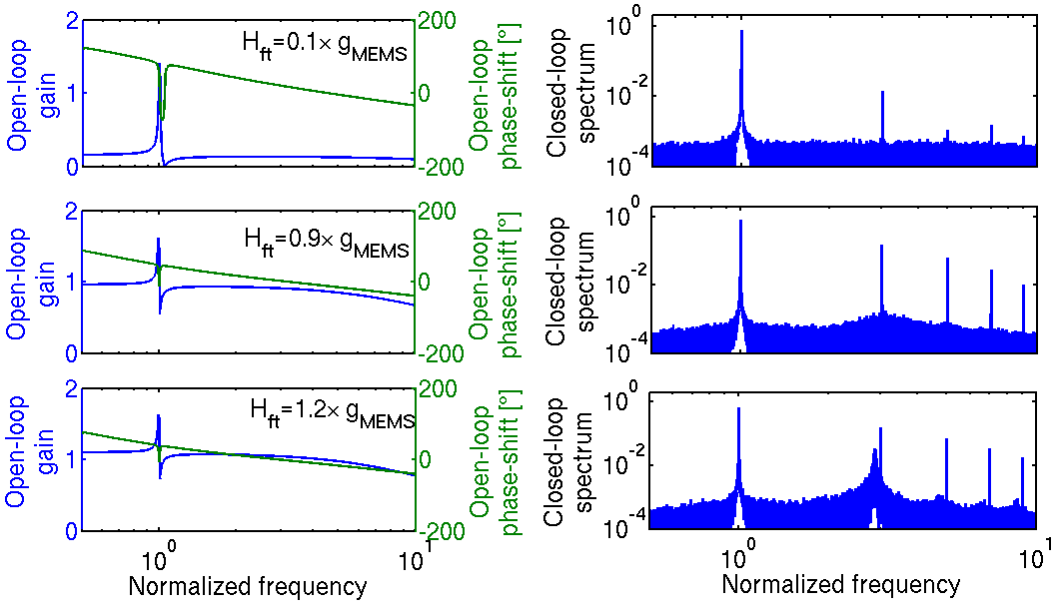

Figure 1.13: Simulations of the effect of the feed-through transmission in SOLs

(1.35)

The corresponding frequency resolution is thus:

$$\sigma_{f_r} = \frac{1}{\frac{\partial \psi_{MEMS}}{\partial f}(f_{osc})\sqrt{T_{meas}}} \times \left[\frac{S_{thermo}}{F_{l-c}^2} + \frac{S_{MEMS_{\bar{th}}}}{|F_{l-c} \times H_{mecha} H_{det}|^2} + \frac{S_{elec}}{|F_{l-c} \times H_{mecha} H_{det} H_{connec}|^2}\right] \quad (1.36)$$

F_{l-c} and S_{thermo} are intrinsically limited by the MEMS characteristics. It is important to design a MEMS with a strong detection gain, low MEMS-to-electronics connection losses and a low electronic noise in order to achieve a oscillator frequency resolution as close as possible to its ideal value defined as:

$$\sigma_{f_r - ideal} = \frac{f_r}{2QF_{l-c}}\sqrt{\frac{S_{thermo}}{T_{meas}}} \quad \text{if } H_{ft} \ll g_{MEMS}. \quad (1.37)$$

1.3.1.3 Effect of feed-through transmission in SOLs

Subsection 1.1.2 describes how $\frac{\partial \psi_{MEMS}}{\partial f}\Big|_{f_r}$ reduces with the feed-through transmission and thus the frequency resolution can be degraded. Moreover, it can be shown that the feed-through can create some parasitic oscillations that can further reduce the performance of the oscillator. Simulations were made for different levels of feed-through transmission gain on a similar loop than depicted in figure 1.11a. The

feed-through is modeled with a real gain independent of the frequency. The amplitude of the oscillations are controlled with a saturation block. The phase-shift of the loop is adjusted with a block having the following transfer function: $\frac{1-jf/f_c}{1+jf/f_c}$ that has a gain equal to 1. The results of the simulations are depicted in figure 1.13 and show that parasitic oscillations can appear in the loop. Indeed, the feed-through modifies the gain and phase-shift of the MEMS resonator and thus the oscillation conditions can also be satisfied at other frequencies.

Similarly to the design of electronic amplifiers, one can impose some margin on the gain of the loop at frequencies where the open-loop phase-shift crosses $n \times 2\pi$ (n being an integer). For example, in the realizations described in chapter 3, a gain of 10 dB was imposed between the gain at f_r and the gain at frequencies where the open-loop phase-shift crosses $n \times 2\pi$.

1.3.1.4 Nonlinear self-oscillating loop

It should be mentioned that the design of a purely linear electronic circuit is impossible in practice due to the quadratic response of CMOS transistors. Imperfections created by nonlinear parts of the oscillators (that will be described in this subsection) are therefore present for all SOL but with different degrees of degradations in the frequency resolution. Moreover, the design and the realization of a highly linear phase-shifter and an amplitude limiter can be difficult and expensive to fabricate.

One can find examples whereby a saturation block is implemented rather than automatic gain control to limit the oscillations amplitude [Gelb 1968, Arndt 2010, Akgul 2009, Verd 2008]. This is mainly because its implementation can be very simple. It uses an electronic amplification block that has a low dynamic range, i.e. the electronics saturates and its gain reduces when the input amplitude is larger than its dynamic range. The gain of the sustaining electronics reduces as the amplitude of the oscillation in the system grows and thus the steady-state oscillation amplitude can be controlled. It is also possible for some MEMS topologies to use the nonlinearity of the MEMS resonator as a saturation mechanism. On the other hand, the distortions and the nonlinear behavior of the saturation block can modify the contribution of the noise sources on the resolution of the oscillator. The effect is complex and was rarely theoretically treated in the literature [Demir 2000]. However, based on a Taylor expansion, a simple model of the nonlinear electronic circuit transfer function $H_{elec-NL}$ can be:

$$H_{elec-NL} = H_{elec}\left(1 + HD_2 v_{elec} + HD_3 v_{elec}^2 + ...\right), \tag{1.38}$$

where H_{elec} is the linear electronic circuit transfer function, v_{elec} is the complex amplitude of the electronics input signal, HD_2 and HD_3 are constant coefficients that can be determined from the electronics nonlinear behavior. In the case of small nonlinearity, it is assumed that $HD_2 v_{elec} \ll 1$ and $HD_3 v_{elec}^2 \ll 1$. One can introduce an additive noise to the input signal:

$$\mathsf{v}_{elec}(t) = v_{elec}\cos(2\pi f_{osc} t) + \mathsf{v}_{\mathsf{noise}}(t), \tag{1.39}$$

where $\mathsf{v}_{\mathsf{noise}}(t)$ respects $S_{v_{elec}} = \mathcal{F}\left[\Gamma_\tau\left(\mathsf{v}_{\mathsf{noise}}(t)\right)\right]$ and $\mathbb{E}\left\{\mathsf{v}_{\mathsf{noise}}(t)\right\} \ll v_{elec}$ (i.e. the noise is small compared to the signal). The electronics output signal is (if only the 2^{nd} harmonic distortion is considered: $HD_3 = 0$)

$$\begin{aligned}\mathsf{v}_{\mathsf{act}}(t) = H_{elec}\Big\{&v_{elec}\cos(2\pi f_{osc}t) + \mathsf{v}_{\mathsf{noise}}(t) + \\ &HD_2\left[v_{elec}^2\cos^2(2\pi f_{osc}t) + \mathsf{v}_{\mathsf{noise}}^2(t) + 2v_{elec}\cos(2\pi f_{osc}t)\,\mathsf{v}_{\mathsf{noise}}(t)\right]\Big\}.\end{aligned} \tag{1.40}$$

The term $v_{elec}^2\cos^2(2\pi f_{osc}t)$ introduces harmonics at $2 \times f_{osc}$ and does not affect the frequency resolution of the oscillator. The term $\mathsf{v}_{\mathsf{noise}}^2(t)$ can be considered as negligible compared to the other term because $\mathbb{E}\left\{\mathsf{v}_{\mathsf{noise}}(t)\right\} \ll v_{elec}$ and $HD_2 v_{elec} \ll 1$ implies that $HD_2\mathbb{E}\left\{\mathsf{v}_{\mathsf{noise}}^2(t)\right\} \ll v_{elec}$. The signal $\mathsf{v}_{\mathsf{noise}}(t)$ can be expressed by its one-side Fourier transform: $\mathsf{v}_{\mathsf{noise}}(t) = \int_0^\infty V_{noise}(\nu)\exp(-j2\pi\nu t)\,\mathrm{d}\nu$. Thus:

$$\begin{aligned}\mathsf{v}_{\mathsf{act}}(t) = H_{elec}\Bigg\{&v_{elec}\cos(2\pi f_{osc}t) + \int_0^\infty |V_{noise}(\nu)|\cos(2\pi\nu t + \arg V_{noise}(\nu))\,\mathrm{d}\nu + \\ &HD_2\left[2v_{elec}\cos(2\pi f_{osc}t)\int_0^\infty |V_{noise}(\nu)|\cos(2\pi\nu t + \arg V_{noise}(\nu))\,\mathrm{d}\nu\right]\Bigg\}.\end{aligned} \tag{1.41}$$

Thus:

$$\begin{aligned}\mathsf{v}_{\mathsf{act}}(t) = H_{elec}\Big\{&v_{elec}\cos(2\pi f_{osc}t) + \mathcal{F}^{-1}\left[V_{noise}(\nu)\right] + \\ &v_{elec}HD_2\mathcal{F}^{-1}\left[V_{noise}(f_{osc}+\nu)\right] + v_{elec}HD_2\mathcal{F}^{-1}\left[V_{noise}(f_{osc}-\nu)\right]\Big\}\end{aligned} \tag{1.42}$$

The nonlinearity create some frequency aliasing and up-converts the flicker noise close to the oscillating frequency. The figure 1.14 illustrates the aliasing of the colored noise around the oscillation frequency. Note that this computed phase-noise corresponds to $S_{\varphi_{elec+MEMS}}$ that is the phase-noise injected in the loop. The Leeson's formula then describes how the injected phase-noise is shaped by the closed-loop.

It is also possible to introduce in the sustaining electronics a comparator so that the output signal is in a two-state regime: the signal is either equal to a voltage V_1 or V_2. With this architecture, the oscillation amplitude is controlled with ease through V_1 and V_2. More importantly, since the comparator output signal is logic, digital architectures can be used what simplifies the realization of the phase-shifter and any other filters. For example, the phase-shifter block can be realized using Delay-Lock-Loop (DLL). A DLL can introduce any desired phase-shift whatever the signal frequency is [Susplugas 2004]. Comparator can also be applied in order to filter other frequencies than f_r, assuming that their amplitude are small compared to the one at f_r [Bahreyni 2007]. The drawback of this topology is that it introduces large distortions, thus the issues inherent to the saturation blocks are emphasized.

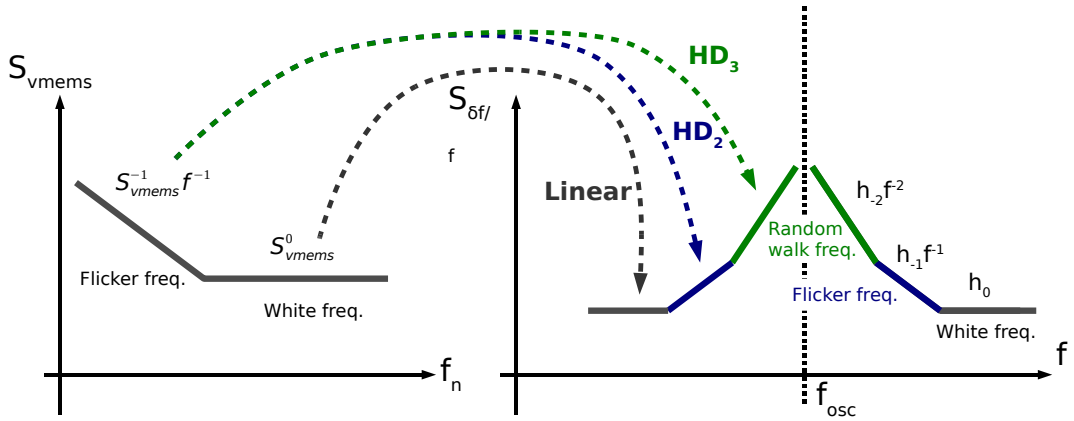

Figure 1.14: Frequency aliasing of the flicker noise in a nonlinear oscillator

1.3.1.5 Dynamic range

It is shown in appendix A that the dynamic range of self-oscillating loops is larger than 10% what corresponds to the typical dynamic range of the MEMS resonator. In this case, the dynamic range is not limited by the SOL but by the MEMS resonator itself.

1.3.2 Frequency-locked loop

Numerous example of frequency-locked loop (FLL) can be found in the literature [Ekinci 2004a, Feng 2007, He 2008, Yang 2006, Ivaldi 2011a, Mile 2010]. FLL are generally preferred to SOL architectures because they are more versatile: they can be used on many different types of resonators with different resonance frequencies; they are less sensitive to feed-through and parasitic environment. On the other hand, an FLL architecture requires a VCO and a phase-comparator that can be expensive, difficult to design and area consuming. As a matter of fact, to the author's knowledge, no ASIC with an FLL-architecture to operate MEMS resonators have been realized.

1.3.2.1 Theory of operation

A Frequency-Locked Loop consists in constantly maintaining the phase-shift introduced by the MEMS to its value at f_r. The term frequency-locked loop [Rubiola 2008] is employed because the phase-shift variations of the MEMS are converted into actuation frequency variations. The output variable of the loop is therefore a term proportional to the resonator actuation frequency.

In figure 1.11b, the phase-comparator compares the phase-shift introduced by the MEMS (between the MEMS input and the amplifier output, the phase-shift introduced by MEMS-to-electronics connections and the amplifier is supposed to be

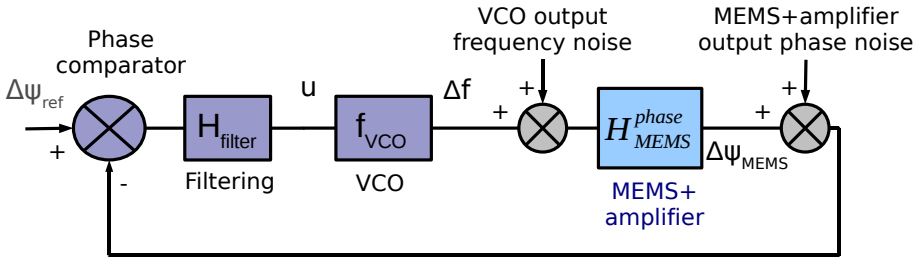

Figure 1.15: Simplified FLL topology including its intrinsic noise sources

constant around f_r and compensated) to the desired phase-shift i.e. the MEMS phase-shift at f_r. If there is a phase-shift difference, the MEMS actuation frequency is modified so that the phase-shift difference is reduced. It is therefore necessary to analyze the MEMS phase-shift response to the frequency of the actuation voltage f_{act}:

$$\psi_{MEMS} = \arg\left[H_{MEMS}\right] \underset{f\approx f_r}{\approx} -\frac{\pi}{2} - \left.\frac{\partial \psi_{MEMS}}{\partial f}\right|_{f_r} \times \left(f_{act} - f_r\right). \tag{1.43}$$

Introducing the phase-shift difference $\Delta\psi_{MEMS}$ between the MEMS phase-shift and the desired phase-shift $\psi_{MEMS}\left(f = f_r\right) = -90°$:

$$\Delta\psi_{MEMS} = \psi_{MEMS}\left(f\right) - \psi_{MEMS}\left(f = f_r\right) = \left.\frac{\partial \psi_{MEMS}}{\partial f}\right|_{f_r} \Delta f, \tag{1.44}$$

where $\Delta f = f_{act} - f_r$. With the introduced notations, the figure 1.11b can be simplified to figure 1.15. Note that $\Delta\psi_{ref}$ is 0 and that the transfer function of the (MEMS+amplifier) block is different from the one in section 1.1 since it relates Δf to $\Delta\psi_{MEMS}$. It is given by equation (1.44) and in order to avoid any confusions, it will be noted:

$$\begin{aligned} H^{phase}_{MEMS}(f) &= \frac{\Delta\psi_{MEMS}}{\Delta f} \underset{f_{act}\approx f_r}{=} \left.\frac{\partial \psi_{MEMS}}{\partial f}\right|_{f_r}. \\ &= \frac{2Q}{f_r} \quad (\text{if } H_{ft} \ll g_{MEMS}) \end{aligned} \tag{1.45}$$

Based on fig. 1.15, one can determine the transfer function H_{FLL} between $\Delta\psi_{ref}$ and $\Delta\psi_{MEMS}$:

$$H_{FLL}(f) = \frac{\Delta\psi_{MEMS}}{\Delta\psi_{ref}} = \frac{H^{phase}_{MEMS} f_{VCO} H_{filter}}{1 + H^{phase}_{MEMS} f_{VCO} H_{filter}}, \tag{1.46}$$

where f_{VCO} and H_{filter} are respectively the transfer functions of the VCO and the filter.

The VCO converts the input signal u into a signal with the frequency $f_r + \Delta f$. From fig. 1.15, the transfer function of the VCO relates the input voltage u command into

a frequency variation Δf and is therefore a constant gain: $\Delta f = f_{VCO} \times u$ contrary to the representation in PLLs where the VCO is modeled by an integrator. The filter can be a first order low-pass filter as in [Ekinci 2004a, Ekinci 2004b, Feng 2007, Yang 2006], the transfer function of the filter is then:

$$H_{filter} = \frac{G_{filter}}{1 + j\frac{\Delta f}{f_{filter}}}, \tag{1.47}$$

where G_{filter} and f_{filter} are respectively the low-frequency gain and the cut-off frequency of the filter. f_{filter} is set to values lower than the resonator's bandwidth and thus determines the bandwidth of the oscillator. Higher order filters are also possible as in [Kharrat 2008] in order to improve the robustness of the loop and its time response but they will not be analyzed in this manuscript. From the expressions of H_{MEMS}^{phase}, f_{VCO} and H_{filter}, H_{FLL} can be expressed as:

$$H_{FLL} = \frac{\frac{\partial \psi_{MEMS}}{\partial f}\Big|_{f_r} f_{VCO} G_{filter}}{\frac{\partial \psi_{MEMS}}{\partial f}\Big|_{f_r} f_{VCO} G_{filter} + 1 + j\frac{\Delta f}{f_{filter}}}. \tag{1.48}$$

To make the FLL lock correctly at $f_{osc} = f_r$, H_{FLL} should be as close as possible to 1 at low Δf so that $\Delta\psi_{MEMS}$ is equal to the control signal $\Delta\psi_{ref}$ i.e. $\psi_{MEMS} = \Delta\psi_{MEMS} + \psi_{MEMS}(f = f_r) = \psi_{MEMS}(f = f_r)$. Thus, the low-frequency gain of the filter must be large:

$$G_{filter} \gg \frac{1}{\frac{\partial \psi_{MEMS}}{\partial f}\Big|_{f_r} f_{VCO}} \underset{H_{ft} \ll g_{MEMS}}{=} \frac{f_r}{2Q f_{VCO}}. \tag{1.49}$$

In practice, the MEMS resonator and mostly the VCO have a non-zero response time introducing delay in the loop, what limits G_{filter} to an upper value that is function of f_{filter} (i.e. the oscillator bandwidth).

Finally, since the VCO input signal is proportional to the VCO output frequency and therefore the oscillating frequency; the oscillating frequency of the system is usually measured with u. The oscillating frequency f_{osc} has the following expression:

$$f_{osc} = f_{VCO} \times u + f_r. \tag{1.50}$$

1.3.2.2 Resolution of the FLL oscillator

The different noises in the FLL are responsible for some fluctuations on u and limit the resolution of the oscillation frequency measurement. The resolution of the system then is usually analyzed from the PSD of u denoted S_u. Figure 1.15 presents the noise introduced by the VCO, the MEMS and the amplification block. They are respectively modeled as a frequency and a phase noise.

The VCO is an oscillator and has a similar frequency noise than the one described in subsection 1.3.1 (assuming that the VCO output frequency is f_r):

$$S_{\Delta f_{VCO}} = \left[(f_r - f)^2 + \left(\frac{f_r}{2Q_{VCO}} \right)^2 \right] S_{\varphi_{VCO}} \underset{f \approx f_r}{\approx} \left(\frac{f_r}{2Q_{VCO}} \right)^2 S_{\varphi_{VCO}}, \tag{1.51}$$

where Q_{VCO} is the quality factor of the VCO and $S_{\varphi_{VCO}}$ is the open-loop phase-noise expressed at the output of the VCO.

Similarly to section 1.3.1, the phase-noise of the MEMS+electronics has the following expression:

$$S_{\varphi_{MEMS+elec}} = 2\frac{S_{thermo}}{v_{amp}^2} \left| H_{mecha} H_{det} H_{connec} H_{amp} \right|^2 + 2\frac{S_{MEMS_{\bar{th}}}}{v_{amp}^2} \left| H_{connec} H_{amp} \right|^2 + 2\frac{S_{elec}}{v_{amp}^2}. \tag{1.52}$$

The contribution of the noise of the VCO, the MEMS and the electronics is determined from the noise at the input of the VCO:

$$S_u = \frac{\left| H_{MEMS}^{phase} H_{filter} \right|^2 S_{\Delta f_{VCO}} + \left| H_{filter} \right|^2 S_{\varphi_{MEMS+elec}}}{\left| 1 + H_{filter} f_{VCO} H_{MEMS}^{phase} \right|^2}. \tag{1.53}$$

The theory of operation of the FLL imposes that around f_r, $\left| H_{filter} f_{VCO} H_{MEMS}^{phase} \right| \gg 1$. Out of the resonance (i.e. for large Δf) H_{filter} becomes small and H_{MEMS}^{phase} is a bounded function so that $S_{\Delta f_{VCO}}$ and $S_{\varphi_{MEMS}}$ are filtered for $|\Delta f| > f_{filter}$. The noise can be considered as null at frequencies out of the bandwidth of the filter.

The oscillating frequency is determined from the input signal of the VCO: $f_{osc} = f_r + u \times f_{VCO}$. The frequency-noise of the FLL S_f is therefore:

$$S_f = f_{VCO}^2 S_u. \tag{1.54}$$

The contributions of the VCO , MEMS and amplifier noises are measured as a relative frequency variation at the input of the VCO:

$$S_{\delta f/f} \underset{f \approx f_r}{\approx} 2 \left(\frac{1}{f \left. \frac{\partial \psi_{MEMS}}{\partial f} \right|_{f_r}} \right)^2 \left[\underbrace{\frac{S_{thermo}}{F_{l-c}^2}}_{\text{Thermomechanical noise}} + \underbrace{\frac{S_{MEMS_{\bar{th}}}}{\left| F_{l-c} \times H_{mecha} H_{det} \right|^2}}_{\text{Other MEMS noise}} + \right.$$

$$\underbrace{\frac{S_{elec}}{\left|F_{l-c}\times H_{mecha}H_{det}H_{connec}\right|^2}}_{\text{Amplifier noise}}+\underbrace{\left(\left.\frac{\partial\psi_{MEMS}}{\partial f}\right|_{f_r}\frac{f_r}{2Q_{VCO}}\right)^2\frac{S_{\varphi_{VCO}}}{2}}_{\text{VCO noise}}\Bigg]. \tag{1.55}$$

Note that if the VCO's phase-noise is low (i.e. $S_{\varphi_{VCO}} \ll 2S_{thermo}/F_{l-c}^2$) and if the quality factor of the VCO is large compared to the one of the MEMS then the contribution of the VCO on the resolution of the FLL can be neglected. In fact, this conditions set a limit in the use of a FLL-architecture as it requires a VCO with phase-noise far better than the MEMS resonator otherwise the VCO degrades the performance of the loop. However, the development of MEMS resonators for sensing application tends to fabricates small resonators with low output electrical signal. The resonator output phase-noise it thus generally larger than the ones of laboratory signal generators.

Assuming that the VCO phase-noise can be neglected, one can see that the PSD of the FLL phase-noise is then similar to the one of the self-oscillating loop:

$$S_{\delta f/f}=\frac{S_{\varphi_{MEMS+elec}}}{\left[f_{osc}\frac{\partial\psi_{MEMS}}{\partial f}\left(f_{osc}\right)\right]^2}. \tag{1.56}$$

Thus:

$$\begin{aligned}\sigma_{f_r}&=\frac{1}{\frac{\partial\psi_{MEMS}}{\partial f}\left(f_{osc}\right)}\sqrt{\frac{S_{\varphi_{MEMS+elec}}}{2T_{meas}}}\quad\text{(FLL frequency resolution)}\\&=\frac{f_r}{2Q}\sqrt{\frac{S_{\varphi_{MEMS+elec}}}{2T_{meas}}}\quad\text{if } H_{ft}\ll g_{MEMS}.\end{aligned} \tag{1.57}$$

The two closed-architectures have theoretically the same mass-resolution. Measurements in [Levy 2010] also presents a resonator whose the frequency resolutions in SOL and FLL are similar.

1.3.2.3 Effect of the feed-through transmission in FLLs

The oscillation frequency range of the FLL can be controlled through the signal u and thus it is possible to prevent parasitic oscillations. If the resonator is embedded in an FLL architecture, parasitic oscillations should be prevented.

The effect of the slope-reduction of the resonator phase-shift remains as decribed in subsection 1.1.2. Thus, if the feed-through transmission is large, the frequency resolution of the loop can be reduced.

1.3.2.4 Nonlinear frequency-locked loop

Similarly to SOL-architecture, the MEMS and the electronics of a FLL-architecture can introduce some nonlinearity. Besides the MEMS resonator, the first amplifier and the phase-comparator are likely to introduce sensible non-linearity depending on its technological implementation. Similarly to SOL-architecture, the design of such blocks should minimize the non-linearity with respect to the flicker noise in order to prevent any frequency resolution degradation.

1.3.2.5 Dynamic range

In a frequency-locked loop, the dynamic range is limited by the frequency range of either the phase-comparator, the VCO or the MEMS. The dynamic range of the MEMS is similar to the one treated in the self-oscillating loop section. Whatever electronics is used (lab equipment or analog integrated circuit), the dynamic range of the phase comparator and the VCO can be of several orders of magnitude [datasheet c, datasheet a] [Calvo 2009]. The dynamic range of the system will be limited by the MEMS dynamic range.

1.4 Oscillating frequency measurement

In an FLL-architecture the oscillating frequency is straightforwardly measured with u. In the case of SOL-architecture, the measurement of f_{osc} is not direct and different frequency measurement techniques with their pros/and cons are described in this section. The aim of this section is to evaluate architectures that can measure the frequency of an oscillator with an accuracy larger that the oscillator frequency noise (evaluated with the Allan deviation).

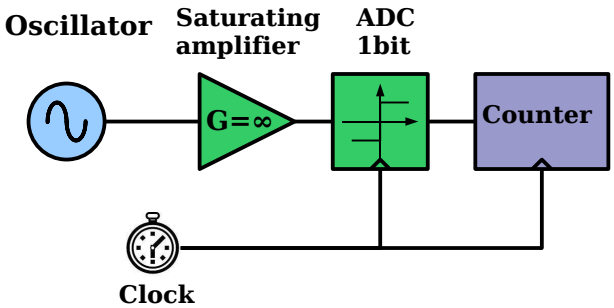

Figure 1.16: Period-counting

1.4.1 Period-counting

The most intuitive measurement technique consists in measuring the periods of the oscillator output signal. The oscillator output signal is connected to a 1-bit analog-to-digital converter that is sampled with a reference clock (fig 1.16). One can then count how long lasts each period (between 2 successive raising edges) thanks to the reference clock signal. In order to reduce quantization noise due to the finite frequency of the reference clock, one should average several periods of the output signal of the oscillators. Moreover, the number of periods taken into account should be adapted to the desired measurement bandwidth (determined from the Allan deviation).

A common measurement scheme consists measuring the time t_0 of the first raising edge. The number of periods N between $t = 0$ and $t = T_{meas}$ are counted and the time t_{N+1} of the following transition is then measured. The mean value of the signal frequency can be determined from:

$$\frac{1}{f_{osc}} = \frac{t_{N+1} - t_1}{N}. \tag{1.58}$$

The resolution of the period-counting represents the accuracy of the frequency measurement. The time resolution in this method is $\delta t = 1/f_{CLK}$ where f_{CLK} is the frequency of the clock. The measurement resolution is determined from equation (1.58):

$$\frac{\delta f}{\langle f \rangle} = \sqrt{2}\frac{1}{N f_{CLK} \langle T \rangle} \quad \text{(period-counting resolution)}, \tag{1.59}$$

where $\langle f \rangle$ and $\langle T \rangle$ are the mean value of the signal's frequency and period respectively. The factor $\sqrt{2}$ is due to the fact that two measurements are required to evaluate the oscillating frequency.

The period-counting architecture is simple to realize but it should include a high quality internal oscillator with a frequency (much) larger than the oscillator to be measured and a negligible Allan-deviation. MEMS resonators considered in this work have a resonance frequency up to 100 MHz and Allan-deviation around 10^{-7} at 1 s making the proposed frequency measurement method valid using a commercial quartz crystal [datasheet b]. Indeed, the relative frequency variation that can be measured with a quartz is around 10^{-9}.

1.4.2 Delay-based measurement

Another frequency measurement method consists in mixing the oscillator output signal with the same signal delayed by a time τ (see figure 1.17). The phase-shift between the signal before and after the delay block is measured using an analog or

a digital mixer and a low-pass filter. The frequency variations are converted into phase-shift variations through the delay block. By measuring the phase-difference $\Delta\phi(t)$ one can determine the oscillation frequency. The delay τ can be implemented with a "real" delay with a transfer function $H_{delay} = e^{j\tau}$ or with a first order low-pass filter $H_{delay} = \frac{1}{1+jf/f_c}$ that introduces a phase-shift. A general expression of the signal to be measured is $\mathsf{v}(t) = v_0 \sin[2\pi f_{osc} t + \varphi(t)]$ where v_0 is the amplitude of the signal. The oscillator signal delayed by τ is expressed as.

$$\begin{cases} \mathsf{v}_{delay}(t) = v_0 \sin[2\pi f_{osc}(t-\tau) + \varphi(t-\tau)] & \text{if } H_{delay} = e^{j\tau} \\ \mathsf{v}_{delay}(t) = \frac{v_0 \sin\left[2\pi f_{osc} t + \varphi\left(t - \frac{\arctan(f_{osc}/f_c)}{2\pi f_{osc}}\right) - \arctan\left(\frac{f_{osc}}{f_c}\right)\right]}{\sqrt{1+(f_{osc}/f_c)^2}} & \text{if } H_{delay} = \frac{1}{1+jf_{osc}/f_c} \end{cases}. \quad (1.60)$$

Thus, the phase-shift between $\mathsf{v}(t)$ and $\mathsf{v}_{delay}(t)$ is:

$$\begin{cases} \Delta\phi(t) = 2\pi f_{osc}\tau + \varphi(t) - \varphi(t-\tau) & \text{if } H_{delay} = e^{j\tau} \\ \Delta\phi(t) = \arctan(f_{osc}/f_c) + \varphi(t) - \varphi\left(t - \frac{\arctan\left(\frac{f_{osc}}{f_c}\right)}{2\pi f_{osc}}\right) & \text{if } H_{delay} = \frac{1}{1+jf_{osc}/f_c} \end{cases}. \quad (1.61)$$

The value of τ must be chosen so that $\tau < 1/f_{osc}$ (i.e. the delay is lower than a period) and so that $2\pi f_{osc}\tau$ is larger than the phase-noise (the introduced delay is measurable). The value of f_c must be chosen to maximize the frequency-to-phase slope:

$$\begin{aligned} \frac{\partial \Delta\phi_{noiseless}}{\partial f}(f_c) \text{ is mazimized} &\Rightarrow \frac{\partial^2 \Delta\phi_{noiseless}}{\partial f_c \partial \mathrm{f}} = 0 \\ &\Rightarrow \frac{2\frac{1}{f_c}\frac{f_{osc}^2}{f_c^3} - \frac{1}{f_c^2}\left[1+\left(\frac{f_{osc}}{f_c}\right)^2\right]}{\left[1+\left(\frac{f_{osc}}{f_c}\right)^2\right]^2} = 0 \Rightarrow f_c = f_{osc} \end{aligned} \quad (1.62)$$

Finally, the phase-difference is then filtered over a measurement time T_{meas} (similarly to the period-counting measurement scheme).

This measurement scheme has shown good results and is commonly used according to the literature [Albrecht 1991, Bahreyni 2007, Rubiola 2008]. This method is interesting because the noise out of the resonator's bandwidth is filtered by the phase-comparator before the measurement.

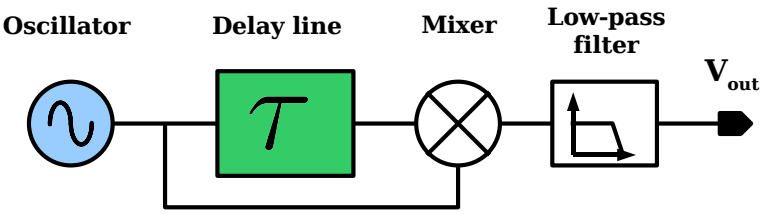

Figure 1.17: Delay-based measurement

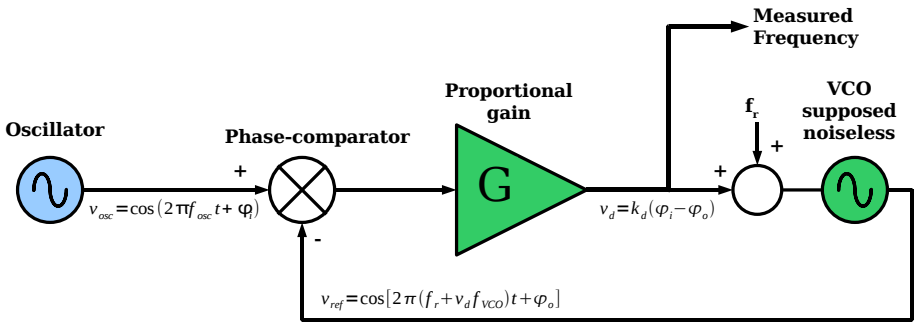

Figure 1.18: PLL-based measurement

1.4.3 PLL-based measurement

This measurement technique is often used to measure the phase-noise of a high-frequency signal source [Rubiola 2008]. It consists in creating another signal source (assumed noiseless) at the same frequency than the signal to measure. The phase-difference between the signal sources is mixed to low-frequency similarly to the previously mentioned FLL. Finally the frequency of the oscillator (blue on the schematic) is measured with the input signal of the VCO.

The analysis and the design of the PLL is very similar to the one of the FLL. The closed-loop transfer function between the input frequency and the measured frequency (i.e. at the VCO input) is:

$$H_{PLL} = \frac{v_d}{f_{osc}} = \frac{2\pi k_d}{j\Delta f + 2\pi k_d f_{VCO}}, \tag{1.63}$$

where k_d is the gain of the phase-comparator and the proportional gain expressed in V/rad and f_{VCO} is the VCO gain expressed in Hz/V. The frequency is properly measured because the gain of H_{PLL} converges when Δf tends to zero. In practice, the phase-comparator and the VCO communicate with a computer: the phase-shift measurement operated by the phase-comparator is sent to the computer and the frequency of the VCO is given by the computer (the proportional gain is implemented by the computer program). The communication between the equipments and the computer introduces some delay in the loop and can make the system unstable.

The PLL-based measurement technique can be employed to track the very-high frequency signal sources [Rubiola 2008]. It however requires a phase-comparator and a VCO and therefore shows no interest compared to FLL architectures.

1.5 Conclusion

In this chapter, a generic model of MEMS resonators was given. It includes the mechanical response of the device and its electromechanical transduction. The main

phenomena that limit the resonator performance were also described: the noise introduced by the device and feed-through parasitics.

Different methods to track the resonance frequency of MEMS resonators were also described. They are divided into two categories: open-loop and closed-loop architectures. Open-loop measurements are very limited in opposition to closed-loop measurements that can achieve good frequency resolution and dynamic range. There are two main closed-loop measurement techniques: self-oscillating loops and frequency locked-loops. The former is cheaper and more compact to fabricate but its frequency resolution can be limited due to distortions and to MEMS feed-through transmission. Frequency locked-loops can overcome these issues but they are complex and expansive. Table 1.1 presents a general comparison of different architectures for the harmonic detection of resonance. In the following chapters, we concentrate our work on oscillator design using a self-oscillating loop architecture because SOLs are more compact. This architecture thus seems the most adequate when the sensors (i.e. MEMS + frequency tracking) are deployed in array such as for mass spectrometry. Finally, methods to measure the oscillation frequency were presented and compared in terms of complexity and performances.

Based on the architecture description of the self-oscillating loop, it is now possible to assess for a given MEMS resonator the mass resolution of the sensor. The following chapter describes and compares in more details different topologies of MEMS resonator and their connection to the electronic circuit. A theoretical assessment of the best achievable mass resolution is calculated for each MEMS resonator.

Table 1.1: Comparison of the different architectures for harmonic detection of resonance. The effect of the feed-through was neglected in the expression of the mass resolution.

	Open-loop measurement		**Close-loop measurement**	
	Frequency Sweep	**Phase-shift variation**	**Self-oscillating loop**	**Frequency locked-loop**
Measurement principle	Determination of the maximum gain	Meas. of the MEMS phase-shift variation	The MEMS oscillates at its resonant frequency	Control of the MEMS phase-shift
Complexity	Requires a VCO and Lock-in amplifier	Requires a VCO and phase-comparator	Simple	Requires a VCO and phase-comparator
Area consumption	Large: >10 000 mm²	Large: >10 000 mm²	Little: can be smaller than 0.1 mm²	Large: >10 000 mm²
Resolution	Low: $\sigma_m = 2m\sqrt{\frac{S_\varphi(MEMS+elec)}{2T_{meas}}}$	High: $\sigma_m = \frac{m}{Q}\sqrt{\frac{S_\varphi(MEMS+elec)}{2T_{meas}}}$	High: $\sigma_m = \frac{m}{Q}\sqrt{\frac{S_\varphi(MEMS+elec)}{2T_{meas}}}$	High: $\sigma_m = \frac{m}{Q}\sqrt{\frac{S_\varphi(MEMS+elec)}{2T_{meas}}}$
Dynamic range	Very large (limited by the MEMS)	Low: ~1%	Large (limited by the MEMS)	Large (limited by the MEMS)
Distortion	Few	Few	Yes (emphasized for non-linear sustaining electronics)	Few
Ease of implementation	Very	Requires calibration	Little	Requires calibration
Sensitivity to feed-through	Low	Low	Varies but can be important	Low

$S_\varphi(MEMS+elec)$ is the power spectral density of the phase-noise introduced by the MEMS and the electronics.

2 Various MEMS resonators topologies and their readout electronics

In this chapter, the mechanical behavior of the resonator is first described. Different electromechanical transduction techniques are then explained for four selected resonator topologies. The equivalent electrical model of those resonators are also presented and discussed. In a third section, the MEMS-to-electronics connection is modeled. The impact on the connection losses and the feed-through described in the chapter 1 are evaluated. Based on the models presented in this chapter, a theoretical comparison of the MEMS resonators for mass sensing applications is proposed. Finally the impact of implementing MEMS resonator in arrays is evaluated and discussed. The phase-noise improvement of summing the response of each resonator in the array is assessed.

2.1 The mechanical resonator

The most popular geometries for precise mass measurement are beams with high aspect ratios [Jensen 2008, Yang 2006, Roukes 2007]. They have low mass, enhancing the mass resolution, and low stiffness simplifying the resonance frequency measurement.

Consider a beam with length L, width b, and thickness h as depicted on fig. 2.1. The (OX), (OY), (OZ) axes are respectively along the length, width and thickness

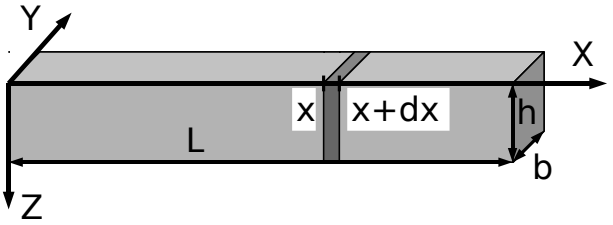

Figure 2.1: Beam dimension and axis definition

of the beam. The beam is submitted to a force per unit length $\mathsf{F_l}(t)$ in the (OY) axis direction (i.e. in-plane motion). The displacement $\tilde{\mathsf{w}}(x,t)$ of the beam is governed by the one-dimension Euler-Bernoulli equation:

$$\rho hb\frac{\partial^2\tilde{\mathsf{w}}(x,t)}{\partial t^2}+\xi\frac{\partial\tilde{\mathsf{w}}(x,t)}{\partial t}+T(\tilde{\mathsf{w}})\frac{\partial^2\tilde{\mathsf{w}}(x,t)}{\partial x^2}+c_{beam}I\frac{\partial^4\tilde{\mathsf{w}}(x,t)}{\partial x^4}=\mathsf{F_l}(t)\,, \tag{2.1}$$

where:

ρ is the density of the beam's material in kg/m^3,

$\tilde{\mathsf{w}}(x,t)$ is the displacement in the (OY) direction in m,

ξ is a damping coefficient in N.s/m^2,

$T(\tilde{\mathsf{w}})$ is the internal stress in the beam equal to $T(\tilde{\mathsf{w}})=c_{beam}hb\ell_1(\tilde{\mathsf{w}})$ in the case of a clamped-clamped beam and equal to zero in the case of free-clamped beam,

$\ell_1(\tilde{\mathsf{w}})$ is the dimensionless strain (relative change of length) in the (OX) direction,

c_{beam} is the beam's Young's modulus in Pa,

$I=\frac{hb^3}{12}$ is the moment of inertia of the beam in the (OY) direction in m^4.

Equation (2.1) can be solved using the Galerkin procedure:

$$\tilde{\mathsf{w}}(x,t)=\sum_{n=1}^{\infty}\mathsf{a_n}(t)\,\Upsilon_n(x)\quad\text{(modal decomposition)}, \tag{2.2}$$

where $\mathsf{a_n}(t)$ in meters describes the frequency response of the beam and $\Upsilon_n(x)$ without units is the n^{th} eigenmode of the beam associated to the boundary conditions. Appendix B describes the behavior of the beam when all of the modes are considered.

In this manuscript, only the first mode is taken into account while the others are neglected. Consequently, the subscripts n are omitted in the rest of the manuscript. From the appendix B and in case of small mechanical displacement compared to b[1], the complex amplitude of the function $\mathsf{w}(t)=\mathsf{a_1}(t)\max\limits_{0\le x\le L}[\Upsilon_1(x)]$ (that is $\mathsf{w}(t)=\mathsf{a_1}(t)\,\Upsilon_1(L/2)$ for a clamped-clamped beam, $\mathsf{w}(t)=\mathsf{a_1}(t)\,\Upsilon_1(L)$ for a cantilever beam), denoted $w(f)$ is given by:

$$H_{mecha}(f)=\frac{w(f)}{F_l(f)}=\frac{\eta_A L}{m(2\pi f_r)^2}\frac{1}{1+j\frac{f}{Qf_r}-\left(\frac{f}{f_r}\right)^2}, \tag{2.3}$$

where

[1] i.e. $\eta_K\tilde{\mathsf{w}}(x,t)\ll b$ where η_K is a constant that only depends upon the mechanical conditions imposed on the beam.

η_A is equal to 1.32 for a clamped-clamped beams, to 0.53 for a cantilever beams (more details are given in the appendix B).

$m = m_{beam} + \kappa_{mass}\Delta m$,

Δm is the mass in kg deposited on to the beam, for example when using it as a mass sensor,

κ_{mass} is a normalization coefficient that depends on the spacial localization of Δm (e.g. punctual or uniform); see appendix B,

$f_r = \frac{1}{2\pi}\sqrt{\frac{c_{beam} I \lambda^4}{mL^3}}$ is the resonance frequency of the beam in Hz,

λ is equal to 4.73 for clamped-clamped beams, to 1.88 for cantilever beams (see appendix B),

$Q = \frac{2\pi f_r m}{\xi L}$ is the dimensionless quality factor of the beam.

Note that in the case of a small mass Δm is added to the beam[2], the resonance frequency becomes:

$$f_r^{\Delta m} = \frac{1}{2\pi}\sqrt{\frac{c_{beam} I \lambda^4}{mL^3}} \approx f_r^0 \left(1 - \frac{\kappa_{mass}\Delta m}{2m_{beam}}\right), \tag{2.4}$$

where $f_r^0 = \frac{1}{2\pi}\sqrt{\frac{c_{beam} I \lambda^4}{m_{beam} L^3}}$ is the unloaded resonance frequency of the beam.

From the fluctuation-dissipation theorem, the beam is submitted to mechanical noise [Cleland 2002]. It can be modelled by a white noise source acting as a force per unit of length on the beam:

$$S_{thermo} = \frac{4k_B T m f_r}{\eta_A^2 L^2 Q} \quad \text{(thermomechanical noise)}. \tag{2.5}$$

2.2 MEMS topologies to make portable, low-power, mass sensors

The literature reports mass sensing experiments with remarkable mass resolution below or around the zeptogram (10^{-21} g) [Jensen 2008, Yang 2006, Ekinci 2004a]. To achieve these excellent mass measurements, NEMS resonators were designed based on a magnetomotive transduction [Yang 2006, Ekinci 2004a] or field emission for carbon nanotubes resonator types [Jensen 2008]. However, these measurements use complex setups and are operated in vacuum.

On the other hand, this manuscript focuses on portable, low-power sensors using on-chip electromechanical transduction. Moreover, with the experience and the culture of Leti, the MEMS resonators should be VLSI- (very large scale integration)

[2] compared to the mass of the beam: $\Delta m \ll \frac{m_{beam}}{\kappa_{mass,n}}$.

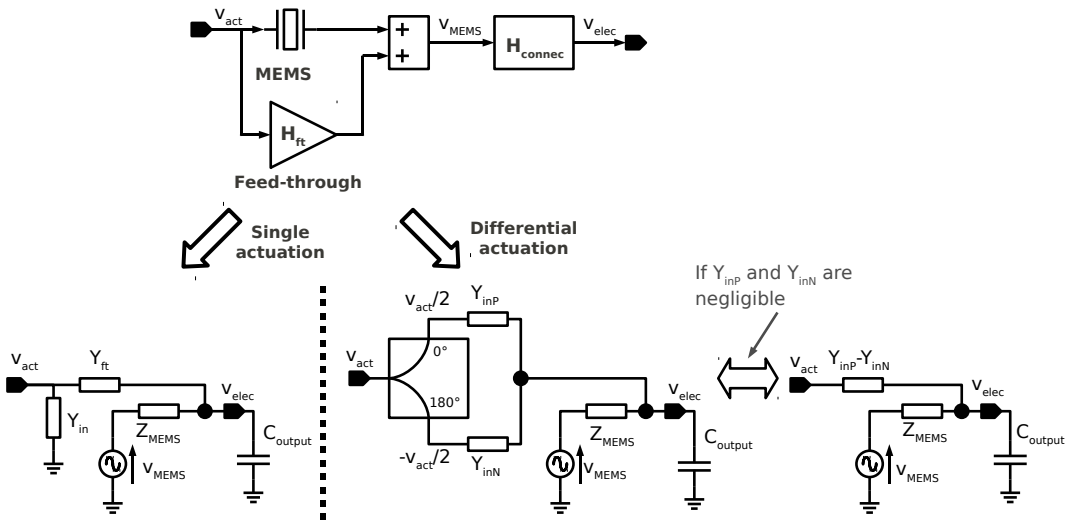

Figure 2.2: Electrical model of a resonator.

compatible so that they can be fabricated on 200 mm-wafers. These constraints deteriorate the achievable mass resolution but make these studies more relevant for commercial applications. For these reasons, we have chosen not to consider neither the magnetomotive [Yang 2006, Ekinci 2004a], piezoshaker [He 2008], or thermoelastic actuation scheme [Bargatin 2007], nor, the optical detection scheme.

Four MEMS topologies are studied in depth. The first one is a clamped-clamped beam with electrostatic actuation and capacitive detection. The second and third MEMS topologies are a clamped-clamped beam and a so-called "crossbeam" with electrostatic actuation and piezoresistive detection. The fourth resonator uses the piezoelectric properties of AlN as its actuation and detection mechanism.

The aim of this section is therefore to provide an electromechanical description of each resonator but also to determine a common electrical model. It will be shown that all these resonators can be described with the electrical schematics depicted in the figure 2.2. The output voltage of the resonators is then equal to

$$v_{elec} = \frac{v_{MEMS}}{1 + j2\pi f Z_{MEMS} C_{output}}, \tag{2.6}$$

where C_{output} is the capacitance at the output of the resonator. Note that in eq. (2.6) the feed-through was neglected, i.e. $Y_{ft} \ll v_{MEMS}/\left(v_{act} Z_{MEMS}\right)$ for a single actuation or $Y_{inP} - Y_{inN} \ll 2v_{MEMS}/\left(v_{act} Z_{MEMS}\right)$ for a differential actuation. The transfer function of the intrinsic feed-through can also be calculated as:

$$H_{ft} = \begin{cases} \frac{Y_{ft} Z_{MEMS}}{1+Y_{fb} Z_{MEMS}} & \text{for single-sided actuation} \\ \frac{(Y_{inP}-Y_{inN}) Z_{MEMS}/2}{1+(Y_{inP}+Y_{inN}) Z_{MEMS}} & \text{for differential actuation} \end{cases}. \tag{2.7}$$

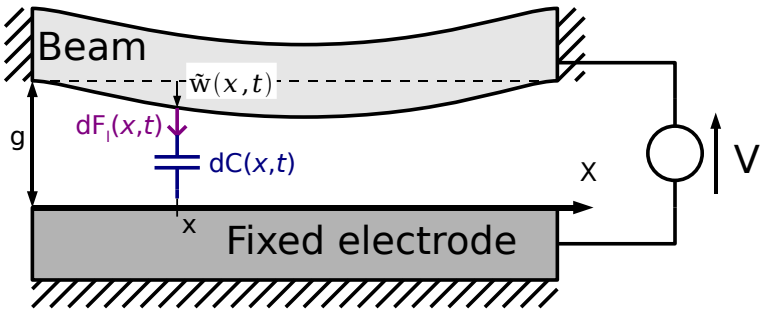

Figure 2.3: Electrostatic actuation and capacitive detection.

2.2.1 Clamped-clamped beam with capacitive detection

2.2.1.1 Electrostatic actuation

Consider two electrodes facing each-other (fig. 2.3), one of which is rigid, whereas the other can bend. The two electrodes have a length L and a thickness h. x is the coordinate along the length of the electrodes and $g - \tilde{\mathsf{w}}(x,t)$ is the distance between the two electrodes at point x. If a voltage $\mathsf{V}(t)$ is applied between the two electrodes, the resulting electrostatic per unit of length is:

$$\mathsf{F_l}(x,t) = \frac{\varepsilon_0 h}{2\left[g - \tilde{\mathsf{w}}(x,t)\right]^2}\mathsf{V}(t)^2 . \tag{2.8}$$

(2.8) simplifies to $\mathsf{F_l}(t) = \frac{\varepsilon_0 h}{2g^2}\mathsf{V}(t)^2$, when it is assumed that $\tilde{\mathsf{w}}(x,t) \ll g$. This assumption is obviously only correct for small displacement of the beam and sets an upper limit to the actuation force F_l. Note however that the voltage-to-force conversion is nonlinear.

To drive at resonance the MEMS, one can create a harmonic force $\mathsf{F_l}(t)$ applying a sinusoidal voltage:

$$\mathsf{V}(t) = V_{DC} + v_{act}\sin(2\pi f t) . \tag{2.9}$$

Thus the resulting expression of $\mathsf{F_l}(t)$ is:

$$\mathsf{F_l}(t) = \frac{\varepsilon_0 h}{g^2}\left[\frac{V_{DC}^2}{2} + \frac{v_{act}^2}{4} + V_{DC}v_{act}\sin(2\pi f t) - \frac{v_{act}^2}{4}\sin(4\pi f t)\right] . \tag{2.10}$$

$\mathsf{F_l}(t)$ has three frequency components: a DC one, the second one at f and the third one at $2f$. The MEMS resonator is mainly sensitive to the frequencies close to f_r and thus if $f \approx f_r$, the complex amplitude of $\mathsf{F_l}(t)$ can be approximated as:

$$F_l(f) = \frac{\varepsilon_0 h}{g^2}V_{DC}v_{act} \quad \text{(electrostatic force)}. \tag{2.11}$$

The electrostatic force increases when the gap between the two electrodes is reduced. This feature has made this transduction scheme very popular in MEMS technology where gaps of 100 nm can be achieved [Verd 2005, Arcamone 2009, Lopez 2009b, Colinet 2010, Lee 2009b].

2.2.1.2 MEMS resonator with capacitive detection

Capacitive detection consists in measuring the variation of capacitance between a proof mass (here, the vibrating beam) and a detection electrode (fig. 2.3). As the beam moves, the capacitance varies and thus the displacement of the beam can be determined from the electrical measurement. Capacitive detection is very popular in MEMS devices as it can be technologically implemented with ease and it is CMOS-compatible (it requires no exotic materials).

The capacitance $\mathsf{C}(t)$ is defined as:

$$\begin{aligned}\mathsf{C}(t) &= \int_0^L \frac{\varepsilon_0 h}{g - \tilde{\mathsf{w}}(x,t)}\mathrm{d}x \approx \int_0^L \frac{\varepsilon_0 h}{g}\mathrm{d}x + \int_0^L \frac{\varepsilon_0 h}{g}\frac{\tilde{\mathsf{w}}(x,t)}{g}\mathrm{d}x \\ &\approx C_0\left[1 + \eta_D\frac{\mathsf{w}(t)}{g}\right] \quad \text{(capacitive detection)},\end{aligned} \tag{2.12}$$

where ε_0 is the permittivity of the air, $C_0 = \frac{\varepsilon_0 hL}{g}$ and $\eta_D = 0.52$ for a clamped-clamped beam. The quantity of interest is:

$$\Delta\mathsf{C}(t) = C_0\eta_D\frac{\mathsf{w}(t)}{g} \quad \text{(capacitive detection)}, \tag{2.13}$$

which reflects the time varying part of the capacitance related to the mechanical motion.

2.2.1.3 Equivalent electrical model of the clamped-clamped beam with capacitive detection

In practice, it turns out that the quantity of interest $\Delta\mathsf{C}$ is generally negligible compared to C_0 when using only a fixed electrode and the mechanical resonance of the MEMS device is deteriorated by a large feed-through. In order to reduce the input-to-output capacitive coupling, a common solution found in the literature consists in implementing a second fixed-electrode. The first fixed electrode actuates the beam while the second electrode is employed to detect the mechanical displacement (fig. 2.4)[3], so that actuation and detection are decoupled. From the notations of figure 2.4, the electrostatic force applied on the beam is given by eq. (2.11) if $v_{MEMS} \ll v_{act}$.

[3] A two-electrodes resonator with differential actuation is also reported in [Juillard 2009, Giner 2011].

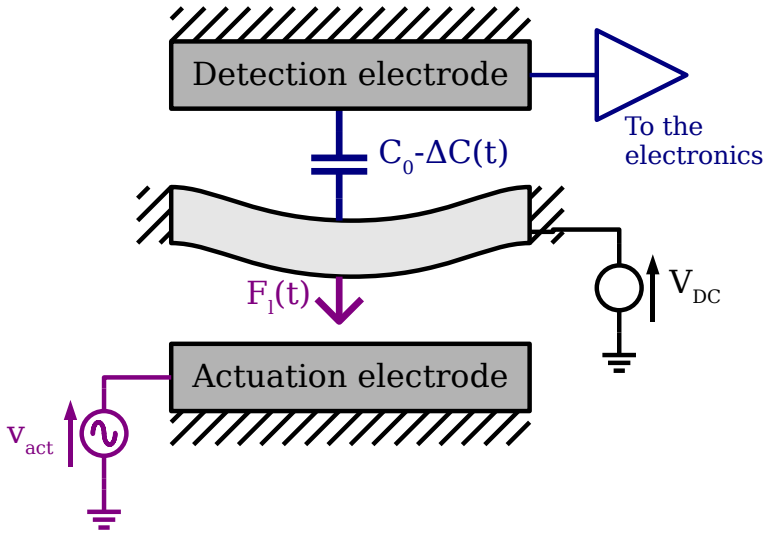

Figure 2.4: 2-port clamped-clamped beam with capacitive detection and electrostatic actuation.

This architecture is electrically modeled by the left schematic of figure 2.2. If $\Delta \mathsf{C}(t)$ is small compared to C_0, it can be assumed that $Y_{in} = j2\pi f C_0$. Based on the Thevenin's theorem [Thevenin 1883], the voltage v_{MEMS} of figure 2.2 is determined when there is no loading at the resonators output. The current $\mathsf{i}(t)$ that flows into the detection electrode is zero:

$$\begin{aligned} \mathsf{i}(t) = \frac{\mathrm{d}}{\mathrm{d}t}\left[\left[\mathsf{C}_0 - \Delta\mathsf{C}(t)\right]\left[V_{DC} - \mathsf{v}_{\mathsf{MEMS}}(t)\right]\right] = 0 \Rightarrow \\ \frac{\mathrm{d}\mathsf{v}_{\mathsf{MEMS}}(t)}{\mathrm{d}t} = V_{DC}\frac{\mathrm{d}}{\mathrm{d}t}\left[\frac{\Delta\mathsf{C}(t)}{C_0}\right] \quad (\text{if } \Delta\mathsf{C}(t) \ll C_0 \text{and } \mathsf{v}_{\mathsf{MEMS}}(t) \ll V_{DC}). \end{aligned} \tag{2.14}$$

The displacement-to-voltage transfer function is then:

$$H_{det}(f) = \frac{v_{MEMS}(f)}{w(f)} = \eta_D \frac{V_{DC}}{g} \quad \text{(capacitive detection)}. \tag{2.15}$$

The output impedance of the capacitive detection is determined when $\mathsf{w}(t) = 0$ and the electrodes other than the detection electrodes are set to the ground. Based on the Thevenin's theorem, the output impedance is the equivalent impedance of C_0.

The architecture benefits from using a single-sided actuation which simplifies the electronic circuit. Moreover only a DC voltage is applied to the moving beam: using a large DC voltage will not interfere with the electronic circuit. It is particularly useful with recent CMOS technologies that have (very) limited maximum voltages (typically around 1 V). On the other hand, the lead access from the electronic circuit to the MEMS resonator can create some coupling between the actuation node and the detection node and thus create some feed-through (a more detailed analysis of

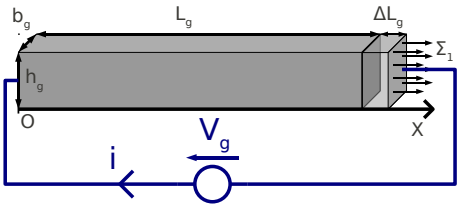

Figure 2.5: Study case of piezoresistivity

the MEMS-to-electronics coupling will be made in section 2.3). Moreover, it should be mentioned that the remaining intrinsic feed-through is negligible compared to a 1-port resonator although it is not totally canceled. The feed-through can be evaluated using electromagnetic finite element simulations.

2.2.2 Clamped-clamped beam with piezoresistive detection

2.2.2.1 Piezoresistive detection

A piezoresistive material sees its resistance varying with the stress applied on the material. Consider a beam with a length L_g, a width b_g and a thickness h_g (fig. 2.5), made of a piezoresistive material with cubic symmetry, such as silicon crystal. The resistance at rest is equal to $R_{g0} = \Phi_{g0} L_g / (b_g h_g)$, where Φ_{g0} is the resistivity of the isotropic material. If a stress along (OX) is applied to the beam, its resistance varies in the following manner [Bao 2000]:

$$\frac{\Delta R_g}{R_{g0}} = \frac{\Delta L_g}{L_g} - \frac{\Delta b_g}{b_g} - \frac{\Delta h_g}{h_g} + \frac{\Delta \Phi_{g0}}{\Phi_{g0}}, \tag{2.16}$$

where ΔR_g, ΔL_g, Δb_g, Δh_g represent respectively the variation of the resistance, the length, width and thickness of the beam. $\Delta \Phi_{g0}$ is the resistivity variation of the beam that changes if the beam is submitted to a stress. From [Bao 2000], the relative resistance variation simplifies to:

$$\frac{\Delta R_g}{R_{g0}} = \gamma_{beam} \frac{\Delta L_g}{L_g}, \tag{2.17}$$

where γ_{beam} is the so-called dimensionless gauge factor of the single crystal material.

Piezoresistive detection makes the fabrication of the resonator more complex as it requires the resonator or a layer of it to be made of a piezoresistive material. Moreover, if the layer is a piezoresistive crystal, the doping level of the layer should be controlled. Finally the detection introduces some white and flicker noise that can limit the performance of this detection scheme.

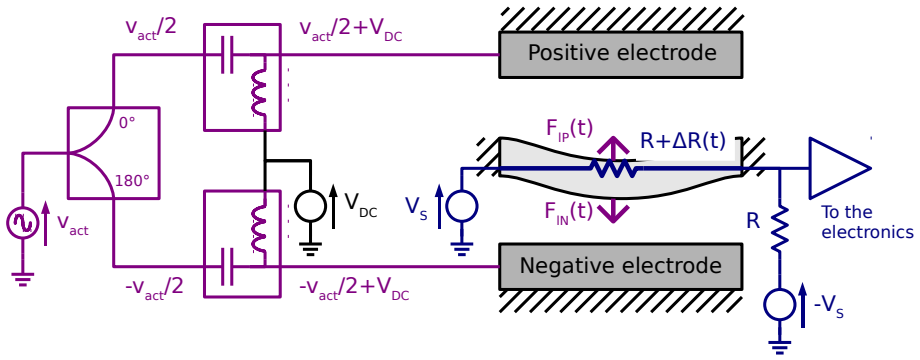

Figure 2.6: Clamped-clamped beam with piezoresistive detection

Piezoresistive readout introduces some white and flicker voltage noise with the following power spectral density in V^2/Hz:

$$S_{PZR} = \underbrace{4k_BTR_g}_{\text{white noise}} + \underbrace{\frac{\kappa_H V_g^2}{\mathcal{D}L_g b_g h_g f}}_{\text{flicker noise}} \quad \text{(piezoresistive noise)}, \tag{2.18}$$

where k_B and T are the Boltzmann constant and the temperature. R_g, V_g and $\mathcal{D}$ are the resistance, the voltage across the beam and the doping level of the resistive beam. κ_H (without units) is the Hooge noise coefficient [Harkey 2000].

2.2.2.2 Electrical model of the resonator

Consider a clamped-clamped beam as depicted on figure 2.6. The electrostatic force per unit of length applied on the beam is again (see eq. (2.11)):

$$F_l(f) = F_{lP}(f) - F_{lN}(f) = \frac{\varepsilon_0 h}{g^2} V_{DC} v_{act} \quad (\text{if } \tilde{\mathsf{w}}(x,t) \ll g). \tag{2.19}$$

The resistance of the beam is denoted R. When the beam is subject to a strain $\Delta L/L$, its resistance varies. Assuming the curvature of the beam is small, we have $\frac{\Delta L}{L} = \frac{1}{2L}\int_0^L \left(\frac{\partial \tilde{\mathsf{w}}}{\partial x}\right)^2 \mathrm{d}x$ (see appendix B) and thus:

$$\frac{\Delta \mathsf{R}}{R}(t) = \frac{\gamma_{beam}}{2L}\int_0^L \left(\frac{\partial \tilde{\mathsf{w}}}{\partial x}\right)^2 \mathrm{d}x = \frac{\gamma_{beam}}{2}\eta_D \left[\frac{\mathsf{w}(t)}{L}\right]^2, \tag{2.20}$$

where $\eta_D = 0.52$. With the electrical connection of figure 2.6, the output voltage $\mathsf{V_{MEMS}}$ is:

$$\mathsf{V_{MEMS}}(t) = -V_S \frac{\gamma_{beam}}{4}\eta_D \left[\frac{\mathsf{w}(t)}{L}\right]^2 \quad \text{(nanowire detection)}. \tag{2.21}$$

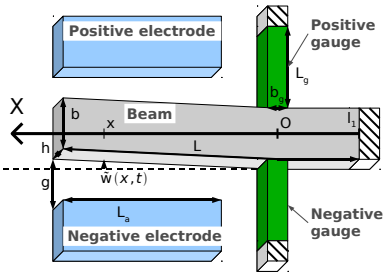

Figure 2.7: Crossbeam with a piezoresistive detection

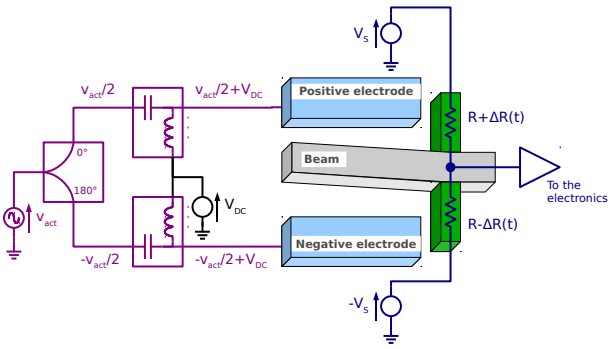

Figure 2.8: Electrical connection of a crossbeam

The detection is clearly nonlinear and the frequency of $\mathsf{V}_{\mathsf{MEMS}}(t)$ is twice the one of $\mathsf{w}(t)$. Nevertheless, if the actuation voltage is at the frequency f_{act} and the electrical response of the resonator is measured at the frequency $2f_{act}$; it is possible to acquire the open-loop response of the resonator. Finally, the output impedance of the Thevenin's model is equal to $R_{MEMS} = R/2$.

An interesting property of piezoresistive detection is that the output impedance R_{MEMS} can be very small compared the equivalent input impedance $1/Y_{inN}$ or $1/Y_{inP}$ and thus the resonator's intrinsic feed-through is largely reduced compared to resonators with a capacitive detection (see eq. (2.7)).

2.2.3 Crossbeam with piezoresistive detection

The crossbeam topology is realized with two piezoresistive gauges placed perpendicularly to the beam close to the anchor (fig. 2.7). The resistance of the gauges is modulated when a perpendicular mechanical stress is applied at $x = 0$. The stress at $x = 0$ is given by [Labarthe 2010]:

$$\begin{aligned}\Sigma(x=0,t) &= \frac{c_{beam} I}{h b_g}\left[\frac{\partial^3 \tilde{\mathsf{w}}}{\partial x^3}\left(0^+,t\right) - \frac{\partial^3 \tilde{\mathsf{w}}}{\partial x^3}\left(0^-,t\right)\right] \\ &= -\frac{c_{beam} I \eta_D}{L^3 h b_g}\mathsf{w}(t), \end{aligned} \tag{2.22}$$

where $\eta_D = 49$. The corresponding resistance variation of one gauge is:

$$\frac{\Delta \mathsf{R}}{R}(t) = \gamma_{gauge}\frac{I \eta_D}{L^3 h b_g}\mathsf{w}(t), \tag{2.23}$$

assuming the gauges and the beams have the same Young's modulus. With the electrical connections of figure 2.8, the voltage $\mathsf{V}_{MEMS}(t)$ is equal to:

$$\mathsf{V}_{MEMS}(t) = V_{beam0} + \frac{\gamma_{gauge}}{12}\frac{b^3}{b_g L^3}\eta_D V_S \mathsf{w}(t) \quad \text{(crossbeam detection)}. \tag{2.24}$$

The output impedance of the Thevenin's model is equal to $R_{MEMS} = R/2$ where R is the resistance of the gauge at rest.

The crossbeam has a linear detection with a low output impedance. The following sections will show that these properties reduce the connection losses which improves the signal-to-noise ratio at the resonator output.

2.2.4 Piezoelectric cantilever

2.2.4.1 Piezoelectric actuation

Piezoelectricity is a reversible phenomenon that converts a mechanical stress into a voltage and vice versa. This phenomenon only exists in particular crystals such as AlN, PZT... The piezoelectric effect is governed by [Sta 1988]:

$$\{\Sigma\} = \{c\}\{\ell\} - \{e\}\{E\}, \tag{2.25}$$

where:

$\{\Sigma\}$ is the (6×6) stress tensor in Pa,

$\{c\}$ is the (6×6) elastic stiffness constant in Pa,

$\{\ell\}$ is the (6×6) dimensionless strain tensor,

$\{e\}$ is the (6×6) piezoelectric constant matrix in C/m^2,

$\{E\}$ is the electric field (a 3 components vector) in V/m.

Piezoelectric actuation of a beam can be achieved by stacking several layers of material, as depicted in figure 2.9, and applying an electric field across the piezoelectric material and so that the beam is subject to a bending moment. The technological stack is composed of two electrodes with a piezoelectric layer in-between, but also an elastic layer to emphasize the deflection. It is assumed that the piezoelectric behavior is governed by the e_{ZX} coefficient or also referred as e_{31} coefficient in the literature (all other coordinates of $\{e\}$ are neglected): when a voltage is applied in the (OZ)-direction to an infinitesimal volume $\mathrm{d}x \times b \times \mathrm{d}z$ of the piezoelectric layer, it creates a stress in the (OX)-direction. The resulting moment in the (OY) direction is then [Brissaud 2003, Ivaldi 2011b]:

$$\begin{aligned}\mathcal{M} &= \int_{z=h_{eb}+h_s/2-z_0}^{z=h_{PZE}+h_{eb}+h_s/2-z_0} -bze_{ZX}\mathsf{E_Z}(x,t)\,\mathrm{d}z \\ &= -b\frac{2h_{eb}+h_s-2z_0}{2}e_{ZX}\mathsf{v_{act}}(t),\end{aligned} \tag{2.26}$$

where $v_{act}(t)$ is the voltage applied on the piezoelectric layer and z_0 is the position of the neutral line defined in [Brissaud 2003].

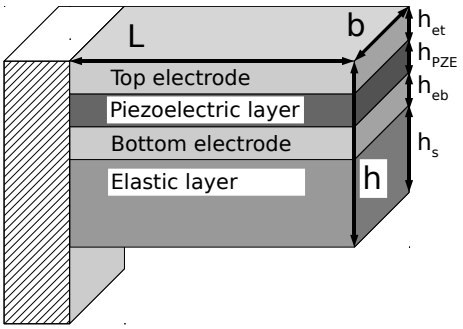

Figure 2.9: Typical piezoelectric stack

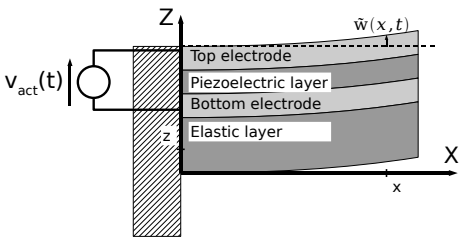

Figure 2.10: Axis and coordinate for a piezoelectric cantilever

To homogenize the calculation with respect to the other resonators, it may be useful to define an equivalent force per unit of length. It determines the equivalent force that induces the same mechanical displacement than the momentum. From the Euler-Bernoulli vibration equation:

$$\rho_{eq} b h \frac{\partial^2 \tilde{\mathsf{w}}(x,t)}{\partial t^2} + \xi \frac{\partial \tilde{\mathsf{w}}(x,t)}{\partial t} + r_{eq} \frac{\partial^4 \tilde{\mathsf{w}}(x,t)}{\partial x^4} = \frac{\partial^2 \mathcal{M}}{\partial x^2}, \tag{2.27}$$

where $\rho_{eq} = (\rho_s h_s + \rho_{eb} h_{eb} + \rho_{PZE} h_{PZE} + \rho_{et} h_{et})/h$ is the equivalent beam density, h is the total thickness of the beam and r_{eq} is the equivalent beam rigidity [Brissaud 2003]. The discontinuity of the applied voltage at $x = L$ creates a momentum on beam. Eq. (2.27) can be solved using the Galerkin's method [Ivaldi 2011b]:

$$m\ddot{\mathsf{w}}(t) + \frac{m 2\pi f_r}{Q}\dot{\mathsf{w}}(t) + m(2\pi f_r)^2 \mathsf{w}(t) = \eta_A b \frac{2h_{eb} + h_s - 2z_0}{2L} e_{ZX} \mathsf{v_{act}}(t), \tag{2.28}$$

where the resonance frequency of the beam is expressed as: $f_r = \sqrt{r_{eq} b \lambda^4 / (mL^3)}/(2\pi)$. $\eta_A = 5.5$. The corresponding force per unit of length is:

$$\mathsf{F_l}(t) = b \frac{2h_{eb} + h_s - 2z_0}{2L^2} e_{31} \mathsf{v_{act}}(t) \quad \text{(piezoelectric actuation)}, \tag{2.29}$$

Piezoelectric actuation does not consume much and has an important actuation gain, defined as $|F_l/v_{act}|$ (that will be highlighted in section 2.4) that makes piezoelectric beam popular for applications such as low-power switches and energy harvesting [Sinha 2009, Chapuis 2007, Defosseux 2011]. The use of piezoelectric cantilevers for mass sensing in liquid environment has also been studied [Maraldo 2007]. The fabrication of such MEMS resonators is however difficult, due to the complex technological stack required, making piezoelectric resonators uncommon in the literature [Masmanidis 2007, Karabalin 2009, Ivaldi 2011b].

2.2.4.2 Piezoelectric detection

Piezoelectric detection is based on the indirect piezoelectricity effect, that is the creation of charges when a piezoelectric material is subject to a mechanical displacement [Sta 1988]:

$$\{D\} = \{e\}\{\ell\} + \{\varepsilon\}\{E\}, \tag{2.30}$$

where:

$\{D\}$ is the (3×3) electrical displacement in $\mathrm{C/m^2}$,

$\{\varepsilon\}$ is the (3×3) permittivity of the piezoelectric crystal in $\mathrm{F/m}$.

Consider a piezoelectric crystal, where only the e_{31} is the dominant component of $\{e\}$ and submitted an electric field in the (OZ)-direction. Equation (2.30) becomes:

$$D_Z = e_{ZX}\ell_X + \varepsilon_{PZE}E_Z. \tag{2.31}$$

For the piezoelectric cantilever depicted in figures 2.9 and 2.10, the current that flows into the piezoelectric layer has the following expression:

$$\begin{aligned} \mathsf{i}(t) &= b\int_0^L \frac{\mathrm{d}D_Z}{\mathrm{d}t}(x,t)\,\mathrm{d}x \\ &= b\int_0^L \left[e_{ZX}\frac{\mathrm{d}\ell_X}{\mathrm{d}t}(x,t) + \frac{\varepsilon_{PZE}}{h_{PZE}}\frac{\mathrm{d}V}{\mathrm{d}t}(t)\right]\mathrm{d}x. \end{aligned} \tag{2.32}$$

From [Brissaud 2003], one can find that: $\ell_X = (h_{eb} + h_s/2 - z_0)\frac{\partial^2 \tilde{w}}{\partial x^2}$, thus:

$$\mathsf{i}(t) = \underbrace{e_{ZX}\frac{b}{L}(h_{eb} + h_s/2 - z_0)\,\eta_D\frac{\mathrm{d}\mathsf{w}}{\mathrm{d}t}(t)}_{\text{motional current}} + \underbrace{C_{PZE}\frac{\mathrm{d}V}{\mathrm{d}t}(t)}_{\text{feed-through current}}, \tag{2.33}$$

where $C_{PZE} = \varepsilon_{PZE}\frac{bL}{h_{PZE}}$ is the AlN-layer capacitance and $\eta_D = 1.4$.

2.2.4.3 Electrical model of the resonator

As an 1-port resonator, a piezoelectric cantilever can be electrically described with the BVD model [Van Dyke 1928] depicted in figure 2.11. It consists of a static capacitance (corresponding to C_{PZE}) in parallel with an complex impedance describing the mechanical behavior of the beam. The latter impedance also called motional impedance is composed of a capacitance C_m, a resistance R_m and an inductance L_m in series. At the resonance frequency, the impedance of the capacitance and the inductance cancel each other. The remaining element of the motion impedance is

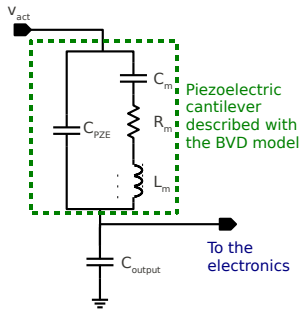

Figure 2.11: BVD model of the resonator

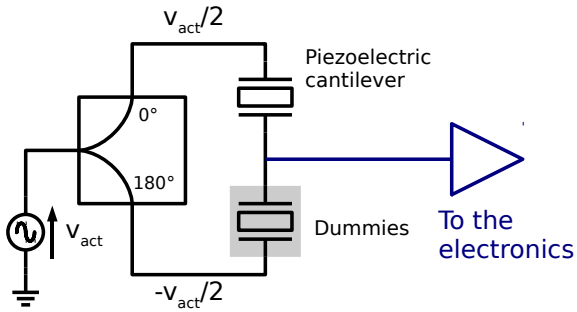

Figure 2.12: Bridge architecture.

the resistance describing the in-phase relation between the actuation voltage and the motion current.

An electrical model of the resonance similar to that of the other resonators can be obtained by using:

$$Z_{MEMS} = R_m = \frac{2\pi f_r m/Q}{e_{ZX}^2 \left(\frac{b}{L}\right)^2 (h_{eb} + h_s/2 - z_0)^2 \eta_D \eta_A}. \tag{2.34}$$

and that v_{MEMS} is a Lorentz function centered on f_r and having a maximum value of v_{act}. The input-to-output admittance is $Y_{ft} = j\omega C_{PZE}$ and, as there are no ground pads, $Y_{in} = 0$.

Usually, the input-to-output impedance is much smaller than R_m. As a result, the resonance signal is very small compared to the feed-through created by C_{PZE}. To circumvent this issue, one should design a 2-ports resonator as discussed previously. However, this approach is quite delicate due to the complex technological stack required to fabricate piezoelectric cantilevers[4]. The feed-through can however be reduced by implementing the resonator in a bridge architecture (fig. 2.12). The dummy component can be either an identical but unreleased resonator or a variable capacitance and resistance with an admittance equal to Y_{ft} at the resonance. The resonator and the dummy elements are actuated with a signal in counter-phase so that the feed-through is canceled.

2.2.5 Conclusion

We have presented various actuation and detection transduction techniques that are low-power and CMOS compatible. Table 2.1 gives a summary of the expressions of the parameters of the electrical model associated with each MEMS resonator.

[4]It should however be mentioned the work published in [**?**] where 2-ports resonators where fabricated using either piezoelectric or piezoresistive detection.

Single-sided actuation			
	Y_{in}	Y_{ft}	Z_{MEMS}
Clamped-clamped beam with capacitive detection	$j2\pi fC_0$	$\ll j2\pi fC_0$	$\frac{1}{j2\pi fC_0}$
Clamped-clamped beam with piezoresistive detection	0	$j2\pi fC_0$	$\frac{\Phi_{g0}L}{2hb}$
Crossbeam with piezoresistive detection	0	$j2\pi fC_0$	$\frac{\Phi_{g0}L_g}{2hb_g}$
Piezoelectric cantilever	0	$j2\pi fC_{PZE}$	R_m
Differential actuation			
	Y_{inP}	Y_{inN}	Z_{MEMS}
Clamped-clamped beam with piezoresistive detection	$j2\pi fC_0$	$j2\pi fC_0$	$\frac{\Phi_{g0}L}{2hb}$
Crossbeam with piezoresistive detection	$j2\pi fC_0$	$j2\pi fC_0$	$\frac{\Phi_{g0}L_g}{2hb_g}$

Table 2.1: Electric parameters of the MEMS resonators.

The clamped-clamped beam with capacitive detection is the simplest one to fabricate among the four resonators but suffers from a high sensitivity to feed-through and a large output impedance. Piezoresistive detection provides a lower output impedance, however the associated fabrication process requires a piezoresistive material (that can be doped silicon and in that case the fabrication process is not made more complex except one should have a good control of the doping level). Note that piezoresistive detection also introduces some noise and that can deteriorate the signal-to-noise ratio of the resonator. Finally, piezoelectric cantilevers require a complex technological process but provide a linear actuation and detection transduction with high gain. The performance of piezoelectric cantilevers is also limited by intrinsic feed-through issues.

The different dimensions of all these resonators and the peculiarities of each actuation and detection scheme make their comparison complex. However, after describing effects of the MEMS-to-electronics interconnection and based on the system architectures of the chapter 1, section 2.4 intends to compare the performance of these different resonators and their limitations.

2.3 Interconnections between the MEMS resonator and the readout electronics

The integration of MEMS resonators with their readout electronics is crucial to reduce the MEMS-to-electronics connection losses and the feed-through. These char-

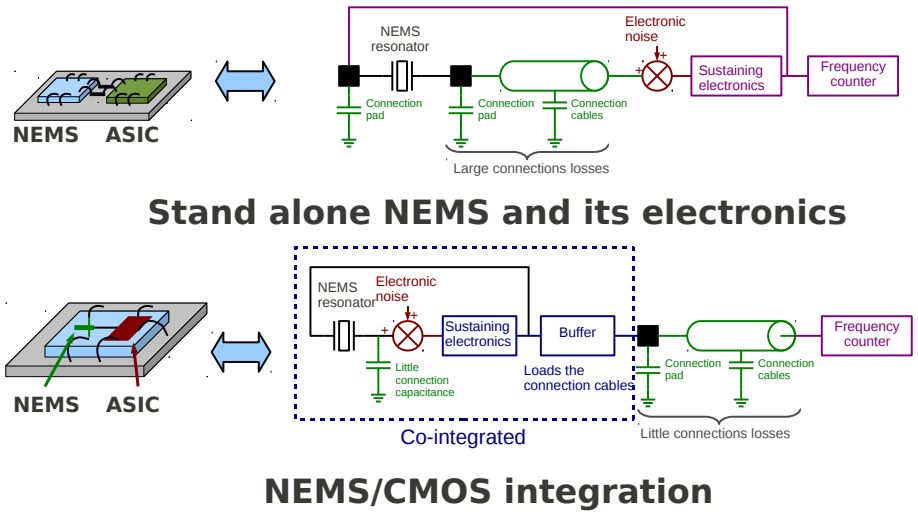

Figure 2.13: Representation of different NEMS/CMOS connection topologies

acteristics must be considered in the design of the oscillator as they can degrade the resolution of the loop or make the implementation of the self-oscillating loop more complex. Connection losses can attenuate the MEMS output signal and thus emphasize the electronic noise (see subsection 1.3.1.2). The feed-through can shadow the MEMS resonance making it difficult to measure and reducing the resolution of the MEMS component (see subsection 1.1.2) or can make the loop unstable (see subsection 1.3.1.3)

Connection losses and feed-through can be analyzed based on the electrical model of the resonator described in section 2.2. In subsection 2.3.1, the connection losses are determined using simple models of the electronics and the MEMS-to-electronic connection. The study highlights the impact of the connections that limit the resonator output signal and the signal-to-noise ratio at the output of the readout electronics. Each connection implementation is then described in a more realistic way. Finally, heterodyne architectures are described and their limitations are discussed.

2.3.1 Basic model of the MEMS-to-electronics connection losses

2.3.1.1 Presentation of a basic electrical model

The simplest approach to evaluate the connection losses consists in modeling the connections by a grounded capacitance C_{connec}. The equivalent impedance of C_{connec} is compared to the MEMS output impedance to determine the connection losses (fig 2.14):

$$H_{connec} = \frac{v_{elec}}{v_{MEMS}} = \frac{1}{1 + j2\pi f Z_{MEMS} C_{output}}. \tag{2.35}$$

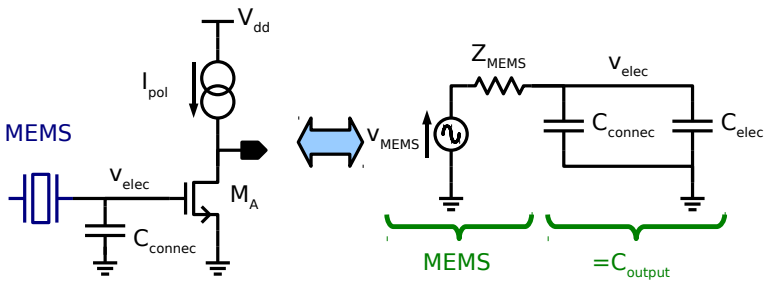

Figure 2.14: Simple schematic of the MEMS-to-electronics connection.

The connection losses are low if the MEMS output impedance is low compared to the equivalent impedance of the connection capacitance (corresponding to a low connection capacitance).

There are 3 major MEMS-to-electronics connection scheme: 2D co-integration, 3D co-integration and wire-bonding (fig. 2.13). Stand-alone resonators are economically interesting because the MEMS fabrication process is simple and decouples the fabrication yield of MEMS and ASIC, thereby reducing the process development of the device. However the connection capacitance between the MEMS and its associated electronics is generally larger than 10 pF, which results in a decrease of the MEMS output signal and can limit the frequency resolution of the sensor.

On the other hand, integrating the MEMS and its electronic circuit on the same wafer can reduce the MEMS-to-electronics connection capacitance to as little as 1 fF (fig. 2.13). The fabrication process however is much more complex than for stand-alone MEMS. The CMOS process flow and the MEMS design must be adapted in order to be compatible: most of the foundries refuse to do such an adjustment due to the inherent cost of associated technological developments.

3D co-integration may allow to overcome the former drawbacks as the fabrication of the electronics and of the MEMS are separated, still ensuring low MEMS-to-CMOS connection capacitance. A typical value of 1 fF is taken in this manuscript for such 3D-integration. The CMOS circuit can be realized using a standard process flow and can even be tested separately from the MEMS once the CMOS fabrication steps are completed. After that, another SOI-wafer is bonded on top of the CMOS wafer. The MEMS structural material is usually a mono-crystalline silicon layer that is connected to the back-end metal layers of the CMOS circuit.

2.3.1.2 Simple electrical model of the first amplification stage in an ASIC and the corresponding connection losses

A trade-off must be found regarding the design of the first transistor of the CMOS circuit (fig. 2.14): if the transistor is small, the transistor generates a large noise. On the other hand, a large transistor has an important input capacitance and thus increases the MEMS-to-electronics losses. From the Berkeley level 1 model of the

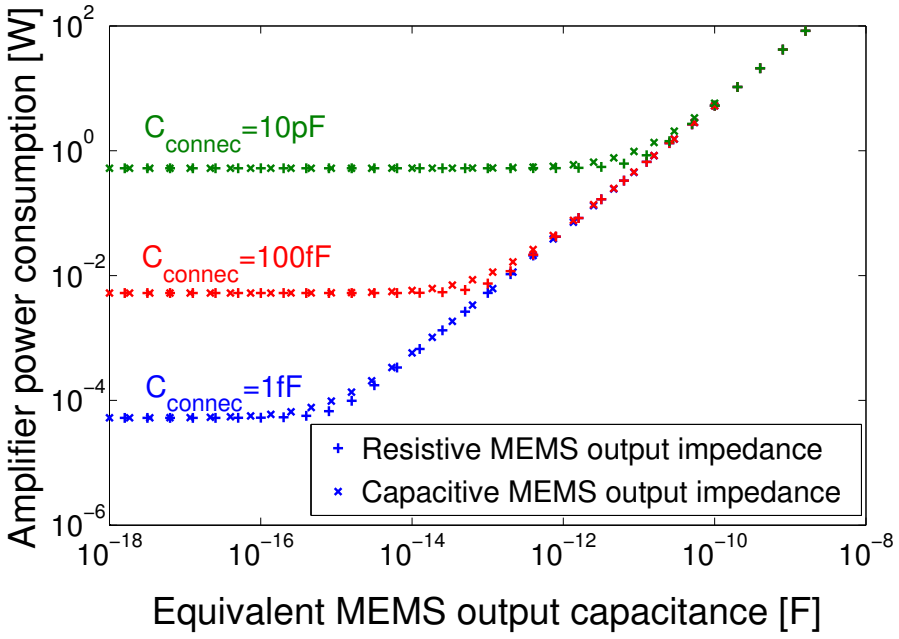

Figure 2.15: Optimal amplifier power consumption versus equivalent MEMS output capacitance

transistors [Sansen 2006], it is possible to determine the optimal transistor dimensions and the corresponding optimal power consumption. The Gate-Source capacitance is expressed as $C_{gs} = \frac{2}{3} C_{ox} W_A L_A$ where C_{ox}, W_A, L_A are respectively the oxide capacitance per unit of area, the width and length of the transistor. It results in a connection loss of:

$$H_{connec} = \frac{1}{1 + j2\pi f_{osc} Z_{MEMS} \left(C_{connec} + \frac{2}{3} C_{ox} W_A L_A \right)}. \tag{2.36}$$

Note that in (2.36), the effect of the Gate-Drain capacitance was neglected which is correct only if the gain of the amplifier and the transistor length are small. This assumption should be verified for the considered CMOS design kit and the amplifier topology. The PSD of the electronic noise expressed at the input of the transistor is (if only the white noise is considered):

$$S_{M_A} = \frac{8 k_B T L_A}{3 \mu_N C_{ox} W_A V_{dssat}}, \tag{2.37}$$

where μ_N and V_{dssat} are the mobility and the Drain-Source saturation voltage of the transistor, respectively. The corresponding signal-to-noise ratio expressed at the transistor's input is:

$$SNR = \frac{v_{MEMS}^2 T_{meas}}{S_{MEMS} + \frac{8 k_B T L_A}{3 \mu_N C_{ox} W_A V_{dssat}} \left| 1 + j2\pi f_{osc} Z_{MEMS} \left(C_{connec} + \frac{2}{3} C_{ox} W_A L_A \right) \right|^2}.$$

(2.38)

In order to optimize the SNR, the second term in the denominator should be minimized:

$$\frac{8k_BTL_A}{3\mu_N C_{ox}W_A V_{dssat}}\left|1+j2\pi f_{osc}Z_{MEMS}\left(C_{connec}+\frac{2}{3}C_{ox}W_AL_A\right)\right|^2 = \underbrace{\frac{8k_BTL_A^2}{3\mu_N C_{ox}V_{dssat}}}_{\text{only depends on } L_A}\underbrace{\frac{\left|1+j2\pi f_{osc}Z_{MEMS}\left(C_{connec}+\frac{2}{3}C_{ox}W_AL_A\right)\right|^2}{W_AL_A}}_{\text{only depends on } W_AL_A} \quad (2.39)$$

L_A should therefore be taken to its minimum value L_{tech} imposed by the CMOS design rules while the transistor active area W_AL_{tech} should be optimized:

$$W_A = \begin{cases} \frac{3\sqrt{1+(2\pi f_{osc}C_{connec}R_{MEMS})^2}}{4\pi f_{osc}C_{ox}R_{MEMS}L_{tech}} & \text{if } Z_{MEMS}=R_{MEMS} \\ \frac{3(C_{connec}+2C_{MEMS})}{2C_{ox}L_{tech}} & \text{if } Z_{MEMS}=\frac{1}{j2\pi f_{osc}C_{MEMS}} \end{cases}. \quad (2.40)$$

It is also quite common to analyze the power consumption of the circuit $P_{amp} = V_{dd}\frac{\mu_N C_{ox}}{2}\frac{W}{L}V_{dssat}^2$, where V_{dd} is the supply voltage of the CMOS technology. Based on the HCMOS9 design kit from ST Microelectronics, the figure 2.15 presents the evolution of the amplifier power consumption for the optimal dimensions (W_A given by (2.40) and $L_A = L_{tech}$) versus the equivalent MEMS output capacitance i.e $1/(2\pi f_{osc}Z_{MEMS})$. If the MEMS output impedance is purely capacitive then the results presented in fig. 2.15 are independant of f_{osc}. Otherwise, the equivalent output capacitance should be evaluated with respect to f_{osc}. From fig. 2.15, we see that in some cases, the optimal power consumption is too large for practical application. Figure 2.16 depicts the corresponding MEMS-to-electronics connection losses versus the equivalent MEMS output capacitance. In the figure, the blue, green and red regions represent the typical range of the output capacitance of the capacitive, piezoelectric and crossbeam detection scheme.

2.3.2 Interconnection schemes

The previous study highlights the interest of 2D- or 3D-integration of the MEMS and its associated electronics especially for capacitively-transduced resonators. The following subsections aim at refining the model of the connection losses in the case of wire-bonding and 2D or 3D co-integration. The technological flow associated with each connection scheme is described, as well as their associated equivalent electrical models.

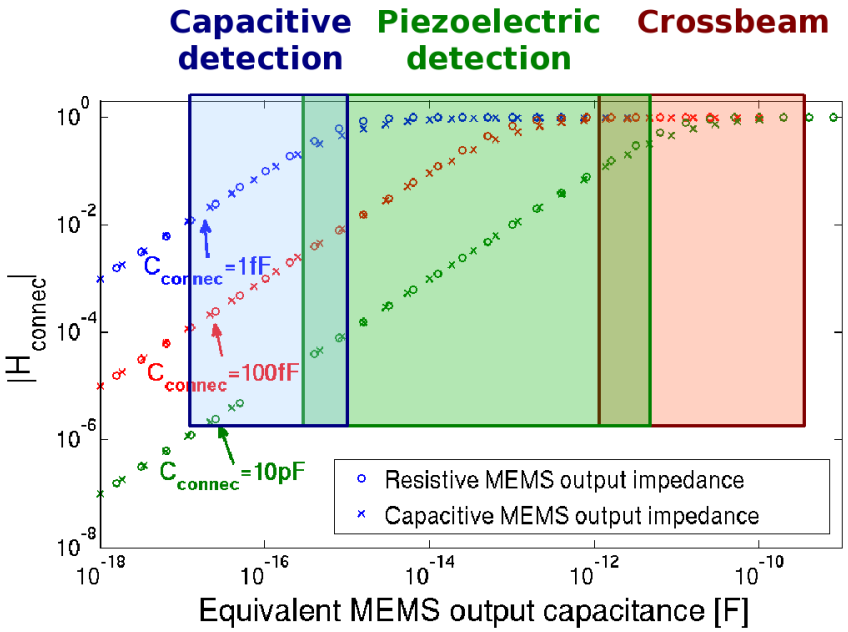

Figure 2.16: NEMS-to-electronic connection losses versus the equivalent MEMS output capacitance. The crosses represent H_{connec} for a resonator with a resistive output impedance and the circles represent H_{connec} for a resonator with a capacitive output impedance.

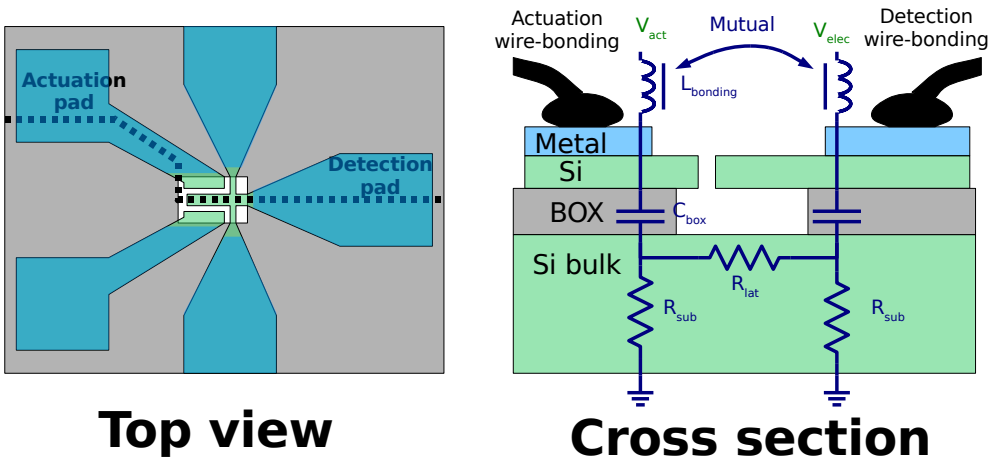

Figure 2.17: Simplified representation of a stand alone MEMS resonator and its connection pads (not to scale).

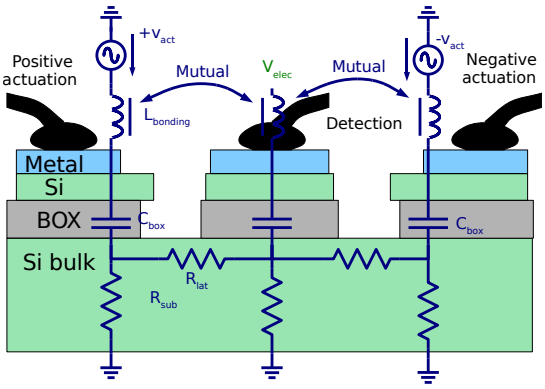

Figure 2.18: Cross-section representation of a stand-alone MEMS with differential actuation

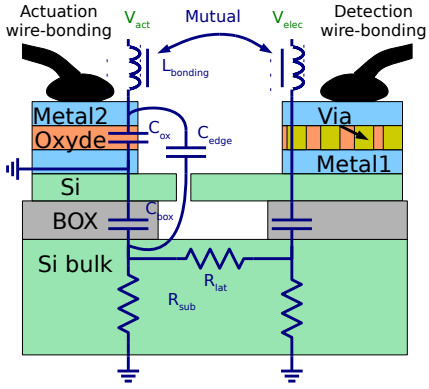

Figure 2.19: Cross-section representation of a stand-alone MEMS with shielded actuation

2.3.2.1 Stand alone MEMS connected to the electronics by wire bonding

One of the simplest methods to fabricate MEMS resonators is to start from a SOI-wafer[5]. These resonators are defined using only the top silicon layer. The geometry of the resonator is realized using a lithography step and an anisotropic etching. The resonator is then released using the BOX (buried oxide) layer of the SOI-wafer as a sacrificial layer and an isotropic wet or gaseous etching (fig. 2.17). See for example [Mile 2010].

The resonator is connected to the electronics via pads. Such pads are large conductive areas in doped silicon or in metal on which a thin wire (named "bonding wire") can be welded and its other extremity connected to the electronics. For the wire to be properly bonded, the pad area is usually taken to 100×100 µm^2 or more. In the case when the silicon is not very much doped, so as to improve piezoresistive detection of the MEMS resonator, the resistance of the path between the pads and the MEMS electrodes can be large. To reduce the corresponding resistances, it is then common to add a metal layer on top of the pads and on the paths from the pads to the MEMS electrodes. Knowing the area of the pads and of the paths, it is possible to determine a capacitance C_{BOX} of the BOX layer (fig. 2.17). Generally, the bottom face of the silicon bulk is connected to the ground and a resistance R_{sub} from the BOX/silicon bulk interface to the ground should be included in the electrical model. A resistance R_{lat} can be defined between the two capacitance C_{BOX} corresponding to the actuation and detection pads. Finally the bonding wires can act as transmission and reception antennas, and be modeled by an inductance $L_{bonding}$ with a mutual coefficient $M_{bonding}$ between each of them. $L_{bonding}$ and $M_{bonding}$ depend on the length of the wires, the distance and the angle between each of them.

In differential actuation schemes, the two actuation pads and paths are symmetrically designed (fig. 2.18). The voltages on each actuation pad are in counter-phase

[5] `http://www.soitec.com/fr/`

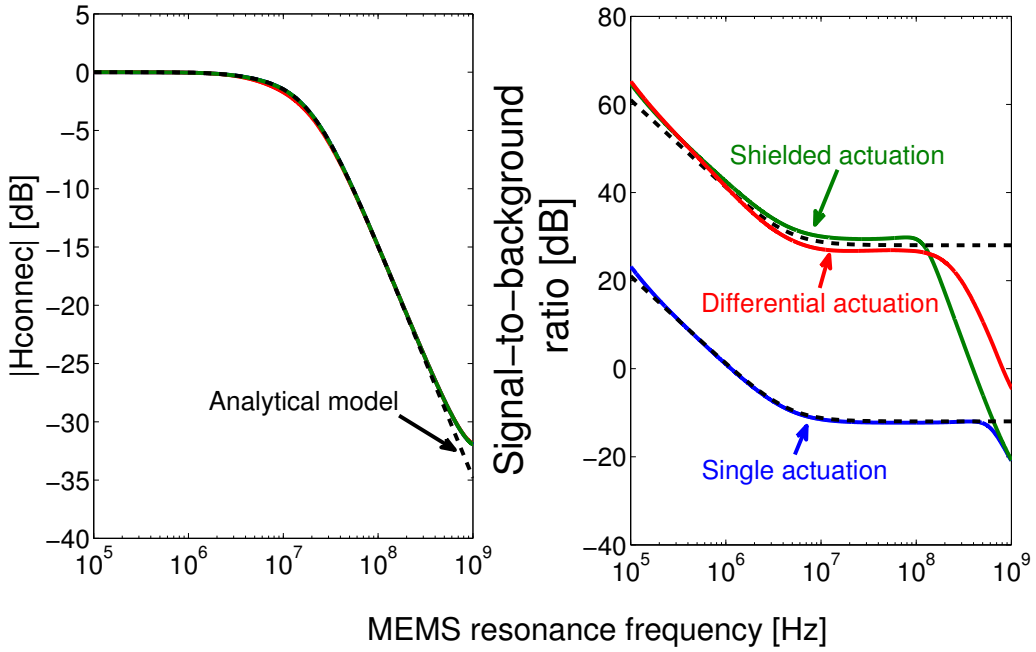

Figure 2.20: SPICE simulations of $|H_{connec}|$ and SBR versus the MEMS resonance frequency for different actuation implementations of a crossbeam resonator. The curves in dashed lines depict the analytical formulas.

so that their feed-through contribution cancel each other at the MEMS output. Note that it is not necessary for the resonator to have a differential actuation as the feed-through analyzed in this section is created from the MEMS-to-electronics access and not in the resonator itself. In the case of a resonator with single-sided actuation (such as in a clamped-clamped beam with capacitive detection of subsection 2.2.1) the second pad and path are in an open-circuit configuration. A feed-through can however appear because of dispersions in the bonding wires or in the area of the pads and paths.

Another technique to reduce feed-through is to use a second layer of metal. The actuation path is then realized using the top layer of metal while the lower metal layer is grounded (fig. 2.19). The latter metal layer acts like a shield preventing the actuation voltage from being transmitted to the substrate. This however increases the capacitance C_{ox} between the actuation path and the ground because the oxide layer between metal layers tends to be thin in CMOS processes. The capacitance can be increased by a factor two to three compared to the BOX-capacitance. Due to fringing effects, a capacitance C_{edge} between the actuation path and the bulk remains but it is reduced by two or three orders of magnitude. The capacitance C_{ox} can be reduced by increasing the oxide thickness or adding a third metal layer when technologically possible (in this case the second layer is filled with an oxide layer and increases the distance between the metal 1 and 3).

For the connection scheme depicted in figure 2.17, the expression of v_{elec} can be largely simplified if the effect of the inductance is neglected and if it is assumed that $R_{lat} \ll R_{sub}$ (i.e. the distance between the actuation and the detection paths is small compared to the thickness of the bulk) :

$$\begin{aligned} v_{elec} &= \frac{\left(1 + j2\pi f \frac{R_{lat}C_{BOX}}{2}\right) v_{MEMS} + j2\pi f \frac{Z_{MEMS}C_{BOX}}{2} v_{act}}{1 + j2\pi f \left(\frac{R_{lat}C_{BOX}}{2} + \frac{Z_{MEMS}C_{BOX}}{2} + Z_{MEMS}C_{elec}\right) - (2\pi f)^2 R_{lat} Z_{MEMS} C_{BOX} C_{elec}} \\ &\approx \frac{v_{MEMS} + \frac{Z_{MEMS}}{R_{lat}} v_{act}}{1 + \frac{Z_{MEMS}}{R_{lat}} \left(1 + 2\frac{C_{elec}}{C_{BOX}}\right) + j2\pi f Z_{MEMS} C_{elec}} \quad \text{if } 2\pi f \gg \frac{2}{R_{lat}C_{BOX}}. \end{aligned} \tag{2.41}$$

Note that in the case of a differential actuation, a term $\Delta R_{lat}/R_{lat}$ is factored to v_{act} in eq. (2.41) where ΔR_{lat} is the fabrication mismatch in R_{lat} or is a result of a mismatch in the differential actuation. In the case of the implementation with a shielded actuation, the term C_{BOX} is factored to v_{act} in the first line of eq. (2.41) is replaced by C_{edge}. The feed-through is thus reduced by C_{edge}/C_{BOX}.

The signal-to-background ratio SBR can be expressed as:

$$SBR = \left| \frac{g_{MEMS} H_{connec}}{H_{ft}} \right| = \begin{cases} g_{MEMS} \frac{R_{lat}}{|Z_{MEMS}|} & \text{for a single-sided actuation} \\ g_{MEMS} \frac{R_{lat}}{|Z_{MEMS}|} \frac{R_{lat}}{\Delta R_{lat}} & \text{for a differential actuation} \\ g_{MEMS} \frac{R_{lat}}{|Z_{MEMS}|} \frac{C_{BOX}}{C_{edge}} & \text{for a shielded actuation} \end{cases}. \tag{2.42}$$

If g_{MEMS} is smaller than 1, it is clear that a feed-through reduction technique is necessary to observe properly the resonance of the resonator.

Figure 2.20 presents, for different integration schemes, the evolution of $|H_{connec}|$ and of the SBR versus the MEMS resonance frequency. The parameters taken for the simulations are given in table 2.2 and the MEMS parameters are those of the crossbeam resonator experimentally characterized in chapter 3). In the case of differential actuation, 100 Monte-Carlo simulations were made with a 1%-standard deviation on the dimensions except for the bonding wire length and the mutual inductance where a 10%-standard deviation was taken (it is considered that the bonding is less reproducible). The SBR represented in figure 2.20 corresponds to the mean value of the SBR obtained through these simulations. In the case of shielded actuation, $C_{egde}/C_{BOX} = 1\%$. Note that the chosen value of $C_{elec} = 7$ pF includes the electronic input capacitance (≈ 2 pF) and the capacitance of the PCB board on which the resonator chip and the ASIC are bonded (≈ 5 pF). One can see a good match between the simulations and equations (2.41) and (2.42) which validates the assumptions made to obtain our formula.

One can see in equation (2.42) that the SBR is inversely proportional to Z_{MEMS}. It is therefore interesting to design MEMS with low output impedance in order to simplify the measurement of the MEMS resonance. Crossbeam resonators, thanks to piezoresistive detection and the usually small aspect ratio of the gauges, have a small output impedance, which in most cases is smaller than that of the other

parameter	value
Wire length	5 mm
Pad area	100×100 µm^2
Path area	100×10 µm^2
Distance between paths	20 µm
BOX thickness	145 nm
Bulk thickness	750 µm
$L_{bonding}$	5 nH
$M_{bonding}$	0.25 nH
C_{BOX}	2.7 pF
R_{sub}	682 kΩ
R_{lat}	26 kΩ
Z_{MEMS}	1.25 kΩ
g_{MEMS}	1.18×10^{-2}
C_{elec}	7 pF

Table 2.2: Parameters of the study of the substrate coupling.

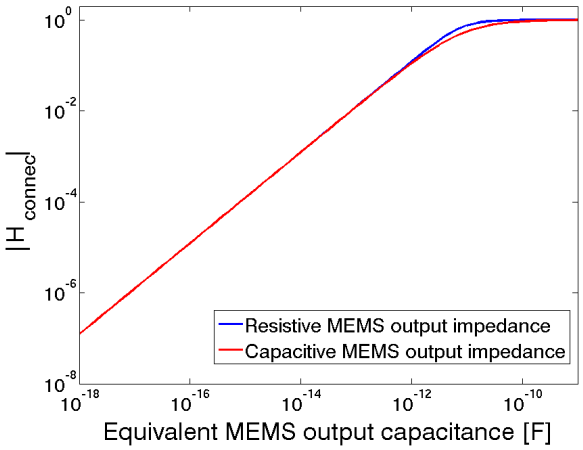

Figure 2.21: Connection losses versus the equivalent MEMS output capacitance.

MEMS resonators. The results presented in figure 2.20 are therefore a best case scenario, among the MEMS resonators. It therefore explains why there are, up to the author's knowledge, no measurement of stand-alone MEMS resonators with single-sided actuation and homodyne detection[6] at high frequency.

Finally, figure 2.21 depicts the evolution of $|H_{connec}|$ versus the MEMS output capacitance: the evolution of $|H_{connec}|$ remains similar to the one obtained with the simple model of subsection 2.3.1.

2.3.2.2 MEMS-CMOS 2D co-integration

The 2D co-integration process flow used in Leti starts with the fabrication of the resonator: the silicon is doped, the resonator shape is defined with anisotropic etching, then the MEMS is released using isotropic etching, which removes the BOX layer. The resonator is then protected with an oxide deposition. A standard CMOS SOI process flow is applied to fabricate the electronics next to the resonator. The electronics is then protected while the oxide layers over the resonator are removed. Isotropic etching is finally used to remove the oxide protecting the resonator and releasing the structure. A minimum distance of a few micrometers should be taken

[6]The measured frequency is equal to the actuation frequency as opposed to down-mixing architecture [Bargatin 2005].

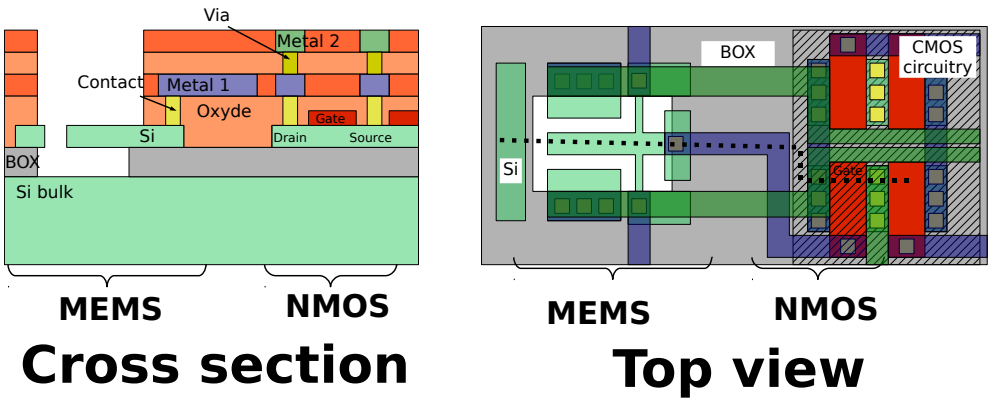

Figure 2.22: Simplified illustration of a 2D-cointegrated MEMS/CMOS system. On the top view, the oxide layers and the bulk are not depicted

between the CMOS circuit and the MEMS resonator so that the electronics is not affected by the resonator's final release.

2D-integration makes it possible to suppress the actuation and detection pads of the resonator. The paths between the resonator and the CMOS circuit are therefore reduced and so is their parasitic coupling. One can estimate that the actuation paths are a few tens of micrometers long over one micrometer wide. The detection path is minimized and is about equal to $10 \times 1\ \mu m^2$. With such dimensions, the signal-to-background ratio is increased as depicted in figure 2.23. The lower feed-through makes it possible to design oscillators using non-differential actuation. Differential actuation can however be implemented to improve the signal-to-background ratio in the case of resonators with larger output impedance (e.g. capacitive detection).

2.3.2.3 MEMS-CMOS 3D-integration

The 3D monolithic integration implemented in Leti consists in first fabricating the integrated circuit using a standard CMOS process with two metal layers. Another SOI-Silicon wafer is bonded on top of the first wafer. The bulk substrate of the second wafer is then removed. The Si-layer of the second wafer is used to fabricate the MEMS resonator. The underlying oxide layer is etched to release the structure while another oxide layer (in blue on fig. 2.24) is used to stop the release etching from contaminating the CMOS circuit.

The electrical paths between the resonator and the sustaining electronic circuit are very similar to 2D-integration. The major difference originates from the holes that connect the top silicon layer to the metal layer (fig. 2.24). They can introduce a serial resistance and inductance. However, the electrical simulations do not show any significant difference between 3D- and 2D-integration.

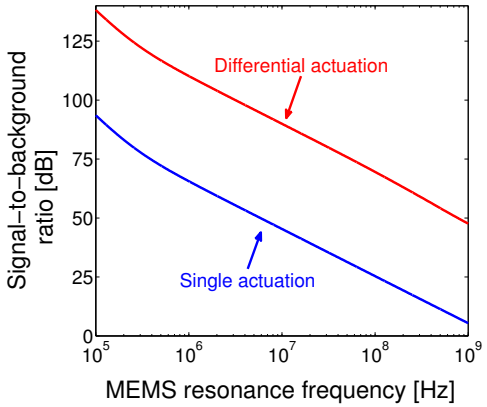

Figure 2.23: Feed-through gain in a 2D-integrated NEMS/CMOS oscillator

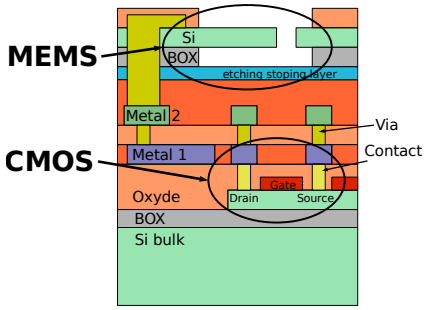

Figure 2.24: Simplified illustration of a 3D-cointegrated MEMS/CMOS system

2.3.3 Heterodyne architectures

Heterodyne architectures take advantage of a nonlinearity in the MEMS actuation or detection in order to acquire the resonator output signal at a different frequency than it was actuated. With this measurement scheme the feed-through can be reduced as the resulting parasitic signal is at a different frequency than the detected signal. The connection losses can also be reduced if the resonator output signal is at a low frequency. On the other hand, the feedback electronic circuit can be more complex as it should modify the frequency of the resonator output signal.

One of the simplest heterodyne architecture uses a quadratic nonlinearity in the actuation or the detection scheme in order to obtain a resonator output signal at twice the frequency of the actuation signal. In the case of electrostatic actuation:

$$\mathsf{F}_{\mathsf{I}}(t) = \frac{\varepsilon_0 h}{g^2}\left[\frac{V_{DC}^2}{2} + \frac{v_{act}^2}{4} + V_{DC}v_{act}\sin(2\pi f t) - \frac{v_{act}^2}{4}\sin(4\pi f t)\right]. \tag{2.43}$$

If v_{act} is at frequency $f_r/2$ then $\mathsf{F}_{\mathsf{I}}(t)$ has a frequency component at f_r. If the detection is linear, the resonator output signal is at f_r while the actuation voltage is at the frequency $f_r/2$ (fig. 2.25). However, the feed-through can not be completely cancelled out. For example, the electronics may not be purely linear and include a quadratic term. The feed-through signal at the input of the electronics would then be up-converted to twice its frequency: f_r. Moreover, quadratic terms may also be found in the resonator detection for instance (e.g. the self-heating effect in a piezoresistive element). Moreover, in a non heterodyne architecture, the voltage V_{DC} can be large so that v_{act} can be reduced and thus a low feed-through at the input of the electronics can be obtained[7]. If the resonator is actuated quadratically, v_{act} is

[7]It is considered that the product $V_{DC} \times v_{act}$ is adjusted so that the actuation force corresponds to the critical actuation force.

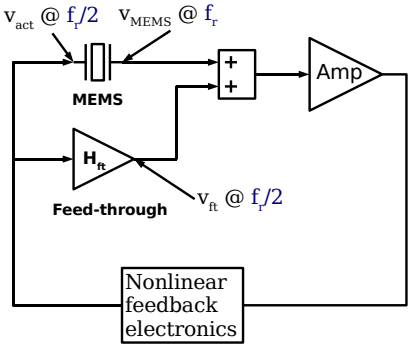

Figure 2.25: Heterodyne architecture.

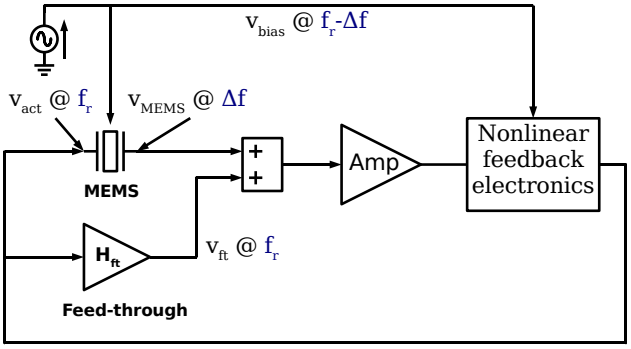

Figure 2.26: Downmixing architecture.

chosen so that $v_{act}^2/2 = V_{DC}v_{act}$ (i.e. the actuation force corresponds to the critical actuation force). In this scenario, v_{act} can be larger than in linear actuation and thus the feed-through at the input of the electronics is also increased. Furthermore, the quadratic terms in the resonator transduction amplifies the noise because the signal is squared but the noise is multiplied by the signal (and not squared). Finally, if the resonator is embedded in a self-oscillating loop, the feedback electronics must divide the input frequency by two (in order to close the loop). To the author's knowledge, there is no linear circuit capable of achieving this task and thus a digital circuit must be employed that can emphasize the colored noise as expressed in subsection 1.3.1.4.

A more advanced heterodyne architecture described in [Bargatin 2005] is referred as the down-mixing architecture (fig. 2.26). It requires a 2-port resonator for which the voltage applied on the detection port is at a frequency slightly smaller than the actuation frequency: $f_{det} = f_{act} - \Delta f$. The varying electrical component (a resistance for piezoresistive detection or a capacitance for capacitive or a piezoelectric detection) is biased by the voltage applied on this port. The resonator output signal includes a term at the frequency Δf. The frequency difference Δf can be very small, which simplifies the electronic design and reduces the connection losses in the case of resistive detection. However, as for the previous heterodyne architecture, the nonlinearity or the electronics of the MEMS resonator can also create some feed-through. Consider for instance, the quadratic term in the electronics. The feed-through introduces, at the electronics input, frequency terms at f_{act} and $f_{act} - \Delta f$. The quadratic term in the electronics response can mix the two frequency terms resulting in another signal at Δf. Overall, heterodyne architecture usually have smaller feed-through than homodyne ones.

2.3.4 Conclusion on MEMS-to-electronics interconnections

This section has described the major types of MEMS-to-electronics connections, their technical challenges and their impact on the sensor performance. 2D co-

integration presents optimal performances but is difficult to fabricate. Stand-alone MEMS connected to the electronics by wire-bonding have simple fabrication process but the performances of the sensor are limited by large connection loss and high feed-through. 3D co-integration is technologically challenging because two wafers must be assembled together. However, it has the advantage of decoupling the fabrication process of the CMOS circuit from the MEMS resonator and, thus, makes the fabrication process of the resonator more flexible.

In the subsection 2.3.1, a simple model of the parasitic introduced by the connections was presented. Based on the proposed model a methodology was defined to design the electronics and to evaluate the sensor performances.

2.4 MEMS resonators mass resolution comparison

2.4.1 Model presentation

From (i) the system architecture description of self-oscillating loops presented in chapter 1, (ii) the electrical description of the MEMS resonator, and (iii) the model of the MEMS-to-electronics connection of section 2.3.2, it is possible to theoretically

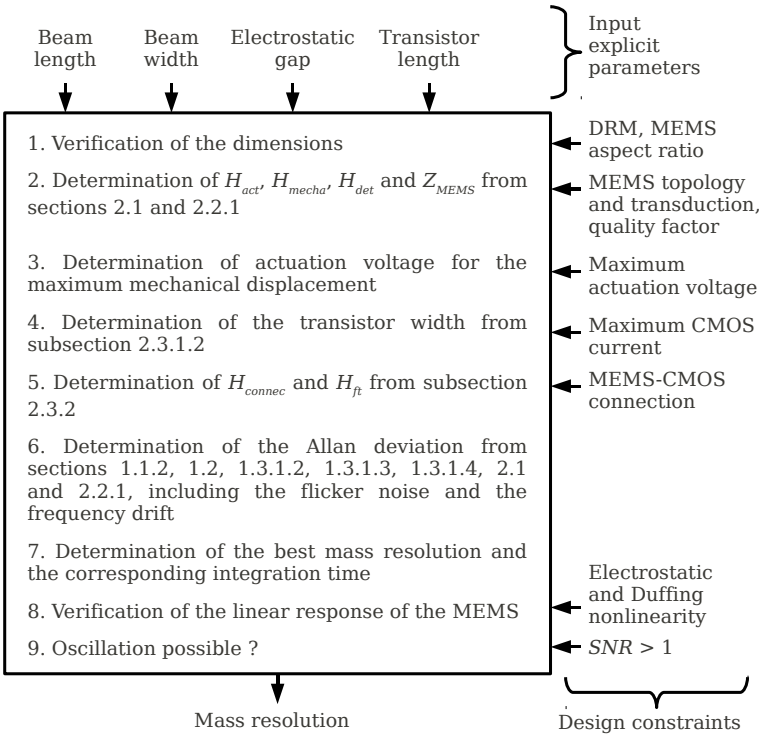

Figure 2.27: Simplified illustration of the function to determine the optimal design for a clamped-clamped beam with capacitive detection.

assess the mass resolution of the MEMS-based sensor. The gain of the MEMS-actuation and detection transduction techniques and the MEMS-to-CMOS connection topologies can be compared and the performance improvement of using a more complex integration scheme as presented in section 2.3 can be evaluated.

The proposed methodology is based on an optimization routine that seeks for the best design (in terms of mass resolution) of the MEMS resonator and the CMOS circuit. The presented results are based on the SOI-65nm CMOS technology from STMicroelectronics. This CMOS-process is one of the most aggressive analog technologies that make it possible to design compact, low-noise and high frequency electronic circuits. If the same design rules are used for the MEMS fabrication, the lithography rules of the process makes it possible to design MEMS resonators with nanometer dimensions that "should" enhance their performances.

The optimization routine uses several input variables that should be optimized. Associated with those variables other implicit parameters are determined from the design rules described in the previous sections. Example of implicit variables are the integration time, the actuation voltage or the transistor width, the latter being determined from subsection 2.3.1. The optimization routine is bounded by several constraints imposed by the fabrication and the environmental properties. Examples of such constraints parameters are the MEMS resonator topology, the MEMS-to-electronics connection, the fabrication process and the associated DRM[8] or the quality factor of the resonator. The figure 2.27 presents the input variables and the design constraints for a clamped-clamped beam with capacitive detection. A simplified description of function used to evaluate the mass resolution and thus to determine the optimal design variables is also depicted in the figure.

The aspects considered in the model of the sensor performance are listed below:

- The electromechanical MEMS resonator response is based on the model presented in sections 2.1, and 2.2.
- The electrical behavior of the MEMS-to-CMOS connection and the electronic circuit is based on the model presented in section 2.3. The width of the transistors is determined from eq. (2.40).
- The feed-through is modeled as described in section 2.3 and its effect on the frequency-resolution was modeled as presented in section 1.1.2. The cases of single-sided and differential actuation are evaluated.
- The electronics harmonic distortions are taken to -40 dB corresponding to simulations on a typical low-distortion electronic circuit. The harmonic distortions of the MEMS (if any) are based on the model of section 2.2.
- The noise sources considered in this work regarding the resonator are the thermomechanical noise, the Johnson noise and $1/f$-noise in the piezoresistive elements (if any); regarding the circuit the white- and flicker-electronics noise at its input and the flicker noise at the electronics output.

[8]DRM stands for Design Rule Manual of the considered fabrication process

- The frequency drift of the sensors is modeled for a 0.1°C-temperature deviation. The corresponding coefficient is taken constant and equal to 100 ppm.
- Based on the white and flicker noise, the harmonic distortion and the frequency drift, the maximum integration time is calculated.
- The effect of the temperature in the piezoresistive elements (if any) of the resonator is modeled based on analytical modeling.

The constraints imposed on the optimization routine are listed below:

- The lithography rules for the MEMS and the electronics design are based on the SOI-65nm Dkit from STMicroelectronics.
- The thickness of the resonators is imposed by the process flow.
- A maximum voltage of 1 V is taken for the AC-value of the electrical signal. The polarization current of the first electronic amplifier is taken to 1 mA.
- The current density in the piezoresistive elements is limited to a value lower than the melting point of the material.
- Boundaries on the MEMS resonator actuation are taken so that the resonator response can be considered as linear: in the case of electrostatic actuation, the mechanical displacement is ten times smaller than the gap. In the case of duffing nonlinearity, the equivalent stiffness is ten times smaller than the beam stiffness.
- It is ensured that the signal-to-noise ratio within the bandwidth of the resonator is larger than 1.

This approach is necessary to compare the transduction mechanisms previously cited in this document: because they uses different physical properties and with different dimensions, it is difficult compare them objectively.

Finally it should be recognized that the results provided in this section are subject to some limitations as in all models. The purpose of the work presented in this section is mostly to give an impartial comparison of the performances of varous MEMS topologies. The performances of the sensors should be taken with some reserve but can be used to provide an order of magnitude of the expected mass resolution. The major limitations of the modeling are listed below:

- The quality factor in vacuum is considered constant (i.e. $Q = 1000$) for every resonators and for all dimensions. The crossbeam measured at Leti tends to have a quality factor around $Q_{crossbeam} \approx 5000$ while the quality factor of the nanowires are around $Q_{nanowire} \approx 1000$ due to its higher aspect ratio and the one of piezoelectric can be lower because of residual stress between the layers of the cantilever. Moreover the quality factor tends to reduce at small dimensions, because the more aggressive fabrication process degrades the mechanical properties of the MEMS layers.

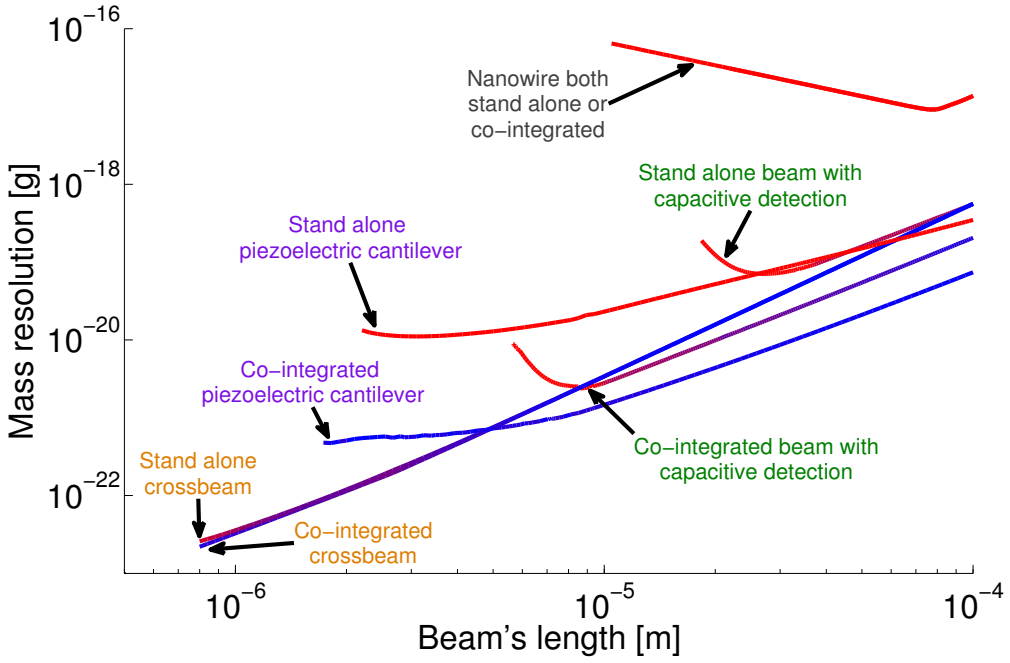

Figure 2.28: Graphic representation of the theoretical mass resolution versus the beam's length.

- Only the second harmonic distortion of the electronics was considered in the model. Moreover it was considered as constant over the dimensions of the electronic circuit. Finally, the flicker noise at the electronics output was supposed constant and equal to $\sqrt{S_{act}} = 1\ \mu V/\sqrt{Hz}$ at 1 Hz.
- The doping level of the piezoresistive elements was taken constant and equal to $10^{19}\ cm^{-3}$. The values of the doping-depend coefficient are based on characterizations: $\gamma_{Si} = 160$, $\Phi_{Si0} = 10^{-4}\ \Omega/m$, $\kappa_H = 10^{-5}$.

2.4.2 Results and discussions

As can be seen table 2.3 gives the results of the optimization presented in the previous subsection and figure 2.28 depicts the evolution of the theoretical mass resolution for a varying beam length. The connection losses of the MEMS resonator using capacitive detection are very important. The large connection losses reduce the signal-to-noise ratio and make the device very sensitive to feed-through. As a matter of fact, the latter issue limits the dimensions of the resonator. Differential actuation or any other mean of feed-through cancellation are therefore crucial to increase the signal-to-background ratio, reduce the dimensions of the resonator and thus improves its mass resolution. It should also be emphasized that due to the large connection losses, the dominant noise comes from the electronic circuit (except

MEMS topology	clamped-clamped beam with capacitive detection		Crossbeam	
	Stand-alone	Co-integration	Stand-alone	Co-integration
Length	59 µm **27µm**	17 µm **8.3µm**	0.8 µm **0.8µm**	0.8 µm **0.8µm**
Width	295 nm **295nm**	295 nm **295nm**	80 nm **80nm**	80 nm **80nm**
Gap	110 nm **110nm**	110 nm **110nm**	110 nm **125nm**	125 nm **125nm**
Gauge length			160 nm **160nm**	160 nm **160nm**
Gauge width			80 nm **80nm**	80 nm **80nm**
Resonance frequency	0.73 MHz **29MHz**	7.9 MHz **38MHz**	220 MHz **220MHz**	220 MHz **220MHz**
Mass-resolution	400 zg **78 zg**	17 zg **2.5 zg**	0.35 zg **0.029 zg**	0.026 zg **0.024 zg**
Integration time	12 s **6.5 s**	1.7 s **0.7 s**	0.34 s **0.32 s**	0.27 s **0.27 s**
Actuation gain	331 µm/V **14 µm/V**	2.9 µm/V **0.13 µm/V**	16 nm/V **12 nm/V**	12 nm/V **12 nm/V**
Unloaded detection gain	24 V/µm **24 V/µm**	24 V/µm **24 V/µm**	1.2 V/µm **1.2 V/µm**	1.2 V/µm **1.2 V/µm**
Connect. losses	92 dB **107 dB**	63 dB **69 dB**	21 dB **21 dB**	0 dB **0 dB**
SNR	77 dB **80 dB**	108 dB **118 dB**	121 dB **123 dB**	127 dB **127 dB**
Main source noise	Electronic **Electronic**	Thermomech. **Electronic**	Thermomech. **Thermomech.**	Thermomech. **Thermomech.**
SBR	4.7 dB **11 dB**	4.4 dB **12 dB**	−10 dB **28 dB**	11 dB **51 dB**
Limiting factor	Feed-through **Feed-through**	Feed-through **Feed-through**	Lithography **Lithography**	Lithography **Lithography**

MEMS topology	Nanowire		1-port piezoelectric cantilever	
	Stand-alone	Co-integration	Stand-alone	Co-integration
Length	79 µm **79 µm**	79 µm **79 µm**	64 µm **50µm**	2.8 µm **1.8µm**
Width	295 nm **295nm**	295 nm **295nm**	2.8 µm **80nm**	82 nm **80nm**
Gap	110 nm **110 µm**	110 nm **110 nm**		
SiN thickness			366 nm **1800nm**	110 nm **180nm**
Resonance frequency	409 kHz **409 kHz**	409 kHz **409 kHz**	0.11 MHz **1.1MHz**	18 MHz **21MHz**
Mass-resolution	10200 zg **10200 zg**	10200 zg **10200 zg**	13000 zg **210 zg**	1.3 zg **0.53 zg**
Integration time	161 s **161 s**	161 s **161 s**	0.93 s **0.4 s**	0.09 s **0.12 s**
Actuation gain	1.1 mm/V **1.1 mm/V**	1.1 mm/V **1.1 mm/V**	120 µm/V **4.9 µm/V**	1.1 µm/V **0.58 µm/V**
Unloaded detection gain	Nonlinear **Nonlinear**	Nonlinear **Nonlinear**	26 V/mm **0.2 V/µm**	5.1 V/µm **3.3 V/µm**
Connect. losses	10 dB **10 dB**	0 dB **0 dB**	25 dB **57 dB**	34 dB **32 dB**
SNR	5.2 dB **5.2 dB**	5.2 dB **5.2 dB**	161 dB **163 dB**	178 dB 168 **dB**
Principal noise	Johnson **Johnson**	Johnson **Johnson**	Thermomech. **Electronic**	Thermomech. **Thermomech.**
SBR			0 dB **2 dB**	0 dB **29 dB**
Limiting factor	Low v_{MEMS} **Low v_{MEMS}**	Low v_{MEMS} **Low v_{MEMS}**	Feed-through **Feed-through**	Feed-through **Form factor**

Table 2.3: Comparison between different MEMS topologies. The results in bold correspond to resonators with differential actuation, the other corresponds to a single-sided actuation.

for the co-integrated resonator with single-sided actuation). Note finally, that the unloaded capacitive gain of the resonator is large but is degraded by the connection losses.

The crossbeam resonator features much lower detection losses thanks to its piezoresistive detection. The crossbeam can then be designed with its lowest dimensions. However, when the crossbeam dimensions are small, the beam becomes stiff and the actuation voltage, that provokes a mechanical displacement to a tenth of the electrode's gap, is large and emphasizes the electrostatic nonlinearity: it reduces the maximum integration time. Overall, the mass resolution improves only moderately if the resonator dimensions are reduced by a certain point. It should finally be underlined that the large signal-to-noise ratio of this resonator topology makes the characterization of the device simpler. As a matter of fact, the mass resolution announced by the model is much better than the state-of-the-art but it will be shown in the chapter 3 that a large flicker noise introduced by the resonator limits its frequency resolution.

The nonlinear detection of the piezoresistive nanowire emphasizes the noise sources in the oscillator. The resonator is actuated at f_r but its output signal frequency is $2f_r$. Moreover, while the resonator output signal is proportional to the square of the mechanical displacement, the noise at the output of the resonator is proportional to the product of the thermomechanical noise with the mechanical displacement. The noise and especially the close-to-carrier colored noise is amplified by the nonlinearity making it difficult to shrink the dimensions of the resonator. Note finally that the resonator presented in table 2.3 has a very large length-to-thickness aspect ratio and thus a low stiffness in the out of plane direction. The release of the mechanical structure will thus probably be critical.

Piezoelectric cantilevers use a linear actuation and detection transduction technique, which makes them more insensitive to nonlinearity and thus to flicker noise. If a bridge architecture is used, the intrinsic feed-through provoked by the AlN-capacitance is reduced and resonators with smaller dimensions can be designed. The piezoelectric actuation and detection scheme exhibit a large gain making is possible to achieve large resonator output signals and (very) large signal-to-noise ratio, thus improving the mass resolution of the sensor. If a piezoelectric cantilever is co-integrated with a CMOS-circuit and uses a differential actuation, its mass resolution should reach state-of-the-art mass resolution [Jensen 2008]. However, the implementation of piezoelectric resonators co-integrated with a CMOS-circuit is technologically very difficult.

Overall, the study shows that the resonators with capacitive detection suffer from feed-through and high connection losses making it difficult to operate them at low dimensions. The nanowire performances are poor due to the frequency aliasing in the nonlinear detection transduction making the considered topology unadapted for closed-loop mass measurement. Finally the two most promising candidates for mass measurement are the crossbeam and the piezoelectric cantilever. The former can

be fabricated with ease but suffers from an actuation transduction that introduces large harmonic distortion thus emphasizing the colored noise and limiting the mass-resolution of the sensor. The piezoelectric resonator has linear electromechanical transduction, which improves the mass-resolution of the oscillator. The topology is however difficult to fabricate and has a large intrinsic feed-through.

2.5 Collectively addressed MEMS arrays

It is usually admitted that implementing MEMS resonators in collectively addressed array increases the SNR because the output signals of the resonators add up in a coherent way, whereas their output noises add up in a statistical way[Ekinci 2004a]. The SNR should therefore increase with the number N of resonators in array according to $SNR \propto N$. However, there is still no example in the literature of CMOS-integrated MEMS array and only a limited number of stand-alone MEMS array realizations [Lee 2004, Bargatin 2008, Kharrat 2009]. The resonators should however be identical and the added mass to be measured should be introduced deposite on each resonators.

Nevertheless, to what extent arrays improve the SNR has never been analyzed in detail. In this section, we demonstrate that the intrinsic electrical behavior of the resonator and its surrounding environment determine an upper limit of the SNR. The case of co-integrated MEMS/CMOS and stand-alone MEMS arrays are studied. For these configurations, the SNR is studied as a function of the number of resonators. The best achievable SNR and the optimum number of MEMS resonators are also analytically determined.

Subsection 2.5.1 focuses on the determination of the total gain of the MEMS array and its readout electronics. The signal-to-noise ratio at the electronics output and the minimal number of MEMS resonators to reach the best performance are determined in subsections 2.5.3 and 2.5.2. Finally the previous analytical results are compared with SPICE-simulations in subsection 2.5.4.

2.5.1 Amplification gain

An array of N MEMS resonators connected in parallel is depicted in figure 2.29. The output electrical signal of each device is summed into the input of the electronics as shown in figure 2.29. The transistor is biassed by an ideal current source. C_{load} represents the input capacitance of the following electronic stage (e.g. a buffer stage). Its typical value is $C_{load} = 100$ pF.

The output voltage of each resonator drives its own output impedance Z_{MEMS}, the on-chip routing parasitic capacitance C_p, the capacitance of the MEMS-to-electronics capacitance C_{connec} divided by the number of resonators (depending

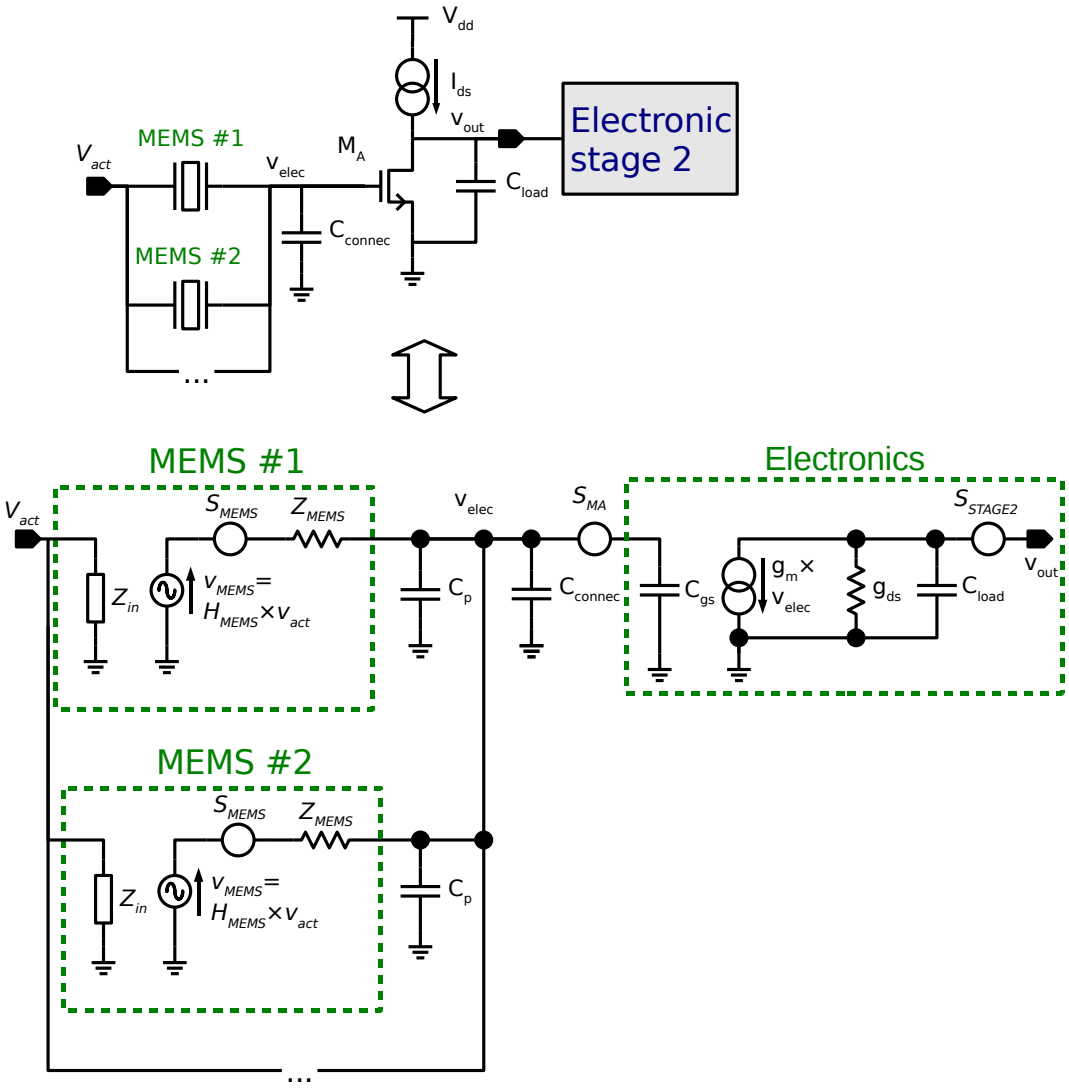

Figure 2.29: Schematic of the MEMS array and its readout electronics.

on the MEMS/CMOS connection configuration: for MEMS/CMOS co-integration $C_{connec} = 0$, for wire-bonding connection $C_{connec} = 10$ pF, for coaxial cable connection, $C_{connec} = 100$ pF) and the input capacitance of the electronics also divided by the number of resonators. The small signal drain-source current produced by the transistor flows into its intrinsic admittance and C_{load}.

The transistor is modeled with the Berkeley level 1 model [Sansen 2006]. Its dynamic behavior is described by an input capacitance C_{gs}, a transconductance g_m and an output admittance g_{ds}. Note that the feedback capacitance C_{gd} has been neglected in order to simplify the study. This assumption is only valid in case of low-gain amplifiers and should be verified with the design kit. The Drain-Bulk capacitance C_{db} can be neglected compared to C_{load}: $C_{db} \ll C_{load}$. The MEMS gain $\frac{v_{elec}}{v_{act}}$ can be calculated from the sum of the MEMS output voltages:

$$v_{elec} = NH_{MEMS}(f)\, v_{act} \frac{1/Z_{MEMS}}{N/Z_{MEMS} + j2\pi f\left(NC_p + C_{connec} + C_{gs}\right)}. \tag{2.44}$$

Hence

$$\frac{v_{elec}}{v_{act}} = \frac{NH_{MEMS}(f)}{N + j2\pi f Z_{NEMS}\left(NC_p + C_{connec} + C_{gs}\right)}. \tag{2.45}$$

Then the total gain $G = \frac{v_{out}}{v_{act}}$ can be deduced:

$$G = \left| \frac{-g_m H_{MEMS}(f)}{\left[g_{ds} + j2\pi f C_{load}\right]\left[1 + j2\pi f Z_{MEMS}\left(C_p + \frac{C_{connec}+C_{gs}}{N}\right)\right]} \right|. \tag{2.46}$$

Assuming that the amplifier is properly designed (i.e. $g_{ds} \gg 2\pi f C_{load}$), the total gain has the following expression:

$$\begin{aligned} G &= \left| \frac{H_{MEMS}(f)}{1 + j2\pi f Z_{MEMS}\left(C_p + \frac{C_{connec}+\frac{2}{3}C_{ox}W_A L_A}{N}\right)} \right| \frac{2L_A}{K_{eN}\left(V_{gs} - V_{tN}\right)} \\ G &\underset{N\to\infty}{\longrightarrow} \left| \frac{H_{MEMS}(f)}{1 + j2\pi f Z_{MEMS} C_p} \right| \frac{2L_A}{K_{eN}\left(V_{gs} - V_{tN}\right)}. \end{aligned} \tag{2.47}$$

We make the assumption that N is large enough so that the admittance of $\left(C_{connec} + C_{gs}\right)/N$ can be neglected compared to the equivalent admittance of C_p and Z_{MEMS}: $2\pi f\left(C_{connec} + C_{gs}\right)/N \ll \sqrt{\left(2\pi f C_p\right)^2 + 1/Z_{MEMS}^2}$.

2.5.2 Signal-to-noise ratio optimization

The noises in this architecture arise from the MEMS devices, the transistor and the following electronic stage. The noise at the output of the MEMS device (thermomechanical noise and Johnson noise) is modeled with a voltage PSD of S_{MEMS}. The voltage PSD of the noise produced by the transistor on its gate is $S_{M_A} = \frac{8k_BT}{3g_m}$. The following electronic stage at the transistor drain has a voltage PSD of $S_{STAGE2} = \left(5 \text{ nV}/\sqrt{\text{Hz}}\right)^2$. This value is typical for a measurement equipment, (e.g. the SR830 lock-in amplifier) or a commercial amplifier. It can also be reached with ease in an integrated circuit. Flicker noise is not considered in this subsection but the validity of this assumption will be confirmed in subsection 2.5.4. The SNR at the input of the electronics can be calculated:

$$SNR = \left|\frac{v_{elec}^2}{S_{MEMS+elec}}\right| = \frac{G^2 v_{act}^2}{S_{MEMS+elec}} = \frac{\left|\frac{H_{MEMS}(f_r)v_{act}}{1+j2\pi f_r Z_{MEMS}\left(C_p+\frac{C_{connec}+C_{gs}}{N}\right)}\right|^2 T_{meas}}{\underbrace{S_{STAGE2}\left[\frac{K_{eN}\left(V_{gs}-V_{tN}\right)}{2L_A}\right]^2}_{STAGE2 \rightarrow i_{NEMS}} + \underbrace{\frac{8k_BT}{3g_m}}_{M_A\, noise} + \underbrace{\frac{S_{MEMS}/N}{\left|1+j2\pi f_r Z_{MEMS}\left(C_p+\frac{C_{connec}+C_{gs}}{N}\right)\right|^2}}_{MEMS\, noise}}. \tag{2.48}$$

Thus:

$$SNR \underset{N\rightarrow\infty}{\longrightarrow} \frac{\left|\frac{H_{MEMS}(f_r)v_{act}}{1+j2\pi f Z_{MEMS}C_p}\right|^2 T_{meas}}{S_{STAGE2}\left[\frac{K_{eN}(V_{gs}-V_{tN})}{2L_A}\right]^2 + \frac{8k_BT}{3g_m}}. \tag{2.49}$$

For a given MEMS resonator and for a given implementation, the single way to optimize the SNR is to minimize the term $S_{STAGE2}\left[\frac{K_{eN}(V_{gs}-V_{tN})}{2L_A}\right]^2 + \frac{8k_BT}{3g_m}$. In other words, implementing MEMS resonators in arrays reduces the MEMS noise-to-signal ratio by a factor N to the point that it can be neglected compared to the electronic noise. Note that if the electronic noise sources are not considered, the signal-to-noise ratio is then, as expected, equal to $N\left|\frac{H_{MEMS}(f)v_{act}}{S_{MEMS}}\right|^2 T_{meas}$.

Since the effect of the interconnection capacitance and of the input capacitance of the electronics is negligible when N is large, the SNR can be made arbitrarily large by designing electronics with large L_A and g_m. However, a limitation is always imposed by the maximum polarization current I_{max} and as a matter of fact, the voltage power spectral density of the transistor noise on its gate has a finite value:

C_{connec}	0	1 pF	10 pF	100 pF
$N_{min-cap}$	1	2	20	196
$N_{min-noise}$	5	4	1	1

Table 2.4: Minimal number of MEMS versus C_{connec}

$S_{M_A} = \frac{4k_BT(V_{gs}-V_{tN})}{3I_{max}}$. In a well-designed circuit, the following stage is designed according to the input voltage noise and the voltage gain of the previous electronic stage, so that the input voltage noise of stage 2 is negligible compared to the output voltage noise of stage 1: S_{STAGE2} is neglected. In these circumstances, the maximum signal-to-noise ratio is:

$$SNR_{max} = \left| \frac{H_{MEMS}(f_r) v_{act}}{1 + j2\pi f_r Z_{MEMS} C_p} \right|^2 \frac{3I_{max} T_{meas}}{4k_B T \left(V_{gs} - V_{tN}\right)}, \tag{2.50}$$

2.5.3 Minimal number of MEMS resonators to reach the best array performance

Equation (2.48) shows that implementing MEMS resonators in array reduces the effect of C_{connec} and C_{gs}. Indeed, the low-pass filter term in equation (2.48), is reduced by increasing N until it reaches $\left|1 + j2\pi f_r Z_{MEMS} C_p\right|^2$. Assuming that the MEMS-noise is negligible (this hypothesis should be verified a posteriori), one can determine the number of resonators N required to achieve close-to-maximal SNR by solving the following condition $1 + \left(2\pi f Z_{MEMS} C_p\right)^2 > \left(2\pi f_r\right)^2 Z_{MEMS}^2 \left(C_{connec} + C_{gs}\right)^2 / N^2$. Thus:

$$N_{min-cap} > \frac{2\pi f_r Z_{MEMS} \left(C_{connec} + C_{gs}\right)}{\sqrt{1 + \left(2\pi f_r Z_{MEMS} C_p\right)^2}} = \frac{2\pi f_r Z_{MEMS} \left[C_{connec} + \frac{4I_{ds} L_A^2}{3\mu_N (V_{gs}-V_{tN})^2}\right]}{\sqrt{1 + \left(2\pi f_r Z_{MEMS} C_p\right)^2}}. \tag{2.51}$$

Table 2.4 gives $N_{min-cap}$ for several values of C_{connec} and for a minimal transistor length of 0.13 µm. The values of the other parameters are given in table 2.5. Obviously $N_{min-cap}$ increases with C_{connec}.

One must then verify the a priori hypothesis that the noise of the MEMS resonators can be neglected. In other words, one must verify that the following condition is satisfied:

$$\frac{4k_BT\left(V_{gs} - V_{tN}\right)}{3I_{max}} \gg \frac{1}{N} \frac{S_{MEMS}}{\left|1 + 2\pi f_r Z_{MEMS} \left(C_p + \frac{C_{connec}+C_{gs}}{N}\right)\right|^2}. \tag{2.52}$$

Equation (2.52) amounts to a second order equation, from which the minimal number of MEMS resonators $N_{min-noise}$ can be easily analytically deduced. The numerical results expressed in table 2.4 ($N_{min-noise}$ criteria corresponds as previously

to a SNR-reduction of 3dB compared to SNR_{max}). For low values of C_{connec}, the term $(2\pi f_r)^2 Z_{NEMS}^2 \left(C_p + \frac{C_{connec}+C_{gs}}{N}\right)^2$ in equation (2.52) is negligible compared to 1 and $N_{min-noise}$ is governed by $N_{min-noise} = \frac{3I_{max}}{4k_BT(V_{gs}-V_{tN})} S_{MEMS}$. For high values of C_{connec}, the capacitive attenuation diminishes the MEMS output signal, the MEMS noise becomes negligible and the minimal number of MEMS resonators in array is determined from equation (2.51).

In fact, the two conditions imposed by $N_{min-cap}$ and $N_{min-noise}$ must be respected. $N_{min-cap}$ tends to increase with Z_{MEMS} and C_{connec} contrarily to $N_{min-noise}$. Thus $N_{min-noise}$ tends to dominate for co-integrated resonators whereas $N_{min-cap}$ tends to dominate for stand-alone resonators.

2.5.4 Results, discussions

SPICE simulations of arrays were made for N from 1 to 100 000. The simulated transistor is taken from ST Microelectronics HCMOS9 design kit. The dimensions of M_A are optimized for each N and C_{connec} based on the Berkeley level 1 model of the transistor. Its width was then adjusted in order to adapt to the more advanced SPICE model of the design kit.

The results in terms of SNR are given in figure 2.30 for several values of: C_{connec}. The simulated MEMS resonator is a crossbeam [Mile 2010] (fig. 2.31a) with the dimensions given in table 2.31b.

The other parameter values are referenced in table 2.5. At the resonance frequency, $H_{MEMS}(f_r)$ is calculated from [Arndt 2011]:

$$H_{MEMS}(f_r) = 3.83 \frac{\varepsilon_0 \gamma_{Si}}{c_{Si}} Q V_{DC} V_g \frac{l}{g^2 b_g}. \tag{2.53}$$

The MEMS output signal increases with N and saturates to the limit $H_{MEMS}(f_r)\, v_{act}$ (the voltage of the Thevenin model of the MEMS resonator). The MEMS output signal improvement with N reaches therefore a maximum. Moreover as N is getting larger, the SNR increases as well as the value $(\frac{(H_{MEMS} v_{act})^2}{S_{MEMS}})$. Indeed, the signal output of the MEMS array scales as N, whereas the standard deviation of the noise scales as $\sqrt{N}$.

The two previously mentioned limitations (described by $N_{min-cap}$ and $N_{min-noise}$) to the SNR of the MEMS array can be observed in figure 2.30. When C_{connec} is lower than 10 pF, the performance of the MEMS array is mostly driven by the MEMS noise sources and not by the MEMS output capacitance (C_{connec} and C_{gs}). For larger values of C_{connec}, the MEMS output capacitance strongly attenuates the MEMS output signal. In this case, the aim of implementing MEMS resonators in array is to reduce the connection capacitance. Finally, the number of resonators

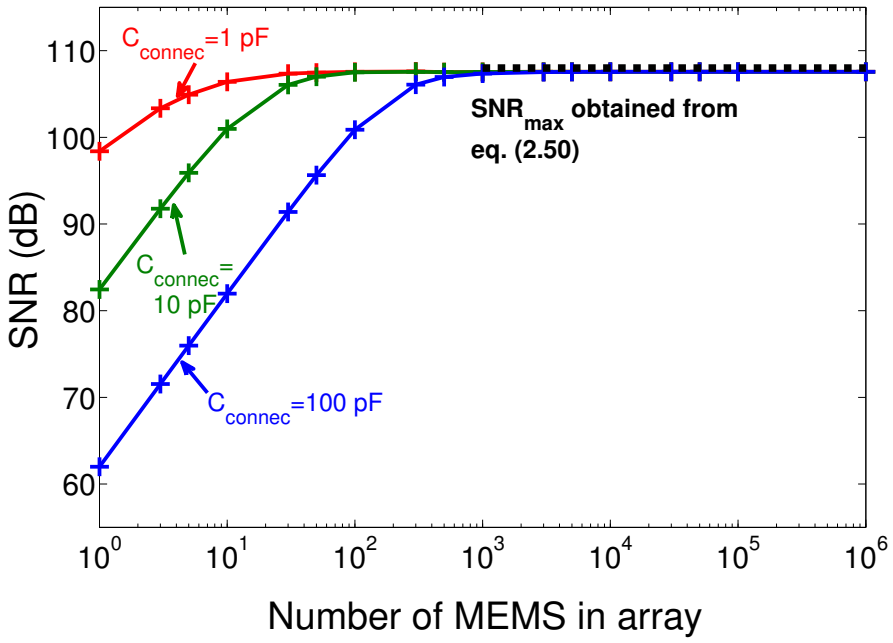

Figure 2.30: SNR versus the number of MEMS for 3 values of the connection capacitance. The crosses (+) correspond to the simulated points and are linked with a line. The value of SNR_{max} is represented by the dashed horizontal line.

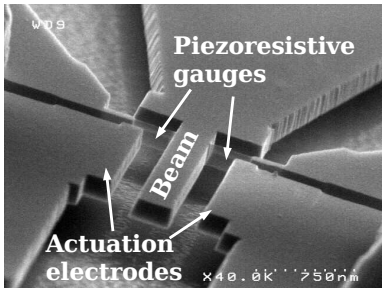

(a)

Parameter	Value
Beam's length	$L = 1.6$ µm
Beam's width	$b = 130$ nm
Beam's thickness	$h = 50$ nm
Gauge's length	$l_g = 100$ nm
Gauge's width	$b_g = 50$ nm
Electrode-beam gap	$g = 80$ nm

(b)

Figure 2.31: Crossbeam MEMS: (a) SEM illustration, (b) dimensions of the resonator

parameter	value
Layout capacitance	$C_p = 10$ fF
MEMS resonance frequency	$f_r = 89$ MHz
Resonator quality factor	$Q = 100$
Air permittivity	$\varepsilon_0 = 8.85 \times 10^{-12}$ F/m
Silicon gauge factor	$\gamma_{Si} = 120$
Silicon Young modulus	$c_{Si} = 169$ GPa
DC-actuation voltage	$V_{DC} = 5$ V
AC-actuation voltage	$v_{act} = 1$ V
Voltage applied on each gauge	$V_S = 0.1$ V
Resonator output voltage	$H_{MEMS} v_{act} = 1.0$ mV
Resonator output impedance	$Z_{MEMS} = 3.5$ kΩ
Resonator thermomechanical noise	$S_{thermo} = \left(5.5 \text{ nV}/\sqrt{\text{Hz}}\right)^2$
Measurement time	$T_{meas} = 1$ s
Electronics maximum polarization current	$I_{max} = 100$ µA
Transistor's gate polarization voltage	$V_{gs} = 0.6$ V
Threshold voltage	$V_{tN} = 0.28$ V
Electron mobility	$\mu_N = 18$ Vm^{2}s^{-1}
SNR_{max} (see eq.(2.50))	108 dB

Table 2.5: Study parameter values for a doping level of 10^{19} cm^{-3}

where the SNR reaches a limit on figure 2.30 shows a good correspondence with the values of table 2.4.

As shown by equation (2.50), the SNR for an infinite amount of MEMS resonators does not depend upon C_{connec}. Clearly, for a sufficient number of MEMS devices, the SNR will be the same whether the resonators are co-integrated or not with their readout electronics.

The resistive behavior of the MEMS gauges introduces some flicker noise. However, from [Harkey 2000], the corner frequency of the flicker noise compared to the thermomechanical white noise of the MEMS device (corresponding to the frequency at which the PSD of the flicker noise is equal to that of the thermomechanical white noise) is around 2.7 MHz. The corresponding Hooge noise coefficient was taken to $\kappa_H \approx 10^{-5}$. The corner frequency of the transistor used in the different simulations for a large MEMS array is 1.6 MHz. The low corner frequencies of the transistor and gauge flicker noise validates the hypothesis made in section 2.5.2 that the flicker noise can be neglected.

It should be highlighted that in this study, neither the technological dispersions, nor the increase of C_p with N (arising from the complex layout routing that should be implemented) have been modeled. The technological dispersions are likely to further reduce the performance of MEMS arrays. It is possible to use an analytical approach,

rather than costly Monte-Carlo simulations, to account for dispersions on the central frequency. This can be done using [Bargatin 2008] if the dispersions are assumed to follow a Cauchy law, or [Kharrat 2009] in the case of a normal law. In the former case, the standard frequency deviation $\sigma = 1\%$ results in a loss of 10 dB, whereas in the latter case, the loss is only 7.2 dB. Note that the value of SNR_{max} reduces due to dispersions as the quality factor of the resonators becomes larger. Nevertheless, these results still demonstrate the high interest of having MEMS connected in arrays especially when a stand-alone readout electronics is used for which the connection capacitance are large.

2.5.5 Conclusion of collectively-addressed MEMS arrays

After introducing a simple electrical model of the MEMS resonators, an array of MEMS devices all connected to a common amplifier was analytically studied. It shows that the performance in terms of SNR of the MEMS array is larger than that of a stand-alone MEMS resonator. However as N increases, the SNR of the array reaches a limit whether the array is co-integrated or not with its electronics. This limit was analytically studied and depends on the electronics input noise, the MEMS output signal and impedance. The minimal number of MEMS to achieve close to optimal performance depends mainly on the connection configuration. Stand-alone MEMS arrays are interesting candidates to improve the resonators performances up to ones of co-integrated MEMS/CMOS system without the cost of a specific process development. This study therefore provides a simple analytical assessment of the best achievable performances.

SPICE simulations for an array of crossbeam MEMS resonator were performed. They show similar results to those predicted by the analytical study. They also show that the SNR improvement is small ($\leq$ 10 dB) for architectures with low connection capacitance as MEMS/CMOS co-integrated or 3D-integrated architecture. An improvement of 45 dB can be reached for stand-alone electronics configuration (where $C_{connec} \approx 100$ pF). Although the results presented here are based on a single active transistor circuit, one should expect similar results with more complex electronics architecture (OTA, cascode...). Even by including possible technological dispersions, this would not change the overall results presented here

2.6 Conclusion

In this chapter the electromechanical behavior of various resonators was described. Different electromechanical actuation and detection transduction techniques were presented using simple analytical expressions. Different MEMS-to-electronic connection implementations were presented and compared. Their intrinsic connection losses and feed-through were presented and techniques to improve the MEMS-to-electronic connections were proposed and evaluated.

These MEMS resonators were then compared based on the system architecture description presented in chapter 1, the description of the MEMS resonator and the electrical model of the oscillator. It was shown that the crossbeam resonator and the piezoelectric cantilever are very promising candidates for mass sensing applications. Thanks to its simple technological fabrication and the possibility to co-integrate it with ease with a CMOS circuit, the clamped-clamped beam using a capacitive detection is also an interesting candidate for minute mass sensing.

Finally the implementation of MEMS resonators in array was explored and the electrical limits due to the CMOS circuit were determined. This study reveals a major interest of array in the case where resonators are fabricated on a different wafer than the CMOS circuit.

The following chapter presents different MEMS resonators and oscillators realized and characterized during this PhD study.

3 Practical realizations

In this chapter, the design and the characterization of MEMS-based closed-loop oscillators are presented. In section 3.1, the performance of two different self-oscillating loops (one based on a piezoelectric cantilever, the other on a piezoresistive crossbeam) realized with discrete electronics is assessed. Section 3.2 describes the design of an ASIC to self-oscillate multiple stand-alone crossbeams. This ASIC uses both analog and digital electronics and is composed of sustaining electronic circuits and frequency counters. On the same ASIC, this electronics was duplicated 4 times so that 4 MEMS resonators can be controlled independently. Finally, the section 3.3 describes the design and characterization of resonators integrated on the same wafer with their electronic circuit. Capacitive clamped-clamped beams and piezoresistive crossbeams were co-integrated with a dedicated CMOS readout circuit.

3.1 Self-oscillating loops using discrete electronics

The realization of two self-oscillating loops with discrete electronics is hereby presented. This type of electronics makes possible to quickly design and optimize oscillators but are limited in terms of flexibility and can introduce larger electronic noise as it will be discussed. In a first part, the realization of an oscillator with a piezoelectric micro-cantilever is described. This resonator is actuated under atmospheric pressure in order to evaluate its potential for gas sensing (it will be shown that its mass resolution is poor because of the large dimensions of the device). In a second part, the implementation of a piezoresistive crossbeam in a self-oscillating loop is described. As opposed to the piezoelectric cantilever, the crossbeam is actuated in vacuum to improve the signal-to-background ratio (working in vacuum is justified for mass spectrometry applications).

3.1.1 Self-oscillating loop with a piezoelectric micro-cantilever

Hereby is described the design and the characterization of the self-oscillating loop with a piezoelectric cantilever. First the dimensions and the fabrication process of the piezoelectric micro-cantilever are detailed. Then, a method on how to circumvent the feed-through intrinsic to piezoelectric resonators is proposed. This feed-through reduction technique consists in using a variable capacitance and a variable resistance implemented in a bridge architecture. The overall topology of the oscillator is then

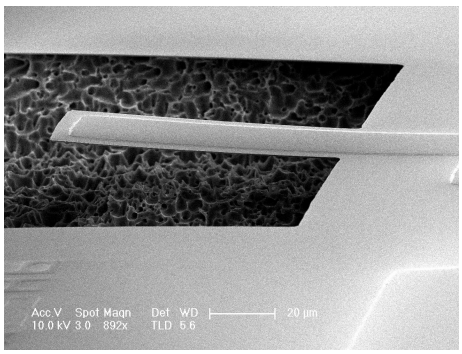

Figure 3.1: SEM caption of the micro-cantilever.

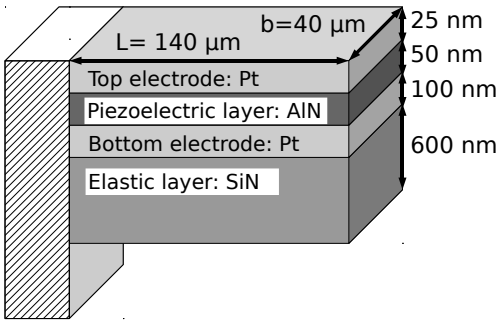

Figure 3.2: Technological stack of the piezoelectric cantilever.

justified. In a third part, different frequency resolution measurement techniques to evaluate the performance of the self-oscillating loop are described and compared. Finally, the frequency resolution of the self-oscillating loop is compared with the one of an FLL-architecture.

3.1.1.1 Presentation of the piezoelectric micro-cantilever

The self-oscillating loop is realized using a 50 nm-thick AlN piezoelectric resonator (fig. 3.1). The resonating element is a micro-cantilever composed of the following material stack (depicted in figure 3.2) deposited on a standard silicon wafer (from bottom to top): 600 nm-thick silicon nitride, 100 nm-thick platinum, 50 nm-thick AlN, 25 nm-thick platinum. Fabricated with standard CMOS compatible, surface micro-machining technology [Ivaldi 2011b], the 140×40 µm^2-cantilever area is defined with two Ultra Violet lithography steps. A XeF_2 plasma isotropic etching technique is used to release the cantilever (the silicon bulk acts as a sacrificial layer).

With such dimensions, the resonance frequency is theoretically 42 kHz but was measured at 36 kHz. The difference is believed to originate from a too aggressive release process, consequently part of the clamping area is also free-standing, i.e. less rigid.

The measured resonator output voltage corresponding to a critical amplitude displacement of 100 nm is around 3 mV versus 4.2 mV obtained theoretically (see subsection 2.2.4).

3.1.1.2 Feed-through reduction

In 1-port piezoelectric cantilevers, a major issue to deal with is the large intrinsic feed-through introduced by the piezoelectric static-capacitance. Figure 3.3 depicts the behavior of the equivalent capacitance of the micro-cantilever versus frequency: the useful signal is about 30-times smaller than the intrinsic feed-through. The most

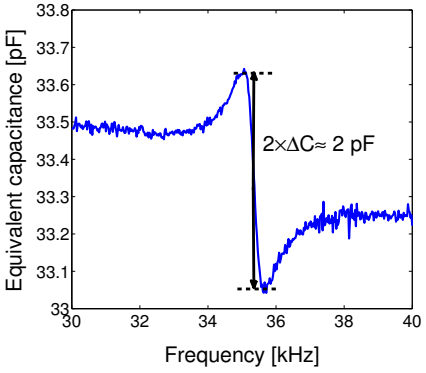

Figure 3.3: Equivalent capacitance of the PZE cantilever measured with a HP4194 impedance meter.

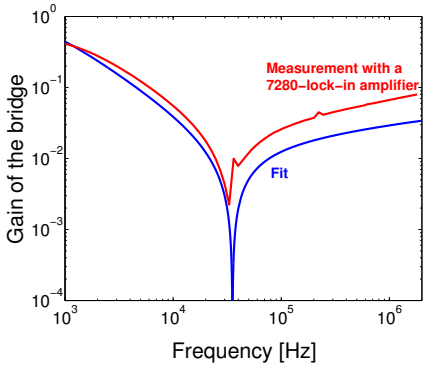

Figure 3.4: Evolution of the MEMS+first amplifier gain in the bridge implementation (see figure 3.6).

common feed-through reduction technique consists in implementing the resonator in a bridge architecture using an identical but unreleased micro-cantilever or a variable capacitance to cancel the feed-through. We have chosen the implementation that uses a variable resistance and capacitances because the feed-through could be further reduced around f_r than when an identical unreleased cantilever is implemented. Indeed it is believed that the release affects the dimensions of the cantilever and creates a mismatch between the static capacitance of the released and the unreleased cantilever.

Moreover, the AlN-layer introduces non-null dielectric losses that can be modeled by introducing an imaginary part to C_{PZE}: $C_{PZE} \approx C_{PZE}(1 + jd)$ where $d \ll 1$ represents the dielectric losses (measured to $d \approx 1\%$). They can be canceled by implementing a variable resistance in parallel to the variable capacitances. Finally, the value of $|C_{PZE}|$ varies with the frequency. Using an HP4194 impedance meter, one can model the evolution of C_{PZE} as:

$$C_{PZE} = C_{PZE0}\left(\frac{f}{f_r}\right)^{p_{ft}}(1 + jd)\,, \tag{3.1}$$

where $p_{ft} \approx -4.4 \times 10^{-3}$ (from measurements) is a fitting parameter and $C_{PZE0} = 33$ pF (from measurements) is the value of the AlN-capacitance at f_r. The figure 3.4 compares experimental data with the model of the bridge gain versus frequency. Therefore the model correctly describes the behavior of the bridge and the resulting feed-through. The difference between the model and the measurement is due to an imperfect adjustment of the variable components (the resistance or the capacitances). Figure 3.5 depicts the measurement of the gain of the bridge around f_r. One can see that the signal-to-background is close to 3 making it possible to implement the micro-cantilever in a self-oscillating loop.

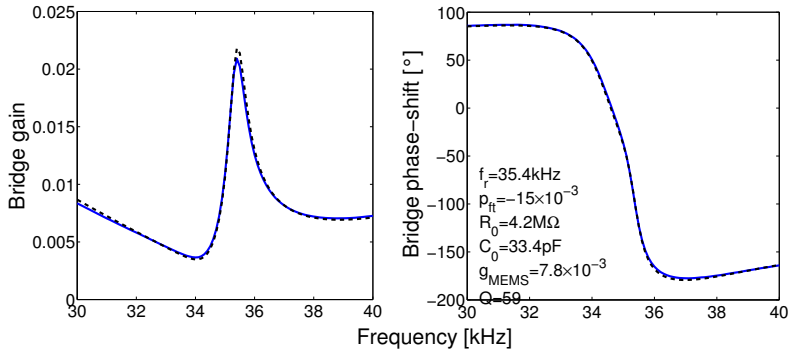

Figure 3.5: Gain and phase-shift of the bridge around the resonance frequency.

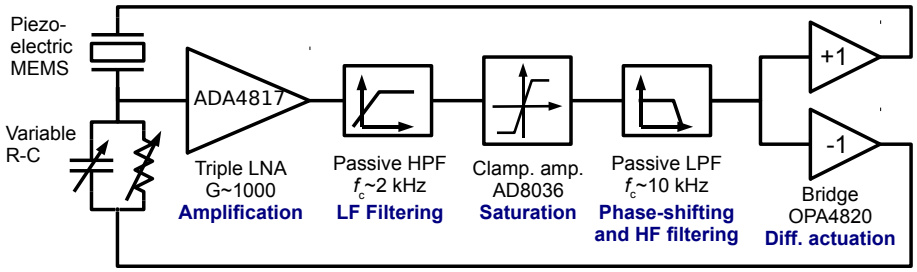

Figure 3.6: Simplified schematic of the self-oscillating loop.

3.1.1.3 Topology of the self-oscillating loop

The attenuation introduced by the MEMS resonator is compensated using a low-noise ADA4817 commercial amplifiers with large bandwidth. The MEMS-to-electronics connection losses are minimized by connecting the first amplifier very close to the MEMS resonator. The resulting connection capacitance is estimated to be smaller than 10 pF. The oscillation amplitude in closed-loop is controlled using an AD8036 clamping amplifier. The major challenge in the design of the loop is to filter the feed-through out of f_r: figure 3.5 shows that below and higher than f_r, the feed-through signal is larger than the resonance signal. Figure 3.5 shows that the phase-shift varies from $+90°$[1] to $-180°$, what can be explained by the fact that the static capacitance C_{PZE} is smaller than the variable capacitances at high frequency. The phase-shift at the resonance frequency is around $-90°$. In order to respect the oscillating conditions, the phase-shift should be translated up by $+90°$ so that the overall open-loop phase-shift is $0°$ at f_r. The corresponding phase-shift should then vary between $+180°$ and $-90°$.

To avoid at low-frequency that the phase-shift is equal to $n \times 2\pi$ (n is an integer), the order of the high-pass filters should be equal to 1. At high-frequency, the phase-shift is lower than $-90°$ preventing also the low-pass filtering from being larger than a

[1]The 90°-value, larger than the expected value of 0° for a Lorentz behavior, is due to the variable resistance that acts as a low-pass filter and thus unbalances the bridge.

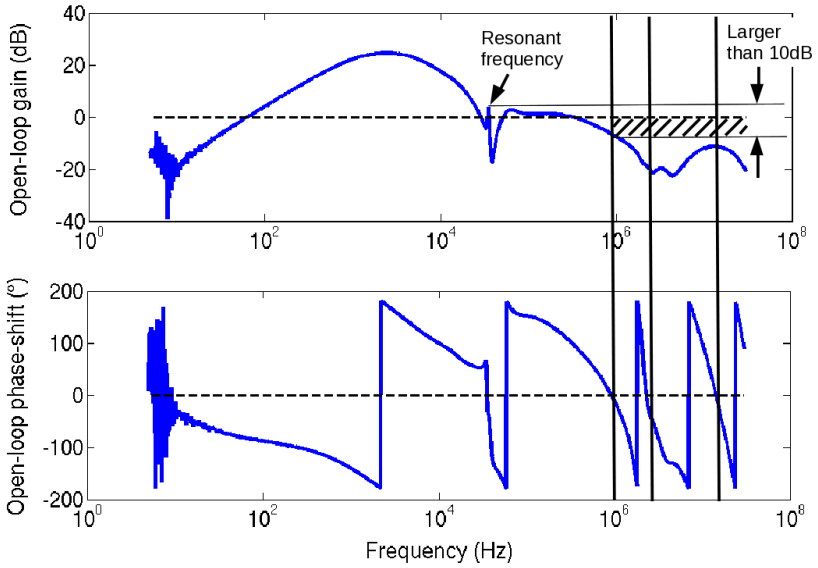

Figure 3.7: Gain and phase-shift response of the open-loop

2^{nd} order filter. In fact, it was observed that because many amplifiers were used in the loop, the phase-shift reduces rapidly starting at 100 kHz. Only a first low-pass filter could be introduced in the loop otherwise the loop became unstable at high frequencies. In addition to the feed-through filtering, the open-loop phase-shift is adjusted to -2π at f_r either with a low- or a high-pass filter. It was observed that using the low-pass filter as the phase-shifter provides a better open-loop response because it largely attenuates the feed-through at high frequency. It reduces the feed-through to a gain lower than 0 dB well before the amplifiers bandwidth reduces the open-loop phase-shift to $-n \times 2\pi$. Considering the cut-off frequency given in figure 3.6, the open-loop response of the self-oscillating loop respects the Barkhausen conditions only at f_r (fig. 3.7): the open-loop gain at f_r is larger than +3 dB. At frequencies where the open-loop phase-shift is equal to $n \times 2\pi$, the open loop gain is lower than −7 dB.

3.1.1.4 Frequency resolution of the oscillator

The frequency fluctuations of the closed-loop are measured with several techniques all on the same device. This subsection reports the frequency resolution measured directly with an oscilloscope acquiring the signal. In order to improve the measurement duration, the oscillator output signal was mixed with a signal source at a frequency slightly smaller than the oscillator frequency so that the resulting frequency is low (around 100 Hz). The frequency resolution of the loop is also evaluated with a frequency counter and with delay-based measurement. Each of these techniques turns out to give similar results that will be discussed in the following paragraphs

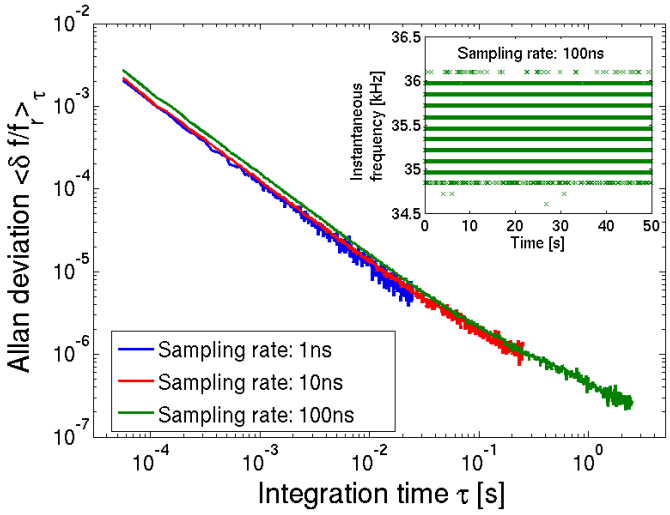

Figure 3.8: Allan deviation measured directly with an oscilloscope and for 3 different sampling rates. The maximum integration time on the graph is a 20^{th} of the measurement duration in order to properly estimate the variance. The inset presents the instantaneous frequency for a sampling rate of 100 ns.

Direct measurement using an oscilloscope The output signal of the oscillator is measured using an oscilloscope. The instantaneous frequency is determined using a post-processing method which calculates the time lapse between two successive rising edges. Three sets of measurements were made with different oscilloscope sampling times: 1 ns, 10 ns and 100 ns. The measurement duration is then set according to the maximum number of points that the oscilloscope can handle in a single acquisition. Using the oscilloscope DPO7254, it is possible to acquire up to 500 millions points. The figure 3.8 presents the Allan deviation of the oscillator (calculated from eq. (1.15) at page 14) for the 3 different sampling rates. From the inset, the measured frequency with a sampling rate of 100 ns is discretized and thus not properly measured: the period variation of the oscillator is quantified by the finite resolution of the oscillator sampling rate. Consequently, the frequency resolution is degraded as seen on figure 3.8. The sampling rate of the oscilloscope is therefore empirically determined to 10 ns. The corresponding measurement duration is 5 s and the maximum integration time is 0.25 s (a twentieth of the acquisition time in order to get a proper estimation of the variance). However, it is wished to estimate the Allan deviation at larger integration time in order to determine its minimal value. The downmixed measurement technique discussed hereafter details how this measurement can be achieved.

Downmixed measurement using an oscilloscope In order to increase the acquisition duration, the oscillator output signal is downmixed with a supposedly ideal signal source at a frequency f_{source} slightly lower than the oscillating frequency. Figure 3.9a describes the measurement setup used. The resulting down-

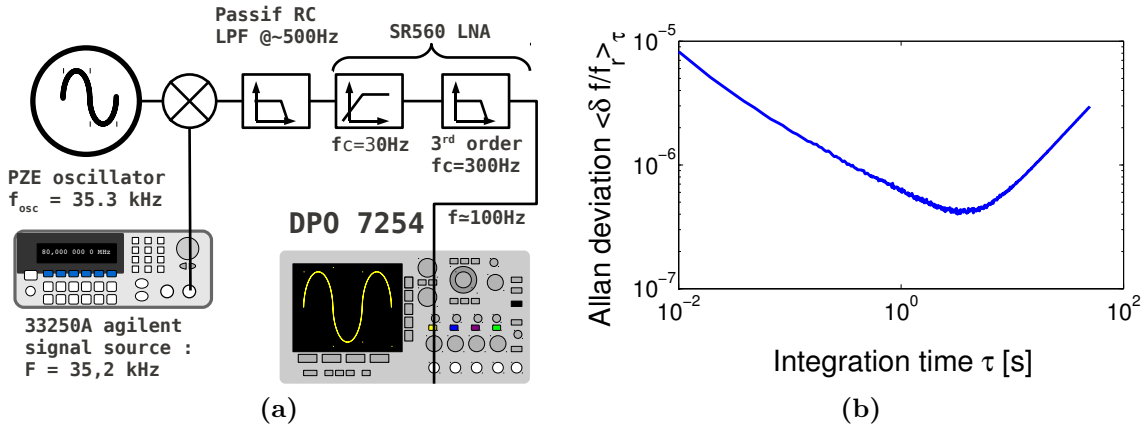

Figure 3.9: (a) Schematic of the Allan deviation measurement using a down-mixing architecture, (b) plot of the Allan deviation versus the integration time.

mixed signal is composed of two frequencies: one at low frequency $|f_{osc} - f_{source}|$ and one at high frequency $f_{osc} + f_{source} \approx 2f_{osc}$. Using low-pass filters, it is possible to measure $|f_{osc} - f_{source}|$ with a high accuracy. It can be shown that with $|f_{osc} - f_{source}| \approx 100$ Hz and $f_{osc} \approx 36$ kHz, a 4^{th} order low-pass filter must be employed in order to correctly filter the high frequency term.

Because the downmixed signal is at a lower frequency, the sampling rate of the oscilloscope can be reduced and thus one can acquire larger measurement durations: the counter part of this technique is that low integration times cannot be explored unlike the direct measurement method. The corresponding Allan variation is depicted in figure 3.9b and shows an Allan minimum deviation around 4.0×10^{-7} for an integration time of 3.2 s. At higher integration times, the Allan deviation increases with a slope close to 1 (fitted to 0.94) what seems to correspond to a frequency drift.

Measurement with a frequency counter The frequency resolution of an oscillator can also be evaluated using a dedicated equipment such as a frequency counter. The frequency counter measures the number of rising edge during a given gate time and then calculates the corresponding mean frequency. This equipment however is subject to several limitations.

First, due to the low communication rate of the GPIB connection with computer, the gate time cannot be smaller than 0.1 s. Moreover, the GPIB connection, introduces some dead time during which the frequency in not measured. From [Barnes 1990], the dead time emphasizes the effect of the frequency drift and thus imposes a constraint on the gate time. Finally, the frequency measurement algorithm[2] used by the frequency counter seems to be sensitive to the frequency drift since the Allan deviation varies with the gate time and integration time (fig. 3.10).

[2]Agilent refuses to provide information about this algorithm.

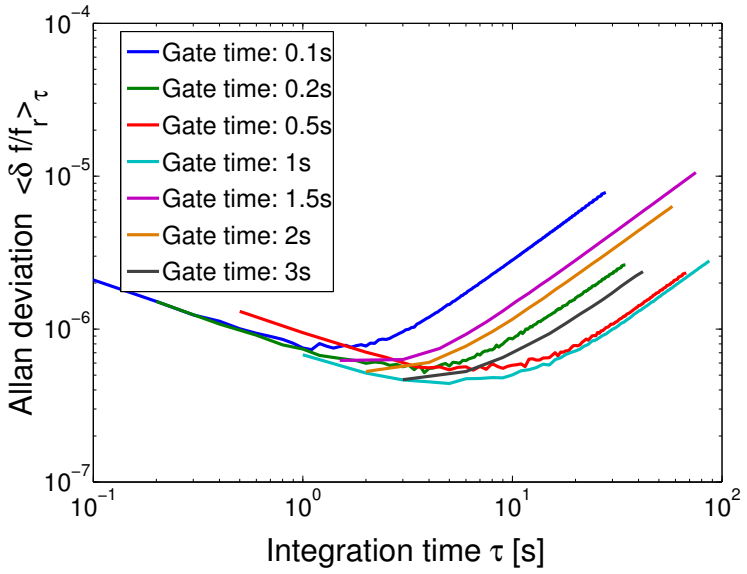

Figure 3.10: Allan deviation measured with a frequency counter.

The frequency counter however provides reasonable frequency resolution measurement with a minimum of 4.4×10^{-7} for an integration time of 5 s and a gate time of 1 s. This result is quite consistent with the one obtained with the downmixed technique.

Delay-shift based measurement This measurement is based on the technique described in section 1.4.2 and is depicted in figure 3.11a. It provides a minimal frequency resolution of 3.9×10^{-7} (for an integration time of 2.4 s. Once again, this result is consistent with the previous ones.

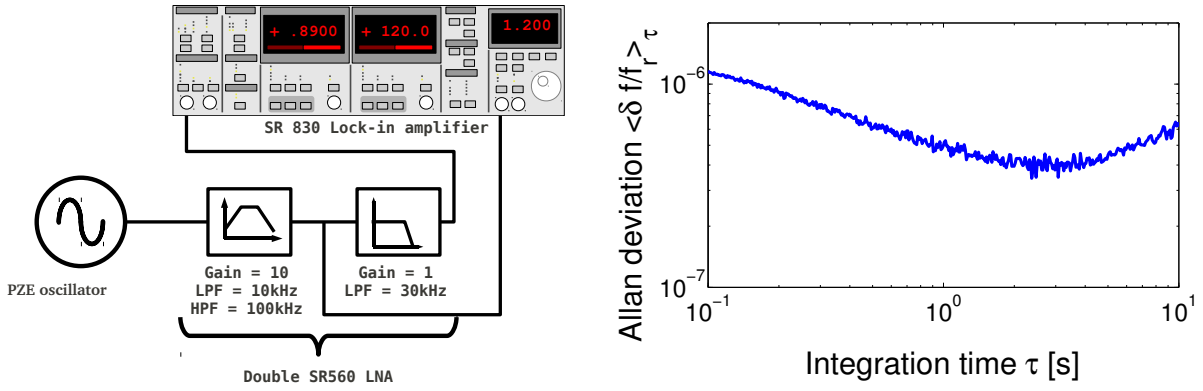

Figure 3.11: (a) Schematic of the phase-shift based measurement, (b) evolution of the Allan deviation versus the integration time.

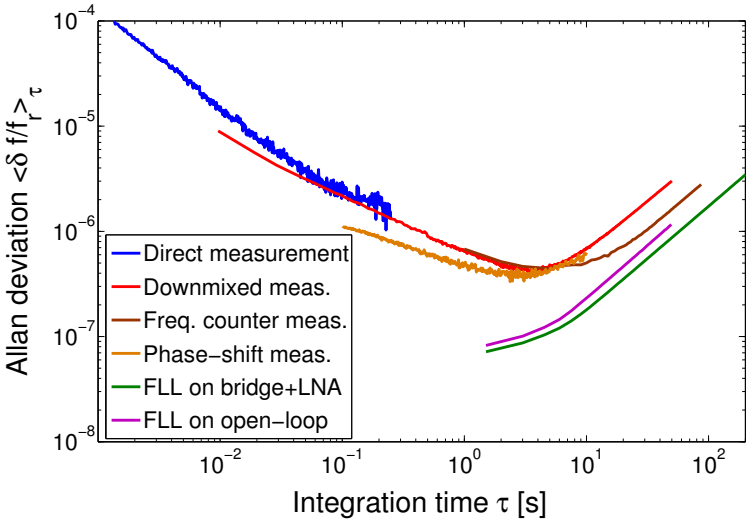

Figure 3.12: Comparison of the Allan deviation of the SOL- and FLL-architecture.

3.1.1.5 Frequency resolution comparison of the SOL with FLL[3]

The frequency resolution measured with a self-oscillating loop is compared with the one obtained with a frequency locked-loop implemented with laboratory equipments, externally controlled via a GPIB communication link and a Labview interface (not that the same microcantilever is used in all measurements). First, the frequency resolution of the FLL was measured only with the bridge implementation and with a single commercial amplifier. As in the SOL, the amplifier is connected as close as possible to the MEMS in order to minimize the MEMS-to-electronics connection losses. In a second measurement, the frequency resolution of the FLL is evaluated on the complete open-loop scheme of the SOL architecture, including the passive filters, the clamping amplifier and the supplementary amplifiers (the loop is opened between the second ADA4817-amplifier and the third one). The GPIB communication between the lock-in amplifier, the computer and the VCO introduces some delays in the loop and thus limits the minimum integration time to about 1.5 s. The frequency resolutions measured with the FLL-architecture and the SOL-architecture are depicted in figure 3.12. One can see that the minimum frequency resolution using a FLL-architecture corresponds to the minimum integration time. The corresponding frequency resolution is about 8 times lower than the one of a SOL-architecture.

From the cantilever mass $m_{PZE} \approx 25$ ng and equation (1.12) of page 13, the mass resolutions are about $\sigma_{m-SOL} \approx 9.8$ fg for the SOL-implementation and $\sigma_{m-FFL} \approx 1.3$ fg for the FLL-implementation. These mass resolutions are not as good as other NEMS-based examples in the literature due to the large dimensions of the cantilever, and because the measurements were made at ambient pressure. From [Ivaldi 2011b], the theoretical gas resolution for the DMMP is around 660 ppb.

[3]This work was performed with the help of Paul Ivaldi

Parameter	Value
Beam's length	$L = 5$ µm
Beam's width	$b = 300$ nm
Beam's thickness	$h = 160$ nm
Gauge's length	$L_g = 500$ nm
Gauge's width	$b_g = 80$ nm
Electrode- beam gap	$g = 200$ nm

Table 3.1: Dimensions of the cross-beam.

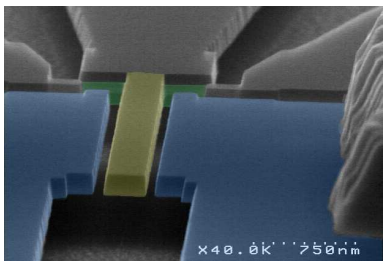

Figure 3.13: Image of the cross-beam. In blue, the actuation electrodes; in yellow, the beam and in green, the piezoresistive gauges.

It is believed that the SOL-architecture introduces a larger frequency noise due to the large feed-through out of the resonance frequency: at low-frequency, the white and flicker noises are amplified by the feed-through transmission and are then up-converted close to the oscillation frequency by the nonlinearity present in the loop. However, more experimental measurements and simulations are required to confirm this possible explanation. A V-shape feed-through is difficult to model in a time-dependent simulation. A measurement setup enabling to adjust a V-shape feed-through level would be a way to further study this topic.

3.1.1.6 Conclusion on the piezoelectric cantilever based self-oscillating loop

It was shown that using a bridge architecture and with careful filtering, it is possible to implement a piezoelectric micro-cantilever in a self-oscillating loop. After comparing the pros and cons of different frequency resolution measurements, it was shown that the piezoelectric cantilever implemented in a self-oscillating loop has a frequency resolution around 4×10^{-7}.

Using a FLL-architecture on a similar piezoelectric cantilever but with different dimensions[4], Ivaldi [Ivaldi 2011b] measured frequency resolution close to 10^{-8} making it an interesting gas sensor with concentration resolutions close to 10 ppb for DMMP vapors [Ivaldi 2011a]. Although the frequency resolution of the SOL-architecture is degraded compared to a FLL-architecture, it can be an interesting low-cost alternative to the expensive components required to implement the FLL-architecture.

3.1.2 Self-oscillating loop with a piezoresistive crossbeam

In this subsection, a piezoresistive crossbeam and its electrical connections are first described. The open-loop characterizations are then presented. The frequency res-

[4]We did not have access to these components because the number of functional devices was limited.

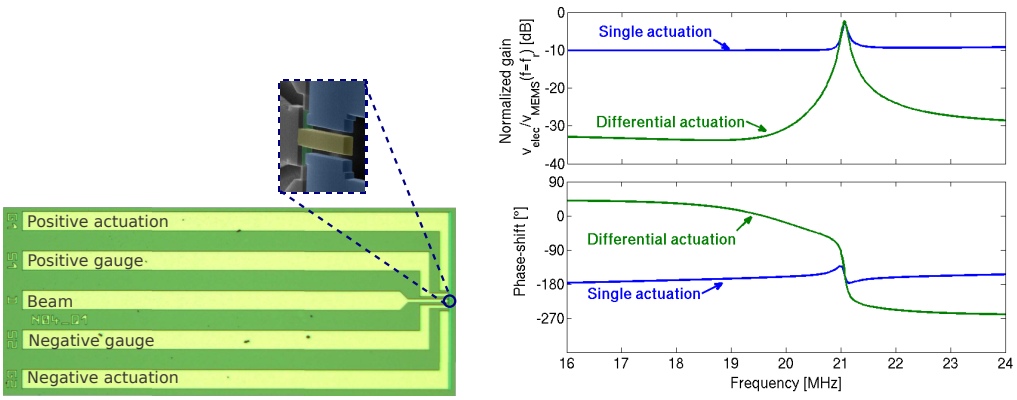

(a) (b)

Figure 3.14: (a) Optical image of the electrical connections of the crossbeam, (b) simulated on-chip parasitic feed-through and connection loss (the gain was normalized to the voltage at the resonator if no capacitance is present at the output of the resonator).

olution of the closed-loop system is presented in subsection 3.1.2.3 and compared to its theoretical value determined in chapter 2. Finally, the response time of the oscillator is evaluated.

3.1.2.1 Crossbeam presentation

The crossbeam characterized in this subsection has the dimensions given in table 3.1. The figure 3.13 depicts a scanning electron microscope image of such resonator. The theoretical resonance frequency is 21 MHz.

The crossbeam is designed for gas sensing applications[5]. The packaging and the on-chip electrical connections of the resonators were designed accordingly: the crossbeam is distanced from the electrical pads of about 2 mm so that the resonator can be encapsulated with ease [Li 2010, Arcamone 2011]. The figure 3.14a presents the electrical leads to the resonator captured with an optical microscope. As a consequence, large connection losses between the resonator and the first electronic amplification stage are induced. Moreover, due to the geometrical configuration of the electrical leads, the feed-through should increase drastically. Electromagnetic simulations[6] of the on-chip electrical environment were performed and are depicted on figure 3.14b. An error of 0.3 dB and 4° was introduced in the differential actuation that corresponds to the typical imperfection of the hybrid coupler (Pulsar JF-03-412).

With the typical parameters used in section 2.4, the expected signal-to-background

[5]However we have characterized the device in vacuum for future mass spectrometry applications.
[6]performed by Gérard Billot and Jean-Baptiste David

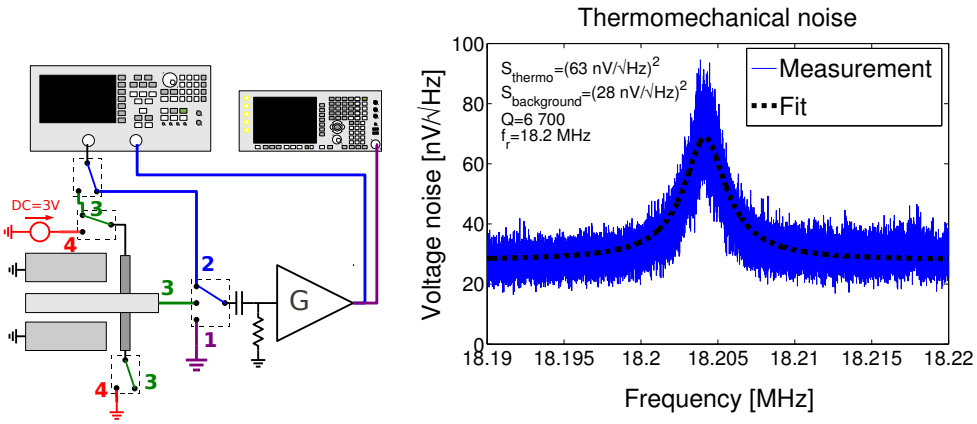

(a) (b)

Figure 3.15: (a) Measurement setups 1 in magenta, 2 in blue, 3 in green and 4 in red. (b) Noise spectrum at the first electronic amplifier output.

ratio using a single-sided actuation is around $G_{SBR} = 7$ dB, $\Delta\psi_{SBR} = 48°$ and around $G_{SBR} = 30$ dB, $\Delta\psi_{SBR} = 180°$ using a differential actuation. A differential actuation is therefore required in order to simplify the implementation of the self-oscillating but also to optimize the frequency resolution.

3.1.2.2 Open-loop characterization

We have measured the following parameters of the crossbeam resonator and the first amplifier: the electronics gain and induced noise, the connection losses and the gauge factor.

In order to measure the electronic gain and induced noise, a network analyzer (HP8753E) and a spectrum analyzer (N9020A) connected to the amplifier were used (as depicted in magenta and blue on fig. 3.15a): $G_{amp} = 14$ dB and $S_{elec} = \left(6.4 \text{ nV}/\sqrt{\text{Hz}}\right)^2$ around 18 MHz. The datasheet of the amplifier announces a voltage noise of 4 $\text{nV}/\sqrt{\text{Hz}}$. The amount of measured noise is acceptable since the resistance of the circuit (required to adjust the amplifier gain) introduces extra voltage noise.

In order to evaluate the connection losses, one can connect the first port of the network analyzer to a gauge of the crossbeam (the second gauge is kept unconnected) and the second port to the output of the electronic circuit (in green on fig. 3.15a). From the gain of the electronic circuit and the value of the resistance of the gauge, it is possible to determine the capacitance at the output of the crossbeam: $C_{connec} + C_{elec} = 30$ pF. The measured value of $C_{connec} + C_{elec}$ is reasonable as the on-chip crossbeam output capacitance is estimated to be around 20 pF and the connection capacitance introduced by the SMA-connectors between the MEMS-chip and the amplifier is around $5 - 10$ pF . Overall, the MEMS-to-electronics connection losses

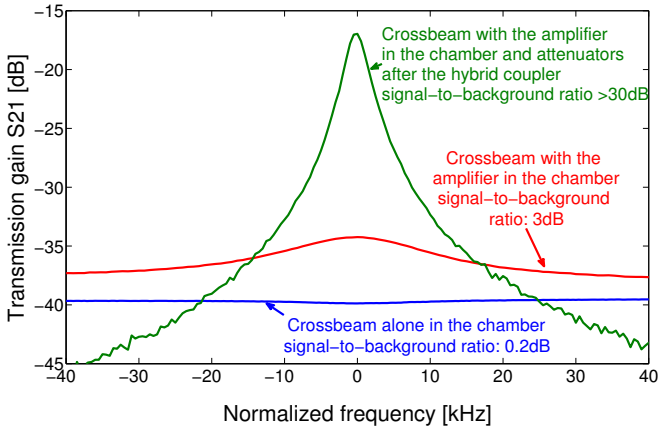

Figure 3.16: Differentially actuated crossbeam frequency response for different measurement setups. NB: however that the applied voltage slightly differs between each measurement setups.

can then be evaluated to: $|H_{connec}| = 1/|1 + j2\pi f_r Z_{MEMS} C_{output}| = -21$ dB.

In order to measure the gauge factor and the thermomechanical noise of the crossbeam, the gauges are polarized with a DC voltage of 3 V and the actuation electrodes are grounded (in red on fig. 3.15a). The spectrum of the electronic output is recorded with the spectrum analyzer (fig. 3.15b). The thermomechanical noise is clearly observed: $S_{thermo} = 63$ nV/$\sqrt{\text{Hz}}$ (measured at the output of the amplifier). From this value, the gauge factor of the silicon was extracted: $\gamma_{Si} = 77$ *[He 2006]*.

It has been observed that there is a large capacitive coupling in-between the cables that link the resonator in the vacuum chamber and its readout electronics: the transmission gain is around -40 dB at 20 MHz. The resonance of the crossbeam is therefore difficult to observe and embedding an amplifier inside the chamber to reduce connection losses and the coupling in-between the cables is necessary (fig. 3.17 and 3.16). In addition to this issue, some imperfections in the hybrid coupler used to create a differential actuation were detected. This issue can however be reduced by implementing two attenuators at the output of the hybrid coupler to adjust the phase-shift and attenuation induced by the passive device.

Figure 3.16 shows that the gain and the phase-shift of the system have to be adjusted to ensure the resonator's self-oscillation. Using a similar electronic circuitry than in subsection 3.1.1 (fig. 3.17), the gain of the open-loop is larger than 0 dB. An AD8037 clamping amplifier sets a finite adjustable limit to the oscillation amplitude. The phase-shift in the loop is adjusted with a delay line rather than with filtering. The delay line is implemented using a coaxial cable with a length of about 2 meters. The figure 3.18 presents the open-loop gain and phase-shift of the system: the oscillation conditions are fulfilled only at f_r.

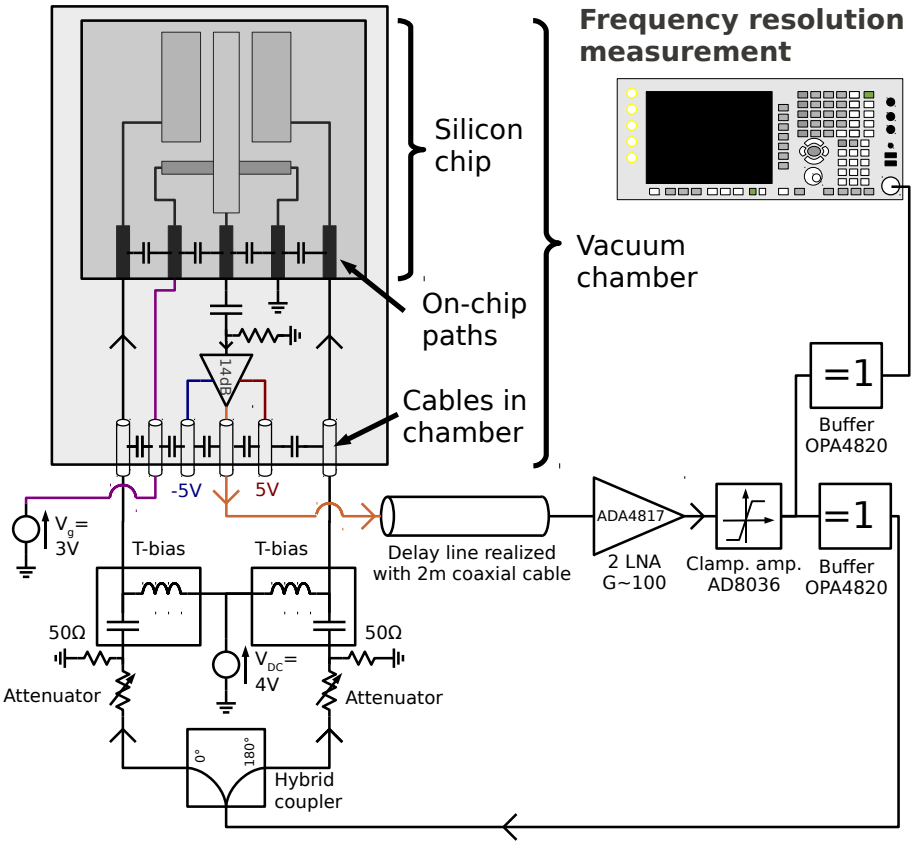

Figure 3.17: Simplified schematic of the closed-loop.

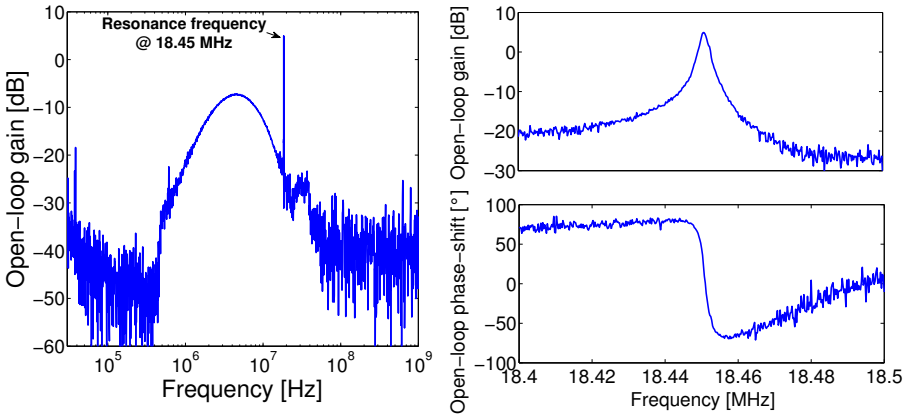

Figure 3.18: Open-loop transfer function versus frequency

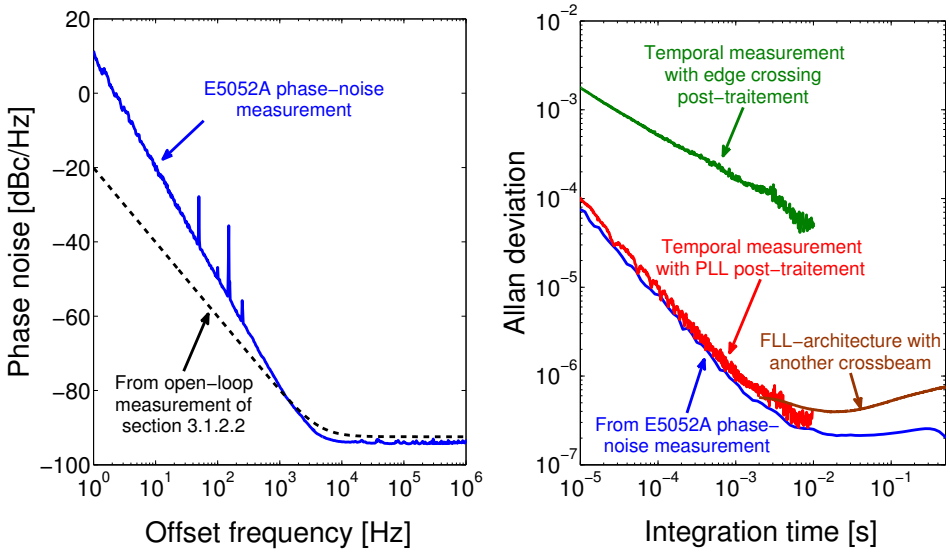

Figure 3.19: Phase noise spectrum and Allan-deviation of the oscillator.

3.1.2.3 Frequency resolution measurement

The frequency stability of the closed-loop oscillator is measured with two different techniques: a spectral acquisition and a temporal acquisition. In the first acquisition, the oscillator signal is measured with an E5052A signal source analyzer. The Phase-noise spectrum depicted on figure 3.19 is then converted into its equivalent Allan deviation through the equations (1.17) and (1.30) of pages 14 and 22. Note that this measurement was not possible with the piezoelectric cantilever because the signal source analyzer frequency range starts from 10 MHz. Moreover, the phase-shift based measurement used in the previous subsection is difficult to implement because the cables introduce large phase-shifts at this frequency: the phase-shift variations are thus difficult to calibrate.

The temporal acquisition uses a DPO7254 oscilloscope as discussed previously in subsection 3.1.1.4. The instantaneous frequency is extracted from the time lapse between two consecutive rising edges. The Allan deviation is then calculated by averaging these instantaneous frequencies as for the piezoelectric cantilever (fig. 3.19). This simple signal processing shows a large error in the evaluation of the Allan-deviation. The error is believed to be due to the poor oscillator signal-to-noise ratio at the bandwidth of the loop (what was not the case for the piezoelectric cantilever). In order to extract more accurately the frequency resolution of the oscillator, a digital PLL-based post-processing of the oscilloscope signal is implemented (fig. 3.19). With this post-processing technique, the temporal measurement corresponds to the frequency measurement. It should be emphasize that this so-called digital PLL processing used to evaluate the frequency resolution is different from the one described in subsection 1.4.3. Indeed, the data acquisition is made with the oscilloscope (equivalent to an 8-bit Analog-to-Digital Converter) and the digital

PLL processing is made at a software level coded in C-language. Therefore, there is no need of hardware equipment such as a VCO and a phase-comparator. The Silicon area consumption to implement this post-processing technique should therefore be small.

It was also attempted to measure the frequency resolution of the oscillator using a frequency counter but the results were similar to the temporal acquisition using the rising edge-based post-processing. It therefore seems that the algorithm used in the apparatus is based on the transition times of the signal and thus does not evaluate properly the frequency resolution of the loop.

It clearly appears on the Phase-noise spectrum, that for low offset frequency, the oscillator noise spectrum is dominated by flicker noise. However the origin of this flicker noise remains unclear and is under investigation.

The best frequency resolution of the resonator is around 2×10^{-7} at $T_{meas} = 20$ ms. With the dimensions of the resonator, the corresponding mass resolution is $\sigma_m = 110$ zg. The model presented in section 2.4 however predicts a mass resolution around $\sigma_{m-th} = 1$ zg at $T_{meas-th} = 1$ s (considering the crossbeam dimensions, the quality factor and the actuation DC voltage used in the measurement). The difference in mass resolution is due to the large flicker noise in the oscillating loop. However, it should be recognized that the mass resolution of this 18 MHz crossbeam is comparable with the state-of-the-art mass resolution of NEMS embedded in self-oscillating loops which is $\sigma_{m-\text{Feng2008}} = 50$ zg at $T_{meas-\text{Feng2008}} = 200$ ms [Feng 2008][7] . The mass resolution of the presented self-oscillation loop is therefore twice larger than the state-of-the-art, but with an integration time 10-times smaller (larger measurement bandwidth).

3.1.2.4 Response time of the oscillator

When MEMS resonators are electrostatically actuated, a simple method to assess the time response of a sensor is to modify the DC-actuation voltage. Indeed, the DC voltage slightly shifts the resonance frequency of the resonator through the well-known "spring-softening" effect. The response time of the oscillator can be evaluated from the transition time between one DC voltage to another. The DC voltage source that polarizes the actuation electrodes was replaced by a FG120 pulse generator at a frequency of 274 Hz[8]. The oscillator output signal is acquired with the DPO7254 oscilloscope and the signal was processed with the digital PLL algorithm discussed here-above. The evolution of the oscillation frequency versus time is depicted on figure 3.20. The signal is fitted using an exponential time response and it is evaluated that the oscillator time response is below 100 µs.

[7] Unfortunately, the mass resolution corresponding to an integration time of 20 ms is not given in this paper.

[8] An arbitrary frequency was chosen that would not be miss-confused with the harmonics of the 50 Hz-frequency of the domestic supply and whose period would be close to the time response of the sensor.

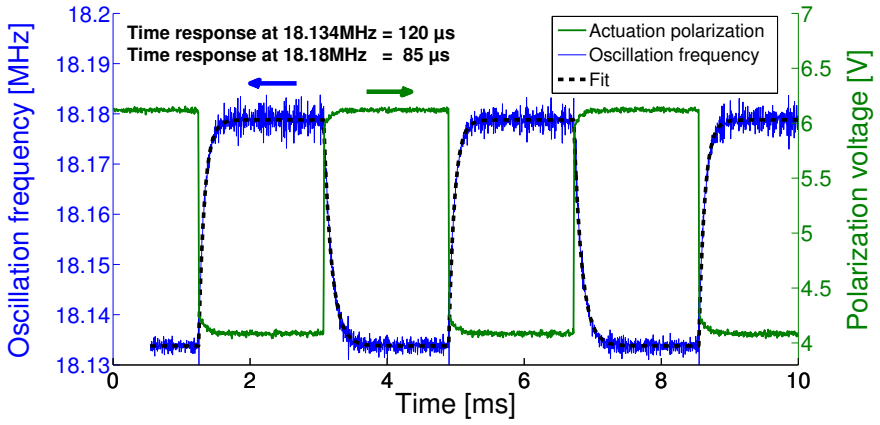

Figure 3.20: Evolution of the oscillation frequency versus time when the DC-actuation electrodes are polarized with a pulse generator.

Such a 18 MHz crossbeam implemented in a self-oscillating loop architecture can therefore be used to sense mass changes with sub-milliseconds sampling rates. However at such a low integration time, the mass resolution is deteriorated to about 5 ag.

3.1.2.5 Conclusion of crossbeam based self-oscillating loop with discrete electronics

In this subsection, inherent difficulties with stand-alone nano-resonators were analyzed and circumvented in order to implement them in self-oscillation. The on-chip feed-through was reduced using differential actuation; the parasitic coupling in the vacuum chamber cables was reduced by introducing an amplifier in the chamber. Finally, the imperfections of the hybrid coupler were reduced using two attenuators.

The gain and noise characteristics of the 18 MHz crossbeam were measured and correspond to the values in the literature. Finally, we have shown that the open-loop gain and phase-shift of the resonator and its feedback circuit can be adjusted so that the system oscillates only at f_r.

The frequency resolution of the oscillator was then measured using a frequency and a temporal acquisition. The two acquisition methods presented similar results if a PLL-algorithm is used to analyze the temporal acquisition. From the phase-noise measurement of the oscillator, it was shown that the noise spectrum is dominated by flicker noise but its origin remains unclear at this stage.

Finally, the time response of the sensor was evaluated. The corresponding time response was measured to $T_{meas} = 85$ µs allowing to use the crossbeam self-oscillating loop as a mass sensor with sampling rates below millisecond.

Resonator	Piezoelectric cantilever	Piezoresistive crossbeam
Beam's mass	25 ng	560 fg
Resonant frequency	36 kHz	18 MHz
Frequency resolution	4×10^{-7}	2×10^{-7}
Mass resolution	9.8 fg	100 zg
Integration time	$3 - 5$ s	20 ms
Gas resolution for DMMP	660 ppb	910 ppb for $Q_{air} = 150$

Table 3.2: Comparison between the different self-oscillated resonators.

3.1.3 Conclusion of self-oscillating loops using discrete electronics

Two self-oscillating loops were realized with discrete electronics: the first one involves a big MEMS resonator which has interesting gas resolutions. The challenge encountered during the design of the loop was to filter the V-shape feed-through in order to prevent parasitic oscillations. The frequency resolution of the loop was evaluated with different measurement techniques that have consistent results. The overall frequency resolution of the SOL-architecture is however degraded compared to the MEMS resonator embedded in a FLL-architecture.

The second self-oscillating loop uses a 18 MHz piezoresistive crossbeam. The major task in the implementation was to design a homodyne setup measurement that would reduce the feed-through signal. The frequency resolution of the resonator was acquired with other measurement techniques then the 36 kHz-SOL since the crossbeam resonance frequency is much higher. With with such dimensions, the crossbeam presents an excellent mass resolution that is comparable with the state-of-the-art.

Table 3.2 compares the performances of these two different self-oscillating loops: their relative frequency resolutions of each oscillator are similar. However with its small dimensions, the crossbeam can sense excellent mass resolution. On the other hand, the piezoelectric cantilever is interesting for gas measurement whereby a resolution of 660 ppb for DMMP vapors can be achieved. Note however that the crossbeam resonator presents also interesting resolution for gas sensing (the oscillator under atmospheric pressure has however not been realized yet).

3.2 Integrated circuit for multiple crossbeams

3.2.1 Objective of the integrated circuit

The oscillators realized in the previous section use commercial electronics that are connected to the stand-alone resonator through coaxial cables. This approach is

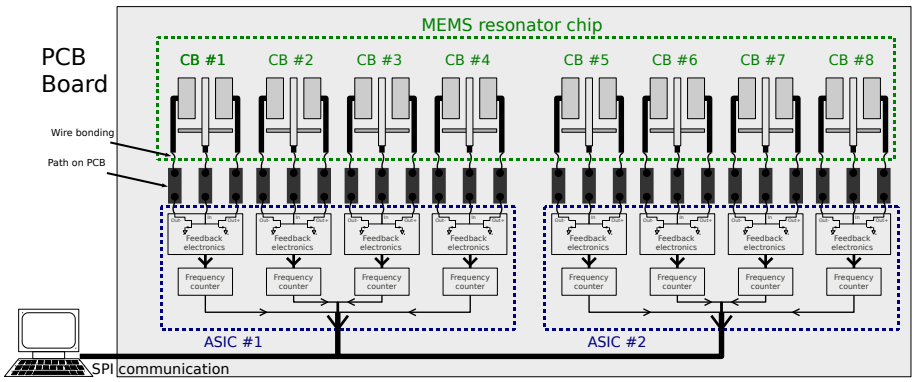

Figure 3.21: General architecture of the arrays of oscillators with stand-alone ASIC (the piezoresistive gauges connection are not represented to simplify the illustration).

justified for operating a single MEMS resonator but is difficult to implement when several MEMS devices are used, the number of connections being too large. Whereas most research groups in the literature concentrate their research on the realization of sensors with mass resolution towards single molecule resolution and with complex measurement setups [Jensen 2008, Yang 2006]; we have chosen to concentrate our study on the realization of arrays of MEMS resonators. The use of stand-alone integrated circuits with homodyne architecture makes possible to fabricate arrays of sensors with medium density: up to tens or hundreds of sensors can be realized.

In this section, we present the design of a stand-alone ASIC including four independent feedback circuits in order to self-oscillate multiple crossbeam resonators in parallel (fig. 3.21). The crossbeams addressed by the ASIC are the same as in the previous section. The inherent connections between the resonators and the feedback electronics are largely reduced because the ASIC and the silicon chip including the MEMS resonator can be implemented close to each-other and because the areas of the resonator chip and the ASIC are small (typically around $10 - 100$ mm^2). The 2 chips are connected to a common PCB board and are only distanced by a few millimeters. The inherent delay and parasitic resonances that would be introduced by connection cables are therefore largely reduced. This would not be possible with discrete electronics.

The SOL architecture has been preferred to the FLL one for several reasons:

- it would have been arduous to implement an FLL-architecture using only analog circuits. Indeed an analog VCO and phase-comparator can be difficult to design and can be area consuming.
- If the architecture uses digital electronics then it requires an analog-to-digital converter. In order to measure the phase-shift of the signal with $1 - 10°$ accuracy, the analog-to-digital converter should be of $6 - 8$ bits (i.e. $360°/2^6$) at a frequency larger than 25 MHz. From [Oliveira 2010], the area of such a

circuit would be of 0.12 mm^2 minimum. It will be shown that this area is large compared to the overall circuit.

- It can be argued that a downmixing architecture (see subsection 2.3.3) can be employed in order to reduce the constraints on the analog-to-digital converter because the sampling frequency is reduced. However, this architecture would impose large constraints on the front-end analog filtering needed before the analog-to-digital converter.

Overall, it is believed that an FLL-architecture would be too challenging (in terms of design time and risks) to design the proposed application.

Implementing both the complete feedback electronics and a frequency counter seems a much more compact and feasible solution. Only a clock reference, a communication cable with a computer and a DC power are required. The packaged ASIC with an area of 7×7 mm^2 (the actual silicon die is of 2×2 mm^2, the rest of the area is dedicated to the packaging) also offers the possibility of using several ASIC in parallel in order to address dozen or more resonators.

However, the fabrication of several resonators and feedback electronics each on a single chip has some counterparts: some electrical and mechanical coupling may appear between the different resonators or between the different circuits within the ASIC chip. The characterization of the multi-oscillators system makes it possible to assess the coupling when electromagnetic models would probably fail at this task.

3.2.2 Global architecture

The ASIC is composed of 4 blocks containing each a feedback circuit and a frequency counter; a power management block and a SPI communication interface so that the chip can be directly connected to an external computer (fig. 3.22). The ASIC is therefore composed of analog and digital electronics. The analog signal in each oscillating loop is converted into a digital signal and its frequency is measured in real time via the digital frequency counter. The measured frequencies are averaged over a minimal integration time of 10 µs. The averaged oscillation frequency is then sent to a computer through the SPI communication interface. The communication protocol is also used to configure specific parameters (such as the polarization current or the cut-off frequency of the filters) of the self-oscillating circuit.

The frequency counters sampled at 1 GHz consist in counting during a fixed time T_{meas} the number of rising edges of the oscillating signal. In order to achieve a larger accuracy in the frequency measurement, the time of the first and last rising edge are measured and the mean frequency is modified accordingly to the method presented in subsection 1.4.1 of page 33. From eq. (1.59) at page 33, a frequency resolution better than 10^{-7} is achieved for $T_{meas} \geq 15$ ms which is compatible with the results of subsection 3.1.2. It should be mentioned that the frequency measurement technique implemented in the ASIC provided poor resolution in subsection 3.1.2. The issue

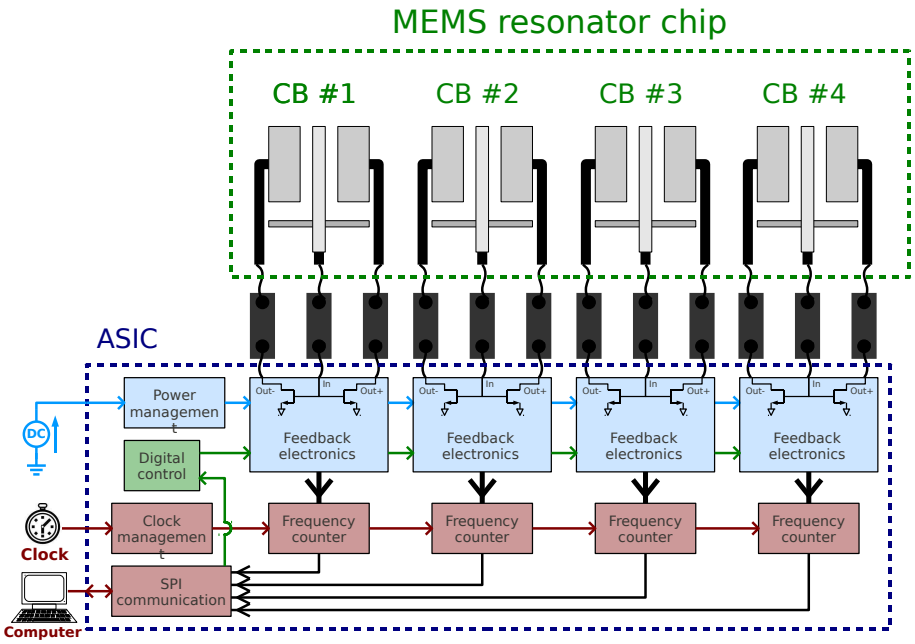

Figure 3.22: General architecture of the ASIC (the piezoresistive gauges connection are not represented to simplify the illustration).

was only discovered after the design of the ASIC but we hope that including the comparator in the loop as it is done in the ASIC can prevent this issue.

The architecture implemented in the ASIC allows to activate or deactivate each oscillator on demand. It also offers the possibility to measure each oscillating frequency in parallel or sequentially. The coupling between each oscillator can thus be evaluated: it is possible for that a frequency shift is detected on an unloaded resonator due to coupling effects with a loaded resonator.

3.2.3 General topology of the proposed oscillator

The ASIC input signal (corresponding to the resonator output signal) is first biased so that the ASIC characteristics are independent of the crossbeam DC output voltage. The electrical signal is then amplified in order to increase its amplitude and to neglect the noise contribution of the following stages. The following analog stages are dedicated to further amplify and to filter the signal in order to prevent parasitic oscillations at other frequencies than f_r. Note that the analog blocks are biased by independent current sources whose values can be adjusted. The tunability of the bias current makes the ASIC more robust and the ASIC characteristics can be modified if needed.

Because the resonator and the ASIC are fabricated on different wafers and connected by wire bonding, it is assumed that the connections could modify the phase response of the crossbeam's resonance and that the phase-shift introduced by the connections

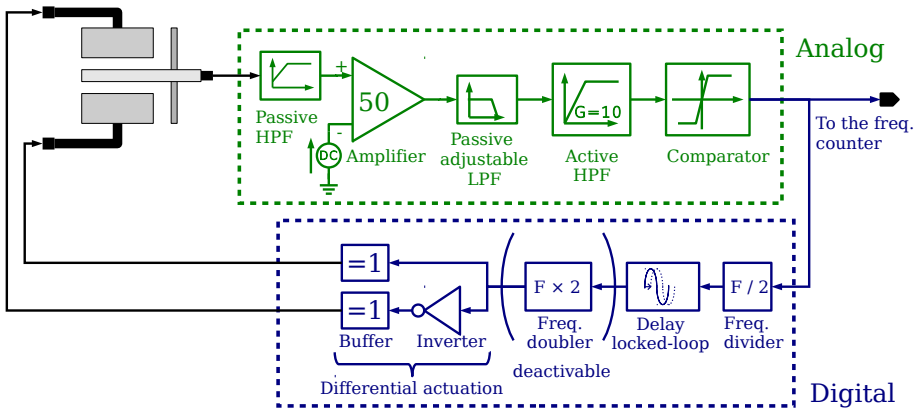

Figure 3.23: General architecture of the self-oscillating loop.

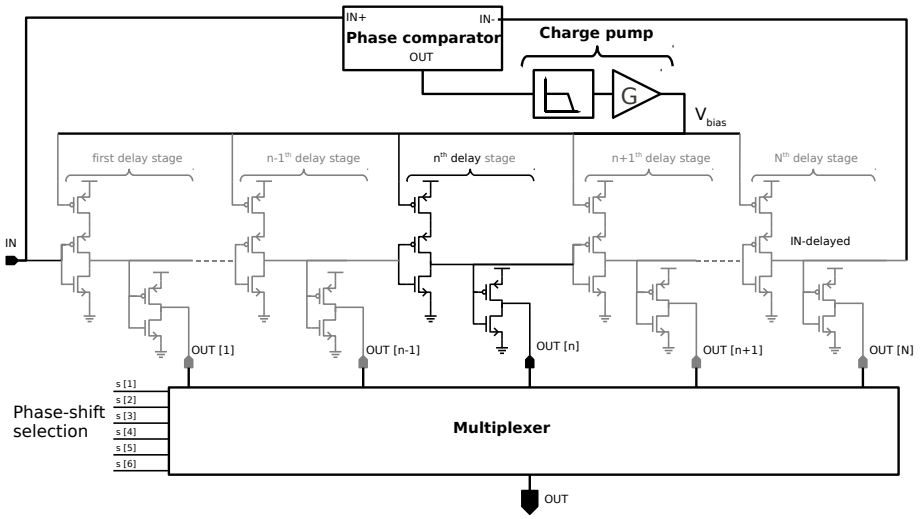

Figure 3.24: Schematic of a delay-locked loop.

would be difficult to predict accurately. The architecture of the oscillator should therefore be capable to phase-shift the input signal to any value. To the author's knowledge there is no analog architecture capable of finely tuning the phase-shift of the signal that is compact and low power.

Therefore, an analog/digital mixed architecture has been preferably implemented. It uses a delay lock loop (DLL) that consists of a series of delay blocks which are controlled by a feedback loop (fig. 3.24). Each delay block is basically an inverter and therefore the delay introduced by each block is a function of its bias current. It is then possible by adjusting the bias current to control the delay introduced by each stage. The output of the last delay block ($IN - delayed$) is compared to the input signal (IN) with a phase comparator. The delay of each delay block is then controlled through a charge pump so that a 2π-phase-shift is imposed between the signal IN and the signal $IN - delayed$. The phase-shift introduced by the n^{th}-delay block is then $2\pi \times \frac{n}{N}$ where N is the number of delay blocks. Using a multiplexer it

is then possible to select any output of the delay line and therefore select a signal with the desired phase-shift according to the input signal. A delay line composed of 64 blocks was implemented: the phase-shift resolution of the DLL is therefore $2\pi/64 < 6°$. Note that the DLL can also be used to compensate any phase-shift introduced by the rest of the feedback circuit.

Saturating the signal at the output of the analog front-end into a 1-bit signal makes it also possible to easily control the amplitude of the oscillation because it is fixed by the supply voltage. The counterpart of this approach is that the comparator, used to convert the analog signal into a 1-bit digital signal, is highly nonlinear and thus transposes the flicker noise close to the carrier (see subsection 1.3.1.4 at page 25). For this reason, one should filter the flicker noise to limit this effect. The next subsection will discuss in more details this aspect.

Finally large 2.5 V buffers are designed to drive the crossbeam with a high actuation power.

NB: the design of the different blocks of the ASIC was divided between the actors of the project. I designed the analog blocks and realized their layout as well as the comparator layout.

3.2.4 Analog circuit design

The simplified schematic of the analog part of the circuit depicted in figure 3.25 is composed of the following stages:

- a biasing block,
- a low-noise amplifier (LNA),
- a low-pass filter,
- an active high pass filter with a gain of 10,
- and a comparator with an adjustable offset.

Low-noise amplifier A fully differential low-noise amplifier is designed. The DC voltage on each input transistors (M_{13} and M_{14}) are imposed by the biasing blocks described in the following paragraph. The AC signal to be amplified is then connected through a decoupling capacitance to the positive input of the amplifier. The fully differential architecture of the amplifier makes possible to convert the input signal of the crossbeam into a differential signal. Several other architectures could also convert the MEMS output signal into a differential one but these architectures introduce larger noise [Palmisano 2003]. As a matter of fact, they are not suitable to low-noise and high frequency applications. The dimensions of the transistors are chosen large enough in order to achieve a low white and flicker noise at the input of the amplifier. However, the length of the transistor gates are designed based on the

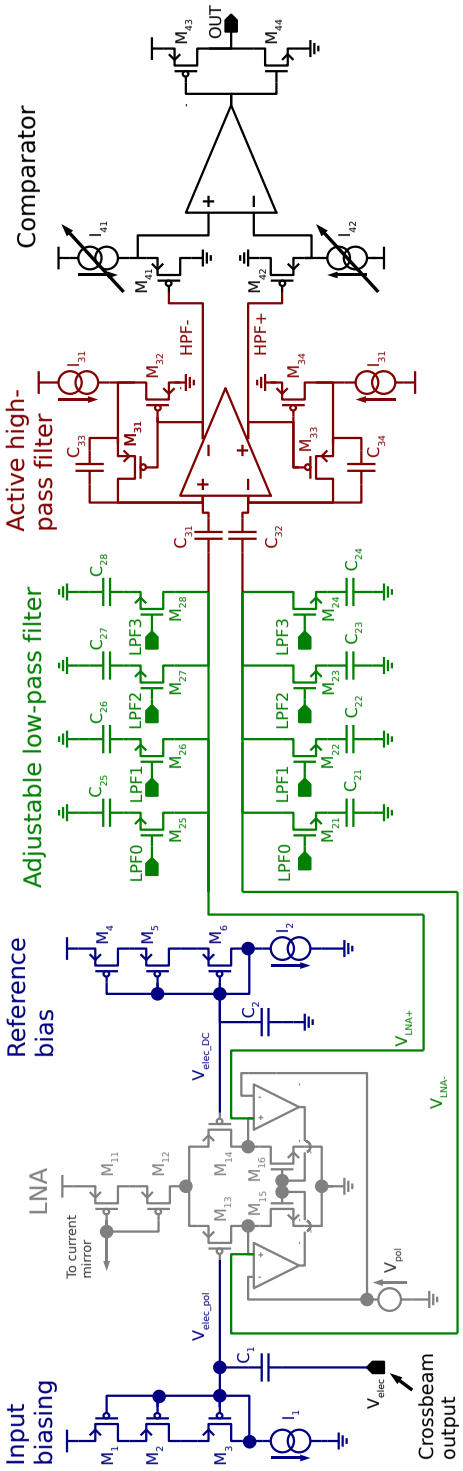

Figure 3.25: Simplified schematic of the analog circuit

trade-off between low-flicker noise and high input capacitance. Overall the amplifier has a typical voltage gain of 20, a bandwidth of 120 MHz and an input noise of 1.5 nV/$\sqrt{\text{Hz}}$.

Finally, as in all fully differential amplifier, a control of the common mode is required. Two other single-ended amplifiers are implemented in order to control the common mode. The power consumption and the capacitance at the output of the LNA are reduced by diminishing the width of the single-ended amplifiers by a factor 10.

Biasing blocks The biasing block with the input decoupling capacitance C_1 makes the electronic circuit independent of the crossbeam resonator's DC output voltage. The biasing stage is composed of transistors with the same length than the ones of the LNA but with a smaller width in order to both reduce the silicon area and the input noise. It might seem that reducing the size of the transistors increases the thermal electronic noise but in our case, the coupling capacitance filters the noise at high frequencies (i.e. around the crossbeam resonance frequency). Indeed, the voltage noise at the input of the LNA can be approximated to:

$$v_{noise-bias} = \frac{\sqrt{8/3 k_B T g_{m-bias}}}{\left| j2\pi f \frac{C_1 C_p}{C_1+C_p} + g_{m-bias} \right|} \approx \frac{\sqrt{8/3 k_B T g_{m-bias}}}{2\pi f \frac{C_1 C_p}{C_1+C_p}} \quad \text{if } g_{m-bias} \ll 2\pi f \frac{C_1 C_p}{C_1 + C_p}, \tag{3.2}$$

where g_{m-bias} is the equivalent admittance of the biasing block and C_p the MEMS-to-electronics connection losses. The equivalent impedance of the transistors should be large in order to have a good impedance matching with the resonator output impedance. Moreover, in order to achieve a very low noise at the LNA input ($\approx$ 0.5 nV/$\sqrt{\text{Hz}}$), the capacitance C_1 should equal to 30 pF. Another biasing block is designed for the other input transistor of the LNA in order to bias identically the amplifier. However, the noise at lower frequencies is large but it is filtered in the further blocks.

The large dimensions of the transistors M_{13} and M_{14} of the LNA introduce a capacitance between their gates and sources. A parasitic path is created between the two inputs of the LNA and thus the AC input signal on M_{13} can be transferred to the gate of M_{14}. The AC signal at the inputs of the LNA varies in phase and the gain of the amplifier vanishes. A large grounded capacitance ($C_2 = 15$ pF) is introduced at the input of the transistor M_{14} in order to reduce the AC signal at M_{14} created by the existing path.

Passive adjustable low-pass filter The passive first-order low-pass filter allow adjusting the bandwidth of the LNA. By introducing a variable capacitance at the amplifier output, the bandwidth of the LNA is modified and thus high frequency-noise can be filtered. A set of capacitances are connected or not to the LNA output via NMOS switches. The capacitance at the amplifier output can be adjusted through 6 configuration bits.

Active high-pass filter The constraints imposed on the high-pass filter are to filter the frequencies lower than 10 MHz while introducing little supplementary noise in the loop. The block cannot be realized with $g_m - C$ filters [Sansen 2006] because the architecture cannot introduce little noise while respecting the impedance criteria (a high input impedance compared to the output impedance of the LNA, and a low output impedance compared to the input impedance of the following comparator).

The proposed structure is a classic differential active first-order high-pass filter based on a differential amplifier designed to introduce a gain close to 50. The feedback loop is composed of a resistance (implemented with the PMOS transistors M_{31} and M_{33}) and capacitance. The structure has a high pass filter behavior and introduces an overall gain close to 10.

The transistors M_{32} and M_{34} are designed to introduce a DC threshold voltage between the input and the output of the high-pass filter so that it reduces the size of the transistors M_{31} and M_{33}. Moreover, this approach reduces the area consumption and improves the reliability of the transistors M_{31} and M_{33}.

Comparator with an adjustable offset The comparator uses two single-sided buffer with adjustable bias current. By adjusting the bias current, the saturation voltage of the transistors M_{41} and M_{42} can be adjusted and a DC offset between V_{comp+} and V_{comp-} can be introduced and adjusted. The variable offset was implemented in the loop in order to compensate any mismatch in the previous amplification stages but also so that parasitic oscillations may be prevented. The comparator then consists of a classic 2-stages single-ended amplifier with an inverter at its output. A special care was given in the layout of such design to prevent any parasitic signal from the inverter (i.e. the digital circuit) to propagate in the analog circuit.

3.2.5 Overall simulations and layout

Figure 3.26 depicts the ASIC layout. As announced, the die area is 2×2 mm^2. The pad ring composed of 48 pads fills a large area and the actual circuit is about 1.5×1.5 mm^2. The circuit is divided between the 4 feedback circuits (with an area of 0.29 mm^2 each) and the digital circuit of control. The layout of a feedback circuit is depicted in figure 3.27. The adjustable current sources occupy the largest area, the area is then decomposed between the analog front-end and the DLL. If a second version of the ASIC is realized, the experience acquired from the characterization of the first chip should allow in the future to remove the adjustable current sources and thus to reduce the area consumption of the chip to 0.15 mm^2 or less. Moreover, with the characterization of the first chip and if the phase-shift introduced by the crossbeam is repeatable, then the DLL might be optional.

Only the analog circuit characteristics are presented in this section because it is the circuit that I designed. It was simulated over a range of temperature from 20° to

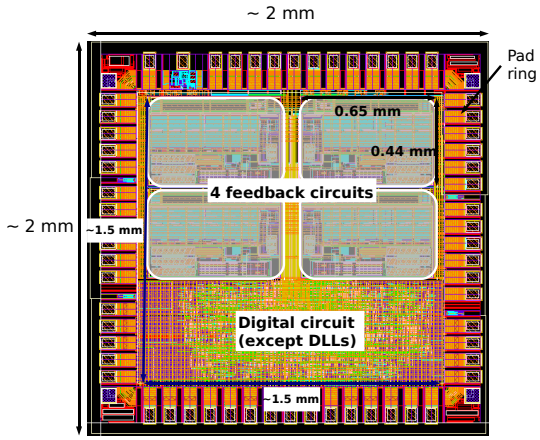

Figure 3.26: Layout of the ASIC.

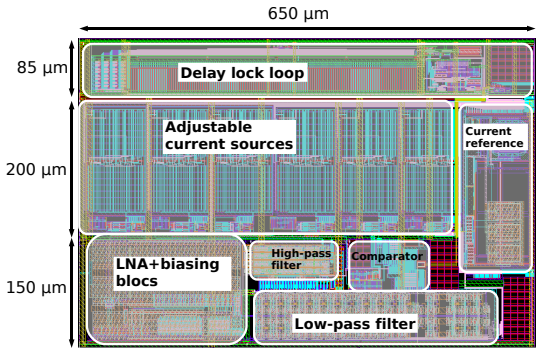

Figure 3.27: Layout of the feedback circuit.

80° and over various process corners. The circuit except the comparator has the following characteristics:

- the gain at 20 MHz is larger than 140,
- the bandwidth can always be larger than 100 MHz,
- the high pass cut-off frequency is in-between 6.5 MHz and 11.5 MHz
- the electronic input noise is lower than 1.8 nV/$\sqrt{\text{Hz}}$.

The overall ASIC is based on a mixed analog/digital architecture whereby the analog front-end filters and amplifiers the signal. The mixed architecture makes the feedback-loop very flexible and best suited to the application. Indeed, the phase-shift, the bandwidth, an offset and the biasing current of the analog stages can be adjusted in the loop. All in all, the architecture remains compact so that is can address multiple resonators: it is possible to implement an array with a typical distance of 500 µm between each resonators.

Furthermore, the flexibility introduced in the loop can be simplified in the case of a second ASIC and thus a more compact ASIC can be realized.

3.3 MEMS/CMOS co-integration

3.3.1 Context and objectives

In the chapter 2, it was theoretically shown that integrating the MEMS on the same wafer as the CMOS circuit reduces both the connection losses and the feed-through. Moreover, the integration of MEMS resonators with CMOS circuits is required to fabricate large arrays of sensors. When millions of MEMS resonators are implemented in arrays, the wire bonding to individually connect the resonators

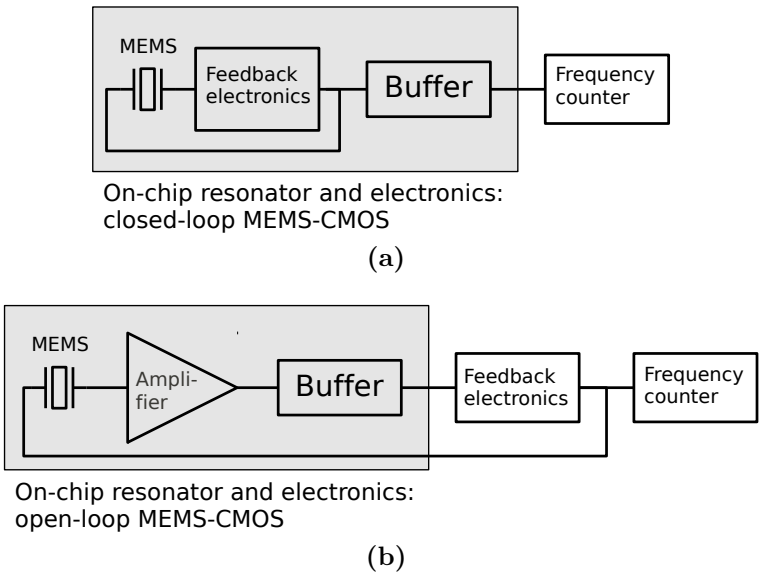

Figure 3.28: General topology of the integrated resonator with the electronics: (a) fully-integrated oscillator, (b) oscillator implemented with an external feedback electronics.

to the sustaining electronics becomes unrealistic and too costly. The fabrication of the resonators and the CMOS circuitry on the same wafer is a necessary technological step to realizes sensors for mass spectrometers. This thematic was investigated in this work through three different projects:

1. In the first project, a ST-0.35µm bulk CMOS process is adapted to be compatible with a MEMS resonator on a SOI-wafer. The integrated MEMS resonator is a clamped-clamped beam that uses an electrostatic actuation and a capacitive detection. The beam and the electrodes of the MEMS are highly doped using a similar doping level than for the transistors contacts.
2. In the second project, a FDSOI-process developed at Leti for digital electronics is adapted to be 2D co-integrated with piezoresistive resonators. This home-made process offers more flexibility, e.g. one can choose the type of SOI-wafer and the doping level of the MEMS (and thus to use piezoresistive detection).
3. In a third project, the 3D-integration where the single-crystal MEMS resonator lays on top of its circuity in a 3D-stack is explored. The fabrication is based on another FDSOI-process developed at Leti for digital electronics.

In each project, the technological process of the CMOS transistors was modified to be adapted to the MEMS resonators. It was then assumed that the characteristics of the transistors may vary from the models of the design kit. The electronic circuits were designed to be flexible and simple. The on-chip systems composed of the resonator and the electronics were designed based on two different strategies: they were either implemented in a closed-loop or an open-loop architecture as depicted in 3.28. In the closed-loop configuration (fig. 3.28a), the output of the feedback

electronics is connected to the resonator actuation voltage. The buffer therefore drives the oscillator signal out of the Silicon chip. The buffer is designed to charge to connection cables between the MEMS-CMOS chip and an external measurement apparatus (e.g. a frequency counter). The feedback electronics is designed so that the MEMS+feedback electronics respect the oscillation conditions. In the open-loop architecture (fig. 3.28b), the oscillator is realized out of the chip by the use of an external feedback circuit. The on-chip open-loop architecture is more flexible and less risky because the gain and the phase-shift of the open-loop can be adjusted externally. In this case, the amplifier is designed to provide a gain sufficient so that the noise of the following stages can be neglected. The reduced constaints on the design of the amplifier makes it possible to design such block with smaller input noise than in the on-chip closed-loop configuration. The buffer is similar to the one of the closed-loop configuration because the connection capacitance between the MEMS-CMOS chip and an external measurement apparatus (here a lock-in amplifier or a phase-shifter to implement a FLL or a SOL) are similar. Overall, fully-integrated oscillators are often preferred in a final product or in the domain of high density arrays of sensors.

In the two first projects, closed-loop architecture were implemented. As mentioned previously, the 2D co-integration reduces in a large manner the connection losses. It will be shown that in the two first projects, the product $g_{MEMS} \times |H_{connec}|$ is close to 1 and thus the gain of the sustaining electronics is low. The feedback circuits can then be based on a Pierce oscillator topology that uses only a single active transistor. A trade-off must be found regarding the dimensions of this transistor: if its area is too large, its input capacitance is large what increases the connection losses. If its length is small, the transistor provides low gain. If its width is too small, than the transistor cannot charge the capacitance of the following electronic stage (i.e. the buffer). The theoretical design of the Pierce oscillator in the case of the resonators with a capacitive or a resistive detection is described in the following subsection.

3.3.2 Theoretical design of a co-integrated MEMS Pierce oscillators

This subsection addresses the feasibility of a fully-integrated MEMS-based Pierce oscillator in cases when the motion of the resonator is converted into an electrical signal through (a) capacitive or (b) resistive detection. Our approach uses a MOS Berkeley level 1 model description of a standard CMOS technology. This methodology can easily determine for a given MEMS or NEMS resonator if it is possible to implement it in a Pierce oscillator scheme, and can also be used as a design rule to shrink the resonator's dimensions down to achieve the highest resonance frequency. As a study case, the approach is illustrated on electrostatically-actuated resonators: (a) a clamped-clamped beam resonator using capacitive sensing, and (b) a piezoresistive crossbeam. Both oscillators are based on a STMicroelectronics

HCMOS9 design kit. The technology makes it possible to fabricate transistors with gate length dimensions as small as 130 nm making it good candidate for high frequency applications without the high fabrication cost and the constraints of more advanced processes.

3.3.2.1 Oscillation conditions

As described in section 1.3.1.1, the Barkausen conditions for a system to oscillate at f_{osc} are:

$$|H_{MEMS}(f_{osc}) \times H_{elec}(f_{osc})| > 1 \text{ and } \arg[H_{MEMS}(f_{osc}) \times H_{elec}(f_{osc})] \equiv 0\ [2\pi]. \tag{3.3}$$

To oscillate at f_r, the electronic circuit must then have a gain at f_r larger than $1/g_{MEMS}$ and a phase-shift ψ_{elec} equal to $-\psi_{MEMS}$. If the electronics introduce a supplementary phase-shift $\Delta\psi$ so that $\psi_{elec} = -\psi_{MEMS} + \Delta\psi$, and if the gain is sufficient, the resonator will still oscillate at a frequency f_{osc} little different from f_r [9]:

$$f_{osc} \approx f_r \left(1 + \frac{\Delta\psi}{2Q}\right). \tag{3.4}$$

By definition, the gain of the MEMS resonator at f_{osc} is smaller than g_{MEMS}. Its value can be approximated to:

$$|H_{MEMS}(f_{osc})| \approx g_{MEMS}\left[1 - \frac{\Delta\psi^2}{2}\right]. \tag{3.5}$$

From equations (3.3) and (3.5) it is seen that to ensure oscillations, $|H_{elec}(f_{osc})|$ must increase as $\Delta\psi$ increases. A trade-off must be established in order to achieve a large electronic gain while introducing small $\Delta\psi$. The goal of the electronic design should then be to maximize the quantity expressed by:

$$|H^{ps}_{elec}(f_{osc})| = |H_{elec}(f_{osc})|\left(1 - \frac{\Delta\psi^2}{2}\right). \tag{3.6}$$

3.3.2.2 Sustaining electronics for a capacitive MEMS resonator

In this subsection, we show that, for the architecture shown in fig. 3.29, there exists optimal transistor dimensions for M_A for which $|H^{ps}_{elec}(f_{osc})|$ is maximized. Approximate expressions of the optimal transistor width W_{A-opt} and length L_{A-opt} are:

$$\begin{cases} W_{A-opt} & \approx \sqrt[3]{\frac{2\pi f_r C_{load} C^2_{connec}}{16 K'_n C^2_{gd0} V_E}} \\ L_{A-opt} & \approx (V_{gs} - V_T)\sqrt[3]{\frac{2K'_n C_{connec}}{2\pi f_r C_{load} C_{gd0} V_E^2}} \end{cases}, \tag{3.7}$$

[9] Obtained from a first order Taylor expansion of H_{MEMS}

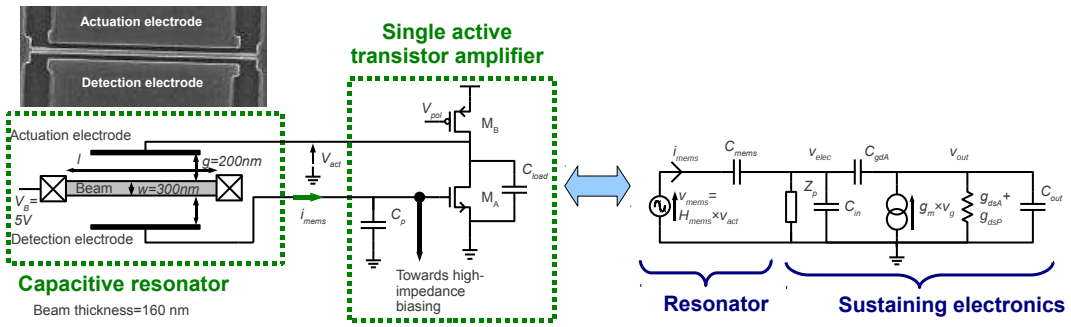

Figure 3.29: Transimpedance amplifier schematic (left) and its equivalent small signal schematic for a capacitively sensed resonator (right).

where

- $C_{load} = 200$ fF is the Pierce oscillator output capacitance,
- $K'_n = 125$ µA/V^2 is the transconductance coefficient,
- $C_{gd0} = 0.5$ fF/µm nominal gate-drain capacitance,
- $V_E = 7.7$ V/µm is the impedance parameter,
- $V_{gs} = 0.6$ V is the gate-source DC voltage,
- $V_T = 0.36$ V is the threshold voltage.

The resulting electronic gain is:

$$\left|H^{ps}_{elec-opt}\left(f_{osc}\right)\right| \approx \frac{3}{8}\sqrt[3]{\frac{2K'_n V_E C^3_{MEMS}}{2\pi f_r C^2_{connec} C_{load} C_{gd0}}}, \tag{3.8}$$

where C_{MEMS} is the output capacitance of the resonator. The corresponding electronic supplementary phase-shift is $\Delta\psi = 0.5$ rad that corresponds to an oscillating frequency of: $f_{osc} \approx 1.00025 \times f_r$.

Description of the circuit Figure 3.29 shows the schematic of the capacitive MEMS-based Pierce oscillator and its small signal equivalent circuit, where:

- g_m is M_A's transconductance,
- Z_P is M_A's gate biasing impedance,
- C_{gdA} is M_A's gate-drain capacitance,
- g_{dsA} is M_A's drain-source admittance,
- g_{dsB} is M_P's drain-source admittance,
- $C_{in} = C_{connec} + C_{gsA}$,
- C_{dbA} is M_A's drain-bulk capacitance,

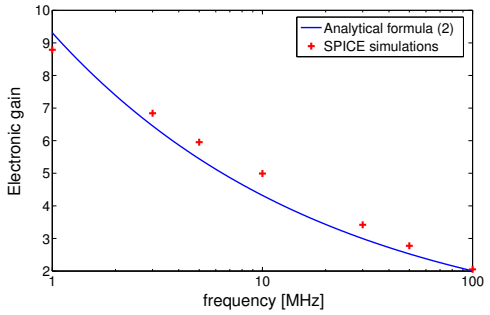

(a)

Frequency (MHz)	M_A: $W_{opt} \times L_{opt}$ (µm×µm)	M_P: $W_P \times L_P$ (µm×µm)	$\left\|H_{e-opt}^{ps}\right\|$
1	0.24×0.36	4.7×1.1	8.8
3	0.24×0.36	4.7×1.1	6.8
5	0.29×0.30	5.5×0.9	6.0
10	0.36×0.24	6.9×0.7	5.0
30	0.51×0.16	9.9×0.5	3.4
50	0.61×0.14	11.7×0.42	2.8
100	0.91×0.13	17.5×0.39	2.1

(b)

Figure 3.30: (a) Comparison between the analytical formula (9) and SPICE simulations, (b) transistors dimensions

- C_{dbB} is M_B's drain-bulk capacitance,
- $C_{out} = C_{load} + C_{dbA} + C_{dbB}$.

The small signal equivalent schematic of the circuit uses the Berkeley level 1 [Sansen 2006] model of the transistors. The electronic design of the Pierce-oscillator consists in determining the optimal dimensions of the transistors M_A and M_P. Their dimensions determine the values of g_m , C_{gsA}, C_{gdA} , g_{dsA} , g_{gsP} , C_{dbA} , C_{dbP} and therefore the amplification capability of the electronics. Note that it is considered that the MEMS resonator output capacitance C_{MEMS} is negligible compared C_{connec} (that is typically in the order to 5 fF).

The resonator output voltage v_{MEMS} is attenuated due to the connection losses and the resulting voltage is v_{elec}. The active transistor M_A amplifies and converts v_{elec} into a current which is then converted back into a voltage through C_{out}. If the effects of C_{gdA}, g_{dsA}, g_{gsP} and Z_P are negligible, the electronic circuit has the following ideal transfer function at a frequency f_{osc}:

$$H_{elec}^{ideal} = \frac{v_{out}}{v_{MEMS}} = \frac{-g_m C_{MEMS}}{j2\pi f_{osc} C_{in} C_{out}} \approx \frac{-g_m C_{MEMS}}{j2\pi f_{osc} C_p C_{load}}. \tag{3.9}$$

Such an ideal circuit introduces a +90 phase shift in the oscillator feedback loop and thus ensures that the oscillations conditions 3.3 can be met at $f = f_r$. However, it is not possible in practice to achieve a large transimpedance gain (i.e. large g_m or small C_{in}) without increasing the values of C_{gdA}, g_{dsA}, g_{gsP} and Z_P. The next sub-section is devoted to the determination of an optimal design of the electronics.

Maximum electronic gain The non-ideal electronic transfer function has the following expression:

$$H_{elec} = -j2\pi f_{osc} C_{MEMS} \left(g_m - j2\pi f_{osc} C_{gdA}\right) / \left\{ \frac{g_{dsA} + g_{dsP}}{Z_P} + j2\pi f_{osc} \left[\left(g_{dsA} + g_{dsP}\right) \left(C_{MEMS} + C_{in} + C_{gdA}\right) + \frac{C_{out} + C_{gdA}}{Z_P} + g_m C_{gdA} \right] - \left(2\pi f_{osc}\right)^2 \left[\left(C_{MEMS} + C_{in} + C_{gdA}\right) \left(C_{out} + C_{gsA}\right) - C_{gdA}^2 \right] \right\}. \quad (3.10)$$

We assume that:

- the MEMS resonator output capacitance is negligible compared to C_p: $C_{MEMS} \ll C_p < C_{in}$,
- the effect of M_P can be neglected (i.e. $g_{dsP} \ll g_{dsA}$, $C_{dbP} \ll C_{load}$),
- the effect of M_A biasing can be neglected (i.e. $Z_P \gg \frac{1}{2\pi f_{osc} C_{out}}$, $Z_P \gg \frac{C_{out}}{C_{in}} \frac{1}{g_{dsA}+g_{dsP}}$),
- the transistors dimensions respect 50 nm $\ll L_A \ll$ 50 µm and $W_A L_A \ll$ 15000 µm^2 so that $C_{gdA} \ll C_{gsA}$, $C_{dbA} \ll C_{load}$, $g_m \gg 2\pi f_{osc} C_{gdA}$,
- the gate-source capacitance of M_A is low compared to the shunt capacitance: $C_{gsA} \ll C_p$.

With the previous consideration, the expression of the electronic transfer function H_{elec} can be written as:

$$H_{elec} = H_{elec}^{ideal} \frac{1}{1 - H_{elec}^{ideal} \left(\frac{C_{dgA}}{C_{MEMS}} + \frac{g_{dsA}}{g_m} \frac{C_p}{C_{MEMS}} \right)}. \quad (3.11)$$

The phase introduced by this circuit is $\psi_{elec} = \pi/2 + \arctan\left[\left| H_{elec}^{ideal} \right| \left(\frac{C_{dgA}}{C_{MEMS}} + \frac{g_{dsA}}{g_m} \frac{C_p}{C_{MEMS}} \right) \right]$ and its gain is $|H_{elec}| = H_{elec}^{ideal} / \sqrt{1 + \left| H_{elec}^{ideal} \right|^2 \left(\frac{C_{dgA}}{C_{MEMS}} + \frac{g_{dsA}}{g_m} \frac{C_p}{C_{MEMS}} \right)^2}$. Assuming $\Delta\psi = \psi_{elec} - \pi/2$ is small, a Taylor expansion of (3.11) yields:

$$|H_{elec}| \approx \left| H_{elec}^{ideal} \right| \times \left(1 - \Delta\psi^2/2\right). \quad (3.12)$$

In other words, $\Delta\psi$ not only introduces a resonator gain reduction (cf. eq. (3.5)) but also a circuit gain reduction. A modified gain ($|H_{elec}^{ps}| = H_{elec}^{ideal} \times (1 - \Delta\psi^2)$) takes into account the resonator gain reduction due to $\Delta\psi$ can be introduced. Starting from the Berkeley level 1 model [Sansen 2006] applied to the transistor M_A:

$$g_m = 2K_n' \frac{W_A}{L_A} \left(V_{gs} - V_T\right), \; g_{ds} = \frac{K_n'}{V_E} \frac{W_A}{L_A^2} \left(V_{gs} - V_T\right)^2, \; C_{gd} = C_{gd0} W_A, \quad (3.13)$$

where W_A, L_A are the width and length of M_A, respectively. The expression of $|H^{ps}_{elec}|$ can then be expressed in terms of W_A and L_A:

$$|H^{ps}_{elec}| = \frac{2K'_n \frac{W_A}{L_A} (V_{gs} - V_T) C_{MEMS}}{2\pi f_{osc} C_p C_{load}} \times \left[1 - \frac{2K'_n \frac{W_A}{L_A} (V_{gs} - V_T)}{2\pi f_{osc} C_p C_{load}} \left(C_{gd0} W + C_p \frac{V_{gs} - V_T}{2LV_E} \right) \right]. \quad (3.14)$$

Maximizing $|H^{ps}_{elec}|$ with respect to W_A and L_A yields to the following expression of the optimal parameters W_{A-opt}, L_{A-opt} and $\left|H^{ps}_{elec-opt}\right|$:

$$\begin{cases} W_{A-opt} & = \sqrt[3]{\frac{2\pi f_{osc} C^2_{connec}}{16 K'_n C^2_{gd0} V_E}} \\ L_{A-opt} & = (V_{gs} - V_T) \sqrt[3]{\frac{2K'_n C_{connec}}{2\pi f_{osc} C_{load} C_{gd0} V^2_E}} \\ \left|H^{ps}_{elec-opt}\right| & = \frac{3}{8} \sqrt[3]{\frac{2K'_n V_E C^3_{MEMS}}{2\pi f_{osc} C^2_{connec} C_{load} C_{gd0}}} \end{cases}. \quad (3.15)$$

As $\left|H^{ps}_{elec-opt}\right|$ depends on C_{MEMS} and thus on the characteristics of the resonator, it is possible to introduce the transimpedance gain of the circuit defined as $Y^{ps}_{elec-opt} = \frac{v_{out}}{i_{MEMS}}$, where i_{MEMS} is the output current of the resonator. The evolution of $\left|Y^{ps}_{elec-opt}\right|$ is depicted in figure 3.30a. SPICE simulations performed with the HCMOS9 design kit from STMicroelectronics confirm the numerical value of $\left|Y^{ps}_{elec-opt}\right|$ and thus of $\left|H^{ps}_{elec-opt}\right|$ as given by (3.15) (note that the transistors dimensions are different for each f_r and therefore for each SPICE simulations as given in (3.15)). The optimization of $\left|H^{ps}_{elec-opt}\right|$ determines that $\Delta\psi$ is constant: $\Delta\psi = 0.5$ rad. It implies that the oscillation frequency is slightly shifted with the following value (here $Q = 1000$):

$$\frac{f_{osc}}{f_r} \approx 1.00025, \quad (3.16)$$

where f_{osc} is the oscillation frequency in the loop. The results of equation (3.15) for $f = f_{osc}$ are therefore also valid at f_r.

Illustration: maximum oscillating frequency for a clamped-clamped beam resonator Let us consider a capacitive clamped-clamped beam with fixed dimensions ($b = 300$ nm, $h = 160$ nm, $g = 200$ nm) and varying length. The fixed dimensions corresponds to the crossbeam measured in subsection 3.1.2. Based on section 2.2.1.2 f_r and g_{MEMS} have the following expressions:

$$f_r = \frac{\lambda^2}{2\pi} \sqrt{\frac{c_{Si}}{12\rho_{Si}}} \frac{b}{L^2}, \; g_{MEMS} = \frac{12\varepsilon_0 \eta_A \eta_D Q}{\lambda^4 c_{Si}} V^2_{DC} \frac{L^4}{b^3 g^3}. \quad (3.17)$$

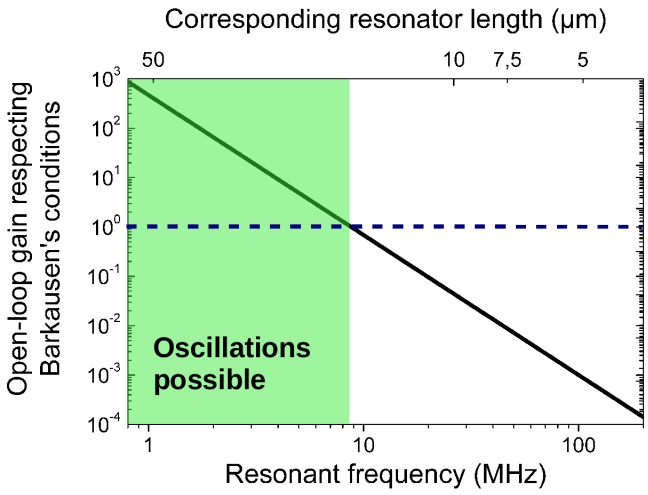

Figure 3.31: Evolution of the oscillator open-loop gain for a capacitively sensed resonator with varying length.

Self-sustained closed-loop oscillations start if: $\left(g_{MEMS} \times \left|H^{ps}_{elec-opt}\right|\right) > 1$. The maximum resonance frequency can be determined by studying the evolution of $\left(g_{MEMS} \times \left|H^{ps}_{elec-opt}\right|\right)$ versus the resonator length (figure 3.31): the maximum resonance frequency is about 8.7 MHz corresponding to a minimal beam length of 17 µm.

3.3.2.3 Sustaining electronics for a resistive resonator

Similarly to subsection 3.3.2.2, we show that for a Pierce oscillator architecture, there exist optimal transistor dimensions for M_A for which $\left|H^{ps}_{elec-opt}\left(f_{osc}\right)\right|$ is maximized:

$$\begin{cases} W_{A-opt} & \approx \sqrt[3]{\frac{9\sqrt{5}}{8}\frac{C_{load}V_E}{2\pi f_r K'_n\left[3C_{gd0}V_E+C_{ox}(V_{gs}-V_T)\right]^2 R^2_{MEMS}}} \\ L_{A-opt} & \approx (V_{gs}-V_T)\sqrt[3]{\frac{15}{8}\frac{K'_n}{(2\pi f_r)^2 C_{load}R_{MEMS}V_E\left[3C_{gd0}V_E+C_{ox}(V_{gs}-V_T)\right]}} \end{cases}, \quad (3.18)$$

where R_{MEMS} is the resonator output resistance. The resulting electronic gain is:

$$\left|H^{ps}_{elec-opt}\left(f_{osc}\right)\right| \approx \sqrt[3]{\frac{25\sqrt{5}}{72}\frac{K'_n V_E^2}{\left(2\pi f_r\right)^2 C_{load}R_{MEMS}\left[3C_{gd0}V_E + C_{ox}\left(V_{gs}-V_T\right)\right]}}. \quad (3.19)$$

The corresponding electronic supplementary phase-shift is $\Delta\psi = 1/\sqrt{5}$ rad that corresponds to an oscillating frequency of: $f_{osc} \approx 1.00024 \times f_r$.

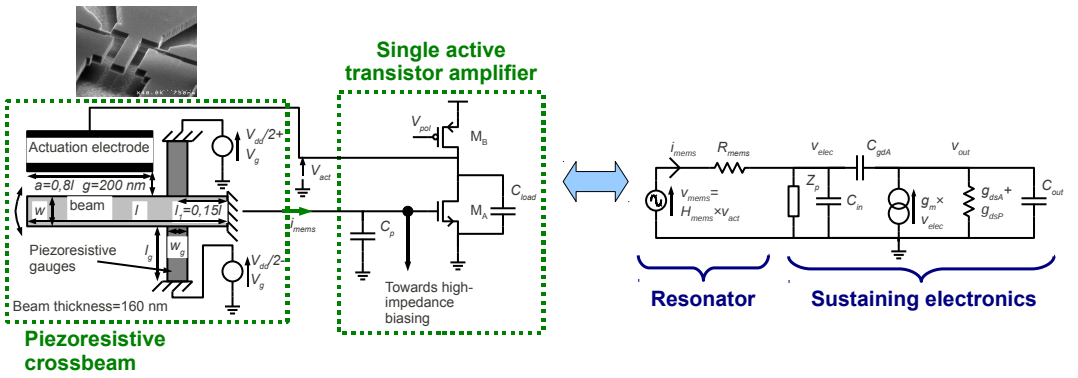

Figure 3.32: Transimpedance amplifier schematic (left) and its equivalent small signal schematic for a piezoresistively transduced MEMS resonator (right).

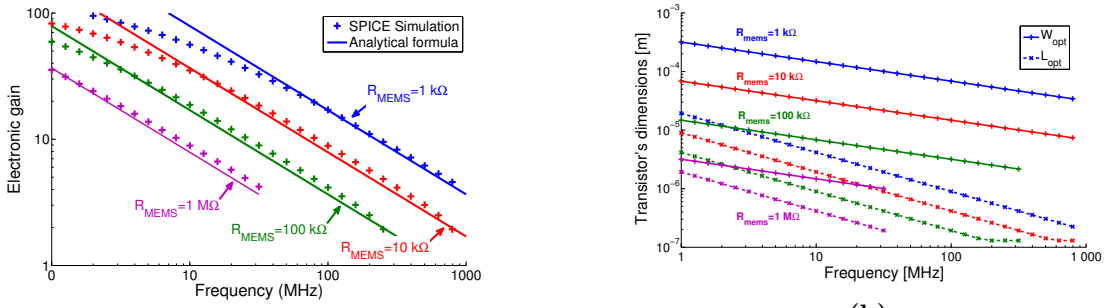

(a) (b)

Figure 3.33: (a) Comparison between the analytical formula (17) and SPICE simulations, (b) transistor dimensions

Description of the circuit Figure 3.32 shows the schematic of the piezoresistive crossbeam-based Pierce oscillator and its small signal equivalent circuit. The circuit is similar to that of the capacitance MEMS-based Pierce oscillator. The electronic circuit has the following ideal transconductance at the frequency f_{osc} if the effect of C_{gdA} , C_{in} , g_{dsA} , g_{gsP} and Z_P are negligible:

$$H_{elec}^{ideal} = \frac{v_{out}}{v_{MEMS}} = -\frac{g_m}{j2\pi f_{osc} C_{out}} \approx -\frac{g_m}{j2\pi f_{osc} C_{load}}. \tag{3.20}$$

Such an ideal circuit introduces a phase-shift of +90 and ensures the oscillations conditions (3.3) are satisfied at $f = f_r$. Similarly to the previous section, the effect of the parasite parameters (i.e C_{gdA}, C_{in}, g_{dsA}, g_{gsP} and Z_P) on the electronic transimpedance are explored.

Maximum transimpedance gain The non-ideal electronic transimpedance is:

$$H_{elec} = -\left(g_m - j2\pi f_{osc} C_{gdA}\right) / \left\{ \left(g_{dsA} + g_{dsP}\right) \left(1 + \frac{R_{MEMS}}{Z_P}\right) + j2\pi f_{osc} \left[g_m R_{MEMS} C_{gdA} + R_{MEMS} \left(g_{dsA} + g_{dsP}\right) \left(C_{in} + C_{gdA}\right) + \left(1 + \frac{R_{MEMS}}{Z_P}\right) \left(C_{load} + C_{gdA}\right) \right] - \left(2\pi f_{osc}\right)^2 R_{MEMS} \left[C_{in} C_{out} + \left(C_{in} + C_{out}\right) C_{gdA} \right] \right\}. \tag{3.21}$$

Similarly to subsection (3.3.2.2), we assume that:

- the effect of M_P can be neglected (i.e. $g_{dsP} \ll g_{dsA}$, $C_{dbP} \ll C_{load}$),
- the effect of M_A biasing can be neglected (i.e. $R_{MEMS} \gg Z_P$),
- the transistors dimensions respect 50 nm $\ll L_A \ll$ 50 µm and $W_A L_A \ll$ 15000 µm^2 so that: $C_{gdA} \ll C_{gsA}$, $C_{dbA} \ll C_{load}$, $g_m \gg 2\pi f_{osc} C_{gdA}$.

The expression of the electronic transfer function H_{elec} can then be simplified as follows:

$$H_{elec} = H_{elec}^{ideal} \frac{1}{1 + 2\pi f_{osc} \left| H_{elec}^{ideal} \right| \left(C_{gdA} + C_{in}/A_0\right) + j \left[2\pi f_{osc} C_{in} R_{MEMS} - \frac{\left| H_{elec}^{ideal} \right|}{A_0 R_{MEMS}} \right]}. \tag{3.22}$$

In order to achieve the proper phase-shift, the circuit is designed so that the output current from the MEMS resonator flows in its output impedance: $1/R_{MEMS} \gg 2\pi f_{osc} C_{in}$. This approach has two consequences:

1. The circuit can no longer operate if the resonance frequency is larger than $f_{osc} \gg 1/\left(2\pi R_{MEMS} C_{in}\right)$ because the current will flow into C_{in} and the phase-shift of the circuit will no longer respect the Barkausen conditions,
2. If the product $2\pi f_{osc} R_{MEMS}$ is low (compared to $1/C_p$), the circuit input capacitance can be increased and as a result, the transistor M_A becomes larger.

The last consequence may contradict the hypothesis taken in subsection (3.3.2.2) ($C_{gsA} \ll C_p$). In fact, for a resistive MEMS resonator, we have to assume that: $C_{gsA} \gg C_p$. As in subsection (3.3.2.2), a modified electronic gain $|H_{elec}^{ps}| = |H_{elec}^{ps}| \left(1 - \Delta\psi^2\right)$ is introduced that takes into account the reduction of the resonator gain:

$$H_{elec} = \frac{H_{elec}^{ideal}}{\left[1 + 2\pi f_{osc} \left| H_{elec}^{ideal} \right| \left(C_{gdA} + \frac{C_{gsA}}{A_0}\right)\right] \left[1 + \left(\frac{2\pi f_{osc} C_{gsA} R_{MEMS} - \frac{\left| H_{elec}^{ideal} \right|}{A_0 R_{MEMS}}}{1 + 2\pi f_{osc} \left| H_{elec}^{ideal} \right| \left(C_{gdA} + \frac{C_{gsA}}{A_0}\right)} \right)^2 \right]}. \tag{3.23}$$

Finally, one can assume that $2\pi f_{osc} C_{gsA} R_{MEMS} \ll \frac{\left| H_{elec}^{ideal} \right|}{A_0 R_{MEMS}} \Leftrightarrow \left(2\pi f_{osc} C_{gsA}\right) \times \left(2\pi f_{osc} C_{load}\right) \gg g_{dsA}/R_{MEMS}$ and therefore the phase-shift term $2\pi f_{osc} C_{gsA} R_{MEMS}$

can be neglected. Using the Berkeley level 1 model [Sansen 2006] description of the transistor M_A, the expression of $|H^{ps}_{elec}|$ can then be expressed in terms of W_A and L_A:

$$|H^{ps}_{elec}| = \frac{2K'_n \frac{W_A}{L_A} (V_{gs} - V_T) R_{MEMS}}{2\pi f_{osc} C_{load}} \Bigg/ \Bigg\{ \cdot \left[1 + K'_n \frac{W_A^2}{L_A} (V_{gs} - V_T) R_{MEMS} \left(\frac{C_{gd0}}{C_{load}} + \frac{C_{ox} (V_{gs} - V_T)}{3 C_{load} V_E} \right) \right] \times \left[1 + \left(\frac{\frac{K'_n \frac{W_A}{L_A^2} (V_{gs} - V_T)^2}{2\pi f_{osc} C_{load} V_E}}{1 + 2K'_n \frac{W_A^2}{L_A} (V_{gs} - V_T) R_{MEMS} \left(\frac{C_{gd0}}{C_{load}} + \frac{C_{ox}(V_{gs} - V_T)}{3 C_{load} V_E} \right)} \right) \right] \Bigg\} \quad (3.24)$$

By maximizing $|H^{ps}_{elec}|$ with respect to W_A and L_A, one can find the optimal parameters W_{A-opt}, L_{A-opt} and $\left|H^{ps}_{elec-opt}\right|$:

$$\begin{cases} W_{A-opt} & = \sqrt[3]{\frac{9\sqrt{5}}{8} \frac{C_{load} V_E}{2\pi f_{osc} K'_n \left[3C_{gd0} V_E + C_{ox}(V_{gs} - V_T)\right]^2 R^2_{MEMS}}} \\ L_{A-opt} & = (V_{gs} - V_T) \sqrt[3]{\frac{15}{8} \frac{K'_n}{(2\pi f_{osc})^2 C_{load} R_{MEMS} V_E \left[3C_{gd0} V_E + C_{ox}(V_{gs} - V_T)\right]}} \\ \left|H^{ps}_{elec-opt}\right| & = \sqrt[3]{\frac{25\sqrt{5}}{72} \frac{K'_n V_E^2}{(2\pi f_{osc})^2 C_{load} R_{MEMS} \left[3C_{gd0} V_E + C_{ox}(V_{gs} - V_T)\right]}} \end{cases} . \quad (3.25)$$

The evolution of $\left|H^{ps}_{elec-opt}\right|$ is depicted in fig. 3.33. SPICE simulations performed with the HCMOS9 design kit form STMicroelectronics confirm the numerical value of $\left|H^{ps}_{elec-opt}\right|$ as given by (3.15) (note that the transistors dimensions are different for each f_{osc} and therefore for each SPICE simulations as given in (3.15)). Obviously, the results presented in figure 3.33 are limited at higher frequency by $f_{osc} < 1/(2\pi R_{MEMS} C_p)$ as explained previously. For low frequencies and low R_{MEMS}, the dimensions of M_A given by (3.15) are quite large (see fig. 3.33b), in some cases greater then $L_{A-opt} > 10$ µm and $W_{A-opt} > 100$ µm. This introduces significant discrepancies between the Berkeley level 1 model and the SPICE model of the transistors which explain the errors between the analytical formula and the SPICE simulation for low frequency and R_{MEMS}. However, this inaccuracy in the model is not critical because NEMS oscillator applications (e.g. as small-dimension resonator in mass sensor) tend to require resonators with high resonance frequency and high output resistance. The optimization of $\left|H^{ps}_{elec-opt}\right|$ determines that $\Delta\psi$ is constant: $\Delta\psi = 1/\sqrt{5}$ rad. The oscillation frequency is slightly shifted by (here $Q = 1000$):

$$\frac{f_{osc}}{f_r} \approx 1.00024, \quad (3.26)$$

where f_{osc} is the oscillation frequency in the loop. Once again, the results of (3.15) for $f = f_{osc}$ are also valid at f_r.

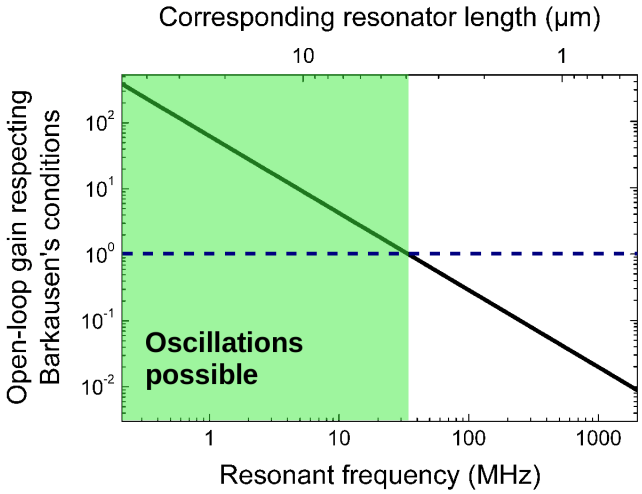

Figure 3.34: Evolution of the oscillator open-loop gain for a MEMS resonator with piezoresistive detection and a varying length (i.e. varying resonant frequency)

Illustration: maximum oscillating frequency for a piezoresistive crossbeam Consider a piezoresistive crossbeam similar to subsection 3.1.2. As with the capacitively sensed resonator, the length of the beam varies in order to sweep a given range of resonance frequency. Based on section 2.2.3, f_r and g_{MEMS} have the following expressions:

$$f_r = \frac{\lambda^2}{2\pi}\sqrt{\frac{c_{Si}}{12\rho_{Si}}}\frac{W}{L^2},\ g_{MEMS} = \frac{\varepsilon_0\gamma_{Si}\eta_A\eta_D Q}{\lambda^4 c_{Si}}V_{DC}V_g\frac{L}{W_g g^2}. \tag{3.27}$$

$R_{MEMS} = \Theta_{Si}\frac{L_g}{2hW_g} \approx 8.1$ kΩ where $\Theta_{Si} = 416$ µΩ.m is the resistivity of the silicon. $V_{DC} = 0.4$ V is the DC component of the actuation voltage, V_g is twice of the effective DC voltage applied on each piezoresistive gauge. From the subsection 3.3, self-sustained closed-loop oscillations will start if: $\left(g_{MEMS} \times \left|H^{ps}_{elec-opt}\right|\right) > 1$. The maximum resonance frequency can be determined by studying the evolution of $\left(g_{MEMS} \times \left|H^{ps}_{elec-opt}\right|\right)$ versus the resonator dimensions (figure 3.34): the maximum resonance frequency is about 35 MHz corresponding to a minimal beam length of 3.9 µm.

3.3.2.4 Conclusion of limits of Pierce oscillators

This section describes the design of a MEMS-based oscillator built around a single active MOS transistor. The paper focuses on the design of the oscillator sustaining electronics and its limitations. A simple analytical formula is provided to determine for a given MEMS resonator the maximum transimpedance gain achievable by the circuit for capacitively or (piezo)resistively sensed MEMS resonators. The formula uses the technological parameter of a Berkeley level 1 model of transistors. It can

Version	b	a	c
L	10.5 µm	14.8 µm	20.9 µm
b	250 nm	250 nm	250 nm
h	1 µm	1 µm	1 µm
g	250 nm	250 nm	250 nm
Mass	6.1 pg	8.6 pg	12.2 pg
f_r	20 MHz	10 MHz	5 MHz
g_{MEMS}	1.1	4.3	17
Z_{MEMS}	360 MΩ	30 MΩ	720 MΩ
$\|H_{connec}\|$	8.8×10^{-3}	6.2×10^{-3}	8.8×10^{-3}
Output noise	1.4 nV/$\sqrt{\text{Hz}}$	2.3 nV/$\sqrt{\text{Hz}}$	7.7 nV/$\sqrt{\text{Hz}}$

Table 3.3: Characteristics of the resonators for $V_{DC} = 5$ V.

therefore also be used to assess the performance of a CMOS process for Pierce oscillator applications. Additionally, this paper presents the study of the maximum resonance frequency achievable to fulfill the self oscillation conditions for a capacitively sensed clamped-clamped beam and for a piezoresistive crossbeam. It confirms the results announced by [Colinet 2009] and provides an expression of the electronics transimpedance gain and the associated transistor's dimensions. In the presented Pierce oscillator configuration, the minimal resonator length and therefore the maximum frequency of the MEMS-based oscillator strongly depend on the mechanical design of the resonator. It remains possible to increase the maximum oscillation frequency by reducing the beam length-to-width ratio, the gap or by increasing the resonator DC-polarization voltages. The electronic architecture exposed in the paper is well adapted to MEMS or NEMS resonator arrays since the electronics area constraint is drastically reduced. However other electronic architectures can be more competitive in terms of robustness, insensibility to parasitic signals (e.g. differential electronic), phase-noise, resonator feed-through reduction (i.e. electronics including filtering or PLL), etc.

3.3.3 2D co-integration of resonators with capacitive detection and a 0.35 µm CMOS circuit[10]

3.3.3.1 Description of the technology and the MEMS resonators

The MEMS resonator and the sustaining electronics are fabricated from the STMicroelectronics 0.35 µm-bulk process. In fact, the MEMS and the CMOS circuit are fabricated on a SOI wafer with a 1 µm layer of SiO_2 and a 1 µm top layer of silicon defining the thickness of the resonator to $h = 1$ µm. The top silicon is so thick that it has been supposed that the electrical behavior of the transistors is very similar

[10]The design of the resonators was made by Julien Arcamone

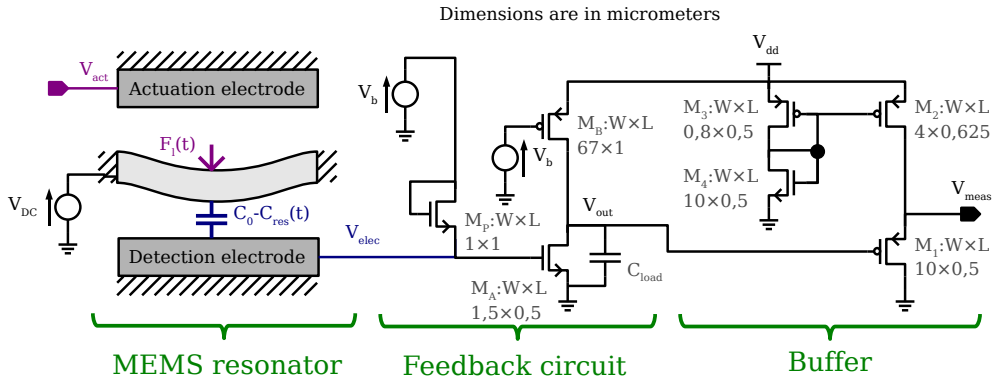

Figure 3.35: Schematic of the electronic circuit. In the Pierce oscillator configuration the node v_{out} and v_{act} are connected.

to the one fabricated on a bulk wafer. The MEMS resonator is first fabricated at CEA-LETI using a 250 nm deep ultraviolet lithography step that limits the resonator geometries. The gap is then filled with SiO_2, a CMP[11] step planarizes the wafer. The resonators are then protected and the wafer is processed in STMicroelectronics. The CMOS circuit is fabricated using standard bulk wafer process without taking into account that the fact that the substrate is SOI. The CMOS circuit being completed it is passivated and the process is completed at Leti. A series of dry-etching steps removes the dielectric layers on top of the resonator. The back-end layers of the CMOS process (oxide and metal layers) are protected using a HFO_2 deposition (a gate oxide). The resonator is then released through an HF isotropic etching.

Due the technological requirements, the thickness of the clamped-clamped beam is $h = 1$ µm. The minimal dimensions and gap of the resonators are 250 nm. From the model of the resonator described in section 2.2.1, it can be shown that the beam width and gap should be taken to its minimum: $b = g = 250$ nm. Finally, three sets of beam length are designed: one at 20.9 µm, the second at 14.8 µm and the last one at 10.5 µm. The corresponding resonance frequencies are 20 MHz, 10 MHz and 5 MHz respectively. The table 3.3 presents the characteristics of the 3 different designed resonators.

3.3.3.2 CMOS circuit design and theoretical assessment of the system[12]

Three different versions of the circuit were designed. The first one is a closed-loop Pierce oscillator. The second is identical to the first but the output of the feedback circuit is not connected to the resonator actuation electrode as depicted in figure 3.35. This open-loop configuration is implemented to study the oscillation

[11] Chemical Mechanical Planarization

[12] Catherine Bour realized the layout of the CMOS circuits. Julien Arcamone designed of the MEMS resonators, their layouts and the MEMS-CMOS connections.

Frequency	20 MHz	10 MHz	5 MHz
Gain	0.57	1.14	2.29
Phase-shift	93°	90°	90°
Input noise	46 nV/$\sqrt{\text{Hz}}$	46 nV/$\sqrt{\text{Hz}}$	47 nV/$\sqrt{\text{Hz}}$
Output flicker noise	1.7 mV/$\sqrt{\text{Hz}}$ at 1 Hz		

Table 3.4: Characteristics of the electronics circuit.

conditions. In the third version, the capacitance of the Pierce oscillator circuit is reduced so the gain of the circuit is increased. For practical reasons, the same three versions of the electronic circuit has been implemented for all the resonators. With the dimensions of figure 3.35, the transfer function of the circuit can be approximated to:

$$H_{elec}(f) \approx -\frac{g_{mA}}{j2\pi f C_{out}} \Rightarrow \begin{cases} |H_{elec}(10\text{ MHz})| & = \frac{g_{mA}}{2\pi f C_{out}} \approx 1.4 \\ \arg[H_{elec}(10\text{ MHz})] & \approx +90° \end{cases}, \tag{3.28}$$

thus the open-loop phase-shift should be close to 0°. In order to achieve an open-loop gain larger than one, V_{DC} should be larger than 24 V, 6.7 V, 2.2 V for the three resonators versions respectively.

Finally, the buffer used to charge the connection capacitance is based on a single stage topology [Sansen 2006]. The dimensions of the transistors are designed to drive an output capacitance around 5 pF that corresponds to the input capacitance (plus a margin) of a commercial amplifier connected directly to the chip.

The characteristics of the overall electronic circuit are presented in table 3.4. Note that in this simple implementation, the electronic noise dominates. The performance of the resonator embedded in the Pierce oscillator can be evaluated for a mechanical displacement of a tenth of the gap. From the model of section 2.4, the corresponding mass resolution in vacuum is theoretically equal to 1.0 ag at $T_{meas} = 0.23$ s, 4.7 ag at $T_{meas} = 0.41$ s, 22 ag at $T_{meas} = 0.74$ s for the 3 resonators versions respectively. These results are comparable with the state-of-the-art works of fully integrated MEMS resonators [Verd 2007, Verd 2008]. As discussed previously, the design of the electronics can be improved by integrating a more complex architecture with a lower input noise: it should be possible to enhance the mass resolution of the oscillator.

3.3.3.3 Layout of the Pierce oscillator

Figure 3.36 depicts an optical image of the Pierce oscillator. The total oscillator area (including the output buffer) is about 80 × 60 µm² making the oscillator an excellent candidate for arrays of sensors.

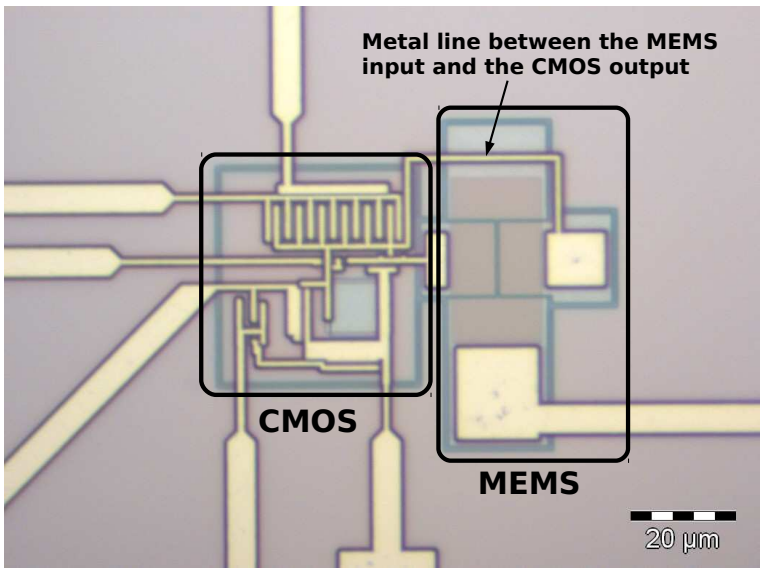

Figure 3.36: Optical image of the Pierce oscillator (the beam is not released yet).

3.3.3.4 Characterization

Stand-alone electronics The fabrication process of a first series of chips omitted the last technological steps: the protection of the CMOS circuit and the release of the MEMS resonator. Obviously, the chips were fabricated more rapidly but only the stand-alone electronic circuits could be characterized. The corresponding measurement setup is depicted in figure 3.37. The response of the electronics is characterized in terms of gain and induced phase-shift (fig. 3.38). The responses of the circuits are consistent with the simulations and thus the fully integrated MEMS oscillators should reach their theoretical performances. However it can be noticed that the buffer bandwidth is smaller than expected: this is probably due to a large connection capacitance between the buffer and the commercial amplifier (larger than 5 pF).

Co-integrated MEMS-CMOS preliminary measurements[13] A few weeks after the end of my PhD contract, some wafers including MEMS resonators co-integrated with the CMOS circuits were completely fabricated for the first time. The first successful characterizations were obtained with clamped-free beams rather than the clamped-clamped beams presented in this manuscript. The chips were tested with the measurement setup depicted in figure 3.39. The mechanical resonance of the beams was both detected under atmospheric pressure and in vacuum (fig. 3.40). The beam measured has the following dimensions: 5.9 µm-long and 250 nm-wide. The measurements under vacuum are very interesting because the signal-to-background ration is large and the open-loop gain is larger than 0 dB: it should be possible to

[13]The preliminary measurement of the MEMS-CMOS chips were made by Julien Arcamone.

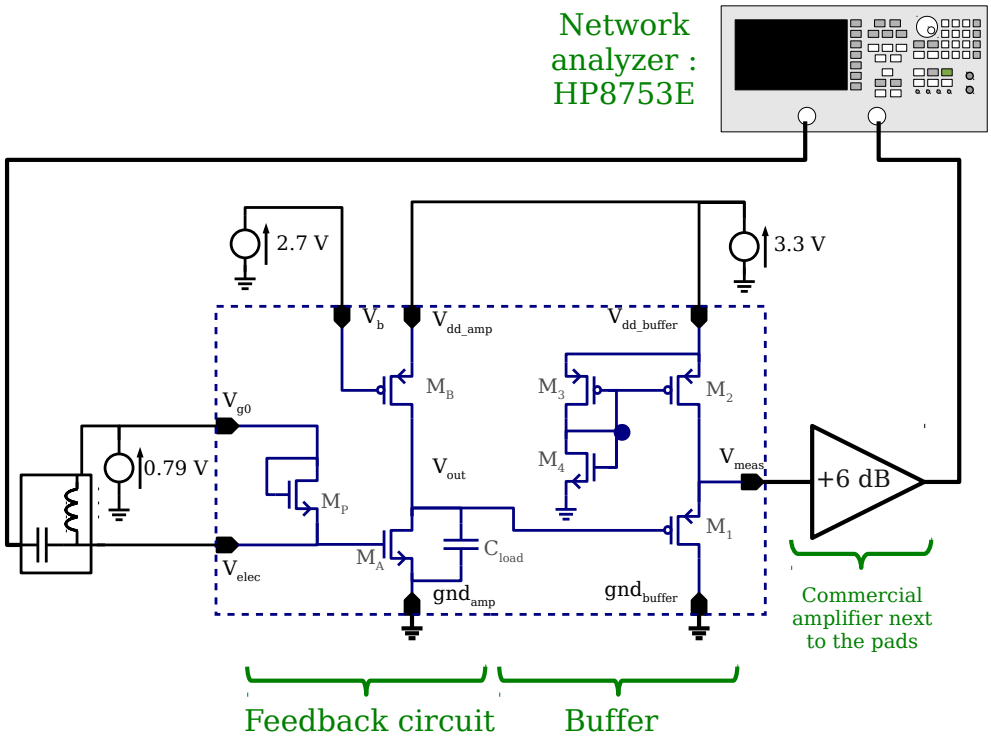

Figure 3.37: Schematic of the measurement setup for the stand-alone circuit.

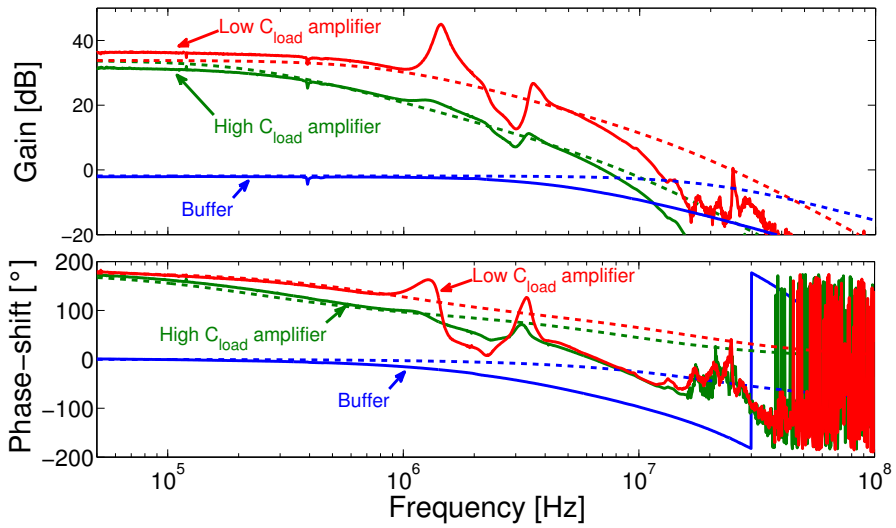

Figure 3.38: Gain of the stand-alone circuits versus frequency. The plain curves corresponds to measurements and the dash lines corresponds to simulations.

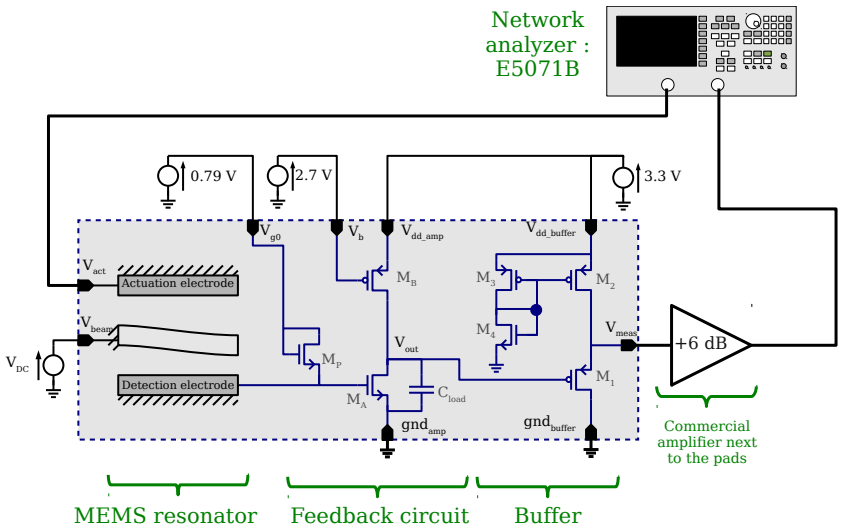

Figure 3.39: Co-integrated NEMS-CMOS measurement setup.

close the loop. In fact, the closed-loop designs are currently being tested.

These preliminary measurements demonstrate the success of the proposed integration approach and announce promising perspectives towards the realization of on-chip MEMS-CMOS oscillators with very small surface consumption. These fabricated chips are particularly interesting compared to other co-integrated chips in the literature [Verd 2006, Arcamone 2007, Uranga 2005, Lopez 2009a, Teva 2007] because the resonator are fabricated from single-crystal silicon. Moreover, the area consumption of the NEMS-CMOS pixel are very compact.

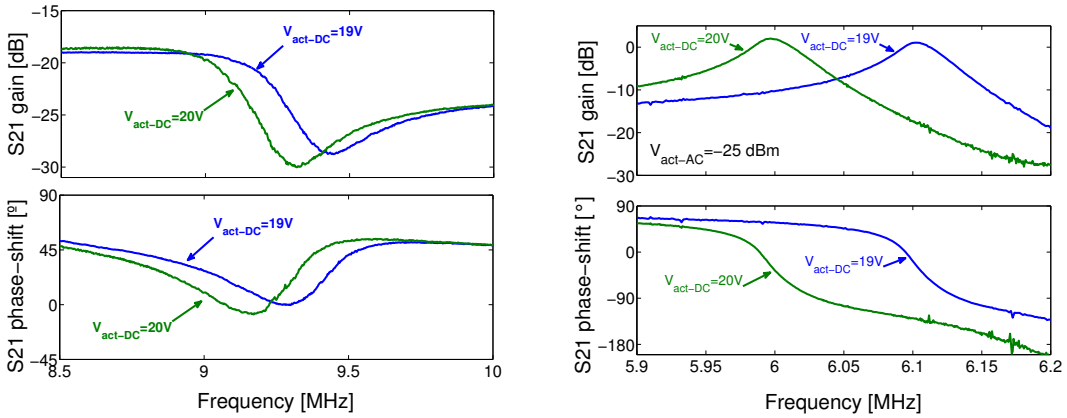

Figure 3.40: Mechanical resonance measurement of the clamped-free beam with capacitive detection under (a) atmospheric pressure, (b) vacuum.

Name	CB1	CB2	CB3	**CB4**	CB5
l	1.5 µm	1.2 µm	2 µm	**1.6 µm**	2.5 µm
w	100 nm	100 nm	100 nm	**130 nm**	50 nm
l_n	100 nm	100 nm	100 nm	**100 nm**	100 nm
w_n	50 nm	50 nm	50 nm	**50 nm**	30 nm
g	60 nm	60 nm	90 nm	**80 nm**	220 nm
Mass	16 fg	13 fg	21 fg	**22 fg**	13 fg
f_r	78 MHz	122 MHz	44 MHz	**87 MHz**	14 MHz
g_{MEMS}	0.35	0.28	0.21	**0.21**	72×10^{-3}
R_{MEMS}	2.2 kΩ	2.2 kΩ	2.2 kΩ	**2.2 kΩ**	3.7 kΩ
$\lvert H_{connec} \rvert$	0.99	0.99	1.0	**0.99**	1.0
Output noise	11 nV/$\sqrt{\text{Hz}}$	12 nV/$\sqrt{\text{Hz}}$	9.6 nV/$\sqrt{\text{Hz}}$	13 nV/$\sqrt{\text{Hz}}$	7.6 nV/$\sqrt{\text{Hz}}$

Table 3.5: Characteristics of the crossbeam when operated in vacuum (doping level $10^{19}\,\text{cm}^{-3}$). The electronics design was optimized for CB4.

3.3.4 2D co-integration of resonators with piezoresistive detection and a 0.3 µm CMOS circuit[14]

3.3.4.1 Description of the MEMS-CMOS technology and of the MEMS resonators

In this project, the electronics is designed with a FDSOI CMOS technology developed at Leti. The transistors are manufactured on a SOI wafer and are fully depleted. Their ultra-thin oxide thickness limits the supply voltage of the electronic circuit to 1.2 V. Their technology is not properly mature yet and was developed for a single metal layer. If two lines have the cross each other without contact, the polysilicon layer (used for the gate) is locally employed as a second conductive layer. This scenario is avoided as much as possible because the resistance of the polysilicon layer is much larger than the metal layer. The process uses a deep ultra-violet lithography what limits the transistor length to 0.3 µm. The thickness of the top silicon layer is 45 nm as required for the FDSOI transistors. The single-crystal MEMS resonators are realized on the same layer and are consequently very thin (among the tiniest in the literature) what should enhance the performance of the device in terms of mass sensitivity.

The possibility to implement single-crystal resonators with a 10^{19} cm^{-3} doping level makes it possible to design piezoresistive crossbeam resonators. The resonators dimensions being defined using electron beam lithography, it is possible to reach more aggressive dimensions than the ones described in subsection 3.1.2. The beam width can be as small as 30 nm and the electrode/beam gap can be as small as 60 nm. With these constraints, different crossbeam resonator were designed (see

[14]The design of the resonators was made by Julien Arcamone and Laurent Duraffourg.

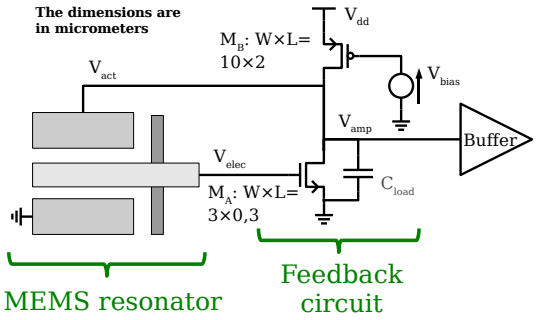

Figure 3.41: Schematic of the Pierce oscillator using a crossbeam.

Gain	+6.3 dB
Phase-shift	97°
Input noise	37 nV/$\sqrt{\text{Hz}}$
Output flicker noise	Not given by the Dkit
CB4 mass resolution	0.4 zg at $T_{meas} = 2.3$ s

Table 3.6: Characteristics of the Pierce oscillator.

table 3.5).

Similarly to the previous case, the resonators are first defined. After being released, a thermal oxidation coats the MEMS with a 10 nm thick SiO_2 layer and an isotropic deposition step of polysilicon is performed to fill the trenches. The CMOS circuit is then fabricated and passivated. Finally, the oxide layers on top of the resonator are etched and the resonators are released using an XeF_2-isotropic selective etching of the filling polysilicon layer. This novel approach is interesting because only back-end oxide should be etched to release the resonator. The release step can be made using XeF_2 etching process is very selective and the CMOS back-end layers are not degraded during the release (as opposed to HF release).

3.3.4.2 CMOS circuit design and theoretical assessment of the system

Different electronic topologies were implemented with the crossbeams. First, a Pierce oscillator was designed to operate in closed-loop configuration. A voltage amplifier was also designed that presents a large amplification gain and a low input capacitance. As opposed to the previous project, it was decided to design the amplifier with optimized dimensions in order to achieve a large gain, high bandwidth and low-input noise.

Pierce oscillator using a crossbeam resonator The electronic architecture of the oscillator is similar to the one of the previous project; only the dimensions of the transistors and of the capacitance differ. For practical reasons, we have chosen to implement the same transistor geometries for all crossbeams of table 3.5 and C_{load} is adjusted to ensure that the open-loop gain is in-between 1 and 2.

With the model of section 2.4 and assuming that the beam displacement is a tenth of the gap, the theoretical mass resolution for the different crossbeam of table 3.5 is 0.4 zg in 2.3 s, 0.2 zg in 1.5 s, 0.6 zg in 3.0 s, 0.3 zg in 1.3 s and 1.0 zg in 7.4 s respectively. The mass resolutions are close to the state-of-the-art. However, it is

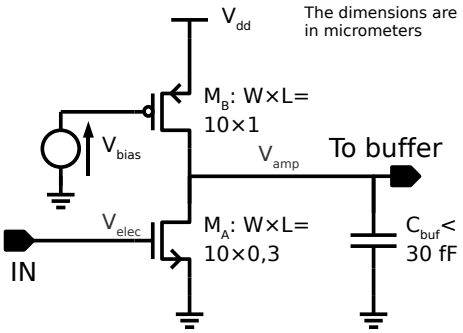

Figure 3.42: Schematic of a voltage amplifier.

Parameter	Value
Gain	35 dB
Bandwidth	330 MHz
Input noise	19 nV/$\sqrt{\text{Hz}}$
Input capacitance	290 fF

Table 3.7: characteristics of the voltage amplifier.

believed that they should be 2 orders of magnitude larger than the predicted ones because of the large anomalous flicker noise measured in subsection 3.1.2.

Voltage amplifier for an open-loop configuration The characteristics of the Pierce oscillator show that the dominant noise in the loop is introduced by the electronics. Thus, it was decided to design another circuit so that its input noise can be smaller. Although the gain and phase conditions in the Pierce oscillator restrain the geometry of the transistors, it is possible to design a dedicated amplifier with larger transistors and with no loading capacitance and thus to reduce the electronics input noise (fig. 3.42). The NMOS transistor amplifies the input circuit while the PMOS transistor acts as a DC current source.

The dimensions of the transistors were designed as follows. First the amplifier gain increases with the length of M_A. It was however simulated that with the minimum length of the technology (0.3 µm), a gain larger than 30 dB can be achieved what is enough. The transistor length was thus set to its minimum value. The width of the transistor is then determined from a trade-off between a low-noise and a low input capacitance. The length of M_B is set larger than L_A so that it introduces a little gain reduction. The width of M_B is then determined from the required biasing current of M_A.

With the dimensions given in figure 3.42, the characteristics of the amplifier are given in table 3.7.

Buffer Based on resonators characteristics, one wants to design a 100 MHz output buffer. In this project, the buffer is designed to drive an output capacitance of 100 pF as opposed to the previous project where the buffer was designed for an output capacitance of 5 pF. A capacitance of 100 pF corresponds to coaxial cables of 1 m and thus the measurement of the chip is more simple. With this constraint, the dimensions of the corresponding transistors are very large and thus introduce a large buffer input capacitance: typically in the order of 1 pF. In this scenario, the

buffer input capacitance would be too large for the designed electronic amplifiers. We have therefore designed a three-stage buffer that progressively adapts the impedance as depicted in figure 3.43. The two first stages charge the input capacitance of the last buffer stage while introducing a low input capacitance: typically smaller than 30 fF. The biasing stage acts as a high pass filter removing the DC voltage created by the amplifier circuit and properly biases the first buffer stage.

From simulations, the flat-band gain of the circuit is about −6 dB and its bandwidth is about 63 MHz.

3.3.4.3 Layout of the Pierce oscillator

Figure 3.45 presents an optical image of the Pierce oscillator. The Pierce oscillator area (excluding the output buffer) is smaller than 30×20 µm² (without optimization) making the oscillator an excellent candidate for arrays of sensors. The buffer area can be excluded in this assessment because in future MEMS-CMOS systems, the oscillation frequency could be counted digitally on the chip, avoiding the use of such buffers.

3.3.4.4 Characterization

Stand-alone electronics The electrical characterization of the electrical test structures (transistors and capacitances) of the CMOS process has revealed a large difference in the threshold value of the transistors. The absolute value of the NMOS and the PMOS threshold voltage increases by 50 − 200 mV. Moreover, the saturation current is larger than expected for the NMOS transistor but lower for the PMOS voltage. The behavior and the performance of the circuits should therefore be affected.

The buffer and the buffer+voltage amplifier were first characterized using the measurement setup depicted in figure 3.46. The frequency response of the buffer and the buffer+voltage amplifier is depicted in figure 3.47. In order to achieve an electronic gain larger than one, the voltage supply of the amplifier stage is increased because the threshold voltage of the transistors was measured larger than in the model of

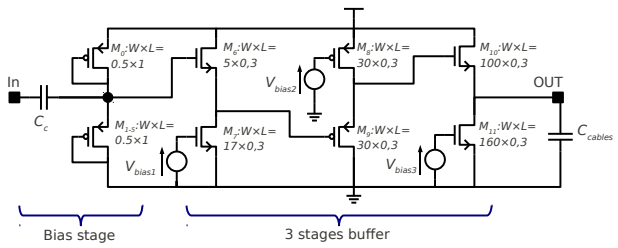

Figure 3.43: Schematic of the high-frequency buffer.

Parameter	Value
Gain	−6 dB
Bandwidth	63 MHz
Input capacitance	4 fF

Figure 3.44: Characteristics of the high-frequency buffer

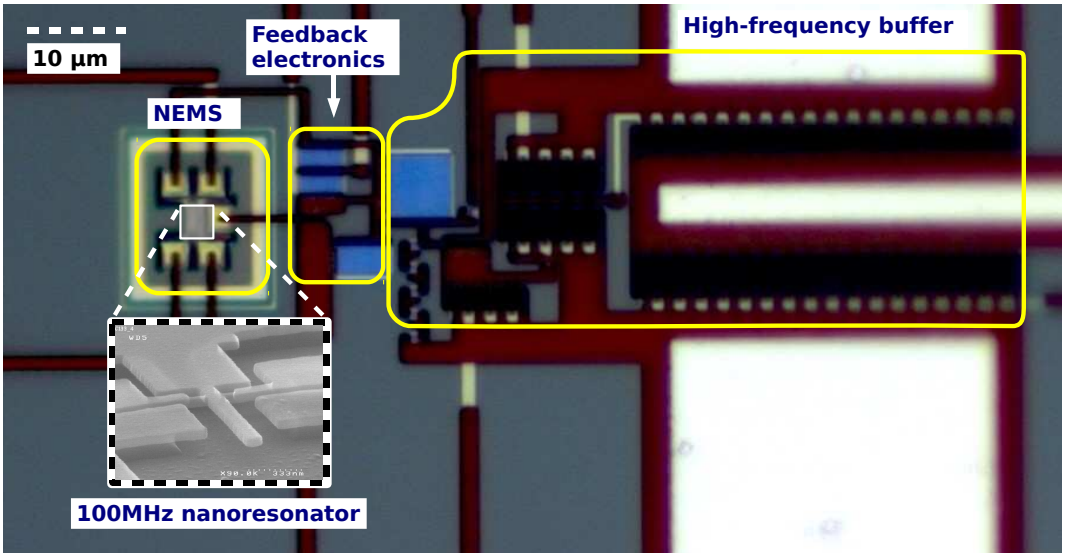

Figure 3.45: Image of the Pierce oscillator, the inset depicts the nanoresonator captured with a scanning electron microscope.

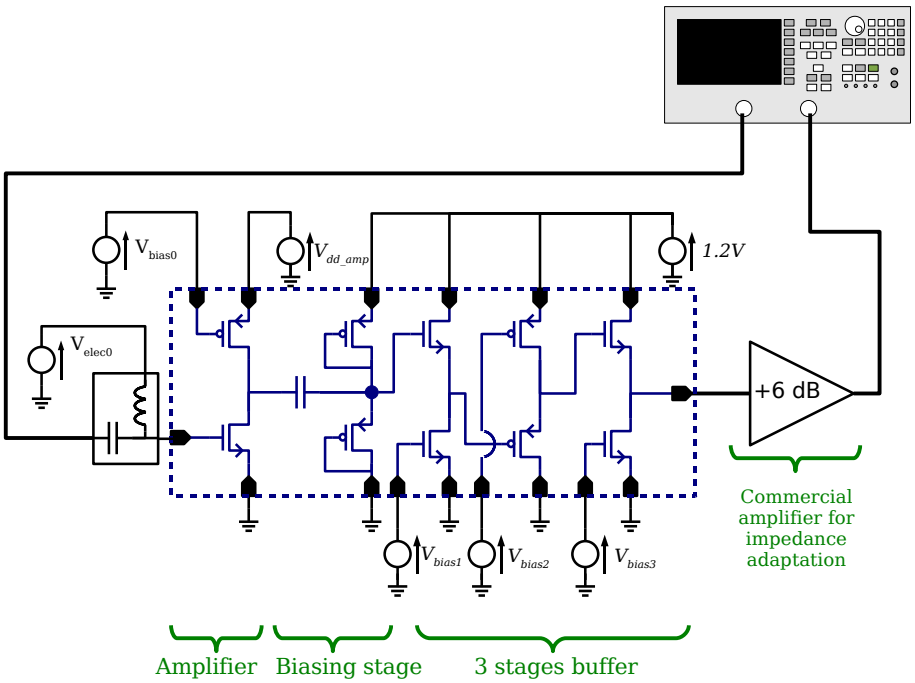

Figure 3.46: Measurement setup for the stand alone circuits.

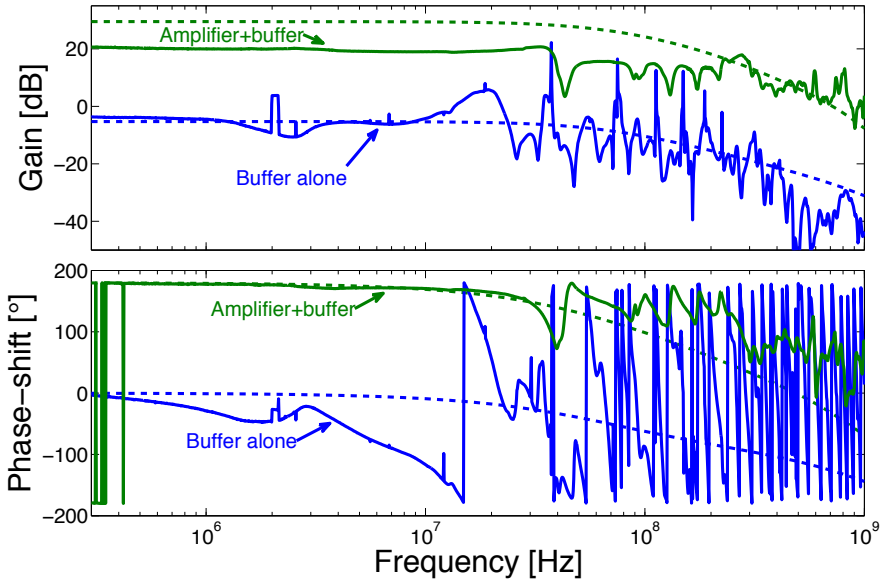

Figure 3.47: Gain of the stand-alone circuits versus frequency. The plain curves correspond to the measurements and the dash lines corresponds to the simulations.

the design kit. The DC voltage applied to the buffer and the biasing stage remain in the typical range defined by the simulations.

At high frequencies, the peaks in the electronic gain are due to electric resonances in the measurement cables and in the electrical pads. In fact, the amplifier+buffer was bonded to a support and thus the pads were not used in this measurement. The peaks are reduced in the response of the amplifier+buffer compared to the buffer response. The large phase rotations in the buffer phase-shift response introduced by the buffer are due to some delay introduced by the cables. Once again, the bonded amplifier+buffer chip presents better results as the calibration of the measurement is of a better quality. However one can see that the buffer gain corresponds to the simulations. The gain of the amplifier+buffer is however lower than the value given by the simulations. It is believed that it is due to process variations (e.g. the variation in the saturation current of the transistors). The gain remains large and compensates the connection losses that would appear in the case of a stand-alone resonator.

The electric response of the CMOS circuits are sufficient to characterize the nanoresonators. It is however clear that further process engineering are necessary in order to realize a repeatable NEMS-CMOS co-integrated chip. Only under this condition, the CMOS circuit can be made more complete including a reliable feedback circuit, a frequency counter and a communication protocol.

Co-integrated MEMS-CMOS preliminary measurements In the last months of my PhD project, the wafers including nanoresonators co-integrated with the elec-

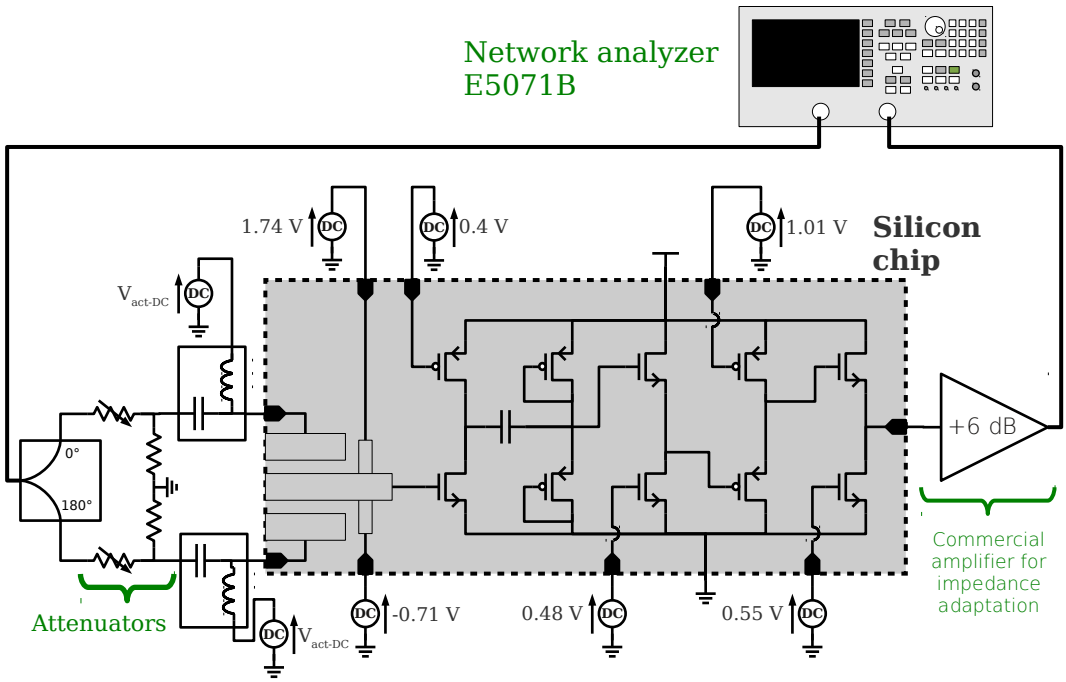

Figure 3.48: Co-integrated NEMS-CMOS measurement setup.

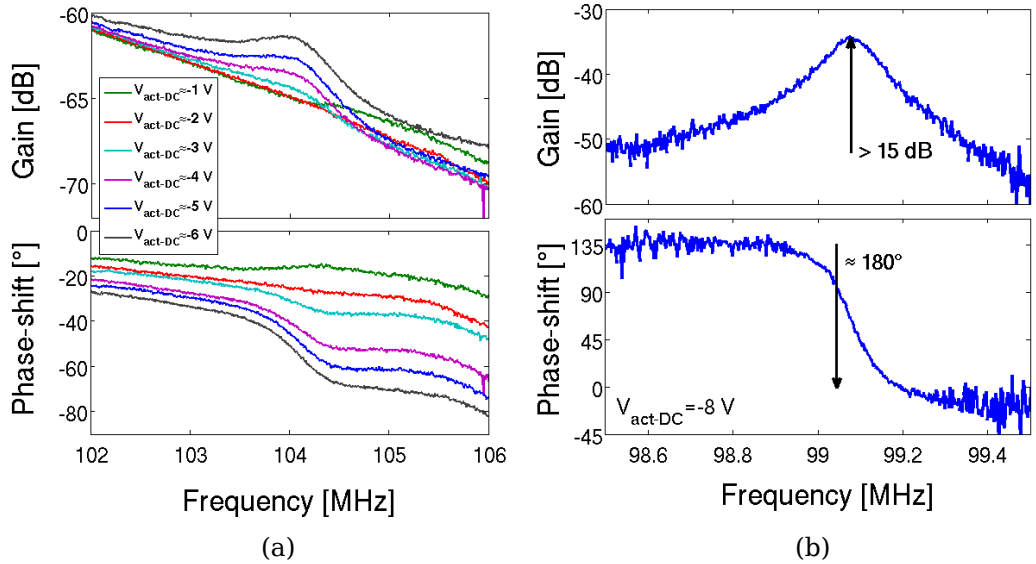

Figure 3.49: Mechanical resonance measurement of the crossbeam under (a) atmospheric pressure, (b) vacuum.

tronics were fabricated. It was shown that only the CB2 crossbeam could be released due to a process error: the beam of the other resonators have all been stuck on the bottom silicon layer during the BOX etching.

The first measurements of such nanoresonators were operated with the circuit including the voltage amplifier. Such systems were measured using a homodyne detection with a differential actuation. Figure 3.48 describes the measurement setup employed to acquire the mechanical resonance of the crossbeam. Figure 3.49 depicts the mechanical resonance of the MEMS-CMOS system either in atmospheric pressure or under vacuum. One can see on the measurements in atmospheric pressure that the mechanical response emerges out of the background when the absolute value of the DC actuation voltage increases. These measurements are the first reported in the literature whereby the mechanical resonance of such light (5.6 fg) and small resonators ($1.2 \times 0.08 \times 0.025$ µm^3) is acquired under atmospheric pressure and using a homodyne detection. If the co-integrated nanoresonator is measured under vacuum, the mechanical resonance is clearly observed. The signal-to-background ratio is larger than 15 dB (close to 20 dB) and the phase-shift response is close to the one of a Lorentz function.

To the author's knowledge, the presented results are the only measurement of nanoresonator with a piezoresistive detection and co-integrated with a compact CMOS circuit at very high frequency ($\approx$ 100 MHz). In fact, this particular piezoresistive detection seems necessary to measure, using a homodyne detection scheme, a nanoresonator with a very high resonant frequency and low dimensions.

Unfortunately, the open-loop gain of the tested devices is too small to implement the devices in an on-chip closed-loop. It is however considered that the buffer stage might largely attenuate the gain of the MEMS-CMOS chip and the open-loop gain at the amplifier output (before the buffer) of the designed Pierce oscillator might be larger than to one measured. Such structures have not been tested yet by lack of time.

3.3.5 3D co-integration of resonators with piezoresistive detection and a 30 nm CMOS circuit[15]

The 3D integration of a MEMS resonator above an integrated circuit makes possible to fabricate the circuit independently from the MEMS resonator. The electronic circuit can then be fabricated with a standard CMOS process and the MEMS process can be adjusted independently. In fact, the 3D-integration of the resonator with a CMOS circuit seems the most relevant integration scheme for arrays of MEMS resonator.

Name	CB1	CB2	CB3	CB4
L	5 µm	4 µm	3 µm	2 µm
b	200 nm	200 nm	200 nm	200 nm
L_g	550 nm	550 nm	550 nm	550 nm
b_g	100 nm	100 nm	100 nm	100 nm
h	150 nm	150 nm	150 nm	150 nm
g	200 nm	200 nm	200 nm	200 nm
f_r	14 MHz	22 MHz	39 MHz	88 MHz
Mass	350 fg	280 fg	210 fg	140 fg
G_{MEMS}	50×10^{-3}	40×10^{-3}	30×10^{-3}	20×10^{-3}
R_{MEMS}	0.8 kΩ	0.8 kΩ	0.8 kΩ	0.8 kΩ
$\|H_{connec}\|$	1	1	1	1
Output noise	8.7 nV/$\sqrt{\text{Hz}}$	9.5 nV/$\sqrt{\text{Hz}}$	10.8 nV/$\sqrt{\text{Hz}}$	12.9 nV/$\sqrt{\text{Hz}}$

Table 3.8: Characteristics of the four different crossbeams implemented with a CMOS circuit . The doping level of 2×10^{19} cm^{-3} and the value of H_{connec} is based on the input capacitance determined in the ASIC design.

3.3.5.1 Description of the technology and the MEMS resonators

In this 3D technology, the CMOS circuits are first fabricated according to a 30 nm CMOS design kit with two metallic layers. The ultra-thin oxide thickness of the technology limits the supply voltage to 1 V. Once the CMOS process is completed, a reverse SOI wafer is bounded on top of the dielectrics of the CMOS wafer. The bulk and the buried oxide are then grinded until reaching the top silicon layer. The crossbeam resonators are fabricated on the silicon top layer whose boron doping level is around 10^{19} cm^{-3} with the 4 sets of dimensions given in table 3.8. Windows are opened above all MEMS resonators in order to remove the dielectrics above the crossbeam by dry etching. Unlike other examples of monolithic integration (the 2D-integration previously presented), the key point here is that the buried sacrificial oxide and the top dielectrics have comparable etching rates since both are deposited oxides. The nominal release distance being 150 nm (half beam-width plus a 50 nm margin), the openings in the dielectrics are separated from any metal line by at least 2.5 µm in order to ensure sufficient margin avoiding any damage of the metal lead.

3.3.5.2 Design of the CMOS circuit and theoretical assessment of the system

A very short timeframe (less than a month) could be allowed to this project. This is way, the strategy employed has been to design a simple electronics in an open-loop configuration. The electronic design is organized as follows: first the dimensions of the buffer's transistors are determined in order to charge the connection capacitance

[15]The resonators design was made by Julien Arcamone

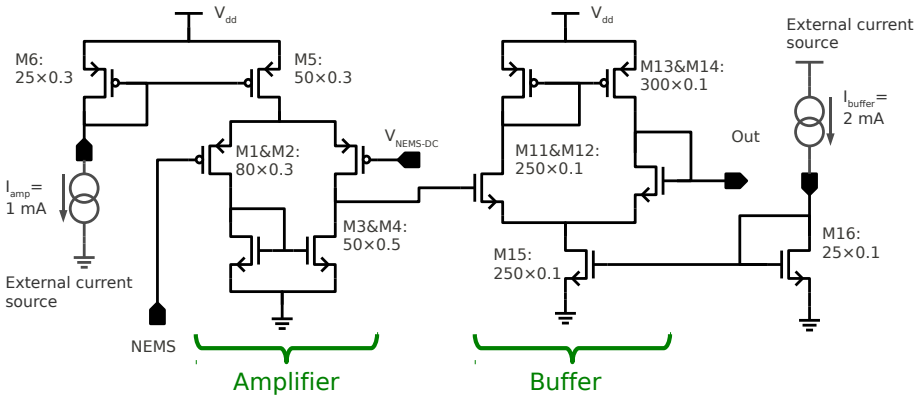

Figure 3.50: Schematic of the 3D-integrated ASIC. The dimension (width and length) of the transistors are in micrometers.

($\approx$ 100 pF). The input capacitance of the buffer was then measured and the amplifier is designed so that it could charge the buffer's input capacitance. It has been assumed during the electronic design that the input capacitance of the amplifier is small so the connection losses are negligible. Finally the amplifier and the buffer are both biased with independent external current sources.

This methodology has the advantage of rapidly designing the electronics. However the design of the first amplifier is not based on the characteristics of the resonator but on the buffer's ones. It will be shown that the electronic noise is comparable to the resonator's output noise.

Buffer design The buffer architecture is based on an operational amplifier whose output and the minus input are connected. The differential architecture was chosen over the non-differential architecture (like on the previous projects) because this topology is less sensitive to the DC voltage at its input [Gray 2001]. However it requires a third transistor between the supply voltage and the ground and is therefore more sensitive to a variation of the threshold voltage of the transistors.

The dimensions of the transistors M_{11}/M_{12}, and M_{13}/M_{14} are equal by pairs. It ensures that the output signal is close to the input signal while being capable to drive large capacitance. In order to achieve a bandwidth of $f_{buf} = 100$ MHz, the biasing current is determined to be $I_{buffer} = 2 \times 10$ mA. The saturation voltage of the transistors M_{11}/M_{12}, $V_{dssat11} = 0.1$ V, is set on purpose to a low value in order to reduce I_{buffer}. To achieve $I_{buffer} = 2 \times 10$ mA with $V_{dssat11} \approx 0.1$ V, the aspect ratio of M_{11} and M_{12} must be larger than: $\frac{W}{L} > 2500$ (determined from simulations). The length of M_{11} and M_{12} is taken to $L_{11} = 0.1$ µm what minimizes the area occupied by the transistors while ensuring a proper copy of the buffer input voltage. The corresponding input capacitance of the buffer is around $C_{buf} = 1$ pF (with a margin). The transistors M_{13} and M_{14} must be designed for $V_{dssat13} < 0.25$ V while $I_{13} = 10$ mA. Increasing $V_{dssat13}$ allows reducing the

Parameter	Electronics			
	Gain	Bandwidth	Input capacitance	Input noise
Value	23 dB	106 MHz	150 fF	14 nV/$\sqrt{\text{Hz}}$

Overall characteristics				
Resonator	CB1	CB2	CB3	CB4
SNR at $f_r/(2Q)$	109 dB	116 dB	126 dB	130 dB
Mass resolution	4.8 zg	2.5 zg	1.1 zg	0.5 zg

Table 3.9: Characteristics of the 3D-integrated ASIC.

aspect ratio of the corresponding transistor for a given biasing current: it leads to $\frac{W}{L} > 3000$. The transistor M_{15} must respect the following aspect ratio: $\frac{W}{L} > 2500$. The transistors M_{15} and M_{16} are implemented in a current mirror configuration so that M_{15} acts as a current source. With an aspect ratio of M_{15} 10-times larger than M_{16}, the DC-current flowing into M_{15} is 10 times larger than M_{16}. This scaling was chosen in order to reduce the power consumption and the size of the paths in the layout.

As a matter of fact, because the supply voltage of the technology is so low ($V_{dd} = 1V$) and the threshold voltage is quite high ($V_{T-NMOS} \approx 0.5V$), it is difficult to design an upstream amplifier circuit with an NMOS input transistor. Therefore the input transistor of the previous block should be PMOS.

Amplifier design The circuit topology depicted on figure 3.50 amplifies the voltage difference between the MEMS output voltage and a DC voltage $V_{MEMS-DC}$. $V_{MEMS-DC}$ is set by an external voltage source so that it is equal to the MEMS DC output voltage. From simulations, it was determined that the active transistor should have a gate length larger than $L = 0.3$ µm so that the amplifier gain is larger than $G_{amp} > 15$. In order to achieve an amplifier bandwidth larger than 100 MHz, the transistor width and its corresponding biasing current should be larger than $W_1 \geq 80$ µm and $I_1 \geq 1$ mA respectively. The other transistors are designed accordingly to M_1/M_2 and their corresponding current consumption and so that the other transistors do not introduce a gain reduction.

Characteristics of the MEMS+CMOS systems The table 3.9 shows how the CMOS circuit (amplifier + buffer) behavior fulfills the requirements in terms of gain ($>$ 20 dB) and bandwidth ($>$ 100 MHz). The simulations shows that the circuit input noise is lower than 14 nV/$\sqrt{\text{Hz}}$ in the frequency range $[0.5, 100]$ MHz. With these circuit characteristics, the corresponding signal-to-noise ratio and the theoretical mass resolution of the sensor is determined: the mass resolution is close to the state-of-the-art but again, the issue encountered in subsection 3.1.2 might degrade in practice the theoretical results.

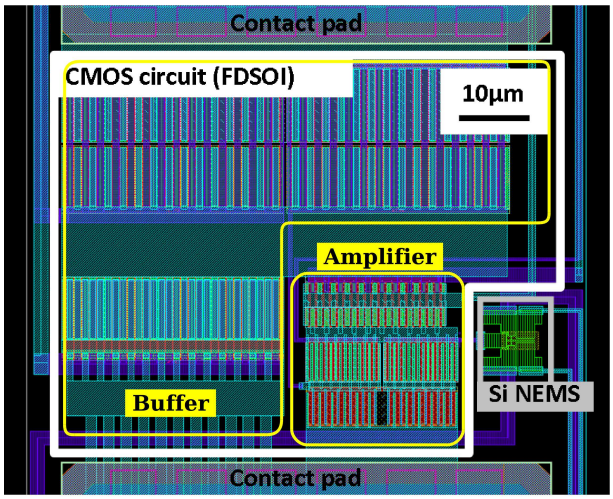

Figure 3.51: Layout view of a crossbeam 3D-integrated with its readout circuit

3.3.5.3 Layout of the resonator+ASIC

The figure 3.51 presents the layout of the crossbeam resonator 3D-integrated with the CMOS circuit. The differential amplifier is located next to the resonator and the buffer covers the rest of the area between the two contact pads. Overall the total area occupied by the resonator and the readout circuit is around 100×100 µm^2. The area covered by the amplifier is however similar to the one occupied by the crossbeam resonator and thus highlights the interest of 3D-integration for arrays of sensors. In fact, in the future, they could even be superposed to optimize the space occupation.

3.3.6 Conclusion of MEMS/CMOS co-integration

This section presents three implementations of MEMS co-integrated with CMOS circuitry, progressing from the simplest integration scheme (2D-integration of a capacitively detected MEMS) to more complex fabrication processes (3D-integration of piezoresistively detected MEMS). The design of the electronic circuit was kept simple to compensate for eventual process vagaries. Several electronic designs were compared in order to establish the most suitable architecture. The CMOS circuits characterized in the different projects are functional but their performances are somewhat lower than that predicted in the simulations.

The 2D co-integration of a capacitively detected MEMS based on a mature CMOS process has electrical characterics very similar to the simulations. The CMOS process was thus only marginally affected by the modification introduced by the MEMS fabrication. This opens the possibility of designing more complex electronic circuitry in order to fabricate complete sensors or array of sensors. The 2D co-integration of

Realization	f_r	Responsitivity	MEMS material	MEMS-CMOS pixel area
2D co-integration of a capacitively detected MEMS	**6 MHz**	1.2 Hz/ag	Single-crystal silicon	$\approx 80 \times 60$ µm^2
2D co-integration of a piezoresistively detected MEMS	**100 MHz**	4700 Hz/ag	Single-crystal silicon	$\approx 30 \times 30$ µm^2
3D co-integration of a piezoresistively detected MEMS	88 MHz	310 Hz/ag	Single-crystal silicon	$\approx 30 \times 30$ µm^2
2D co-integration of a capacitively detected MEMS in [Verd 2006]	**60 MHz**	1.9 Hz/ag	Aluminium	NI
2D co-integration of a capacitively detected MEMS in [Uranga 2005]	**100 MHz**	12 Hz/ag	Polysilicon	$\approx 300 \times 300$ µm^2
2D co-integration of a capacitively detected MEMS in [Teva 2007]	**182 MHz**	98 Hz/ag	Polysilicon	$\approx 300 \times 300$ µm^2

Table 3.10: Comparison of the characteristics of the different co-integrated systems.

a piezoresistive detected MEMS process, however, was more affected by the technological adaptations. Additional process engineering is thus required to obtain a more complete and reliable product.

The MEMS-CMOS preliminary measurements show that with a 2D co-integration scheme, it is possible to measure the mechanical response of a 100 MHz-nanoresonator using a homodyne detection. Indeed, implementing the resonator close to the electronics reduces both the connection losses and the feed-through transmission. Although further measurements are needed, the realization of complete closed-loop SOL seems possible because in this case, the actuation electrodes are removed.

Table 3.10 summarizes the characteristics of the 3 co-integrated designs presented in the manuscript. It also compares them to different realizations described in the literature. One can see that the capacitively detected resonator realized is original because it is fabricated from single-crystal silicon (what should enhance its quality factor) and because the area consumption of the MEMS-CMOS pixel is very small. Its performance expressed in terms of responsitivity is however limited and is difficult to improve because of the issues raised by the capacitive detection (issue detailed in sections 2.4 and 3.3.2). Piezoresistive detection on the other presents a high detection gain and a low output impedance that permit to fabricate light nanoresonators with high resonant frequency.

3.4 Conclusion

This chapter focused on designs and characterizations of self-oscillating loops, from the proof-of-concept of a single oscillator to integrated sensors that can be implemented in arrays. The former uses stand-alone MEMS resonators self-oscillated with discrete electronics. The overall area of the sensors is around 200×200 mm^2 (without optimization) making it difficult to implement the sensors in large arrays.

The first work related to piezoelectric cantilevers showed that it is possible to realize self-oscillating loops despite the large intrinsic feed-through inherent to such components. Different techniques for estimating the frequency resolution have been compared and the pros and cons of each were detailed. Overall, the frequency resolution of the self-oscillation loops is degraded compared to that of the frequency-locked loop probably due to the large feed-through at lower frequencies. In general, because of its low piezoelectric layer thickness and high frequency resolution, the resonator shows a true potential for gas sensing with 10 ppb resolution for DMMP vapors. The second self-oscillating loop uses a crossbeam resonator that should have an excellent mass resolution. To design a crossbeam-based SOL required investigation of different feed-through reduction techniques. This oscillator uses simple electronics and has a frequency resolution similar to that of more complex measurement setups composed of an FLL-architecture with a downmixing implementation. The major noise sources in the loop were characterized and compared to the closed-loop phase-noise. Close to the carrier, the phase noise is dominated by flicker noise that limits the frequency resolution of the sensors. The origin of this noise remains unclear and is under investigation. Overall, the latter sensor has a performance close to the state-of-the-art of mass measurements and with faster response times.

In the second section, the design of an ASIC is described. This circuit addresses multiple crossbeam resonators and comprises 4 self-oscillating loops and their associated frequency counters. The proposed implementation makes it possible to monitor 4 or more sensors in a compact area. The problems associated with coupling between the sensors can be assessed because each oscillator can be deactivated and its oscillating frequency can be measured in series or in parallel. Each self-oscillating loop is composed of an analog front-end that amplifies and filters the resonator output signal. The amplified signal was digitized in order to use a delay-lock loop as a phase-shifter. The architecture allows the phase-shift to be adjusted finely and independently of the frequency. The oscillation amplitude is also controlled with ease by the supply voltage of the digital electronics. Finally, the ASIC was fabricated as a proof of concept so that similar circuits can be monolithically integrated with the MEMS resonator.

The last section focused on the monolithic integration of MEMS resonators with their readout electronics. It describes three different projects in which the MEMS component is fabricated next to the CMOS circuit (2D-integration) or above it (3D-integration). The prospect of fabricating compact sensors composed of the

resonators and the feedback electronics is explored. The area consumption of the sensors is 100×100 µm^2 or less and respects the requirements of arrays of sensors. The tested circuits were all functional but their performances varied. The results demonstrate that the modifications introduced in the CMOS fabrication do not affect the viability of the circuit. The preliminary measurements of MEMS-CMOS components are satisfactory but further work is required to reduce the feed-through transmission so as to operate the resonator in a closed-loop. The presented fully integrated MEMS-CMOS structures are therefore the first steps towards the realization of large arrays of MEMS-based sensors.

General conclusion

During my three years of PhD studies, I explored the use of MEMS resonators in applications that require precise measurement of physical properties. This promising research field involves several scientific domains. To fabricate a sensor from a MEMS resonator, the architecture of the overall system (composed of the MEMS component and the complementary electronics) must be analyzed; the design of the electronics and the mechanical resonator must be optimized; and finally, the inherent practical constraints imposed by the fabrication and characterization process must be surmounted.

In the first chapter, I summarize the requirements and performance of different architectures that can monitor the resonant frequency variations of a MEMS component. Even though my PhD focuses on MEMS resonators (as they are used for mass sensing) this chapter is common to all micro- or nanoresonators. I established that in order to obtain a sensor with a large dynamic range, a closed-loop architecture is required to dynamically track the resonant frequency of the MEMS component. Two major closed-loop architectures are described in the literature: self-oscillating loops and frequency-locked loops. My research focused on self-oscillating loops because their architecture is more compact and better suited to the fabrication of arrays of sensors. In the same chapter, I present the limitations and the constraints imposed by this architecture. Certain aspects of the feed-through and the non-linearity had previously been considered problematic. I confirm this by demonstrating that the feed-through not only degrades the frequency resolution of the sensors but also can make the oscillator unstable. In addition, the non-linearity introduced by the resonator or electronics can amplify the colored noise around the carrier. The last section of the chapter describes different frequency measurement techniques, their operation principles and the advantages and disadvantages of each technique.

The second chapter focuses on the MEMS topologies and implementation schemes that are suitable for mass spectrometry. I describe four MEMS resonators: (i) a clamped-clamped beam with electrostatic actuation and capacitive detection, (ii) a clamped-clamped beam with electrostatic actuation and piezoresistive detection, (iii) a resonator with the shape of a crossbeam, an electrostatic actuation and a piezoresistive detection, and (iv) a cantilever with piezoelectric actuation and detection. I assess their electromechanical transduction and their theoretical mass resolution. In order to properly compare the performances of each MEMS resonator, the MEMS-to-electronics connection was incorporated into the model. I describe three major integration schemes: stand-alone resonators, and 2D- or 3D-integration

of MEMS and electronics. Each integration scheme is electrically modeled from a typical layout design to assess its feed-through and its connection losses. The electrical model leads to analytical formulae that were verified by electrical simulations. The stand-alone fabrication process was found to have the worst performance but it is the cheapest. On the other hand, the 2D-integration fabrication process has few electrical limitations but its technological development is often too expensive for industrial applications.

Piezoresistive crossbeams and piezoelectric resonators have the best mass resolutions. The crossbeam benefits from a more complex mechanical structure than classic beams which improves its piezoresistive detection. The piezoelectric cantilever benefits from a linear electromechanical transduction scheme with high gain but its technological stack can be expensive to develop. In the last section of the chapter, I analyze the benefits of implementing an array of parallel and collectively addressed resonators. Although it is commonly assumed that implementing MEMS resonators in parallel arrays reduces the phase-noise of the array (compared to that of a single resonator), I show that the circuit introduces an electrical limit. This limit must be evaluated to properly assess the performance of such an array.

In the last chapter, I describe the designs and practical realizations made during my PhD project. I first present the construction and characterization of a self-oscillating loop using stand-alone resonators (a piezoelectric cantilever and a crossbeam) and commercial electronic components. A major difficulty with the piezoelectric cantilever is the V-shaped feed-through behavior which requires careful filtering to prevent parasitic oscillations in the loop. The frequency resolution was then measured with different techniques, each having their pros and cons. The frequency resolutions measured with the different techniques are similar but lower than those obtained with an FLL-architecture. With the latter architecture, the MEMS resonator produced good performance for gas sensing: a resolution of 10 ppb was achieved for DMMP vapors. The difference in frequency resolution between the two architectures is believed to be due to the large feed-through at low frequency that accentuated the noise. This oscillator yields practical information on how to construct a low-cost gas sensor. The second self-oscillating loop uses a crossbeam resonator. The major challenge in the design of the loop was to develop a measurement setup that limits the crosstalk within the resonator chip and in access to the chip. The frequency resolution of the loop was similar when measured using temporal and frequency acquisition. The frequency resolution of the self-oscillating loop was found to be similar to that of a frequency-locked loop but in both architectures, a flicker noise degrades the resolution of the sensor compared to that predicted by the model developed in the previous chapter. In the second section of the final chapter, I present the design of an ASIC that can self-oscillate four crossbeams in parallel. The ASIC includes four frequency counters that allow it to measure simultaneously the resonance frequency of the four MEMS components. The ASIC incorporates analog and digital electronics. The crossbeam output signal is first amplified and filtered using analog circuits. The signal is then digitized to simplify the architecture of the

phase shifter while achieving good control. The coupling within the array, a problem inherent to arrays of sensors, could be evaluated with the ASIC design. Moreover, because of its small dimensions (7×7 mm^2), the ASIC can also be implemented in an array comprising 12 or more resonators.

In the last section of the chapter, the principal technological challenge inherent to the fabrication of large arrays of MEMS sensors is explored, namely co-integration of the MEMS and the electronic circuit on the same die. This technological step is necessary towards the construction of arrays incorporating millions of sensors because alternative integration schemes would require too many wire connections. This topic was explored in three projects in which the resonators are either 2D or 3D co-integrated with the electronics. In the first project, I realized different electronic circuits that address 2D co-integrated MEMS resonators with capacitive detection. The second project uses a technological process, developed in Leti, that makes the fabrication more flexible and allows the construction of 2D co-integrated nanowires and crossbeam resonators. This design incorporates resonators with very high resonance frequency (> 100 MHz). In the third project, I designed a high-performance amplifier and a buffer to interface with 3D co-integrated crossbeam resonators. The MEMS/CMOS co-integrated chips are currently being manufactured and their performance should be evaluated in the next months.

Based on the realization of the self-oscillating loop including a crossbeam resonator, a future goal could be to further investigate the origin of the close to carrier flicker noise that limits the performance of the mechanical resonator. Another objective would be to understand why the frequency resolution of the oscillator is improperly evaluated when the frequency counter measures the time lapse between consecutive rising edges. In this context, it would be interesting to operate temporal simulations of a closed-loop with different phase-noise levels and frequency spectra in order to evaluate the limits of the frequency measurement technique. Such simulations are difficult to implement, however, as they are very time consuming.

As described in the manuscript, an integrated circuit was designed and is being fabricated. Obviously, it would be interesting to verify the functionality of the circuitry and then to implement it with one or more resonators. The coupling between the different resonators and sustaining electronics should be assessed to evaluate whether medium dense arrays implemented with stand-alone resonators can be realized. Two approaches could be considered if a second version of the integrated circuit was to be designed. If supplementary manpower can be assigned to the design of such circuitry, the experience acquired with the first realization might allow them to implement a frequency-locked loop architecture in the chip. Another possible approach would be to maintain the self-oscillating loop architecture, but to simplify the circuitry based on the experience acquired with the first realized chip so that the second version would be more compact. An interesting objective would be to construct an integrated circuit capable of self-oscillating 10 or more resonators.

Finally, the first realizations of MEMS-CMOS co-integrated systems are probably

the most promising outcome of my research. The preliminary measured characteristics of such systems are very satisfactory and indeed very promising. Obviously it would be very exciting to compare their characteristics with the other mentioned co-integrated implementations, once they are constructed. This integration scheme is very new in our group and rare in the literature, and it clearly offers many perspectives. The electronic architectures usually employed for resonators should be rethought in order to fulfill the particular demands of nanoresonators. Furthermore when comparing the minute areal demands of a NEMS component with the larger demands of its release area and the area of associated feedback electronics, it is evident that there is an unsatisfactory filling factor. A possible improvement is the realization of a mixed array that would consist of individually addressing compact oscillators as described in section 3.3, with the modification that the resonator is replaced by a small array of collectively addressed resonators. To conclude, NEMS-CMOS oscillators co-integrated into compact pixels are very new and rarely treated in the literature. Any exploratory work in the domain promises to uncover new physical phenomenon at the nanoscale level as well as promising new applications of the technology.

Nomenclature

ADEV	Allan deviation
AGC	Automatic gain control
AVAR	Allan variation
AlN	Aluminum Nitride
ASIC	Application specified integrated circuit
CMOS	Complementary metal oxide semiconductor
FLL	Frequency lock loop
LNA	Low-noise amplifier
MEMS	MicroElectroMechanical Systems
NEMS	NanoElectroMechanical Systems
SOI	Silicon on insulator
SOL	Self-oscillating loop
VCO	Voltage-controlled Oscillator
Dkit	Design kit
DLL	Delay lock loop
DMMP	Dimethyl Methylphosphonate is Sarrin gas simulant
FDSOI	Fully depleted silicon on insulator
NMOS	Negatively doped metal–oxide–semiconductor field-effect transistor
PLL	Phase lock loop
ppb	Particule per billion

ppm	Particule per million
PSD	Power spectral density
$\alpha(t)$	Relative amplitude noise
$\Delta\Phi_{g0}$	Resistivity variation of the gauge
$\Delta\Phi_g$	Resistivity variation of the gauge
Δb_g	Width variation of the gauge
$\Delta\mathsf{C}\,(t)$	Capacitance variation in the capacitive detection
Δf	Frequency difference
Δf	Resonance frequency variation
Δh_g	Thickness variation of the gauge
ΔL_g	Length variation of the gauge
Δm	Added mass
δt	Sampling time of the reference clock
$\Delta\phi$	Phase difference
$\Delta\psi_{MEMS}(f)$	Phase-shift difference between the MEMS phase-shift at f and at f_r
$\Delta\psi_{ref}$	Desired phase-shift difference
$\Delta\psi_{SBR}$	Signal-to-background ratio phase-shift
ℓ_1	Strain of the beam
η_K	Coefficient for the Duffing effect
η_A	Actuation normalization constant
η_D	Detection coefficient
Γ_τ	Auto-correlation function
γ_{beam}	Gauge factor
γ_{Si}	Gauge factor of the silicon
κ_{mass}	Normalization coefficient that depends on how Δm is added to the beam

κ_H	Hooge noise coefficient
λ	Modal coefficient ????
$\{\ell\}$	Tensor of the strain
$\{\Sigma\}$	Tensor of the stress
$\{\varepsilon\}$	Permittivity of the piezoelectric crystal
$\{c\}$	Elastic stiffness constant
$\{D\}$	Electric displacement
$\{E\}$	Electric field
$\{e\}$	Piezoelectric constant
$\langle f \rangle$	Mean value of the frequency
$\langle T \rangle$	Mean value of the period
$\tilde{\mathsf{w}}\,(x,t)$	Displacement of the beam
$\mathbb{E}$	Statistical expectation
$\mathsf{v}_{\mathsf{act}}(t)$	Actuation voltage
$\mathsf{v}_{\mathsf{noise}}(t)$	voltage noise
$\mathsf{v}(t)$	Voltage signal
μ_N	Electron mobility of the transistor
Φ_{g0}	Resistivity of the gauge at rest
Φ_{Si0}	Silicon resistivity at rest
ψ_{MEMS}	Phase-shift introduced by the MEMS resonator
$\Re$	Responsitivity of the MEMS resonator
ρ	Density of the beam
ρ_{eq}	Equivalent mass of the beam per unit of surface
σ_{f_r}	Frequency resolution
σ_m	Minimal detectable mass

τ	Delay
$\Upsilon_n(x)$	Spacial variable in the Galerkin decomposition
ε_0	Permittivity of the air
$\varphi(t)$	Phase noise
ξ	Coefficient of the viscosity of the beam
$\mathsf{a_n}(t)$	Temporal variable in the Galerkin decomposition
b	Width of the beam
$\mathsf{C}(t)$	Capacitance
C_0	Electrostatic capacitance when the beam is at rest
c_{beam}	Modulus of the beam
C_{BOX}	Capacitance of the BOX
C_{elec}	Electronics input capacitance
C_m	Motion capacitance in the BVD model
C_{output}	Capacitance at the output of the resonator
C_{ox}	Oxide capacitance per unit of area
C_{PZE0}	Static capacitance of the piezoelectric layer at f_r
C_{PZE}	AlN-layer capacitance
C_{PZE}	Static capacitance of the piezoelectric layer
C_p	On-chip routing parasitic capacitance
d	Dielectric losses
$\mathcal{D}$	Doping level
f	Frequency
f_{act}	Actuation frequency
f_{CLK}	Frequency of the reference clock
f_c	Cut-off frequency of the high- or low-pass filter

f_{filter}	Cut-off frequency of the filter
f_k	Instantaneous frequency
F_{l-c}	Critical actuation force
$F_{lN}(f)$	Complex amplitude of the negative force applied on the beam per unit of length
$F_{lP}(f)$	Complex amplitude of the positive force applied on the beam per unit of length
$F_l(f)$	Complex amplitude of the actuation force
$\mathsf{F_l}(t)$	Force applied on the beam per unit of length
f_{osc}	Oscillation frequency
f_{r0}	Resonance frequency corresponding to an added mass null
f_r	Resonance frequency of the MEMS component
$f_r^{\Delta m}$	Resonance frequency corresponding to an added mass Δm
f_{source}	Frequency of the signal source
f_{VCO}	Gain of the VCO
g	Gap
G_{amp}	Amplifier gain
G_{filter}	Low-frequency gain of the filter
g_g	Width of the piezoresistive gauge
g_{MEMS}	Gain of the MEMS resonator at f_r
G_{SBR}	Signal-to-background ratio gain
h	Thickness of the beam
$H_\varphi(f)$	Transfer function of the open to closed loop noise
H_{act}	Transfer function of the MEMS actuation
$H_{connec}(f)$	Transfer function of the MEMS-to-electronics connection
$H_{delay}(f)$	Transfer function of the delay bloc

H_{det}	Transfer function of the MEMS detection
$H_{elec-NL}(f)$	Transfer function of the electronics including the nolinearity
$H_{elec}(f)$	Transfer function of the electronics
H_{filter}	Transfer function of the filter
$H_{FLL}(f)$	Transfer function frequency lock loop
$H_{ft}(f)$	Transfer function of the transmission feed-through
h_g	Thickness of the piezoresistive gauge
$H_{HPF}(f)$	Transfer function of the high-pass filter
$H_{LPF}(f)$	Transfer function of the low-pass filter
$H_{MEMSft}(f)$	Transfer function of MEMS resonator including the transmission feed-through
$H_{MEMS}(f)$	Transfer function of the MEMS resonator
$H_{MEMS}^{phase}(f)$	Transfer function of the MEMS in the phase representation
$H_{OL}(f)$	Open-loop transfer function
$H_{PLL}(f)$	Transfer function of the PLL
HD_2	Second order harmonic distorsion
HD_3	Third order harmonic distorsion
I	Moment of inertia of the beam
$\mathsf{i}\,(t)$	Current
k	Stiffness of the MEMS resonator
k_d	Proportional gain
k_B	Boltzmann constant
L	Length of the beam
L	Length of the vibrating mass
L_A	Active transistor length
$L_{bonding}$	Inductance introduced by the wire-bonding

L_g	Length of the piezoresistive gauge
L_m	Motion inductance in the BVD model
L_{tech}	Minimum transistor length imposed by the CMOS process
M	Number of elements f_k
m	Mass of the MEMS resonator
$\mathcal{M}$	Momentum applied on a beam
$M_{bonding}$	Mutual coefficient introduced by the wire-bonding
n	Integer
P_{amp}	Power consumption of the amplifier
p_{ft}	V-shape feed-through frequency coefficient
Q	Quality factor of the resonator
Q_{VCO}	Quality factor of the VCO
R	Resistance
r_{eq}	Equivalent beam rigidity
R_{g0}	Resistance of the gauge at rest
R_{lat}	Lateral resistance in the substrate between two paths
R_{MEMS}	Output impedance of the MEMS resonator
R_m	Motion resistance in the BVD model
R_{sub}	Resistance from the BOX/silicon bulk interface to the ground
$S_{\delta f/f}$	Power spectral density of the relative frequency noise
$S_{\delta f/f}(f)$	Power spectral density of the relative frequency variations
$S_{\Delta f_{VCO}}(f)$	Power spectral density output frequency noise of the VCO
$S_{\varphi-ideal}(f)$	Ideal power spectral density of the SOL phase noise
$S_{\varphi_{MEMS+elec}}(f)$	Power spectral density of the phase-noise
$S_{\varphi_{out}}(f)$	Power spectral density of the output phase noise

$S_{\varphi_{VCO}}(f)$	Power spectral density of the VCO output phase-noise
S_{elec}	Power spectral density of the electronic noise
$S_f(f)$	Power spectral density of the frequency noise
S_{iamp}	PSD of the amplifier input current noise
S_{M_A}	Power spectral density generated by the transistor M_A
$S_{MEMS_{\bar{th}}}(f)$	Power spectral density of the MEMS noise except the thermomechanical noise
S_{PZR}	Power spectral density of the piezoresistive gauge
$S_{thermo}(f)$	Power spectral density of the thermomechanical noise
$S_u(f)$	Power spectral density of the input signal of the VCO
$S_{v_{mems}}(f)$	Power spectral density of v_{elec}
S_{vamp}	PSD of the amplifier input voltage noise
SBR	Signal-to-background ratio
SNR	Signal-to-noise ratio
T	Temperature
t	Time
$T\,(\tilde{\mathsf{w}})$	Intern stress in the beam
T_k	Instantaneous period
t_k	k^{th} transistion time
$T_{meas-opt}$	Optimal measurement duration
T_{meas}	Measurement duration
$u(f)$	Input signal of the VCO
$\mathsf{V}\,(t)$	Voltage
v_0	Amplitude voltage
v_{act-c}	Critical actuation voltage
$v_{act}(f)$	Complex amplitude of the actuation voltage

V_{dd}	Supply voltage of the CMOS technology
V_{dssat}	Drain-Source saturation voltage
$v_{elec}(f)$	Complex amplitude of the electronic input signal
V_g	Applied voltage on the gauge
$v_{MEMS}(f)$	Complex amplitude of the unloaded resonator output voltage
$w\,(f)$	Complex amplitude of the mechanical displacement of the beam
$\mathsf{w}\,(t)$	Mechanical displacement of the beam
W_A	Active transistor width
x	Coordinate along the length of the beam
$y(f)$	Complex amplitude of the mechanical displacement
y_c	Critical mechanical displacement
Y_{in}	Input admittance of the MEMS resonator for a single actuation
$YinN$	Negative input admittance of the MEMS resonator in differential actuation
$YinP$	Positive input admittance of the MEMS resonator in differential actuation
z_0	Coordinate of the neutral line

Bibliography

[Aebersold 2003] R. Aebersold and M. Mann. *Mass spectrometry-based proteomics.* Nature, vol. 422, no. 6928, pages 198–207, Mar 2003.

[Akgul 2009] M. Akgul, K. Bongsang, L.-W. Hung, Y. Lin, W.-C. Li, W.-L. Huang, I. Gurin, A. Borna and C.T.-C. Nguyen. *Oscillator far-from-carrier phase noise reduction via nano-scale gap tuning of micromechanical resonators.* pages 798 –801, June 2009.

[Albrecht 1991] T. R. Albrecht, P. Grutter, D. Horne and D. Rugar. *Frequency modulation detection using high-Q cantilevers for enhanced force microscope sensitivity.* Journal of Applied Physics, vol. 69, no. 2, pages 668–673, Jan 1991.

[Arcamone 2007] J. Arcamone, B. Misischi, F. Serra-Graells, M. A. F. van den Boogaart, J. Brugger, F. Torres, G. Abadal, N. Barniol and F. Perez-Murano. *A Compact and Low-Power CMOS Circuit for Fully Integrated NEMS Resonators.* TCAS II, vol. 54, no. 5, pages 377 –381, May 2007.

[Arcamone 2009] J. Arcamone, M. Sansa, J. Verd, A. Uranga, G. Abadal, N. Barniol, M.A.F. van den Boogaart, J. Brugger and F. Perez-Murano. *Nanomechanical mass sensor for monitoring deposition rates through confined apertures.* In Nano/Micro Engineered and Molecular Systems, 2009. NEMS 2009. 4th IEEE International Conference on, pages 94 –97, Jan 2009.

[Arcamone 2010] J. Arcamone, E. Colinet, A. Niel and E. Ollier. *Efficient capacitive transduction of high-frequency micromechanical resonators by intrinsic cancellation of parasitic feedthrough capacitances.* Applied Physics Letters, vol. 97, no. 4, pages 043505 –043505–3, Jul 2010.

[Arcamone 2011] J. et al. Arcamone. *VLSI silicon multi-gas analyzer coupling gas chromatography and NEMS detectors.* In to be published in the proc. of the IEEE IEDM, 2011.

[Arndt 2010] G. Arndt, E. Colinet and J. Juillard. *Design of a co-integrated CMOS/NEMS oscillator with a simple electronic circuit.* In Design Test Integration and Packaging of MEMS/MOEMS (DTIP), 2010 Symposium on, pages 368 –371, 2010.

[Arndt 2011] G. Arndt, E. Colinet, J. Arcamone and J. Juillard. *A design methodology for fully integrated MEMS and NEMS Pierce oscillators.* Sensors and Actuators A: Physical, vol. In Press, Corrected Proof, pages –, 2011.

[Bahreyni 2007] B. Bahreyni and C. Shafai. *Oscillator and frequency-shift measurement circuit topologies for micromachined resonant devices.* Sensors and Actuators A: Physical, vol. 137, no. 1, pages 74 – 80, 2007.

[Bao 2000] M.H. Bao. Micro mechanical transducers: pressure sensors, accelerometers, and gyroscopes. Handbook of sensors and actuators. Elsevier, 2000.

[Bargatin 2005] I. Bargatin, E.B. Myers, J. Arlett, B. Gudlewski and M.L. Roukes. *Sensitive detection of nanomechanical motion using piezoresistive signal downmixing.* Applied Physics Letters, vol. 86, no. 13, Mar 2005.

[Bargatin 2007] I. Bargatin, I. Kozinsky and M. L. Roukes. *Efficient electrothermal actuation of multiple modes of high-frequency nanoelectromechanical resonators.* Applied Physics Letters, vol. 90, no. 9, pages 093116–093116–3, Feb 2007.

[Bargatin 2008] I. Bargatin. *High-frequency nanomechanical resonators for sensor applications.* PhD thesis, California Institute of Technology, 2008.

[Barnes 1990] J. Barnes and D. Allan. *Variances based on data with dead time between the measurements.* Rapport technique, NIST technical notes 1318, 1990.

[Bienstman 1995] J. Bienstman, H.A.C. Tilmans, M. Steyaert and R. Puers. *An Oscillator Circuit For Electrostatically Driven Silicon-based One-port Resonators.* In Proc. and Eurosensors IX. Solid-State Sensors and Actuators Transducers '95. The 8th International Conference on, volume 1, pages 146–149, 1995.

[Boisen 2000] A. Boisen, J. Thaysen, H. Jensenius and O. Hansen. *Environmental sensors based on micromachined cantilevers with integrated read-out.* Ultramicroscopy, vol. 82, no. 1-4, pages 11 – 16, 2000.

[Boisen 2011] Anja Boisen, Soren Dohn, Stephan Sylvest Keller, Silvan Schmid and Maria Tenje. *Cantilever-like micromechanical sensors.* REPORTS ON PROGRESS IN PHYSICS, vol. 74, no. 3, MAR 2011.

[Brissaud 2003] M. Brissaud, S. Ledren and P. Gonnard. *Modelling of a cantilever non-symmetric piezoelectric bimorph.* Journal of Micromechanics and Microengineering, vol. 13, no. 6, pages 832–844, Nov 2003.

[Burg 2007] T. Burg, M. Godin, S. Knudsen, W. Shen, G. Carlson, J. Foster, K. Babcock and S. Manalis. *Weighing of biomolecules, single cells and single nanoparticles in fluid.* Nature, vol. 446, no. 7139, pages 1066–1069, Apr 2007.

[Calvo 2009] B. Calvo, N. Medrano, S. Celma and M.T. Sanz. *A low-power high-sensitivity CMOS voltage-to-frequency converter.* In Proc. 52nd IEEE International Midwest Symposium on Circuits and Systems MWSCAS '09, pages 118–121, Aug 2009.

[Campbell 2006] G.A. Campbell and R. Mutharasan. *Use of piezoelectric-excited millimeter-sized cantilever sensors to measure albumin interaction with self-assembled monolayers of alkanethiols having different functional headgroups.* Analytical Chemistry, vol. 78, no. 7, pages 2328–2334, Apr 2006.

[Chapuis 2007] F. Chapuis, E. Defay, F. Casset, J.F. Manceau, F. Bastien and M. Aid. *Microswitch with Mixed Piezoelectric and Electrostatic Actuation.* pages 1159 –1162, June 2007.

[Chiu 2008] H.-Y. Chiu, P. Hung, H.W.C. Postma and M. Bockrath. *Atomic-Scale Mass Sensing Using Carbon Nanotube Resonators.* Nano Letters, vol. 8, no. 12, pages 4342–4346, Dec 2008.

[Cleland 2002] A.N. Cleland and M.L. Roukes. *Noise processes in nanomechanical resonators.* Journal of Applied Physics, vol. 92, no. 5, pages 2758–2769, Sep 2002.

[Colinet 2009] E. Colinet, L. Duraffourg, S. Labarthe, S. Hentz, P. Robert and P. Andreucci. *Self-oscillation conditions of a resonant nanoelectromechanical mass sensor.* Journal of Applied Physics, vol. 105, no. 12, pages 124908–8, 2009.

[Colinet 2010] E. Colinet, J. Arcamone, A. Niel, E. Lorent, S. Hentz and E. Ollier. *100 MHz oscillator based on a low polarization voltage capacitive Lamé;-mode MEMS resonator.* In Frequency Control Symposium (FCS), 2010 IEEE International, pages 174 –178, June 2010.

[datasheet a] 33250A datasheet.

[datasheet b] CCSO-914X3-1000 datasheet.

[datasheet c] SR844 lock-in amplifier datasheet.

[Defosseux 2011] M. Defosseux, M. Allain, P. Ivaldi, E. Defay and S. Basrour. *Highly efficient piezoelectric micro harvester for low level of acceleration fabricated with a CMOS compatible process.* pages 1859 –1862, June 2011.

[Demir 2000] A. Demir, A. Mehrotra and J. Roychowdhury. *Phase noise in oscillators: a unifying theory and numerical methods for characterization.* Circuits and Systems I: Fundamental Theory and Applications, IEEE Transactions on, vol. 47, no. 5, pages 655 –674, May 2000.

[Dohn 2005] S. Dohn, R. Sandberg, W. Svendsen and A. Boisen. *Enhanced functionality of cantilever based mass sensors using higher modes.* Applied Physics Letters, vol. 86, no. 23, June 2005.

[Dohn 2007] S. Dohn, W. Svendsen, A. Boisen and O. Hansen. *Mass and position determination of attached particles on cantilever based mass sensors.* Review of Scientific Instruments, vol. 78, no. 10, page 103303, 2007.

[Dohn 2010] S. Dohn, S. Schmid, F. Amiot and A. Boisen. *Position and mass determination of multiple particles using cantilever based mass sensors.* Applied Physics Letters, vol. 97, no. 4, page 044103, 2010.

[Domon 2006] B. Domon and R. Aebersold. *Review - Mass spectrometry and protein analysis*. Science, vol. 312, no. 5771, pages 212–217, Apr 2006.

[Ekinci 2004a] K.L. Ekinci, X.M.H. Huang and M.L. Roukes. *Ultrasensitive nanoelectromechanical mass detection*. Applied Physics Letters, vol. 84, no. 22, pages 4469–4471, May 2004.

[Ekinci 2004b] K.L. Ekinci, Y.T. Yang and M.L. Roukes. *Ultimate limits to inertial mass sensing based upon nanoelectromechanical systems*. Journal of Applied Physics, vol. 95, no. 5, pages 2682–2689, Mar 2004.

[Feng 2007] X.L. Feng, R.R. He, P.D. Yang and M.L. Roukes. *Phase Noise and Frequency Stability of Very-High Frequency Silicon Nanowire Nanomechanical Resonators*. In Solid-State Sensors, Actuators and Microsystems Conference, 2007. TRANSDUCERS 2007. International, pages 327 –330, 2007.

[Feng 2008] X.L. Feng, C.J. White, A. Hajimiri and M.L. Roukes. *A self-sustaining ultrahigh-frequency nanoelectromechanical oscillator*. Nature Nanotechnology, vol. 3, no. 6, pages 342–346, June 2008.

[Gelb 1968] A. Gelb and W. Van der Velde. Multiple-input describing functions and nonlinear system design. Mcgraw-Hill, New-York, 1968.

[Giner 2011] J. Giner, A. Uranga, J.L. Muñoz-Gamarra, E. Marigó, E. Colinet, J. Arcamone and Barniol N. *Cancellation of the Parasitic Current in an integrated CMOS-MEMS Clamped- Clamped Beam Resonator*. In 34th International Conference on Micro and Nano Engineering, 2011.

[Gray 2001] P. Gray, P. Hurst, S. Lewis and R. Meyer. Analysis and design of analog integrated circuits. John Wiley & Sons, 2001.

[Hagleitner 2001] C. Hagleitner, A. Hierlemann, D. Lange, A. Kummer, N. Kerness, O. Brand and H. Baltes. *Smart single-chip gas sensor microsystem*. Nature, vol. 414, no. 6861, pages 293–296, Nov 2001.

[Harkey 2000] J.A. Harkey and T.W. Kenny. *1/f noise considerations for the design and process optimization of piezoresistive cantilevers*. Microelectromechanical Systems, Journal of, vol. 9, no. 2, pages 226 –235, June 2000.

[He 2006] R. He and P. Yang. *Giant piezoresistance effect in silicon nanowires*. Nature Nanotechnology, vol. 1, no. 1, pages 42–46, Oct 2006.

[He 2008] R. He, X.L. Feng, M.L. Roukes and P. Yang. *Self-transducing silicon nanowire electromechanical systems at room temperature*. Nano Letters, vol. 8, no. 6, pages 1756–1761, June 2008.

[He 2010] L. He, Y. P. Xu and M. Palaniapan. *A State-Space Phase-Noise Model for Nonlinear MEMS Oscillators Employing Automatic Amplitude Control*. Circuits and Systems I: Regular Papers, IEEE Transactions on, vol. 57, no. 1, pages 189–199, Jan 2010.

[Ivaldi 2011a] P. Ivaldi, J. Abergel, H. Blanc, E. Colinet, E.B. Myers, M.L. Roukes, P. Andreucci, S. Hentz and E. Defay. *DMMP vapor detection with 50nm thick AlN films based microcantilever.* In Transducers 2011, 2011.

[Ivaldi 2011b] P. Ivaldi, J. Abergel, M.H. Matheny, L.G. Villanueva, R.B. Karabalin, M.L. Roukes, P. Andreucci, S. Hentz and E. Defay. *50 nm thick AlN film-based piezoelectric cantilevers for gravimetric detection.* Journal of Micromechanics and Microengineering, vol. 21, no. 8, page 085023, 2011.

[Jensen 2008] K. Jensen, K. Kim and A. Zettl. *An atomic-resolution nanomechanical mass sensor.* Nature Nanotechology, vol. 3, no. 9, pages 533–537, Sep 2008.

[Juillard 2009] J. Juillard, A Bonnoit, E. Avignon, S. Hentz, N. Kacem and E. Colinet. *Large amplitude motion of an electrostatically-actuated resonant beam operated in closed-loop.* Journal of Applied Physics, 2009.

[Kacem 2008] N. Kacem, S. Hentz, H. Fontaine, V. Nguyen, P. Robert, B. Legrand and L. Buchaillot. *From MEMS to NEMS: Modelling and characterization of the non linear dynamics of resonators, a way to enhance the dynamic range.* In NSTI Nanotech, volume 3, pages 619–622, 2008.

[Karabalin 2009] R.B. Karabalin, M.H. Matheny, X.L. Feng, E. Defay, G. Le Rhun, C. Marcoux, S. Hentz, P. Andreucci and M.L. Roukes. *Piezoelectric nanoelectromechanical resonators based on aluminum nitride thin films.* Applied Physics Letters, vol. 95, no. 10, Sep 2009.

[Kharrat 2008] C. Kharrat, E. Colinet and A. Voda. *H∞ Loop shaping control for PLL-based mechanical resonance tracking in NEMS resonant mass sensors.* In Sensors, 2008 IEEE, pages 1135 –1138, Oct 2008.

[Kharrat 2009] C. Kharrat. *Application des techniques de contrôle sur les réseaux de micro et nanostructures.* PhD thesis, EEATS, 2009.

[Knobel 2008] R. Knobel. *Mass sensors: Weighing single atoms with a nanotube.* Nature Nanotechnology, vol. 3, no. 9, pages 525–526, Sep 2008.

[Kobayashi 2011] K. Kobayashi, H. Yamada and K. Matsushige. *Reduction of frequency noise and frequency shift by phase shifting elements in frequency modulation atomic force microscopy.* Review of Scientific Instruments, vol. 82, no. 3, page 033702, 2011.

[Labarthe 2010] S. Labarthe. *Conception et modélisation d'un nanocapteur de masse par détection piézorésistive.* PhD thesis, Université Joseph Fourier, 2010.

[Lang 1998] H.P. Lang, R. Berger, F. Battiston, J.P. Ramseyer, E. Meyer, C. Andreoli, J. Brugger, P. Vettiger, M. Despont, T. Mezzacasa, L. Scandella, H.J. Guntherodt, C. Gerber and J.K. Gimzewski. *A chemical sensor based on a micromechanical cantilever array for the identification of gases and vapors.* Applied Physics A- Materials Science & Processing, vol. 66, no. Part

1, S, pages S61–S64, Mar 1998. 9th International Conference on Scanning Tunneling Microscopy/Spectroscopy and Related Techniques, HAMBURG, GERMANY, JUL 20-25, 1997.

[Lee 2004] S.e Lee and C.T.-C. Nguyen. *Mechanically-coupled micromechanical resonator arrays for improved phase noise*. In Proc. IEEE International Frequency Control Symposium and Exposition, pages 144–150, 2004.

[Lee 2009a] D. Lee, S. Kim, N. Jung, T. Thundat and S. Jeon. *Effects of gold patterning on the bending profile and frequency response of a microcantilever*. Journal of Applied Physics, vol. 106, no. 2, Jul 2009.

[Lee 2009b] J.E.-Y. Lee and A.A. Seshia. *Parasitic feedthrough cancellation techniques for enhanced electrical characterization of electrostatic microresonators*. Sensors and Actuators A: Physical, vol. 156, no. 1, pages 36 – 42, 2009.

[Leeson 1966] D.B. Leeson. *A simple model of feedback oscillateur noise spectrum*. Proceedings of the institute of electrical and electronics engineers, vol. 54, no. 2, pages 329–&, 1966.

[Levy 2010] R. Levy, A. Dupret and H. Mathias. *Phase noise analysis of the Frequency Tracking Oscillator*. In Frequency Control Symposium (FCS), 2010 IEEE International, pages 624 –628, June 2010.

[Li 2007] Mo Li, H. X. Tang and M. L. Roukes. *Ultra-sensitive NEMS-based cantilevers for sensing, scanned probe and very high-frequency applications*. Nature Nanotechnology, vol. 2, no. 2, pages 114–120, Feb 2007.

[Li 2010] Mo Li, E.B. Myers, H.X. Tang, S.J. Aldridge, H.C. McCaig, J.J. Whiting, R.J. Simonson, N.S. Lewis and M.L. Roukes. *Nanoelectromechanical Resonator Arrays for Ultrafast, Gas-Phase Chromatographic Chemical Analysis*. Nano Letters, vol. 10, no. 10, pages 3899–3903, Oct 2010.

[Lopez 2009a] J L Lopez, J Verd, J Teva, G Murillo, J Giner, F Torres, A Uranga, G Abadal and N Barniol. *Integration of RF-MEMS resonators on submicrometric commercial CMOS technologies*. Journal of Micromechanics and Microengineering, vol. 19, no. 1, page 015002, 2009.

[Lopez 2009b] J.L. Lopez, J. Verd, J. Giner, A. Uranga, G. Murillo, E. Marigo, F. Torres, G. Abadal and N. Barniol. *High Q CMOS-MEMS resonators and its applications as RF tunable band-pass filters*. pages 557 –560, June 2009.

[Mamin 2001] H.J. Mamin and D. Rugar. *Sub-attonewton force detection at millikelvin temperatures*. Applied Physics Letters, vol. 79, no. 20, pages 3358–3360, Nov 2001.

[Maraldo 2007] D. Maraldo and R. Mutharasan. *Detection and Confirmation of Staphylococcal Enterotoxin B in Apple Juice and Milk Using Piezoelectric-Excited Millimeter-Sized Cantilever Sensors at 2.5 fg/mL*. Analytical Chemistry, vol. 79, pages 7636–7643, 2007.

[Masmanidis 2007] S. Masmanidis, R. Karabalin, I. De Vlaminck, G. Borghs, M. Freeman and M.L. Roukes. *Multifunctional nanomechanical systems via tunably coupled piezoelectric actuation.* Science, vol. 317, no. 5839, pages 780–783, Aug 2007.

[Mestrom 2009] R.M.C. Mestrom, R.H.B. Fey and H. Nijmeijer. *Phase Feedback for Nonlinear MEM Resonators in Oscillator Circuits.* Mechatronics, IEEE/ASME Transactions on, vol. 14, no. 4, pages 423 –433, Aug 2009.

[Mile 2010] E. Mile, G. Jourdan, I. Bargatin, S. Labarthe, C. Marcoux, P. Andreucci, S. Hentz, C. Kharrat, E. Colinet and L. Duraffourg. *In-plane nanoelectromechanical resonators based on silicon nanowire piezoresistive detection.* Nanotechnology, vol. 21, no. 16, Apr 2010.

[Naik 2009] A.K. Naik, M.S. Hanay, W.K. Hiebert, X.L. Feng and M.L. Roukes. *Towards single-molecule nanomechanical mass spectrometry.* Nature Nanotechnology, vol. 4, no. 7, pages 445–450, Jul 2009.

[Oliveira 2010] J. Oliveira, J. Goes, M. Figueiredo, E. Santin, J. Fernandes and J. Ferreira. *An 8-bit 120-MS/s Interleaved CMOS Pipeline ADC Based on MOS Parametric Amplification.* Circuits and Systems II: Express Briefs, IEEE Transactions on, vol. 57, no. 2, pages 105 –109, Feb 2010.

[Palmisano 2003] G. Palmisano and S. Pennisi. *CMOS single-input differential-output amplifier cells.* IEEE proceedings- Circuit Devices and Systems, vol. 150, no. 3, pages 194–198, June 2003.

[Paul 2006] M.R. Paul, M.T. Clark and M.C. Cross. *The stochastic dynamics of micron and nanoscale elastic cantilevers in fluid: fluctuations from dissipation.* Nanotechnology, vol. 17, no. 17, pages 4502–4513, Sep 2006.

[Roukes 2007] M.L. Roukes. *Nanoelectromechanical systems: Potential, progress, & projections.* In Proc. MEMS Micro Electro Mechanical Systems IEEE 20th International Conference on, pages 93–94, Jan 2007.

[Rubiola 2008] E. Rubiola. Phase noise and frequency stability in oscillators. Cambridge University Press, 2008.

[Russell 1997] D.H. Russell and R.D. Edmondson. *High-resolution mass spectrometry and accurate mass measurements with emphasis on the characterization of peptides and proteins by matrix-assisted laser desorption/ionization time-of-flight mass spectrometry.* Journal of Mass Spectrometry, vol. 32, no. 3, pages 263–276, Mar 1997.

[Sansen 2006] W. Sansen. Analog design essentials. Spinger, 2006.

[Sinha 2009] N. Sinha, G.E. Wabiszewski, R. Mahameed, V.V. Felmetsger, S.M. Tanner, R.W. Carpick and G. Piazza. *Piezoelectric aluminum nitride nanoelectromechanical actuators.* Applied Physics Letters, vol. 95, no. 5, Aug 2009.

[Sta 1988] IEEE standard on piezoelectricity. 1988.

[Susplugas 2004] O. Susplugas. *Application des boucles à verrouillage de retard à la synthèse de fréquences dans les circuits pour les communications mobiles.* PhD thesis, Ecole Nationale Supérieure des Télécommunications de Paris, 2004.

[Tang 2002] H.X. Tang, X.M.H. Huang, M.L. Roukes, M. Bichler and W. Wegscheider. *Two-dimensional electron-gas actuation and transduction for GaAs nanoelectromechanical systems.* Applied Physics Letters, vol. 81, no. 20, pages 3879–3881, Nov 2002.

[Taylor 2010] J.D. Taylor, B. Elliott, Dickel D., G. Keskar, J. Gaillard, M. J. Skove and A. M. Rao. Oxford handbook of nanoscience and technology, volume 2. Frontiers in Nanoscience and Nanotechnology, 2010.

[Teva 2007] J. Teva, G. Abadal, A. Uranga, J. Verd, F. Torres, J.L. Lopez, J. Esteve, E. Perez-Murano and Barniol N. *VHF CMOS-MEMS resonator monolithically integrated in a standard 0.35?m CMOS technology.* In Micro Electro Mechanical Systems, 2007. MEMS. IEEE 20th International Conference on, pages 779 – 782, 2007.

[Thevenin 1883] L. Thevenin. *Sur un nouveau théorème d'électricité dynamique [On a new theorem of dynamic electricity].* Comptes Rendus hebdomadaires des séances de l'Académie des Sciences, vol. 97, pages 159–161, 1883.

[Uranga 2005] A. Uranga, J. Teva, J. Verd, J.L. López, F. Torres, J. Esteve, G. Abadal, F. Pérez-Murano and N. Barniol. *Fully CMOS integrated low voltage 100 MHz MEMS resonator.* Electronics Letters, vol. 41, no. 24, pages 1327–1328, 2005.

[Van Dyke 1928] K.S. Van Dyke. *The Piezo-Electric Resonator and Its Equivalent Network.* Proceedings of the Institute of Radio Engineers, vol. 16, no. 6, pages 742 – 764, June 1928.

[Verd 2005] J. Verd, G. Abadal, J. Teva, M. V. Gaudo, A. Uranga, X. Borrise, F. Campabadal, J. Esteve, E. F. Costa, F. Perez-Murano, Z. J. Davis, E. Forsen, A. Boisen and N. Barniol. *Design, fabrication, and characterization of a submicroelectromechanical resonator with monolithically integrated CMOS readout circuit.* IEEE Journal MEMS, vol. 14, no. 3, pages 508–519, 2005.

[Verd 2006] J. Verd, A. Uranga, J. Teva, J.L. Lopez, F. Torres, J. Esteve, G. Abadal, F. Perez-Murano and N. Barniol. *Integrated CMOS-MEMS with on-chip readout electronics for high-frequency applications.* Electron Device Letters, IEEE, vol. 27, no. 6, pages 495 – 497, 2006.

[Verd 2007] J. Verd, A. Uranga, J. Teva, G. Abadal, F. Torres, J. Arcamone, J. L. Lopez, F. Perez-Murano, J. Fraxedas, J. Esteve and N. Barniol. *Monolithic 0.35-μm CMOS Cantilever for Mass Sensing in the Attogram Range with*

Self-Excitation. In Proc. International Solid-State Sensors, Actuators and Microsystems Conference TRANSDUCERS 2007, pages 233–236, 2007.

[Verd 2008] J. Verd, A. Uranga, G. Abadal, J. L. Teva, F. Torres, J. L. Lopez, E. Perez-Murano, J. Esteve and N. Barniol. *Monolithic CMOS MEMS Oscillator Circuit for Sensing in the Attogram Range.* Journal of Electron Device Letters, vol. 29, no. 2, pages 146–148, 2008.

[Vittoz 1988] E.A. Vittoz, M.G.R. Degrauwe and S. Bitz. *High-performance crystal oscillator circuits: theory and application.* IEEE JSSC, vol. 23, no. 3, pages 774–783, June 1988.

[Yang 2006] Y.T. Yang, C. Callegari, X.L. Feng, K.L. Ekinci and M.L. Roukes. *Zeptogram-scale nanomechanical mass sensing.* Nano Letters, vol. 6, no. 4, pages 583–586, Apr 2006.

[Zuo 2010] C. Zuo, N. Sinha, J. Van der Spiegel and G. Piazza. *Multifrequency Pierce Oscillators Based on Piezoelectric AlN Contour-Mode MEMS Technology.* Journal of Microelectromechanical Systems, vol. 19, no. 3, pages 570–580, June 2010.

Personal publications

Journals:

J. Juillard, G. Arndt and E. Colinet. *Modeling of Micromachined Beams Subject to Nonlinear Restoring or Damping Forces.* Journal of microelectromechanical systems, vol. 20, pages 165-177, 2011.

G. Arndt, E. Colinet, J. Arcamone, J. Juillard. *A design methodology for fully integrated MEMS and NEMS Pierce oscillators.* Sensors and Actuators A: Physical, vol. 172, pages 293-300, 2011.

Conferences with proceedings:

J. Juillard, G. Arndt and E. Colinet. *Enhancing the frequency stability of a NEMS oscillator with electrostatic and mechanical nonlinearities.* In Eurosensors'09, Procedia Chemistry, Lausanne : Switzerland, 2009.

G. Arndt, E. Colinet, J. Arcamone and J. Juillard. *Theoretical study of a self-sustained CMOS-integrated nano-oscillator.* In Smart Systems Integration (SMART SYS'10), Como : Italy, 2010.

G. Arndt, E. Colinet and J. Juillard. *Design of a co-integrated CMOS/ NEMS oscillator with a simple electronic circuit.* In Design Test Integration and Packaging of MEMS/MOEMS (DTIP), 2010 Symposium on, 2010.

P. Ivaldi, J. Abergel, G. Arndt, P. Robert, H. Andreucci P. Blanc, S. Hentz and E. Defay. *50 nm Thick AlN Resonant Micro-Cantilever for Gas Sensing Application.* In Frequency Control Symposium (FCS), 2010 IEEE International, 2010.

G. Arndt, E. Colinet, J. Arcamone and J. Juillard. *Limits of a single active transistor-based amplifier designed for co-integrated M-NEMS/CMOS oscillator purposes.* In Eurosensor XXIV Conference, 2010.

G. Arndt, C. Dupre, J. Arcamone, L. Duraffourg, E. Ollier and E. Colinet. *Toward ultra-dense arrays of HF NEMS-CMOS pixels for sensing applications.* Accepted in ISSCC, 2012.

E. Ollier, C. Dupré , G. Arndt, J. Arcamone, C. Vizioz, L. Duraffourg, E. Sage, A. Koumela, S. Hentz, G. Cibrario, P. Meininger, K. Benotmane, C. Marcoux, O.

Rozeau, G. Billiot, E. Colinet, F. Andrieu, J. Philippe, F. Aussenac, D. Mercier, H. Blanc, T. Ernst and P. Robert. *Ultra-scaled high-frequency single-crystal Si NEMS resonators and their front-end co-integration with CMOS for high sensitivity applications*. Accepted in MEMS, 2012.

Conferences without proceedings:

G. Arndt, E. Colinet and J. Juillard. *Conception d'un oscillateur co-intégré NEMS/CMOS*. In Journées Nationales du Réseau Doctoral en Microélectronique, 2010.

G. Arndt, P. Ivaldi, E. Colinet, J. Arcamone, S. Hentz and J. Juillard. *50 nm thick AlN micro-cantilever based self-sustained oscillator*. In 8th International Workshop on Nanomechanical Sensing, 2011.

G. Arndt, E. Colinet, J. Arcamone and J. Juillard. *Resonant NEMS for mass sensing: from system architecture to transistor design*. In International seminar on nanomechanical systems, 2011.

Appendix A: determination of the dynamic range in self-oscillating loops

Similarly to subsection 1.2.2 the following notation are introduced: f_{r0} is the resonance frequency of the MEMS when no mass is loaded. $f_r^{\Delta m}$ is the resonance frequency corresponding to a loading mass Δm.

Low pass filter as the phase-shifter

If the phase-shifter is implemented using a low-pass filter. The phase-shift, close to 90°, introduced by this bloc is only valid for a limited range of frequency. The low-pass filter cut-off frequency can therefore limit the operating frequency range of the oscillator. On the other hand, the gain of the filter increases when the oscillating frequency reduces. The oscillation frequency should first be determined from eq. (1.27):

$$\arg\left[\frac{g_{MEMS}/Q}{1-\left(\frac{f_{osc}}{f_r^{\Delta m}}\right)^2+j\frac{f_{osc}}{Qf_r^{\Delta m}}}\times\frac{G_{amp}}{1+j\frac{f_{osc}}{f_c}}\right]=0\Rightarrow$$

$$\Im\left\{\left[1-\left(\frac{f_{osc}}{f_r^{\Delta m}}\right)^2-j\frac{f_{osc}}{Qf_r^{\Delta m}}\right]\times\left[1-j\frac{f_{osc}}{f_c}\right]\right\}=0\Rightarrow$$

$$f_{osc}=f_r^{\Delta m}\sqrt{1+\frac{f_c}{Qf_r^{\Delta m}}}. \quad (3.29)$$

The maximum detectable added mass corresponds to $|H_{OL}(f_{osc})|=1$:

$$1=\frac{g_{MEMS}/Q}{\sqrt{\left[1-\left(\frac{f_{osc}}{f_r^{\Delta m}}\right)^2\right]^2+\left[\frac{f_{osc}}{Qf_r^{\Delta m}}\right]^2}}\times\frac{G_{amp}}{\sqrt{1+\left(\frac{f_{osc}}{f_c}\right)^2}}\Rightarrow$$

$$\frac{f_c}{Qf_r^{\Delta m}}\left[1+\left(\frac{f_r^{\Delta m}}{f_c}\right)^2+\frac{f_r^{\Delta m}}{Qf_c}\right]=g_{MEMS}G_{amp}/Q\Rightarrow$$

$$\frac{f_r^{\Delta m}}{f_c}\underset{Q\gg1}{\approx}\frac{g_{MEMS}G_{amp}}{2}-\sqrt{\left(\frac{g_{MEMS}G_{amp}}{2}\right)^2-1}. \quad (3.30)$$

The parameter $g_{MEMS} \times G_{amp}$ can be determined from the open-loop gain when there is no loading mass on the MEMS $G_{f_{r0}}$:

$$G_{f_{r0}} = g_{MEMS} \times \frac{G_{amp}}{\sqrt{1+\left(\frac{f_{r0}}{f_c}\right)^2}} \Rightarrow$$

$$\frac{f_r^{\Delta m}}{f_c} = \frac{1}{2}\left[G_{f_{r0}}\sqrt{\left(\frac{f_{r0}}{f_c}\right)^2+1} - \sqrt{G_{f_{r0}}^2\left(\frac{f_{r0}}{f_c}\right)^2 + G_{f_{r0}}^2 - 4}\right] \Rightarrow$$

$$\frac{f_r^{\Delta m}}{f_{r0}} \underset{f_{r0}\gg f_c}{=} \frac{1}{G_{f_{r0}}}\left(\frac{f_c}{f_{r0}}\right)^2 \text{(low-pass filter).} \tag{3.31}$$

For example, if $f_c = f_{r0}/10$ and $G_{f_{r0}} = 3$ dB then $f_r^{\Delta m} \approx f_{r0}/140$. The corresponding dynamic range for the self-oscillating loop using a low-pass filter is therefore much larger than for open-loop measurement techniques.

High-pass filter as the phase-shifter

In the case of a high-pass filter used as a phase shifter, the gain of H_{OL} reduces with $f_r^{\Delta m}$. The gain condition in (1.27) sets a lower-frequency boundary for the operating frequency. Similarly to the case of the low-pass filter, one can find:

$$\frac{f_r^{\Delta m}}{f_{r0}} = \frac{G_{f_{r0}}}{2}\left[\sqrt{\left(\frac{f_{r0}}{f_c}\right)^2+1} - \sqrt{1+\left(\frac{f_{r0}}{f_c}\right)^2\left[1-\left(\frac{2}{G_{f_{r0}}}\right)^2\right]}\right]$$

$$\frac{f_r^{\Delta m}}{f_{r0}} \underset{f_{r0}\ll f_c}{=} \frac{1}{G_{f_{r0}}} \qquad \text{(high-pass filter).} \tag{3.32}$$

The dynamic range of the oscillator using a high-pass filter is lower than using a low-pass filter.?

Delay block as the phase-shifter

If the phase-shifter is realized through delays, the introduced phase-shift varies with the frequency. If f_r reduces, the phase-shift introduced by delays also reduces and thus limits the frequency range for which the oscillation conditions are valid. Similarly to the previous calculations, the oscillating frequency must be determined:

$$\arg\left[\frac{G_{amp}g_{MEMS}/Q}{1-\left(\frac{f_{osc}}{f_r^{\Delta m}}\right)^2 + j\frac{f_{osc}}{Qf_r^{\Delta m}}}e^{i2\pi\tau f_{osc}}\right] = 0 \Rightarrow$$

$$\tan\left(2\pi\tau f_{osc}\right) = \frac{1}{Q}\frac{f_{osc}/f_r^{\Delta m}}{1-\left(f_{osc}/f_r^{\Delta m}\right)^2} \tag{3.33}$$

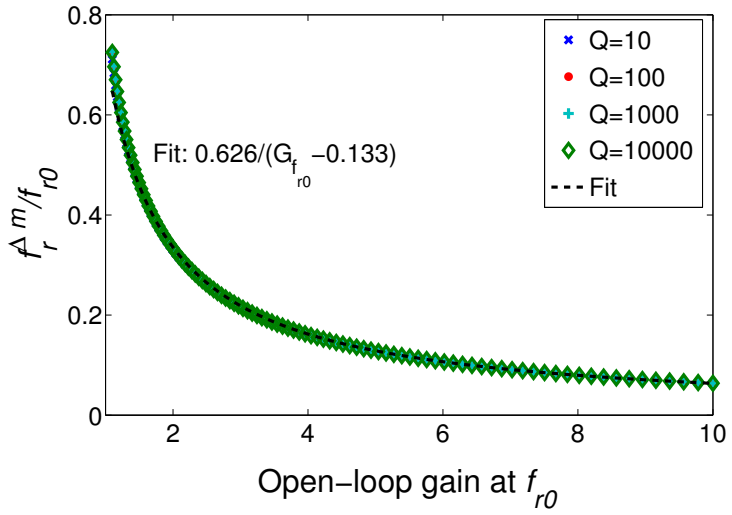

Figure 3.52: Dynamic range of the self-oscillating loop using a delay bloc

The parameter τ is set so that $f_{osc} = f_{r0}$: $\tau = 3/(4f_{r0})$ corresponding to a phase-shift of +90°. Equation (3.33) has no analytical solution and must be solve numerically. Figure 3.52 presents the dynamic range calculated numerically for a self-oscillating loop using delays as phase shifter. This curve can be fited to the following expression:

$$\frac{f_r^{\Delta m}}{f_{r0}} = \frac{0.626}{G_{f_{r0}} - 0.133} \qquad \text{(delay)}, \tag{3.34}$$

thus providing a dynamic resolution of $f_r^{\Delta m} = 0.4 \times f_{r0}$ for $G_{f_{r0}} = 3dB$.

DLL as the phase-shifter

Finally if a DLL bloc is used to ensure the proper phase-shift, the phase-shift and the gain introduced by the bloc does not change with the frequency. However DLL architectures are designed for a frequency range of operation that limits the dynamic range of the oscillator. However the range of operation frequency is often large. For example, in the chapter 3, the design of an ASIC uses a DLL-bloc and its frequency range of operation is larger than 10%.

Appendix B: multi-mode frequency response of a beam

Based on the Euler-Bernoulli equation given in (2.1), it is possible to use the galerkin decomposition:

$$\tilde{\mathsf{y}}(x,t) = \sum_{n=1}^{\infty} \mathsf{a_n}(t)\, \Upsilon_n(x)\,, \tag{3.35}$$

where $\mathsf{a_n}(t)$ is a function in time that describes the frequency response of the beam and $\Upsilon_n(x)$ respects:

$$\forall n_1, n_2 \begin{cases} \frac{\delta^4 \Upsilon_{n_1}}{\delta x^4}(x) = \left(\frac{\lambda_{n_1}}{L}\right)^4 \Upsilon_{n_1}(x) \\ \int_0^L \Upsilon_{n_1}(x)\, \Upsilon_{n_2}(x)\, \mathrm{d}x = L \times \delta_{n_1,n_2} \end{cases}, \tag{3.36}$$

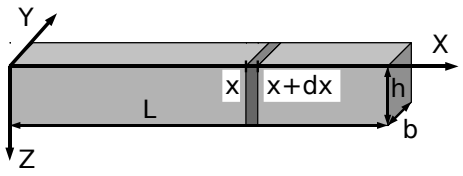

Figure 3.53: Beam dimension and axis definition

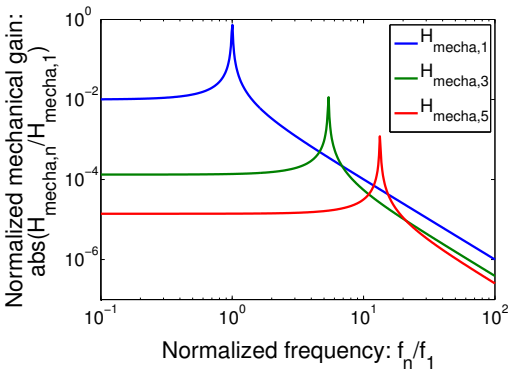

Figure 3.54: Frequency response of the 5 first modes of a clamped-clamped beam. Note that the mode 2 and 4 are null.

and where δ_{n_1,n_2} is the Kronecker delta function that respects:

$$\delta_{n_1,n_2} = \begin{cases} 1, & \text{if } n_1 = n_2 \\ 0, & \text{else} \end{cases}. \tag{3.37}$$

The general solution of eq. (3.36) is:

$$\Upsilon_n = A_n \cos\left(\lambda_n \frac{x}{L}\right) + B_n \sin\left(\lambda_n \frac{x}{L}\right) + C_n \cosh\left(\lambda_n \frac{x}{L}\right) + D_n \sinh\left(\lambda_n \frac{x}{L}\right), \tag{3.38}$$

where A_n, B_n, C_n, D_n and λ_n are parameters to be determined from the mechanical conditions imposed on the beam. Here are the equations imposed by common mechanical conditions:

Clamped end	Free end	Fixed end
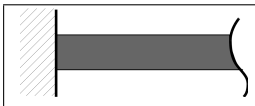	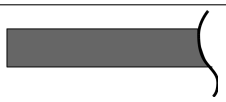	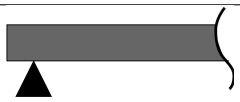
$\forall n,\ \Upsilon_n(x_0) = 0$	$\forall n,\ \frac{\partial^2 \Upsilon_n}{\partial x^2}(x_0) = 0$	$\forall n,\ \Upsilon_n(x_0) = 0$
$\forall n,\ \frac{\partial \Upsilon_n}{\partial x}(x_0) = 0$	$\forall n,\ \frac{\partial^3 \Upsilon_n}{\partial x^3}(x_0) = 0$	$\forall n,\ \frac{\partial \Upsilon_n}{\partial x}\left(x_0^-\right) = \frac{\partial \Upsilon_n}{\partial x}\left(x_0^+\right)$
		$\forall n,\ \frac{\partial^2 \Upsilon_n}{\partial x^2}\left(x_0^-\right) = \frac{\partial^2 \Upsilon_n}{\partial x^2}\left(x_0^+\right)$

Consider for example a clamped-clamped beam at $x = 0$ and $x = L$, then the parameters A_n, B_n, C_n, D_n and λ_n should respect:

$$\begin{bmatrix} 1 & 0 & 1 & 0 \\ 0 & \frac{\lambda_n}{L} & 0 & \frac{\lambda_n}{L} \\ \cos(\lambda_n) & \sin(\lambda_n) & \cosh(\lambda_n) & \sinh(\lambda_n) \\ -\frac{\lambda_n}{L}\sin(\lambda_n) & \frac{\lambda_n}{L}\cos(\lambda_n) & \frac{\lambda_n}{L}\sinh(\lambda_n) & \frac{\lambda_n}{L}\cosh(\lambda_n) \end{bmatrix} \cdot \begin{bmatrix} A_n \\ B_n \\ C_n \\ D_n \end{bmatrix} = \begin{bmatrix} 0 \\ 0 \\ 0 \\ 0 \end{bmatrix} \tag{3.39}$$

For the beam to be in motion, the parameters A_n, B_n, C_n, D_n should be non-null, thus the determinant of the matrix should be null and thus λ_n should respect:

$$\cos(\lambda_n) \times \cosh(\lambda_n) = 1. \tag{3.40}$$

Equation (3.40) has an infinite amount of solutions λ_n. Those solutions are the flexural modes of the beam. The equation cannot be solved analytically and the solutions of it are obtained numerically. Note however, that the coefficient λ_n does not depends on the dimensions of the beam but only on mechanical conditions imposed on the beam. The expression of Υ_n becomes:

$$\Upsilon_n(x) = \Upsilon_{0,n}\left[\cos\left(\lambda_n \frac{x}{L}\right) - \cosh\left(\lambda_n \frac{x}{L}\right) + \beta_n \sin\left(\lambda_n \frac{x}{L}\right) - \beta_n \sinh\left(\lambda_n \frac{x}{L}\right)\right], \tag{3.41}$$

where $\beta_n = -\frac{\cos(\lambda_n)-\cosh(\lambda_n)}{\sin(\lambda_n)-\sinh(\lambda_n)}$ is another coefficient that only depends on λ_n. Finally, the coefficient $\Upsilon_{0,n}$ is determined from the property:

$$\int_0^L \Upsilon_{n_1}(x)\,\Upsilon_{n_2}(x)\,\mathrm{d}x = L \times \delta_{n_1,n_2} \Rightarrow$$
$$\Upsilon_{0,n} = \sqrt{\frac{L}{\int_0^L \left[\cos\left(\lambda_n \frac{x}{L}\right) - \cosh\left(\lambda_n \frac{x}{L}\right) + \beta_n \sin\left(\lambda_n \frac{x}{L}\right) - \beta_n \sinh\left(\lambda_n \frac{x}{L}\right)\right]^2 \mathrm{d}x}}. \tag{3.42}$$

With the properties of $\Upsilon_n(x)$, the Euler-Bernoulli equation becomes:

$$\rho h b \left[\sum_{n=1}^{\infty} \ddot{\mathsf{a}}_\mathsf{n} \Upsilon_n\right] + \xi \left[\sum_{n=1}^{\infty} \dot{\mathsf{a}}_\mathsf{n} \Upsilon_n\right] + c_s I \left[\sum_{n=1}^{\infty} \left(\frac{\lambda_n}{L}\right)^4 \mathsf{a}_\mathsf{n} \Upsilon_n\right] = \mathsf{F}_\mathsf{l}(x,t). \tag{3.43}$$

If the scalar product of the equation is calculate over each $\Upsilon_n(x)$ then n equations are defined[16]:

$$\forall n,\ \ddot{\mathsf{a}}_\mathsf{n} \int_0^L \rho h b \Upsilon_n^2(x)\,\mathrm{d}x + \xi L \dot{\mathsf{a}}_\mathsf{n} + c_{beam} I \frac{\lambda_n^4}{L^3} \mathsf{a}_\mathsf{n} = \int_0^L \mathsf{F}_\mathsf{l}(x,t)\,\Upsilon_n(x)\,\mathrm{d}x, \tag{3.44}$$

If a mass is added on the beam, the parameter $\rho h b$ that represents a mass per unit of length is modified. It should be decomposed into:

$$\rho h b = \rho_{beam} h b + \iint_{\mathcal{A}_{mass}} \rho_{mass} \mathrm{d}y\mathrm{d}z, \tag{3.45}$$

where ρ_{mass} is the density of the added mass and $\mathcal{A}_{mass}$ is the area along the section of the beam occupied by the added mass. From eq. (3.45), the value of $\int_0^L \rho h b \Upsilon_n^2(x)\,\mathrm{d}x$ can be rewritten as:

$$\begin{aligned}\int_0^L \rho h b \Upsilon_n^2(x)\,\mathrm{d}x &= m_{beam} + \iiint_{\mathcal{V}_{mass}} \rho_{mass} \Upsilon_n^2(x)\,\mathrm{d}x\mathrm{d}y\mathrm{d}z \\ &= m_{beam} + \kappa_{mass,n} \Delta m,\end{aligned} \tag{3.46}$$

where $\kappa_{mass,n}$ is a constant that depends on how the mass is added to the beam and on the flexural mode of the beam:

$$\kappa_{mass,n} = \frac{\iiint_{\mathcal{V}_{mass}} \rho_{mass} \Upsilon_n^2(x)\,\mathrm{d}x\mathrm{d}y\mathrm{d}z}{\iiint_{\mathcal{V}_{mass}} \rho_{mass} \mathrm{d}x\mathrm{d}y\mathrm{d}z}. \tag{3.47}$$

The value of $\kappa_{mass,n}$ is given in the following table in the case where the mass is added uniformly to the beam and in the case where the added mass can be considered as punctual.

[16]The scalar product of the function $f(x)$ is defined as: $\int_0^L f(x)\,\Upsilon_n(x)\,\mathrm{d}x$

	Mass added uniformly on the area the beam	Punctual mass located at $x = x_0$
$\kappa_{mass,n}$	$\kappa_{mass,n} = 1$	$\kappa_{mass,n} = \Upsilon_n^2(x_0)$

In the case of punctual mass, the influence of the mass is balanced by $\Upsilon_n^2(x_0)$ and therefore it is not possible to measure its mass without knowing the location of the punctual mass. The phenomenon is described in the articles [Dohn 2005, Lee 2009a, Dohn 2007, Dohn 2010] that also propose solutions overpass this issue.

The maximum displacement of the beam is located at $L/2$ are is denoted $\mathsf{w}(t) = \sum_{n=1}^{\infty} \mathsf{w_n}(t)$, where $\mathsf{w_n}(t) = \mathsf{a_n}(t)\,\Upsilon_n(L/2)$. The equation (3.44) becomes:

$$\forall n,\ m_n \ddot{\mathsf{w_n}}(t) + \frac{m 2\pi f_n}{Q_n}\dot{\mathsf{w_n}}(t) + m(2\pi f_n)^2 \mathsf{w_n}(t) = \Upsilon_n(L/2)\int_0^L \mathsf{F_l}(x,t)\,\Upsilon_n(x)\,\mathrm{d}x, \tag{3.48}$$

where $m_n = m_{beam} + \kappa_{mass,n}\Delta m$. $f_n = \frac{1}{2\pi}\sqrt{\frac{c_{beam} h b^3 \lambda_n^4}{12 m_n L^3}}$ and $Q_n = \frac{2\pi f_n m_n}{\xi L}$ are respectively the resonance frequencies and the quality factor of beam. In the case of small added mass to the beam[17], the resonant frequency behaves as:

$$f_n = \frac{1}{2\pi}\sqrt{\frac{c_{beam} h b^3 \lambda_n^4}{12 m_n L^3}} \approx \frac{\lambda_n^2}{2\pi}\sqrt{\frac{c_{beam}}{12\rho}}\frac{b}{L^2}\left(1 - \frac{\kappa_{mass,n}\Delta m}{2 m_{beam}}\right), \tag{3.49}$$

confirming that the added mass can be measured from the resonant frequency. The corresponding complex amplitude of the mechanical displacement denoted $w(f)$ is calculated from the complex amplitude of $\mathsf{F_l}(x,t)$ denoted $F_l(x)$:

$$\begin{aligned} w(f) &= \sum_{n=1}^{\infty} w_n(f) \\ &= \sum_{n=1}^{\infty} \frac{1}{(2\pi)^2 m_n}\frac{\Upsilon_n(L/2)\int_0^L F_l(x)\,\Upsilon_n(x)\,\mathrm{d}x}{f_n^2 + j\frac{f f_n}{Q_n} - f^2} \\ &= \frac{L F_l}{(2\pi)^2}\sum_{n=1}^{\infty}\frac{\eta_{A,n}}{f_n^2 + j\frac{f f_n}{Q_n} - f^2} \qquad (\text{if } \frac{\partial F_l}{\partial x} = 0), \end{aligned} \tag{3.50}$$

where $\eta_{A,n} = \frac{\Upsilon_n(L/2)}{L}\int_0^L \Upsilon_n(x)\,\mathrm{d}x$ is a parameter that only depends on λ_n. If $F_l(x)$ can be supposed as independent of x, $H_{mecha} = \frac{y}{F_l}$ is equal to a sum of transfer functions $H_{mecha,n}$ defined as:

$$H_{mecha,n} = \frac{\eta_{A,n} L}{m_n (2\pi f_n)^2}\frac{1}{1 + j\frac{f}{Q_n f_n} - \left(\frac{f}{f_n}\right)^2}. \tag{3.51}$$

Figure 3.54 depicts the 5 first modes of $|H_{mecha,n}| / |H_{mecha,1}(f = f_1)|$ in the case where $Q_n = 100$. Around each f_n, the transfer function H_{mecha} can be approximated to $H_{mecha,n}$ of the corresponding mode.

[17] compared to the mass of the beam: $\Delta m = \frac{m_{beam}}{\kappa_{mass,n}}$.

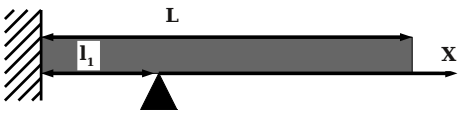

Figure 3.55: Boundary conditions of the crossbeam

Another more complex structure called crossbeam is based on a free-clamped beam with a fixed anchor at a distance l_1 from the clamping (fig 3.55). With the 3 boundary conditions, the general expression of $\Upsilon_n(x)$ is:

$$\begin{cases} \Upsilon_n(x) = A'_n \cos\left(\lambda_n \frac{x}{L}\right) + B'_n \sin\left(\lambda_n \frac{x}{L}\right) + \\ \quad C'_n \cosh\left(\lambda_n \frac{x}{L}\right) + D'_n \sinh\left(\lambda_n \frac{x}{L}\right) & \text{if } x < 0 \\ \Upsilon_n(x) = A_n \cos\left(\lambda_n \frac{x}{L}\right) + B_n \sin\left(\lambda_n \frac{x}{L}\right) + \\ \quad C_n \cosh\left(\lambda_n \frac{x}{L}\right) + D_n \sinh\left(\lambda_n \frac{x}{L}\right) & \text{if } x \geq 0 \end{cases}. \tag{3.52}$$

The boundary conditions imposes that:

$$\begin{cases} A' \cos\left(\lambda_n \frac{l_1}{L}\right) - B' \sin\left(\lambda_n \frac{l_1}{L}\right) + C' \cosh\left(\lambda_n \frac{l_1}{L}\right) - D' \sinh\left(\lambda_n \frac{l_1}{L}\right) = 0 \\ A' \sin\left(\lambda_n \frac{l_1}{L}\right) + B' \cos\left(\lambda_n \frac{l_1}{L}\right) - C' \sinh\left(\lambda_n \frac{l_1}{L}\right) + D' \cosh\left(\lambda_n \frac{l_1}{L}\right) = 0 \\ A' + C' = 0 \\ -A \cos\left(\lambda_n \frac{L-l_1}{L}\right) - B \sin\left(\lambda_n \frac{L-l_1}{L}\right) + C \cosh\left(\lambda_n \frac{L-l_1}{L}\right) + D \sinh\left(\lambda_n \frac{L-l_1}{L}\right) = 0 \\ A \sin\left(\lambda_n \frac{L-l_1}{L}\right) - B \cos\left(\lambda_n \frac{L-l_1}{L}\right) - C \sinh\left(\lambda_n \frac{L-l_1}{L}\right) + D \cosh\left(\lambda_n \frac{L-l_1}{L}\right) = 0 \\ A + C = 0 \\ B' + C' - B - D = 0 \\ -A' + C' + A - C = 0 \end{cases}. \tag{3.53}$$

In order for the solution not to be null, the previous equations should be linearly dependent and therefore λ_n should respect the following condition for a given l_1/L:

$$\frac{1 - \cos\left(\lambda_n \frac{l_1}{L}\right) \cosh\left(\lambda_n \frac{l_1}{L}\right)}{\cos\left(\lambda_n \frac{l_1}{L}\right) \sinh\left(\lambda_n \frac{l_1}{L}\right) - \sin\left(\lambda_n \frac{l_1}{L}\right) \cosh\left(\lambda_n \frac{l_1}{L}\right)} = \frac{1 + \cos\left(\lambda_n \frac{L-l_1}{L}\right) \cosh\left(\lambda_n \frac{L-l_1}{L}\right)}{\cos\left(\lambda_n \frac{L-l_1}{L}\right) \sinh\left(\lambda_n \frac{L-l_1}{L}\right) - \sin\left(\lambda_n \frac{L-l_1}{L}\right) \cosh\left(\lambda_n \frac{L-l_1}{L}\right)}. \tag{3.54}$$

The parameter l_1/L is a design parameter and should be optimized for the crossbeam to achieve the maximum performances. From [Labarthe 2010], it can be shown that the optimum value of l_1/L is $l_1/L = 0.15$. Note that however the following development is valid for any value of l_1/L. The solution of (3.53) provides the

Boundary conditions	λ	Υ_0	β_1	β_2	β_3	β_4	η_A
Clamped-clamped beam	4.73	1.00	-0.98				1.32
Free-clamped beam	1.88	1.00	-0.73				0.53
Crossbeam	2.12	1.00	-4.64	4.80	0.85	-0.70	1.56

Table 3.11: Values of the normalization constants for different types of beam

following expression of $\Upsilon_n(x)$:

$$\begin{cases} \Upsilon_n(x) = \Upsilon_{0,n}\left[-\cos\left(\lambda_n\frac{x}{L}\right)+\cosh\left(\lambda_n\frac{x}{L}\right)+\beta_{1,n}\right. & \\ \left.\sin\left(\lambda_n\frac{x}{L}\right)+\beta_{2,n}\sinh\left(\lambda_n\frac{x}{L}\right)\right] & \text{if } x<0 \\ \Upsilon_n(x) = \Upsilon_{0,n}\left[-\cos\left(\lambda_n\frac{x}{L}\right)+\cosh\left(\lambda_n\frac{x}{L}\right)+\right. & \\ \left.\beta_{3,n}\sin\left(\lambda_n\frac{x}{L}\right)+\beta_{4,n}\sinh\left(\lambda_n\frac{x}{L}\right)\right] & \text{if } x>0 \end{cases}, \tag{3.55}$$

where

$$\begin{cases} \beta_{1,n} = \frac{-1+\cos\left(\lambda_n\frac{l_1}{L}\right)\cosh\left(\lambda_n\frac{l_1}{L}\right)+\sin\left(\lambda_n\frac{l_1}{L}\right)\sinh\left(\lambda_n\frac{l_1}{L}\right)}{\cos\left(\lambda_n\frac{l_1}{L}\right)\sinh\left(\lambda_n\frac{l_1}{L}\right)-\sin\left(\lambda_n\frac{l_1}{L}\right)\cosh\left(\lambda_n\frac{l_1}{L}\right)} \\ \beta_{2,n} = \frac{-1+\cos\left(\lambda_n\frac{l_1}{L}\right)\cosh\left(\lambda_n\frac{l_1}{L}\right)-\sin\left(\lambda_n\frac{l_1}{L}\right)\sinh\left(\lambda_n\frac{l_1}{L}\right)}{\cos\left(\lambda_k\frac{l_1}{l}\right)\sinh\left(\lambda_k\frac{l_1}{l}\right)-\sin\left(\lambda_k\frac{l_1}{l}\right)\cosh\left(\lambda_k\frac{l_1}{l}\right)} \\ \beta_{3,n} = \frac{-1-\cos\left(\lambda_n\frac{L-l_1}{L}\right)\cosh\left(\lambda_n\frac{L-l_1}{L}\right)-\sin\left(\lambda_n\frac{L-l_1}{L}\right)\sinh\left(\lambda_n\frac{L-l_1}{L}\right)}{\cos\left(\lambda_n\frac{L-l_1}{L}\right)\sinh\left(\lambda_n\frac{L-l_1}{L}\right)-\sin\left(\lambda_n\frac{L-l_1}{L}\right)\cosh\left(\lambda_n\frac{L-l_1}{L}\right)} \\ \beta_{4,n} = \frac{-1-\cos\left(\lambda_n\frac{L-l_1}{L}\right)\cosh\left(\lambda_n\frac{L-l_1}{L}\right)+\sin\left(\lambda_n\frac{L-l_1}{L}\right)\sinh\left(\lambda_n\frac{L-l_1}{L}\right)}{\cos\left(\lambda_n\frac{L-l_1}{L}\right)\sinh\left(\lambda_n\frac{L-l_1}{L}\right)-\sin\left(\lambda_n\frac{L-l_1}{L}\right)\cosh\left(\lambda_n\frac{L-l_1}{L}\right)} \end{cases}. \tag{3.56}$$

Finally the coefficient $\Upsilon_{0,n}$ can be determined from the property $\int_0^L \Upsilon_{n_1}(x)\,\Upsilon_{n_2}(x)\,\mathrm{d}x = L\times\delta_{n_1,n_2}$, thus:

$$\begin{aligned} \Upsilon_n^{-2}(x) = &\int_{-l_1/L}^{0}\left[-\cos(\lambda_k x)+\cosh(\lambda_k x)+\beta_{1,n}\sin(\lambda_k x)+\beta_{2,n}\sinh(\lambda_k x)\right]^2 dx+ \\ &\int_{0}^{1-l_1/L}\left[-\cos(\lambda_k x)+\cosh(\lambda_k x)+\beta_{3,n}\sin(\lambda_k x)+\beta_{4,n}\sinh(\lambda_k x)\right]^2 dx. \end{aligned} \tag{3.57}$$

The rest of the development is similar to one of the clamped-clamped beam.

Finally, table 3.11 gives the approximated values of the coefficients λ, Υ_0, β, f_r, η_A for $n=1$ in the case of the clamped-clamped beam, a free-clamped beam and a crossbeam.

Appendix C: comparison of commercial electronic amplifiers

Stand-alone commercial amplifiers are studied in the present section. Usually the input capacitance for high speed amplifiers are of few picofarrad and thus, are close to the value of the input capacitance of an ASIC. One can consider that the connection losses for this electronic implementation are close to the ones of a stand-alone resonator with an ASIC (fig. 2.16). Moreover, commercial amplifiers present less flexibility than in an ASIC: the choice of the amplifier should be made on key characteristics. The figure 3.56 presents a simple model of a commercial amplifier and its noise sources. One can see that for commercial amplifier, not only the voltage noise (i.e. S_{vamp} is the PSD of the amplifier input voltage noise) but also the current noise (i.e. S_{iamp} is the PSD of the amplifier input current noise) should be considered. The amplifier should therefore be chosen to have a low voltage and current noise but also a large bandwidth, low input capacitance and a low input current offset. The latter parameter compared to the output impedance of the resonators and the connection capacitance defines the output offset of the amplifier and should be low compared to the voltage supply.

The signal to noise ratio at the output of the amplifier has the following expression

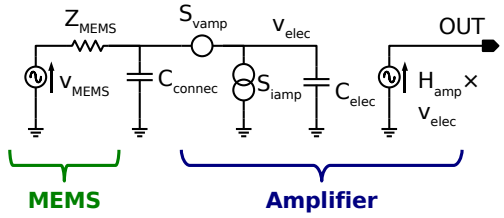

Figure 3.56: Schematic of the MEMS-to-commercial amplifier connection

	Bandwidth	Voltage noise	Current noise
ADA4817	Very high	Low	Very low
AD8099	High	Lowest	High
AD8065	High	High	Lowest
THS4271	Very high	Low	High
OPA657	Very high	Low	Very low

Table 3.12: Characteristics of different commercial amplifier

(the noise from the MEMS resonator is not considered):

$$SNR = \frac{v_{MEMS}}{\sqrt{\left|1 + j2\pi f_{osc} Z_{MEMS} \left(C_{connec} + C_{elec}\right)\right|^2 S_{vamp} + \left|Z_{MEMS}\right|^2 S_{iamp}}} = \frac{v_{MEMS}}{\sqrt{\frac{S_{vamp}}{\left|H_{connec}\right|^2} + \left|Z_{MEMS}\right|^2 S_{iamp}}}. \tag{3.58}$$

Note that the expression of the SNR is only valid if the electronic noise of the following electronic stages is negligible. The gain of the amplifier should therefore be larger than 10 dB with a corresponding bandwidth larger than f_r. The signal to noise ratio was determined for different commercial amplifiers presented in table 3.12. The amplifier have different voltage and current noise and different bandwidths. The figure 3.57 depicts the evolution of the SNR of eq. (3.58) versus different MEMS resonators (the corresponding resonators characteristics are given in table 2.3 and are discussed in section 2.4) and for the presented commercial amplifiers. The SNR of an ASIC co-integrated or not with the MEMS resonator and based on the design rules of subsection 2.3.1 is also depicted in the figure for comparison. If the amplifier has a too small bandwidth to be operated at the resonance frequency of the MEMS (e.g. for the crossbeam), then its corresponding SNR of eq. (3.58) is not depicted. One can see that the performance varies with the amplifier as with the considered MEMS resonator, but overall the performance of the commercial amplifiers are lower than for an ASIC co-integrated or not with the MEMS. It should however be noted that only the noise of the electronics was considered in this study. In the case where the resonator detection transduction is large and the connection losses are low, the noise of the electronics can be neglected and the choice of the commercial amplifier is less relevant.

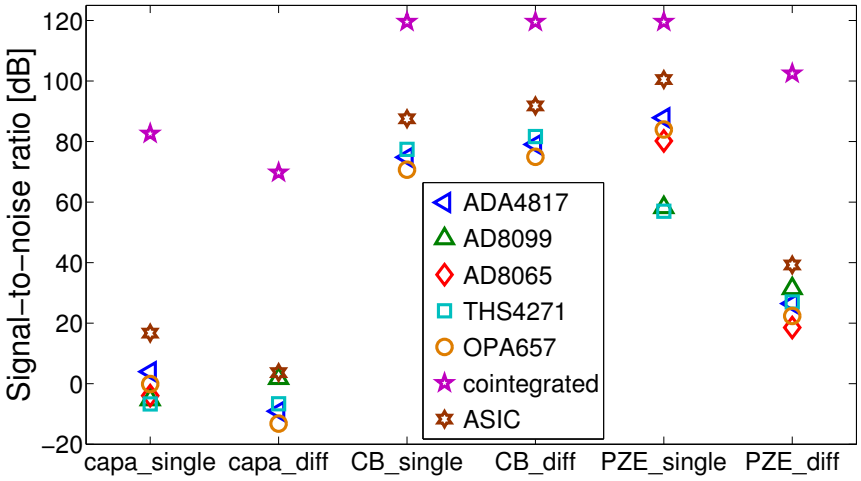

Figure 3.57: Performance of different MEMS resonators for the commercial amplifiers given in table 3.12. "capa" refers to a clamped-clamped beam with capacitive detection, "CB" to crossbeam and "PZE" to piezoelectric cantilever. "single" refers to a single-sided actuation and "diff" refers to a differential actuation.